An experimental study of the stable and unstable operation of an LPP gas turbine combustor.

by

Sulabh Kumar Dhanuka

A dissertation submitted in partial fulfillment
of the requirements for the degree of
Doctor of Philosophy
(Aerospace Engineering)
in The University of Michigan
2008

Doctoral Committee:

Professor James F. Driscoll, Chair
Professor Werner J. A. Dahm
Professor Arvind Atreya
Associate Professor Matthias Ihme

Ekam Satya, Vipro Bahuda Vadanthi
The truth is one, the learned expound it in many ways.
(*The Rig Veda*)

Dedicated to Baba, my maternal grandfather, who led a young boy down a path of discovery and awe, and to my parents, whose love and support have always been my greatest source of strength.

ACKNOWLEDGEMENTS

My time at the University of Michigan has been one that I will never forget and most certainly will benefit me for the rest of my life. I have had the pleasure of working with and learning from not only exceptional individuals but some of the greatest minds in our field. First and foremost, I am extremely grateful for the advising and help provided by Prof. Jim Driscoll. His years of research experience and technical expertise taught me much about doing fundamental research in a manner that would be useful to practical devices and real world engineering. Our numerous discussions over the years in his office, outside on conferences trips to GE (or Dave and Busters), or over fine scotch have no doubt greatly enhanced my grasp of combustion. Often these conversations veered far from our research but were incredibly enjoyable nonetheless. Speaking of which, I feel that Prof. Driscoll you need to purchase some carbon offsets for all the harm that your research (and definitely this one) is causing to the environment. Apart from the technical help offered by him, I am most grateful for the support that he always provided. He picked me up as his student when I was desperately in need and I can never forget that. Furthermore, I could always trust him to boost morale and confidence when things did not go as planned (which was certainly often). New graduate students are always told that the right advisor makes all the difference, and I certainly had a great one.

Most students would be fortunate to have a great advisor, but I actually had the benefit of two. In my initial years here, I worked with Prof. Dahm. It was during that

time that I really gained an appreciation for the beauty of turbulence. His insights into complex problems have served me well throughout my research. Thanks also to Prof. Imhe and Prof. Atreya for taking the time to serve on my defense committee.

I have also had the benefit of working with some of the greatest colleagues one could have. Most of them have also been some of my best friends during this time. Chad Rasmussen and Zac Nagel ensured that my sanity was preserved while working in the FXB. The inception of the 9 AM coffee rule was crucial in getting me (actually all of us) into the building on time and more importantly awake when here. Coffee hour almost certainly became coffee "hour" while the three of us attempted to solve the world's problems. Arguably all three of us would have finished earlier if that time was spent solving our research problems. But what fun would that have been? Photographic evidence exists of one of my most memorable things at Michigan, the moustache competition between the three of us. Alas, I know that was my first and last moustache ever. I appreciate all the help that I received technically from Chad and I learnt a lot while working with him on his project. The lessons learnt there have greatly benefited this project. Zac has been one of my closest friends during my time at Michigan. His generosity and support is something I will always cherish. Most certainly I will take with me memories of working with him in the FXB long hours interrupted by a good friend, TecmoBowl, random discussions, Age of Empires, and more random discussions. Outside the building, Zac taught me to brew beer (useful), finish furniture (perhaps useful), shoot a shotgun (hopefully never needed), and so many more things. Both Pari and I are grateful for the friendship of Zac and Ginelle and we knew that we could always count on having them there when we needed them.

Andy Lapsa has been another good friend and colleague who has contributed

greatly to the successful completion of this project. He spent a lot of time away from his own research to help me take data or discuss the never-ending list of problems. Perhaps one day catalytic combustors will be everywhere and the two of us will get together and remember the time spent working on our initial project. I think it is safe to say that neither of us would regret leaving that even if that day comes. I will remember the nice (weather wise) days of Ann Arbor as those when one of us will try to tempt the other into playing golf. Of course the best days were those when one of us gave into the temptation to head off to Leslie at 2 PM. The other members of the PTCL, or is it PACE (or my personal favorite - the Organization of Combustion Research And Propulsion) have also been very helpful. Danny Micka was always there to run the heater when I needed it and was always willing to drop whatever he needed to get done to get air to me. I am sure that it was a great annoyance for him to replace the paddle each time and I appreciate that. Danny should celebrate as much as me, for Case 1 is finally done. I am sorry that our plans to convert his combustor into the most awesome coffee roaster or the plans to make a pressurized $H_2 - O_2$ potato gun never materialized. Alex Schumaker and Adam Steinberg also provided help through many discussions over all sorts of sweet treats. The quality of their theses and papers will certainly enhance the value of my research. Jacob Temme has been a great help towards the end of my thesis work. He quickly learnt his way around the project and this project could not be handed over to more capable hands. I wish him the best of luck with this project and eagerly await to see the results of his research. Other former students of the Aerospace Engineering department have also been friends in the past years and I will always cherish having known Tom Schwartzentruber, Jeff Sutton, Leo Scalabrin, and Peter Hamlington. They are some of the brightest people I have met and are one of the biggest reasons

I know that my decision to come to Michigan was the right one.

Friends outside of the department ensured that I never forgot the importance of thinking about more than just gas dynamics. Tushar Bansal, Saumil Shah, Akshay Sheorey, Ojas Kulkarni, Shaun D'Souza, Rushali Parikh, Sarika Jain, Sakina Zabuawala, and Alok Jain all have been great friends with whom many a night (sometimes into the morning) and weekends have been spent. Times spent playing Risk or Taboo, enjoying dinner, playing golf, getting the fire started for a barbecue, canoing, listening to music, the list is endless, will always be remembered. If graduate school will remain one of the most memorable times of my life, it is because of friends like them.

We are fortunate in the Aerospace department for having the help of some very talented technicians. Tom "we will take care of it" Griffin, Dave "I will be right up" McLean, Eric "I will get you the air" Kirk, and Terry "this will never work" Larrow are all people who at one time or another ensured that the experiments carried on. Eric was always willing to go and operate the ancient pump even when I had forgotten to ask him in advance. For all the difficulties of working with Terry, the fact remains that he is an incredible machinist. Dave's understanding and knowledge of all things electrical that go into our specific projects is a great asset. It is a shame that the experimental effort of this department has lost someone with his unique skill set. I hope that I will always have the benefit of having such wonderful people to help me.

I must also thank Kishore Kumar, Ustad Nusrat Fateh Ali Khan, and Pink Floyd for their genius. The long nights spent writing this thesis, or for that matter the long nights spent studying for classes that apparently led to this, would have been excruciating (yes even more so) without their music. It will always be a great regret of mine that I was too young when they died (or broke up) to have had the pleasure

of hearing them live.

I have left the people dearest to me for the end. This is for no other reason other than that I have no words sufficient for thanking them. My wife Pari has been my closest friend and greatest supporter all these years. I could not have successfully finished graduate school and this thesis without her love and sacrifice. So many nights and weekends I had to be in the lab while she ensured that I would always return to a warm and loving home. I am excited about the roads I will travel down in the future because she will be by my side.

My family has always been my greatest source of strength. I know that my brother and parents will always be there for me and support me through whatever life will throw at me. My parents believed in me and encouraged me to pursue my aspirations even when that meant sending me halfway across the world and seeing me only rarely. I cannot appreciate enough the sacrifices that they have made, for I would not be writing these words were it not for them. If I have the courage to step onto the tightrope, it is only because I know that they are there as the safety net if I fall. I would have succeeded if I can be the shade of a large tree under which they can lie and rest their tired eyes.

TABLE OF CONTENTS

LIST OF FIGURES

Figure

LIST OF TABLES

Table

CHAPTER I

Introduction

Undoubtedly, one of the biggest drivers of gas turbine combustor technology is the need to reduce the total pollutant emissions. Along with the increased awareness of the harmful effects of emissions from hydrocarbon combustion have come tough regulations around the world that limit the total allowed emissions. A quick survey of the combustion literature confirms that the vast majority of research is motivated by the need to comply with not only current regulations but future ones as well.

The primary emissions from gas turbine engines are carbon-monoxide (CO), unburned hydrocarbons (UHC), and oxides of nitrogen (NO and NO_2, known collectively as NO_x). Of these, NO_x is the primary concern since the majority of emissions is NO_x. For example, in a typical twin engine aircraft, 56.5% of regulated emission mass is NO_x and this number climbs to 90.6% for cruise conditions (Lefebvre (1999)). Though total NO_x emissions from aircraft engines currently comprise only 1% of total NO_x emissions (Fig. 1.1), they are only likely to rise as the number of people taking to the skies continues to increase. Furthermore, aircraft emissions are emitted at higher altitudes where NO_x poses significantly more problems. Starting in 1988, the Committee on Aircraft Environment Protection (CAEP) set down guidelines regulating the NO_x emissions from aircraft engines (Mongia (2003) and Stouffer

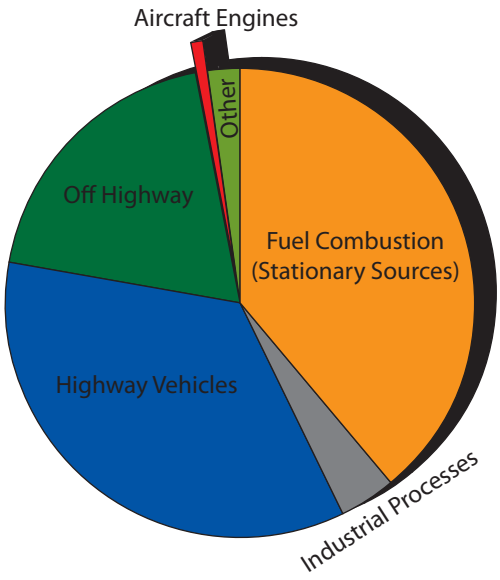

Figure 1.1: The sources of NO_x emissions in the United States in 1999.

et al. (2005)). As shown in Fig. 1.2a, further meetings of CAEP have set lower limits. Regulations such as CAEP and others have most certainly had an impact and total NO_x emissions have been steadily decreasing for the last decade (Fig. 1.2b).

Oxides of nitrogen are formed by three different mechanisms, thermal NO_x, prompt NO_x, and the nitrous oxide mechanism. Of these, thermal NO_x is the most dominant in engine conditions and consists of a sequence of reactions known as the Zel'dovich mechanism. Due to the high activation energy of these reactions, thermal NO_x is important only at temperatures over 1800 K (Correa (1992) and Law (2006)). There is also a clear positive correlation between residence times and total NO_x production, although NO_x production becomes less dependent on the residence time at very low equivalence ratios (Anderson (1975)). Clearly therefore, the best strategies for reducing NO_x emissions from engines is to reduce (or eliminate) any regions of high temperatures and keep residence times to a minimum. It is interesting to note that the opposite strategies are best for reducing CO emissions since high temperatures and long residence times are typically required for ensuring the oxidation of

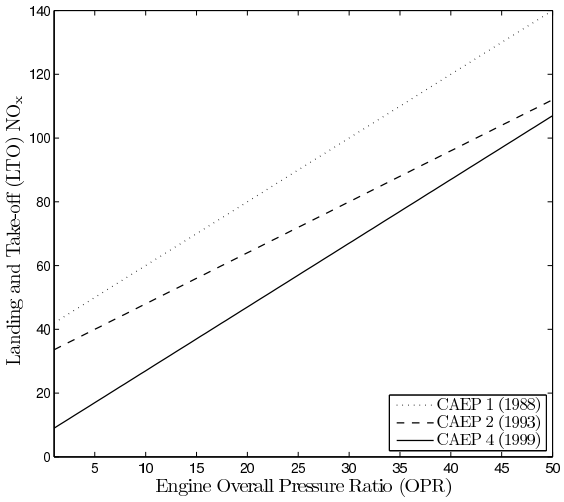

(a) Maximum allowed NO_x emissions during LTO as per the Committee on Aviation Environment Protection (CAEP).

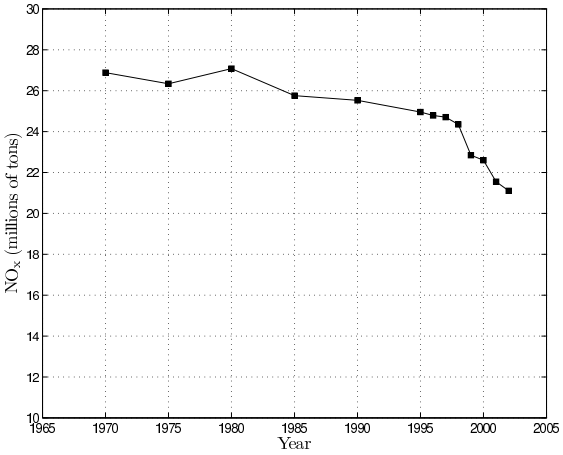

(b) Total NO_x emissions in the United States.

Figure 1.2: Regulations governing NO_x emissions by aircraft engines and total NO_x emissions over the last three decades.

CO to CO_2. Emissions of NO_x however remain the primary concern and the Lean Premixed Prevaporized (LPP) mode of combustion holds the most promise (Correa (1992)).

LPP combustion refers to a combustor design where the ideal is combustion with a homogeneous mixture of fuel and air at equivalence ratios close to the lean blowout limit. For liquid fuels, a homogeneous mixture also requires that the fuel spray be completely vaporized and mixed with the air prior to reaching the flame front. Since the highest temperatures in a flame are usually at the stoichiometric contour, a lean mixture ensures that localized regions of high temperature do not exist anywhere in the combustor. In most modern gas turbine combustors, low residence times are obtained by the use of swirling air which enhances mixing and ensures short flames. However, if it can be ensured that temperatures are low everywhere (below 1800 K), then residence times are no longer an important factor.

All LPP combustors feature two principal components or stages. The first is a section where fuel is injected into the primary air stream. The purpose of this stage is to vaporize the fuel and mix it with the air to produce a homogeneous mixture of reactants at a low equivalence ratio. This is typically accomplished by injecting the fuel as a spray into a cross-flow of swirling air (§1.2.2). It is assumed that prior to reaching the flame, the incoming reactants are a perfectly mixed mixture of gaseous fuel and air. The second stage provides a stable flame location typically through a sudden expansion and recirculation zone(s) created through vortex breakdown (§1.2.1). As is often the case however, the recirculation zones by themselves are insufficient to hold the flame and the use of a diffusion pilot flame is necessary. To the author's knowledge, all LPP combustors currently employ some form of a pilot flame that ensures stable combustion of the primary LPP main mixture.

While LPP combustion ideally offers one of the best strategies for reduced NO_x, there are a number of challenges that limit its performance. First, safety concerns due to the possibility of autoignition and flame flashback limit the distance available for the complete vaporization and mixing of the fuel. Second, as discussed in §1.2.3, operation of LPP combustors near the lean extinction limit naturally puts the combustor at risk of flame blowout or combustion instabilities. General Electric's (GE) Aircraft Engines division has developed an LPP combustor with a novel injector called the Twin Annular Premixed Swirler (TAPS) that hopes to obtain the possible reduction in NO_x emissions while mitigating many of the difficulties encountered with LPP combustors. LPP combustors represent a very complicated geometry and present great challenges to the understanding of their operation.

1.1 Motivation and Approach

This project was funded by GE to probe the TAPS combustor and obtain high quality data for comparison with results from their own modelling efforts. Gutmark and co-workers (Li and Gutmark (2005) and Li and Gutmark (2004)) and Jeng and co-workers (Fu et al. (2005a) and Fu et al. (2005b)) have investigated the flow within the TAPS combustor and the closely related Twin Annular Research Swirler (TARS) combustor. Other researchers have also studied simpler idealizations of gas turbine combustors (known in the literature as model gas turbine combustors) with laser diagnostics. Isothermal flow fields have been obtained by Panduranga Reddy et al. (2006), Al-Abdeli and Masri (2003), and Al-Abdeli and Masri (2004) amongst others. Meier and co-workers (Sadanandan et al. (2008), Weigand et al. (2006), and Meier et al. (2006)) have utilized a number of advanced laser diagnostics to study the flow field and flame in a confined geometry with swirling air. All these studies however have either been non-reacting or with simple gaseous hydrocarbon fuels (typically methane). Furthermore, all of the combustors were operated at atmospheric pressures. While the results of these studies have increased our understanding of gas turbine combustors, there is a need to obtain data in more realistic conditions. Computational efforts such as those by Menon and Patel (2006) and simple experiments (Mie scattering) in realistic conditions by Seyfried et al. (2007) have begun to obtain results for conditions closer to the operating line of an engine. Clearly however, high quality data on the flow field and flame characteristics are needed.

This study was motivated by the need to obtain the flow field within a gas turbine combustor operating in an LPP mode. Specifically, there is a need to capture the primary flow features such as shear layers and recirculation zones. A quantita-

tive understanding of their location(s) and strength(s) is needed to not only provide data for model validation but also aid in furthering our knowledge of the complex flow. Furthermore, the instantaneous flow field is of great interest since vortex structures are often absent in the mean. Therefore, a key objective was to obtain the instantaneous velocities and associated derived quantities in the combustor for both isothermal and reacting conditions.

A second important objective was regarding the location and structure of both the pilot and main flames. The interaction of the flow and reaction zones is important in all reacting turbulent flows and the desire to obtain flame data was a major motivation of this study. As stability poses a considerable problem for LPP combustors, a third objective of this work was to understand the mechanism(s) behind the observed low frequency flame oscillations. The focus of this part of the research was to not only report the conditions under which they occur but also characterize and model them. All of these objectives involved extending existing diagnostics to realistic gas turbine conditions. There are no studies to the author's knowledge that have utilized well established diagnostics such as Particle Image Velocimetry (PIV) and Planar Laser Induced Fluorescence (PLIF) in pressurized combustors running with Jet-A. In order to accomplish the stated objectives therefore, these diagnostics had to be enhanced to work in the conditions studied here.

A unique high pressure combustor facility was designed and fabricated to obtain data in realistic gas turbine combustor conditions. The desire to obtain planar data at those conditions necessitated high optical access for laser sheets and imaging purposes. The flow field was obtained quantitative by PIV. The flame data were obtained by PLIF. As noted earlier, problems associated with both of these diagnostics had to be solved to utilize them in this combustor. In the case of PLIF, calibration

experiments were conducted to assess CH_2O PLIF through simultaneous CH CH_2O PLIF in an unconfined calibration burner. The instability mechanism was developed through the use of the PIV and PLIF data in conjunction with simultaneous high speed pressure and chemiluminescence measurements. It is hoped that the data and analysis presented here will be used to not only assess the accuracy of simulations but will serve to help develop better models and better engines.

1.2 Review of Fundamental Concepts

A number of key concepts developed from simpler configurations by former researchers aids in the understanding of the flow and combustion within the TAPS combustor. Some of these concepts will be discussed in this section.

1.2.1 Vortex Breakdown

It has been known for some time now that a similar change as is observed in vortex cores over the leading edge of delta wings also occurs in a circular duct when the flow has a sufficient amount of swirl. The change in the structure of the vortex is marked by a sudden change in the axial velocity causing a forward stagnation point and local flow reversal. This phenomenon has been termed vortex breakdown and numerous reviews exist in the literature, namely by Hall (1972), Leibovich (1978), Escudier (1988), and most recently by Lucca-Negro and O'Doherty (2001). While a number of theories (some contradictory) have been developed over the years to explain the behavior, the observed experimental trends have in general been consistent across numerous experiments. Vortex breakdown plays an important role in swirl combustors for its ability to generate a localized region of reversed flow that provides the requisite flame stabilization. It is for this reason that swirl combustors have remained such a popular choice over the years for practical combustors (Syred

and Beér (1974)). The GE TAPS combustor also falls under the category of swirl combustors and therefore an understanding of the phenomenon of vortex breakdown is needed to help interpret the velocity results in the TAPS combustor.

In general, vortex breakdown is characterized by the presence of a recirculation zone in a flow that otherwise has only one direction. It has been observed that the initiation of vortex breakdown is heavily dependent on the swirl number and only very weakly dependent on the Reynolds number. The non-dimensional swirl number is defined as the ratio of the angular to the axial momentum of the flow (Beér and Chigier (1983)). In practice it provides (or is obtained from) the ratio of the azimuthal velocity to the axial velocity. For combustors such as the GE TAPS that generate swirl through fixed geometry vanes therefore, the swirl number is a constant for all flow conditions. Escudier and Keller (1985) show that a transition from supercritical to subcritical flow is required for vortex breakdown to occur. Importantly, the rule of thumb provided by Squire (1960) is useful. Here, a flow is subcritical if the maximum swirl velocity exceeds the axial velocity. The experimental trends show that if the swirl exceeds a critical swirl number, then vortex breakdown occurs and a recirculation zone is established along the centerline of the combustor. With further increase in the swirl number, another critical swirl number is reached where this recirculation zone merges with the wake of a flow obstacle such as the fuel injector. It is important to note therefore that any recirculation zone in the wake of the injector in a swirl combustor is due to the combined effect of the wake and vortex breakdown.

It has also been observed by researchers that a favorable pressure gradient (in the general flow direction) moves the vortex breakdown location further upstream and aids in returning the flow to a supercritical state by increasing the axial velocity.

This also explains why the presence of an obstacle by way of an injector promotes vortex breakdown and often moves the breakdown region upstream to a point where it merges with the wake. The return to a supercritical state also has the effect of "closing" the recirculation zone and creating a rear stagnation point such that the flow downstream of this point is in the positive axial direction. This is a desired result and in practice the favorable gradient is created by a contraction in the exit area of the combustor (or duct). As the contraction is increased, the rear stagnation point moves upstream (Li and Gutmark (2005)) and Escudier and Keller (1985) and Chao et al. (1991) have shown that for sufficient contractions, the point could move upstream enough so that no flow reversal exists on the centerline. In such a condition, distinct recirculation zones would exist on either side (also known as a toroidal recirculation zone) of the centerline with the flow along the centerline being positive. This effect is shown in Fig. 1.3a where the an open duct (no contraction) creates an "open" recirculation zone with no rear stagnation point. With a contraction, a rear stagnation point is created (Fig. 1.3b) and further contraction pushes the rear stagnation point upstream (Fig. 1.3c).

While an area contraction provides a reliable means of generating increased axial velocities, combustion offers another way of affecting the vortex breakdown. With the reduction in gas density across the flame, mass conservation requires that there be a corresponding increase in the axial velocity. Since the swirl velocity is not greatly affected by the heat release, the increase in axial velocity will serve to return the flow to a supercritical state from a subcritical state. This return to a supercritical state would also ensure that the recirculation zone is closed. Combustion therefore will drastically affect the size and shape of any recirculation zone created by vortex breakdown. The numerical results shown in Fig. 1.4 confirm this result.

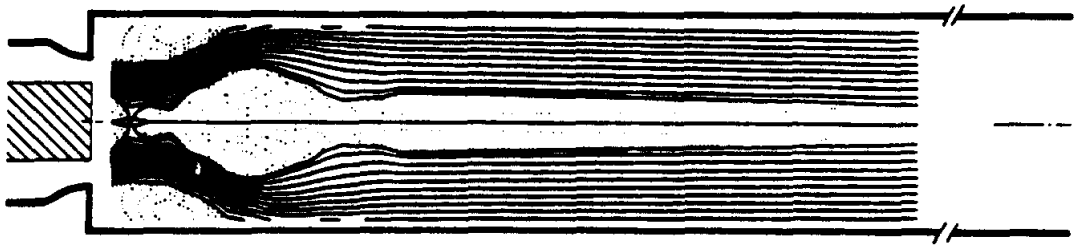

(a) Vortex breakdown in a duct with no contraction.

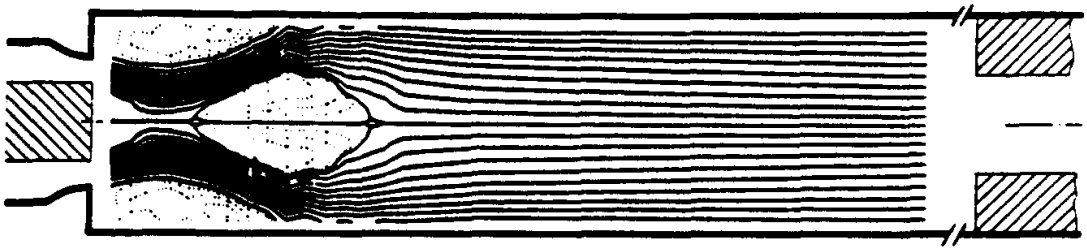

(b) Vortex breakdown in a duct with contraction.

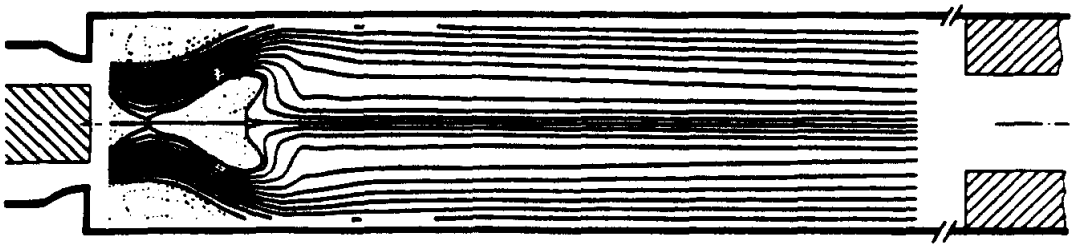

(c) Vortex breakdown in a duct with a higher contraction than (b).

Figure 1.3: Schematic of the vortex breakdown process in a non-reacting swirling flow with a bluff centerbody. The images are reproduced from Escudier (1988).

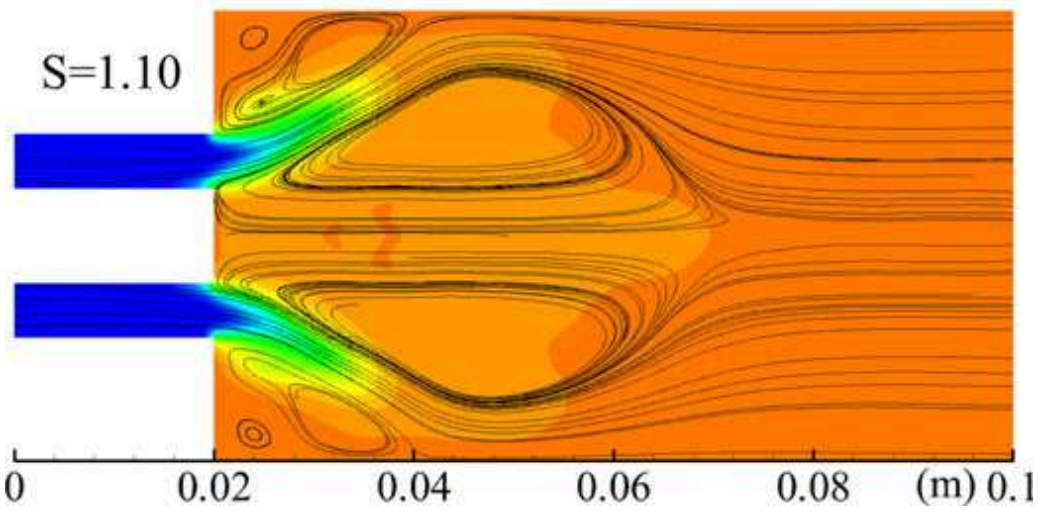

Figure 1.4: Vortex breakdown in a reacting swirling combustor. The image is taken from Huang and Yang (2005).

1.2.2 Spray in a Crossflow and Droplet Combustion

The injection of a liquid jet in a crossflow is one of the most popular means of achieving premixing of the fuel and air upstream of the combustor. In this simple configuration, the liquid fuel is injected perpendicular to a high velocity stream of air to allow pressure and viscous forces to atomize the fuel and mix it with the air to achieve the desired equivalence ratio. The efficiency of this process therefore is of critical importance both to the overall pollutant emissions (Lyons (1981) and Fric (1993)) and combustor stability. The breakup of both liquid jets (Schetz and Padhye (1977); Less and Schetz (1986); Wu et al. (1997); Mazallon et al. (1999)) and sprays (Leong et al. (2001) and Ghosh and Hunt (1998)) in a crossflow has been studied by many researchers. A basic understanding of the breakup process has shown that the process is governed by two mechanisms, surface breakup and column breakup. These two mechanisms are shown schematically in Fig. 1.5. In the first mechanism, called

surface breakup, viscous forces cause large droplets to be sheared and stripped off the surface of the liquid jet. In column breakup, fuel ligaments and droplets are formed from instability waves on the surface of the liquid jet column. As these instabilities grow, the jet finally ruptures at a wave trough. Both of these mechanisms continue to produce finer droplets from the ligaments or larger droplets. In general it has been found that the dominance of one mechanism over another is governed by the non-dimensional Weber number (We) defined as:

$$We = \frac{\rho_\infty U_\infty^2 D}{\sigma_l} \tag{1.1}$$

where ρ_∞ and U_∞ are the density and velocity respectively of the crossflowing air, σ_l is the surface tension of the liquid jet, and D is the injector diameter. Another important parameter is the liquid/air momentum ratio (q) defined as:

$$q = \frac{\rho_{liq} U_{liq}^2}{\rho_\infty U_\infty^2}. \tag{1.2}$$

It has been shown however that at high values of q, the breakup mechanism is only a function of the Weber number (Mazallon et al. (1999)). At high Weber numbers, surface breakup dominates and most of the droplets are formed by the shear imparted by the high velocity air stream (Rachner et al. (2002) and Gopala et al. (2007)). Since the surface breakup mechanism is able to produce a finer mist of liquid fuel, higher Weber numbers are desired.

While a considerable body of literature exists on the breakup process and resulting droplet distributions, there has been surprisingly little research on liquid Jet-A fuels injected in a preheated crossflow at elevated pressures. As the breakup process and droplet vaporization are so dependent on temperature and surface tension, these are big gaps in the literature. Also surprising is the fact that no one to date has attempted to measure or characterize the equivalence ratio distribution downstream

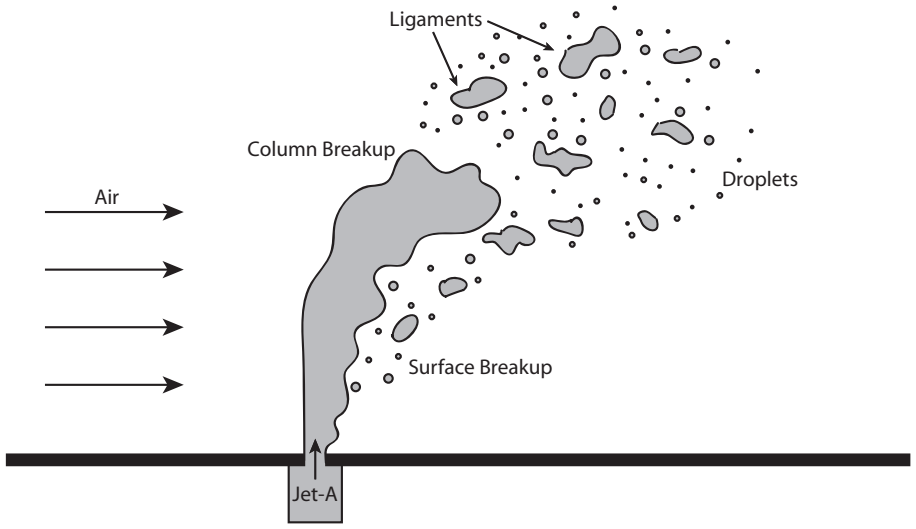

Figure 1.5: Schematic of breakup of a liquid jet injected into an air crossflow. Adapted from Wu et al. (1997).

of the injector. Since the performance of LPP gas turbines relies heavily on this efficient mixing, it is important to gain an understanding on the mixedness of the fuel vapor and air. These issues must be addressed in the research community to better our understanding of a vital process in LPP combustors.

1.2.3 Gas Turbine Combustor Instability Mechanisms

The occurrence of combustion driven instabilities continues to present one of the biggest impediments to the development of low emissions gas turbine combustors. Combustion dynamics cost the industry in excess of $1 billion annually and can account for up to 70% of the non-fuel costs in certain classes of engines (Lieuwen and McManus (2003)). Besides being potentially damaging to the engine, combustion dynamics severely limit the operation envelope of gas turbines and prevent the achievement of their promised reduced emissions levels. These instabilities are aided by the fact that designs for low emissions are ideally suited for driving combustion instabilities. For example, combustors are operated in a lean premixed fashion which is often near the lean blowout point for reducing NO_x levels. Being on the stability

line therefore only makes the combustor more susceptible to perturbations.

The vast majority of combustion instabilities can be described as thermo-acoustic instabilities where the heat release fluctuations and pressure fluctuations couple leading to self-sustained oscillations near the acoustic frequency of the combustor. For almost all practical combustors, this typically translates into frequencies in the hundreds of Hertz or even higher in certain cases. Two primary mechanisms have emerged in the literature for explaining the onset of acoustic instabilities, flame-vortex interactions and feed system coupling. In the flame-vortex interaction mechanism (Poinsot et al. (1987), Schadow et al. (1989), and Lee and Santavicca (2003)), it is assumed that the fluctuations in the flame surface area caused by vortex stretching lead to fluctuations in the total heat release. As the vortices shed by the injector pass through the flame front, they either enhance the reactions or cause local extinction leading to a reduction in the heat release. These heat release fluctuations then have the potential to excite the combustor's natural acoustic frequencies. Lee et al. (2000), Lieuwen et al. (2001), and Lieuwen and Zinn (1998) have explained the feed system coupling mechanism as another potential driver of combustion instabilities. In this mechanism, pressure fluctuations in the combustor lead to fluctuations in the fuel flow causing changes in the equivalence ratio of the reactants arriving at the flame front. Since there is typically some finite length between the fuel injection location and flame front, these fluctuations can amplify the pressure fluctuations if the equivalence ratio fluctuations arrive at the flame front in-phase with the pressure fluctuations. As Venkataraman et al. (1999) have shown, often both of these mechanisms are responsible for combustion instabilities.

As this study has shown however, another form of combustion dynamics exists at frequencies considerably lower than an acoustic frequency. These dynamics are

caused by flashback associated with convective flow reversal. Similar low frequency oscillations caused by flashback have been observed by Plee and Mellor (1978), Keller et al. (1982), Coats (1980), and Vaneveld et al. (1982) amongst others. As explained by Najm and Ghoniem (1994), these low frequency oscillations are often dangerous for the combustor and can be a precursor to other acoustic instabilities. As such, while many practical combustors may experience more problems with acoustic instabilities, lower frequency combustion oscillations can prove to be equally problematic for the operation of LPP combustors.

1.3 Outline

Chapter 2 details the facilities and experimental techniques utilized in this study. The UofM TAPS combustor is described in detail and provides a description of not only the facility but the manner of its operation. A variety of non-intrusive (including laser based) diagnostics was utilized to probe the velocity and flame and are presented in this chapter. To assist in the interpretation of the formaldehyde PLIF results, PLIF of formaldehyde was conducted in a simple lab burner and those findings are included in Chapter 2. Chapter 3 presents the data from formaldehyde PLIF in the TAPS combustor and analysis of both the mean and instantaneous flame location and structure is contained there. The velocity results from Particle Imaging Velocimetry (PIV) for a range of operating conditions, both non-reacting and reacting, are in Chapter 4. Finally, the blowout and stability limits of the TAPS combustor under the studied conditions are presented in Chapter 5. The results of this section have allowed the development of an instability mechanism that is shown to successfully predict the stability limits and frequencies of the combustion instabilities. Chapter 6 contains a summary of the main conclusions from this study.

CHAPTER II

Facilities and Experimental Techniques

Experiments were conducted in a combustor facility designed to house a single GE CFM-TAPS fuel injector. The facility and the design of the GE TAPS injector are described in this chapter. The diagnostics used in this study are also presented here.

2.1 University of Michigan Gas Turbine Combustor

The Michigan Gas Turbine Combustor was designed to operate the GE TAPS flametube at high flowrates of preheated air and at elevated pressures with liquid Jet-A as the fuel. The facility is shown schematically in Fig. 2.1. Air used in the operation of the combustor was supplied through external air tanks that were pressurized to about 138 bar by an Ingersoll Rand compressor. This air was regulated by a dome regulator and heated by a 250 kW Hynes electric heater, both of which are housed in the Supersonic Combustor Lab. This facility has been used by many past studies of supersonic combustion such as those of Yoon (1994), Bryant (1998), Nakagawa (2001), and Rasmussen (2006). For this work however, the output of the heater was diverted to the Gas Turbine Combustor Lab which is located in another lab room of the FXB building.

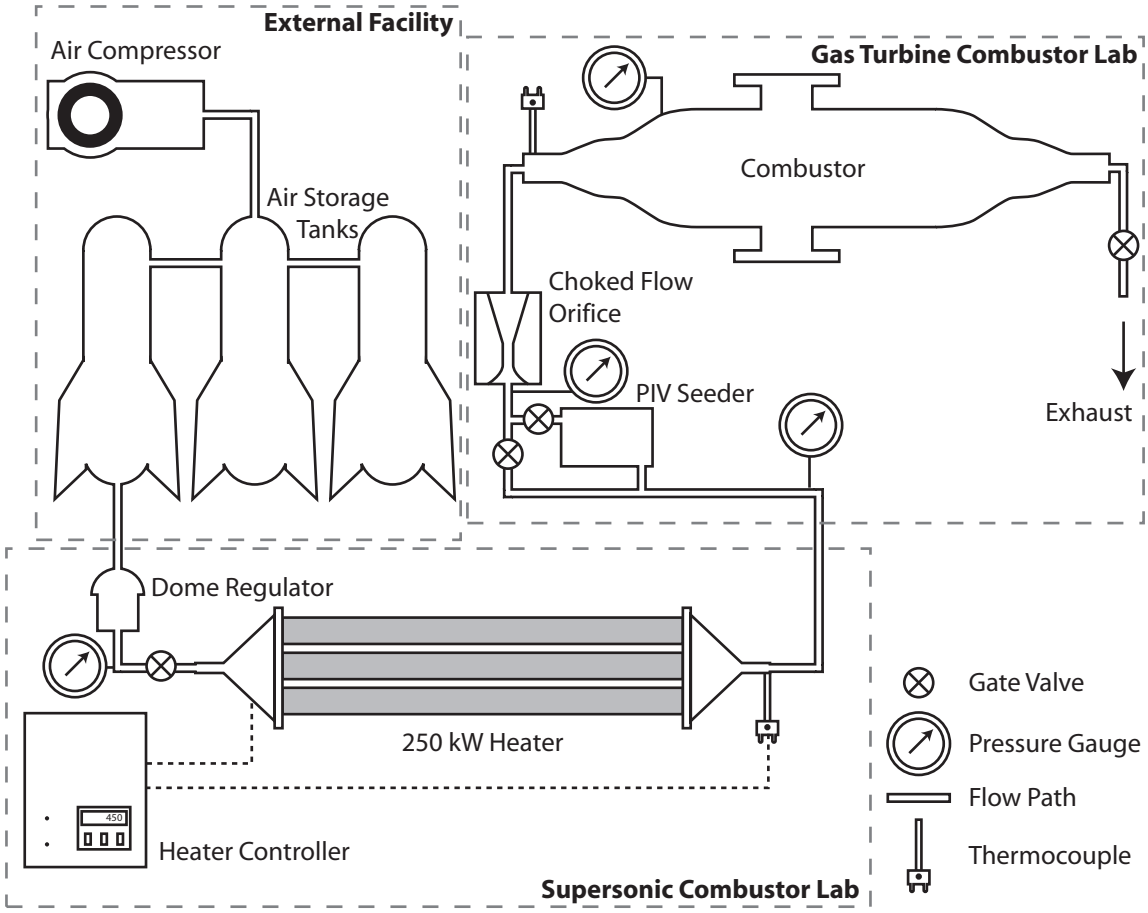

Figure 2.1: The infrastructure supporting the operation of the University of Michigan Gas Turbine Combustor Lab.

Heated air was brought to the GT Combustor Lab via insulated 2" pipes and was metered by a custom built choked flow orifice (Fox Valve). The orifice has a throat diameter of 0.55" and a pressure gauge upstream of the orifice provided an accurate reading of the total air mass flowrate through the combustor. Provided that the orifice was choked, the air mass flowrate (in kg/s) as a function of pressure (in Pa) and temperature (in K) was calculated by using the equation for the mass flowrate through a throat,

$$\dot{m} = \sqrt{\frac{\gamma}{\mathrm{R}}\left(\frac{2}{\gamma+1}\right)^{\frac{\gamma+1}{\gamma-1}}}\frac{p_0 A^*}{\sqrt{T_0}} = 6.20\times10^{-6}\frac{p_0}{\sqrt{T_0}}. \tag{2.1}$$

The use of a choked orifice to meter the flowrate allowed the combustor pressure to be varied without changing the air mass flowrate. A gate valve downstream of the combustor just prior to the exhaust was used to adjust the combustor pressure.

2.1.1 The University of Michigan Gas Turbine Combustor

A custom combustor was fabricated to house the GE TAPS fuel injector and the corresponding flametube. The combustor as shown in Fig. 2.2 was designed to handle high flowrates of preheated air and safely be pressurized to up to 10 bar. To ensure ease of machining, the primary vessel was fabricated from an off-the-shelf 8" Schedule 40 stainless steel pipe. Three commercial sight windows (Ernst Flow) fitted with 5" diameter fused-silica windows provided optical access from the outer vessel. As shown in Fig. 2.3, the three sight windows allowed the laser sheet to enter and exit the combustor from opposing windows to minimize signal noise due to internal reflections. A 5" diameter pipe section attached to the bottom of the combustor accommodates the TAPS injector and allows for fuel connections to be made through the flange attached to the 5" pipe section.

The fuel used for all experiments was commercial Jet-A (supplied by AvFuel).

Instead of a using a fuel pump, the fuel delivery system was as shown in Fig. 2.4. A tank was filled with liquid Jet-A and pressurized to about 8 bar with nitrogen. The pressurized fuel was then delivered to both the pilot and main injectors and metered by calibrated rotameters. The use of a pressurized fuel tank creates a reliable pressure drop and avoids flowrate fluctuations commonly associated with mechanical pumps. Furthermore, with this system, one fuel tank could supply fuel to both the pilot and main fuel injectors.

A flow conditioning section was added upstream of the primary combustor to ensure a symmetric air profile entering the combustor. The section was fabricated from a 15 inch long 8" diameter Schedule 40 stainless steel pipe section and consisted of a 6" porous plate with 0.5" diameter holes, two layers of packed 0.5" glass beads, and a 1.0" thick honeycomb. The flow conditioning section provided the distance and tortuous path necessary to obtain a uniform profile across the eight inch combustor. This was especially important because of the sudden expansion from the 2" supply line to the 8" combustor via two off-the-shelf diffuser sections as shown in Fig. 2.2. Photos of the combustor are shown in Fig. 2.5.

The inner combustor can was supplied by GE Aircraft Engines and it accommodated the TAPS fuel injector. An array of 0.125" diameter holes downstream of the combustion zone allowed cool dilution air to be entrained into the hot products. This arrangement allows the inner combustor walls to be cooled in the same manner as real gas turbine combustors. The total air flowrate therefore was split between the TAPS fuel injector and the downstream cooling holes with the split defined by the area blockage ratio between the two paths. It was not possible to separately meter the two streams and the air mass flowrates were determined a posteriori through the velocity measurements.

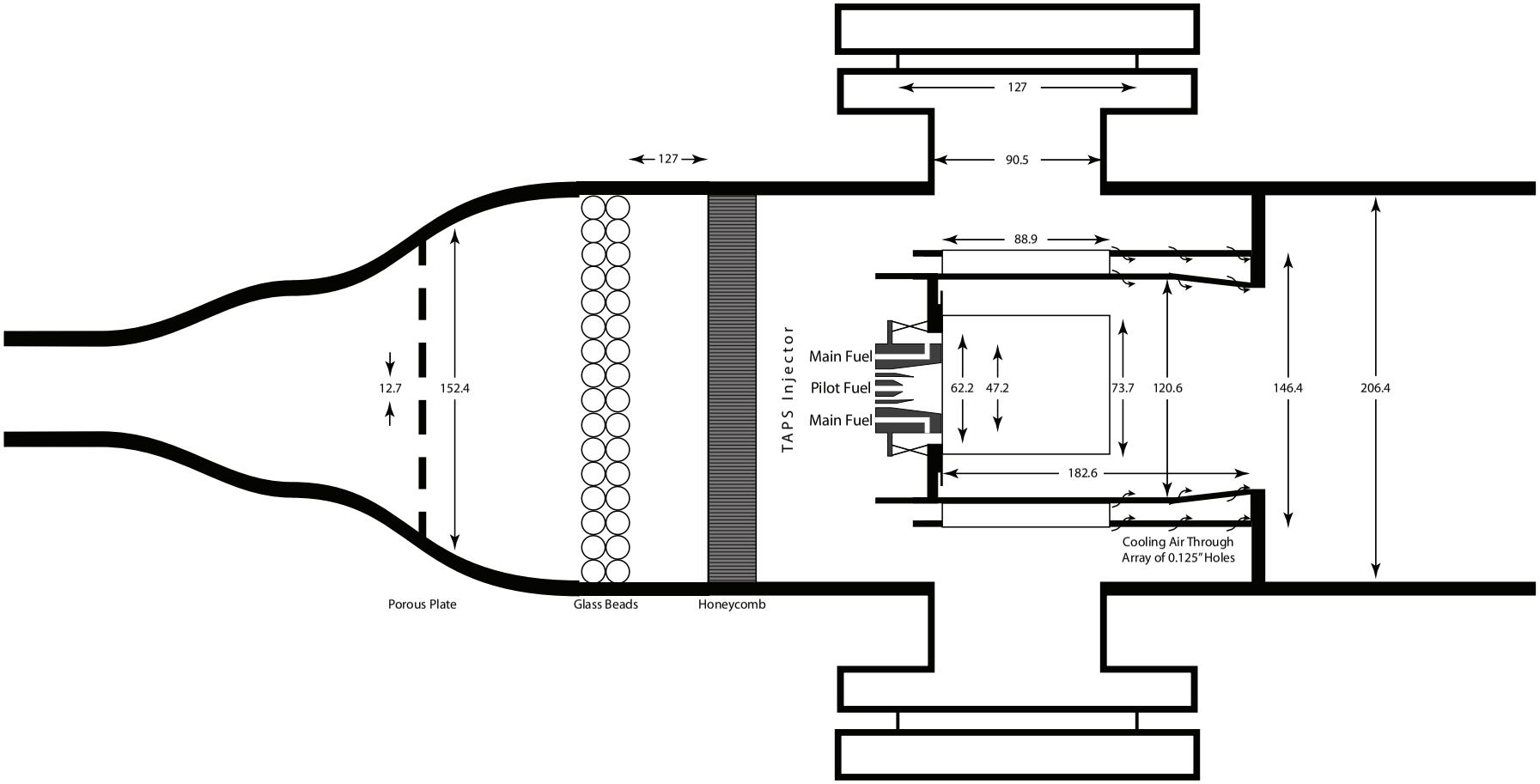

Figure 2.2: Schematic of the UofM GT Combustor designed to house the GE TAPS fuel injector. The flow conditioning section is not shown to scale for clarity and is 600 mm long, consisting of a porous plate, two layers of 1" diameter glass beads, and a 1" thick honeycomb. The TAPS injector is shown in dark grey. The inner rectangle indicates the inner fused-silica glass window and shows the available optical access. All dimensions are in mm.

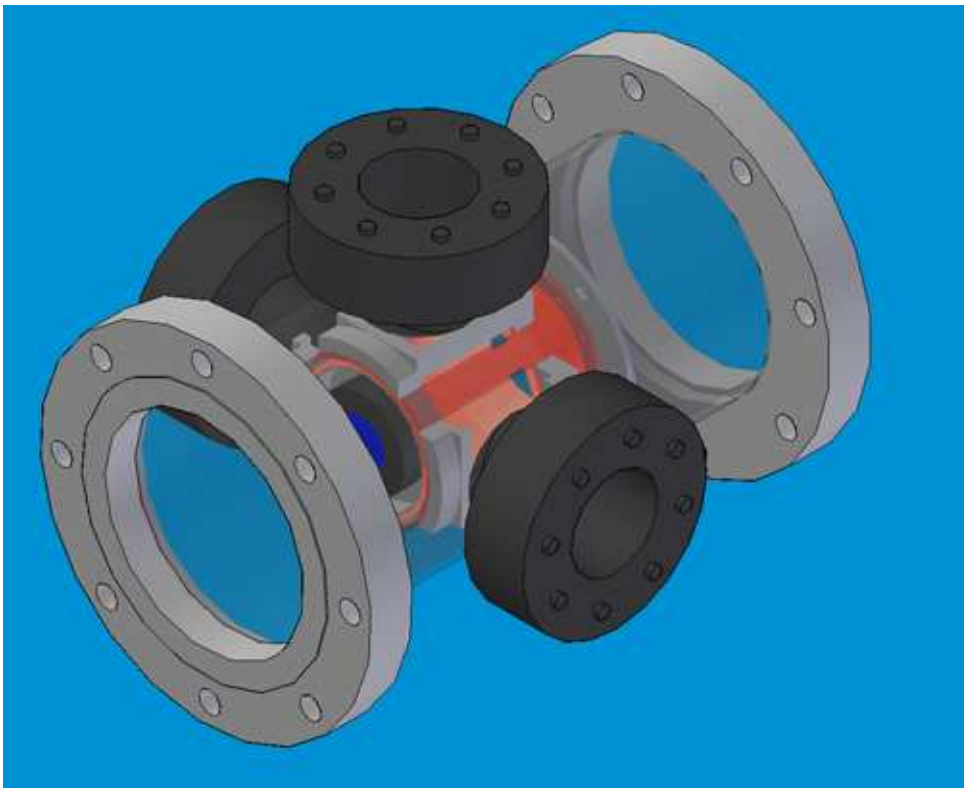

Figure 2.3: A three-dimensional rendering of the combustor showing the placement of the sight windows and the GE TAPS injector within the UofM GT Combustor.

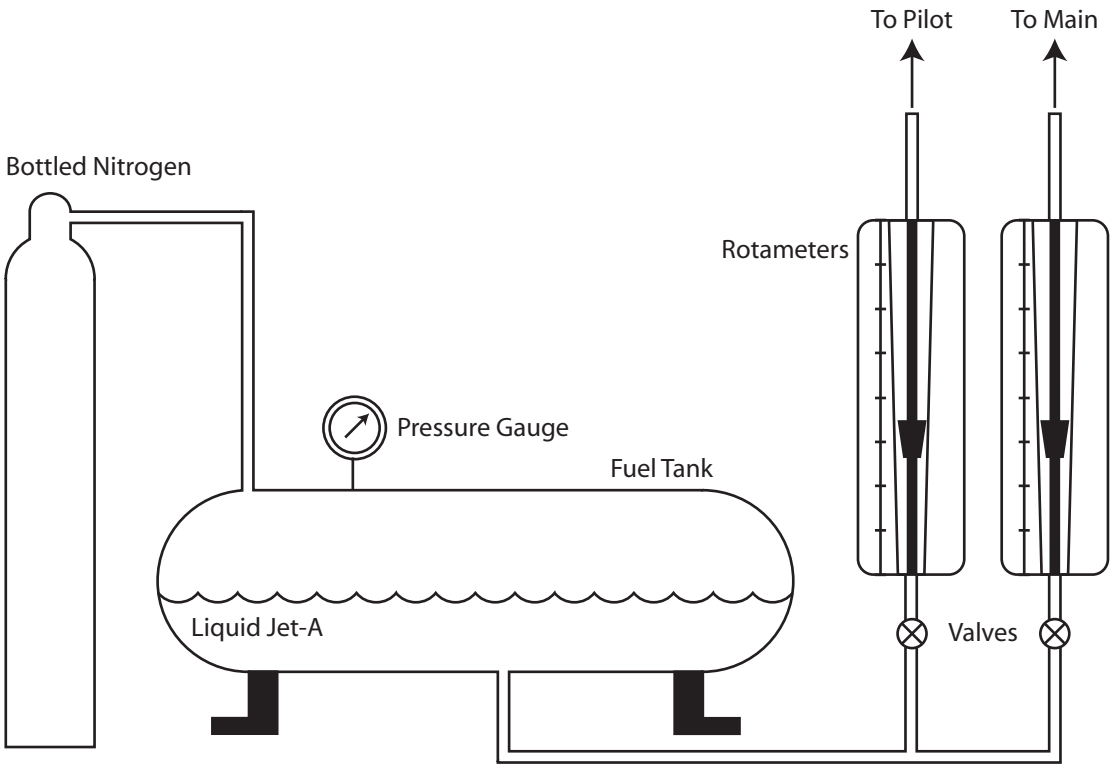

Figure 2.4: Schematic of the fuel delivery system.

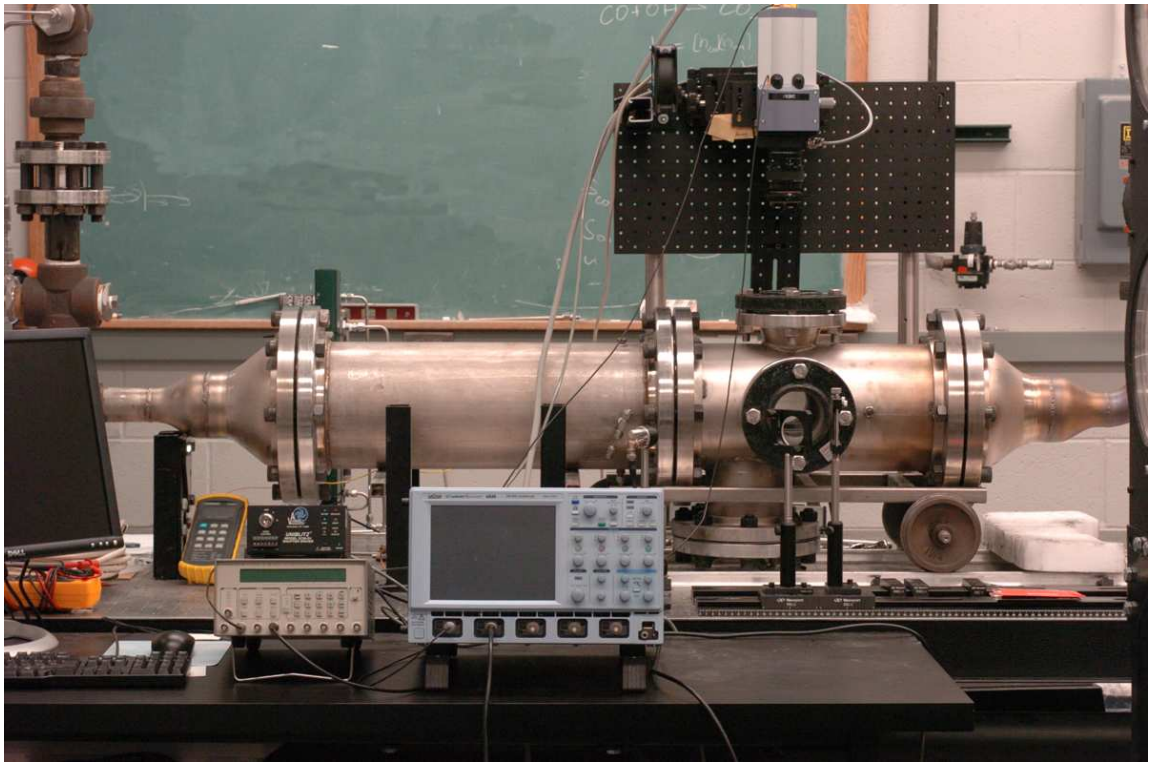

(a) Photo of the Gas Turbine Facility.

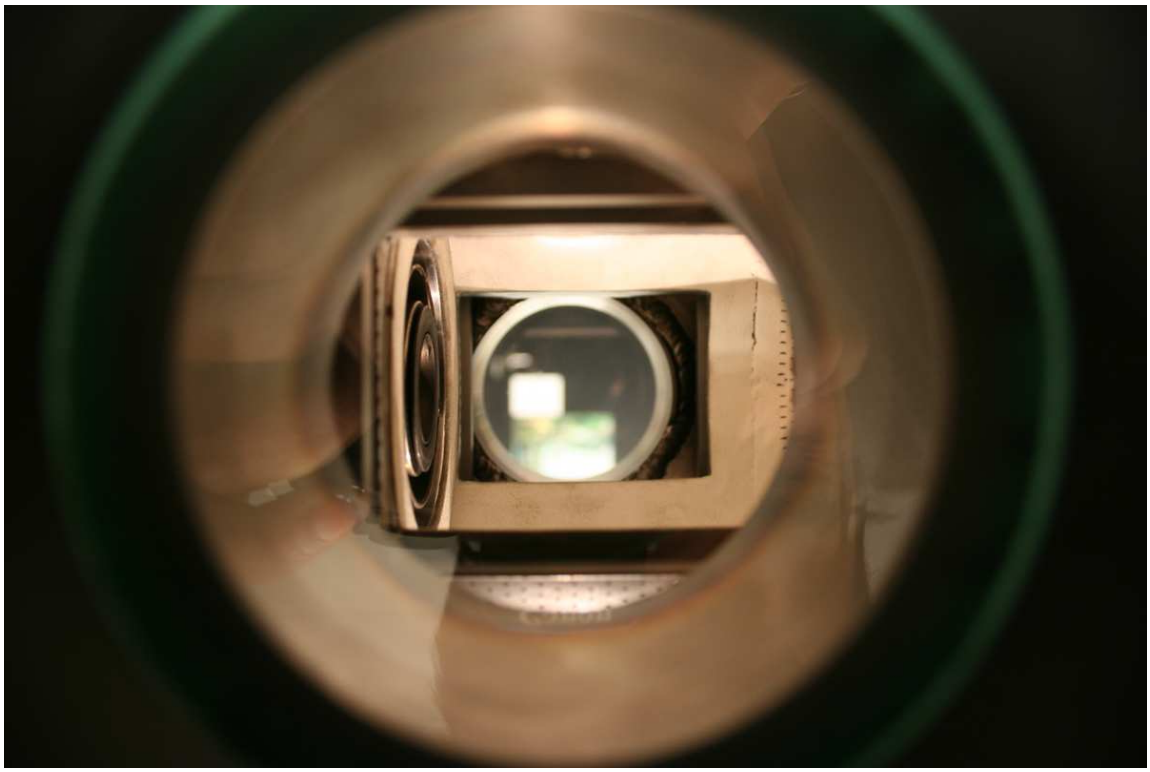

(b) Photo illustrating the available optical access.

Figure 2.5: Photos of the combustor.

2.1.2 Operation of the Combustor

The operation of the combustor typically required three people. The first person needed to be in the Supersonic Combustor Lab to operate the heater and actively control the temperature settings. Though the heater has a controller that can be used to set the heater to output a desired temperature, the controller was found to be too slow in practice. Due to the length of piping between the heater and the experiment, it took a substantial amount of time to reach the desired temperature. Therefore, the controller was typically set to a much higher set-point and then actively adjusted to maintain the desired temperature. This not only required one person to control the heater but posed interesting communication challenges between the two labs. In the Gas Turbine Combustor Lab, two people were required primarily because of the ignition system. The design of the combustor did not allow for a spark plug in the vicinity of the fuel injector(s). Therefore, the Jet-A spray had to be ignited with the aid of a hydrogen torch. For this, a long tube (0.5" diameter) was inserted through the back of the combustor where a Conax fitting ensured a leak proof seal. A 3 ft. long custom built sparker assembly was fed through this tube. The sparker assembly had a central electrode surrounded by a ceramic tube that served to insulate the electrode from another metal tubing around the ceramic. This metal tubing was connected to ground so the spark would jump from the central electrode to the metal sheath. To ignite the Jet-A fuel, first the torch assembly was pushed into the combustor about 3" away from the pilot injector. Then the spark was turned on followed by turning on the hydrogen flow through the 0.5" tube surrounding the spark. This produced a stable hydrogen flame which reliably lit the Jet-A pilot flame. Once the pilot flame was stabilized, the hydrogen torch was turned off and the entire assembly was retracted. This entire process was repeated whenever the flame needed to be lit or

re-lit. It was observed that the there was a small increase in the pressure upstream of the injector (p_3) due to the presence of the flame. Therefore, the combustor pressure was set after the flame was lit and set to the desired flowrate(s). The conditions at which the combustor was operated, along with their designated case names are given in Table 2.1

2.1.3 The GE TAPS Fuel Injector

The TAPS fuel injector is a GE proprietary injector built by Parker-Hannifin Fuel and was provided by GE Aircraft Engines. Details of the TAPS injector along with the upstream face of the combustor are shown in Fig. 2.6 and Fig. 2.7. Since TAPS is an acronym for Twin Annular Premixed Swirler, it is comprised of three sets of swirl annuluses. For the center pilot flow (and corresponding flame), there are two separate co-rotating swirl annuluses. The third air annulus is the main air annulus and is located at the periphery of the injector (from 23.6 mm to 31.1 mm). The swirl for the air in the main annulus is counter-rotating to the pilot swirl and is generated by fixed swirl vanes as shown Fig. 2.8. All three annuluses are open on the back to the incoming air flow as was shown in Fig. 2.2.

Along with the swirl arrangement for the air, a second unique design feature of the injector involves the fuelling arrangement. In the center of the injector is a single atomizer that produces the fuel spray for the pilot flame. Around the periphery of the injector are eight atomizers that inject fuel for the main flame. The fuel is sprayed into the the swirling cross-flow in a manner similar to a jet in a cross-flow. This is done to enhance the mixing of the fuel and air upstream of the primary reaction zone. This arrangement of mixing the fuel and air gives rise to the LPP nature of the combustor.

Case	Air Mass Flowrate $\dot{m}_{air,tot}$ (kg/s)	Preheat Temperature T_3 (K)	Combustor Pressure p_3 (bar)	Pilot Fuel Flowrate $\dot{m}_{f,p}$ (g/s)	Main Fuel Flowrate $\dot{m}_{f,m}$ (g/s)	Fuel Air Ratio F/A
1NR	0.216	422	2.5	0	0	-
1R	0.216	422	2.5	1.8	0	0.0083
2NR	0.260	445	3.1	0	0	-
2R	0.262	444	3.1	1.95	0	0.0074
3NR	0.377	503	4.5	0	0	-
3R	0.379	498	4.5	2.78	0	0.0073
4P	0.230	505	2.0	0.99	0	0.0043
4M	0.230	505	2.0	0.99	2.40	0.015
1Pt1	0.228	505	1.0	1.17	0	0.0051
1Pt2	0.228	505	1.0	1.52	0	0.0067
1Pt3	0.228	505	1.0	1.87	0	0.0082
Main	0.228	505	1.0	1.17	2.49	0.016
2Pt	0.228	505	2.0	0.99	0	0.0043
2Main	0.228	505	2.0	0.99	2.40	0.015

Table 2.1: The conditions at which the combustor was operated in this study. The F/A has been computed based on the total fuel injected divided by the total mass flowrate of air going through the combustor (as given in the second column). Cases 1R, 2R, and 3R represent cases on the engine operating line.

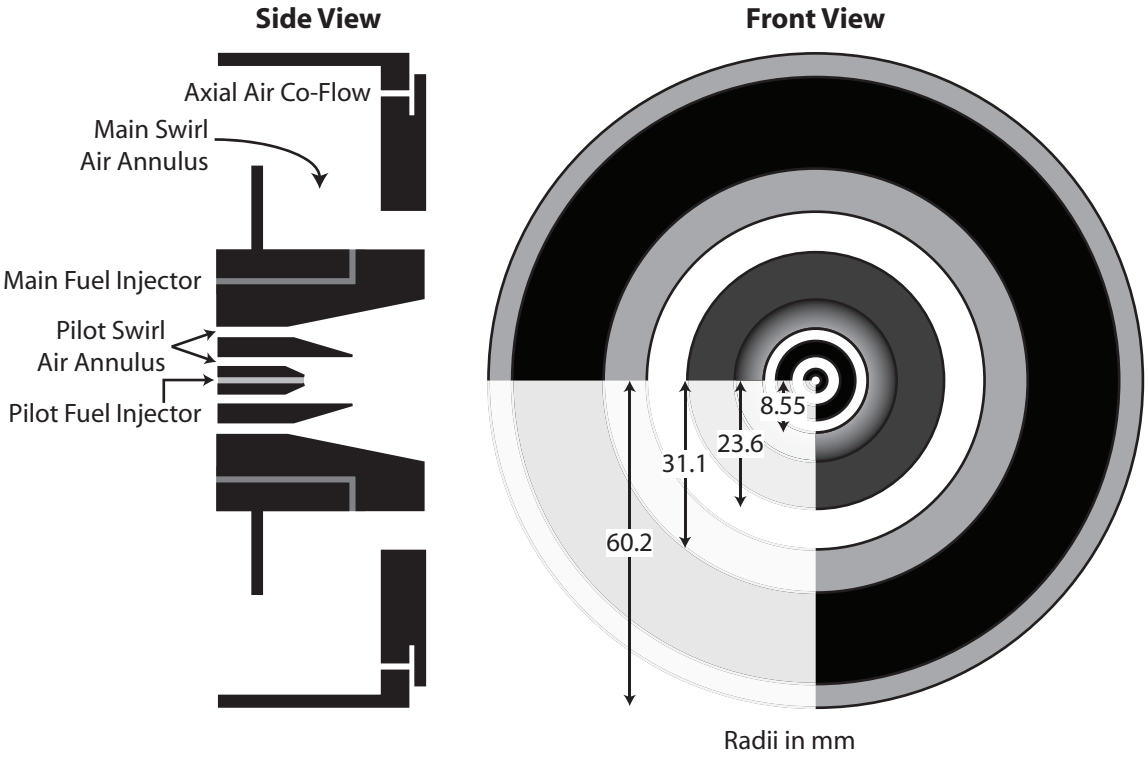

Figure 2.6: Schematic of the TAPS injector and front face of the TAPS combsutor. Dimensions are in mm.

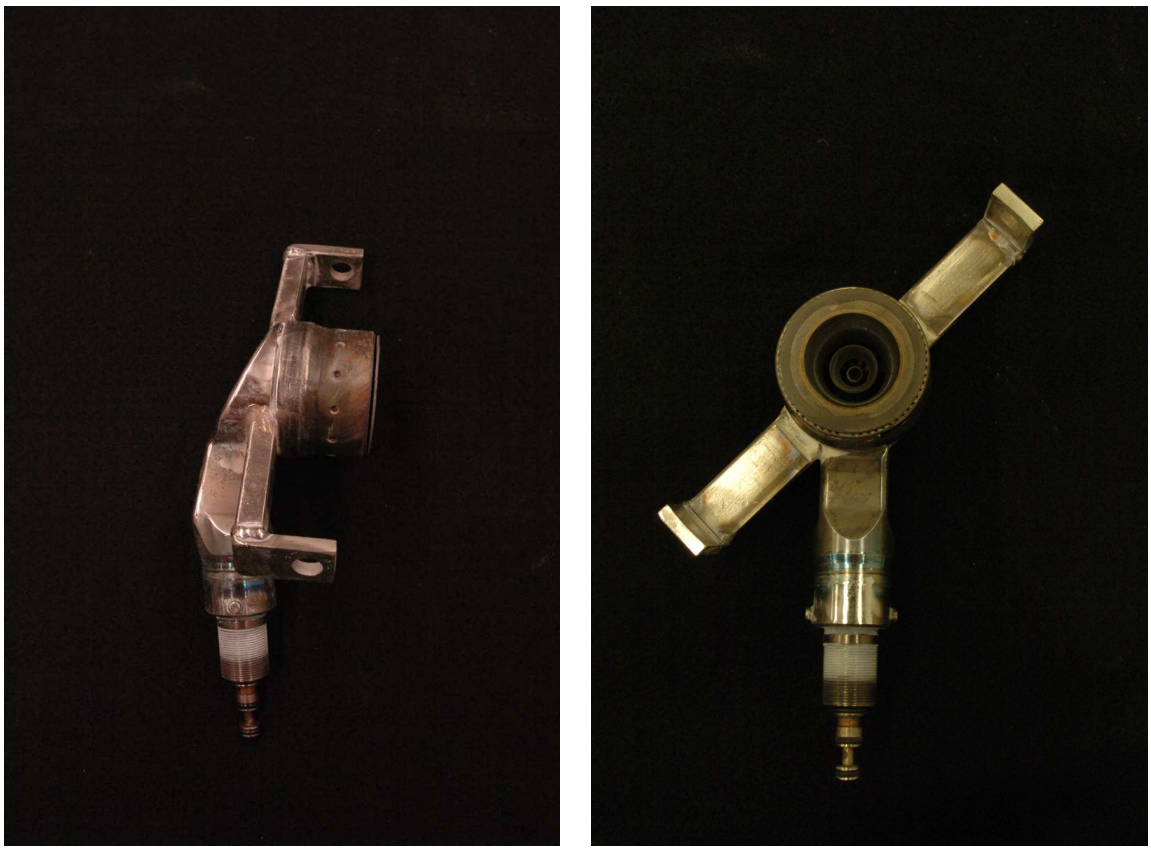

(a) Side view of the TAPS injector.

(b) Front view of the TAPS injector.

Figure 2.7: Photos of the TAPS injector.

Figure 2.8: Photos of the swirl cup or mixer that generates the swirl for the main annulus.

2.2 Particle Image Velocimetry

Particle Image Velocimetry (PIV) is a relatively mature diagnostic that has been utilized to yield instantaneous quantitative velocity field data in a wide variety of geometries and both non-reacting and reacting flows. It was used in this study to quantify both the non-reacting flow in the combustor and for the first time the Jet-A reacting environment in a gas turbine combustor. The diagnostic has been well detailed by numerous past researchers (Raffel et al. (2002)) and has been applied to model gas turbine combustors for reacting and non-reacting conditions (Sadanandan et al. (2008), Panduranga Reddy et al. (2006), Midgley et al. (2005), Ji and Gore (2002)). Only details pertinent to this study will be discussed here.

The PIV setup is shown in Fig. 2.9. Two laser sheets were generated by two separate Nd:YAG lasers (Spectra Physics GCR-250 and Spectra Physics LAB-150) that produce a second harmonic at 532 nm. The 10 ns pulses were combined with a 50:50 beamsplitter and passed through a -150 mm plano-concave lens to form a sheet and then through a -500 mm plano-concave lens to focus the sheet. The sheet thickness at the focal point was 450 μm. The overlap and thicknesses of the two sheets were verified by traversing a knife-edge through the focal point. The laser power then was measured as a function of the knife-edge position and an error-function was fit to the resulting curve. The derivative of this curve yielded a Gaussian curve and the $1/e^2$ value was used to define the sheet thickness. Due to the high swirl velocities in the combustor however, there was considerable out of plane movement of the fluid. To increase the particle residence time in the sheet, the sheet was made thicker by placing the focal point outside of the field of view. In this manner the sheet came to a focus before the region of interest and continued to expand through the field of

view, yielding an average sheet thickness of 1 mm through the measurement plane. This thickness was smaller than the smallest interrogation window size used and therefore did not affect the measurement resolution of the system. Average pulse energies of 60 mJ/pulse were used. The timing of the two pulses was controlled by LaVisions Programmable Timing Unit (PTU v. 8.0) and verified by a fast photo-diode connected to an oscilloscope. For all the experiments, the temporal separation of the two pulses was 2.8 μs.

The resulting scattering from the particles were imaged by a LaVision ImagerPro 4M interline transfer CCD camera, which has a 2k by 2k pixel CCD array. The 70 mm x 70 mm field of view was captured by a 60 mm macro lens (Micro-Nikkor) set to f/11. The lens had to be stopped down to increase the diffraction limited particle image size while still optimizing the signal from the light scattered off of the particles. Flame luminosity posed a major problem to imaging the particles in the reacting flow. Interline transfer cameras typically have very short exposure times for the first frame while the second frame is held open for the time it takes to transfer the data from the first frame onto the on-board buffer. For the LaVision ImagerPro camera, the exposure time for the first frame was 200 ns while it was on the order of 100 ms for the second frame. Such a long exposure is not a problem for non-reacting flows or reacting flows with light gaseous fuels because the background luminosity is low since the light gathered by the camera is essentially limited by the 10 ns duration of the laser pulse. The flame luminosity from a Jet-A flame, especially at elevated pressures, is significant and while the first frame of the camera is able to block out the flame luminosity due to its short exposure, the second frame is unusable due to the high background noise. This problem was overcome through the use of a mechanical shutter in combination with an interference filter. The interference filter (Andover)

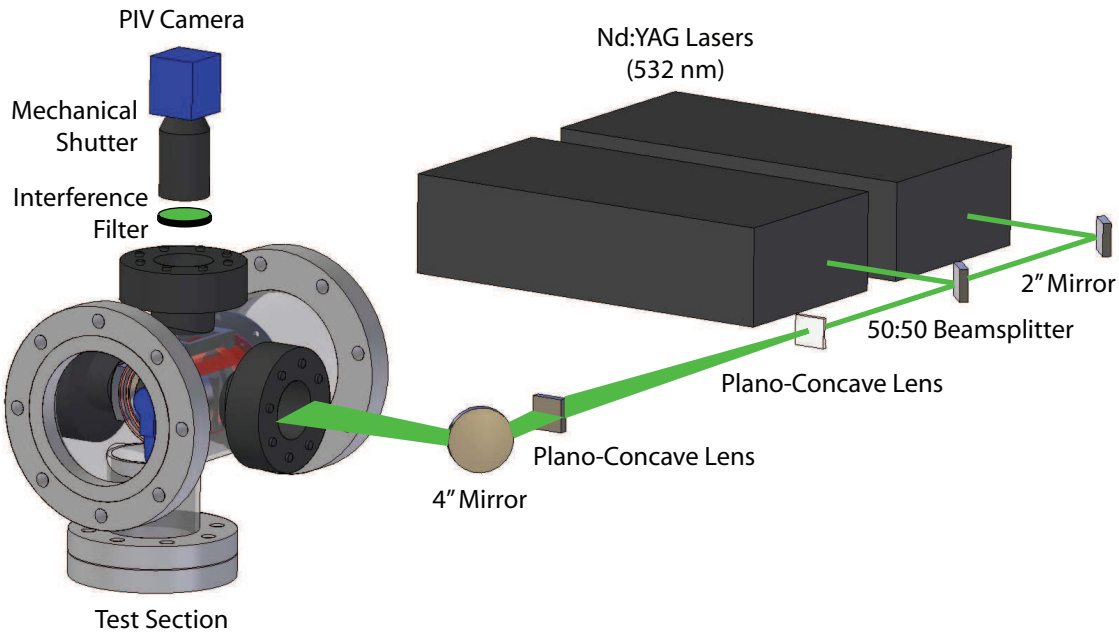

Figure 2.9: Schematic of the setup for PIV.

was centered at 532 nm with a very tight bandpass and a FWHM of only 2 nm. To further reduce noise from the intense luminosity, a mechanical shutter (Uniblitz VS-25) was mounted between the lens and CCD array. Due to the shutter's inherent limitations of opening and closing times, the shutter was programmed to open and close as shown in Fig. 2.10. By opening the shutter prior to the first frame and closing it when the second frame began to be exposed, the exposure times for the first frame remained at 200 ns while the exposure time of the second frame was reduced to approximately 5 ms. This produced the high quality particle images needed for PIV.

The particle images were processed by Davis 7.0 which is a commercial PIV software developed by LaVision. The algorithm involved a standard FFT cross-correlation of the image pair. An adaptive multi-pass approach was used where the correlations were first calculated with 128×128 pixel interrogation windows. The calculated velocity was then used to shift the interrogation window for a second cal-

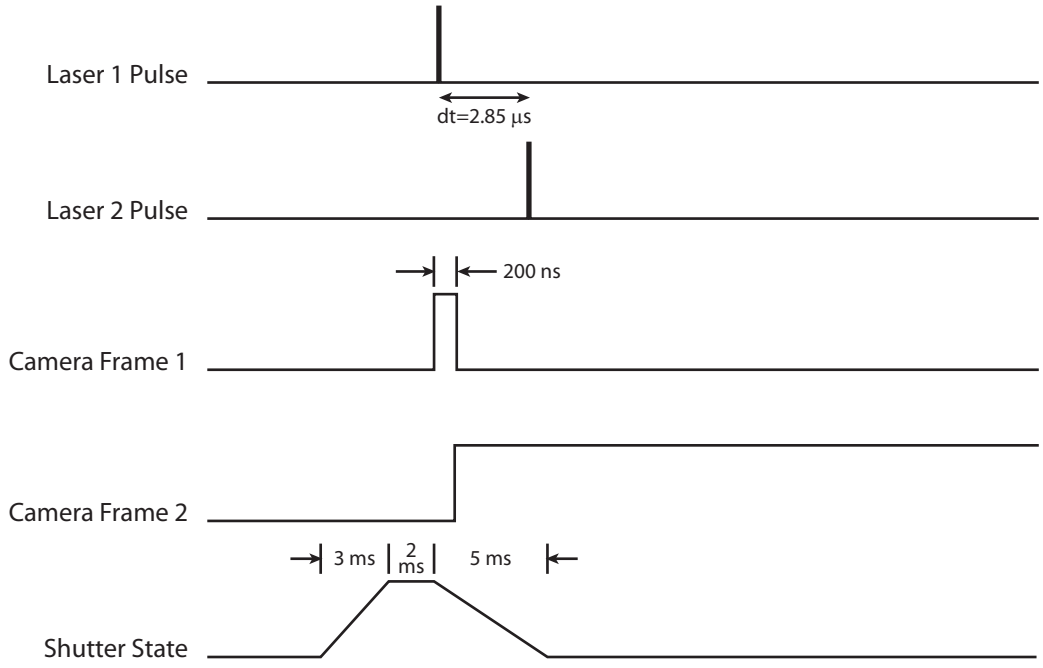

Figure 2.10: Timing diagram for the PIV system with the mechanical shutter. The high state for the camera frames and shutter indicates the open state.

culation with a 64×64 pixel interrogation window. This yielded a spatial resolution of 2.34 mm and was the limiting resolution in the experiment.

For all the data sets, the windows were overlapped by 50% giving a total of 4096 vectors in each image. All the instantaneous raw vector fields were then post-processed using a combination of a median filter, a standard deviation filter, and a peak ratio criterion to remove spurious vectors from the field. The vectors were then smoothed by a 3x3 Gaussian smoothing kernel. Missing vectors were filled in the instantaneous images through an interpolation algorithm involving the neighboring eight vectors. The instantaneous images typically had fewer than 5% missing vectors and missing vectors were not filled in for calculation of the average velocity field.

2.2.1 PIV Seeding

An inherent assumption in PIV is that the seed particles faithfully track the flow. It is important therefore that seed particles be chosen such that the highest gradients in the flow are captured. The Stokes number is used to express the ability of the particle to track the flow and is defined as

$$St = \frac{\tau_p}{\tau_f}, \tag{2.2}$$

where τ_p is the particle's characteristic settling time scale, and τ_f is the characteristic flow time scale (Melling (1997), Westerweel (1997), and Samimy and Lele (1991)). The characteristic settling time scale of the particle can be computed since the particle drag is in the Stokes drag regime (where the Reynolds number based on the particle diameter < 1) and is given by (Melling (1997))

$$\tau_p = \frac{\rho_p d_p^2}{18\mu}. \tag{2.3}$$

The flow time scale is (Melling (1997))

$$\tau_f = 10\frac{\delta}{\Delta U}, \tag{2.4}$$

where δ and ΔU are the relevant length scale and velocity gradient respectively. In this study it was found that the highest velocities were on the order of 40 m/s and taking δ to be the smallest resolved length scale of 2 mm gives the smallest resolvable $\tau_f \approx 60\mu s$. In reacting flows, another obvious necessity is the ability of the particle to survive the high flame temperatures. Various metal oxide particles have been used in the past and aluminum oxide or alumina (Al_2O_3) particles were used in this study. The seed particles were nominally 0.5 μm in diameter, giving a particle relaxation time scale of $\tau_p \approx 2.85\ \mu m$. With this, the worst case Stokes number is $St \approx 5 \times 10^{-3}$,

which is much less than the criterion of $St < 0.5$ suggested by Clemens and Mungal (1991) and Samimy and Lele (1991).

Homogenous seeding of the flow is also critical for high quality velocity vectors. This was achieved by designing the seeder such that it was able to reliably supply the requisite amount of seed for a given air mass flowrate. The seeder shown in Fig. 2.11 was constructed from a modified stainless steel vacuum nipple (MDC Vacuum). The 3/8" input line was feed into the seeder containing the seed and crimped at the end to reduce the exit area and therefore increase the exit velocity. The output from the seeder was attached to the top flange and connected to the primary air line downstream of the main control valve and upstream of the choked flow orifice. With such an arrangement of the seeder bypassing the main control valve, ample pressure drop across the seeder was available. This ensured the high velocities needed in the seeder to adequately stir the seed and entrain it into the air. The seeded air was then mixed with the bulk unseeded air flow upstream of the orifice, ensuring that both streams were correctly metered by the orifice. By seeding the flow considerably upstream of the combustor, homogenous seeding in the entire region of interest was ensured.

2.2.2 PIV Errors

There are a number of sources of uncertainties in the computed velocities that arise from the processing of the particle image pairs. The three main sources are from uncertainties in peak finding, errors arising displacement gradients within interrogation windows, and perception error due to the out-of-plane motion of particles. The first two will always bias the results to give a value that is less than the true velocity while the third is a random error with no bias. Uncertainties in peak finding arise

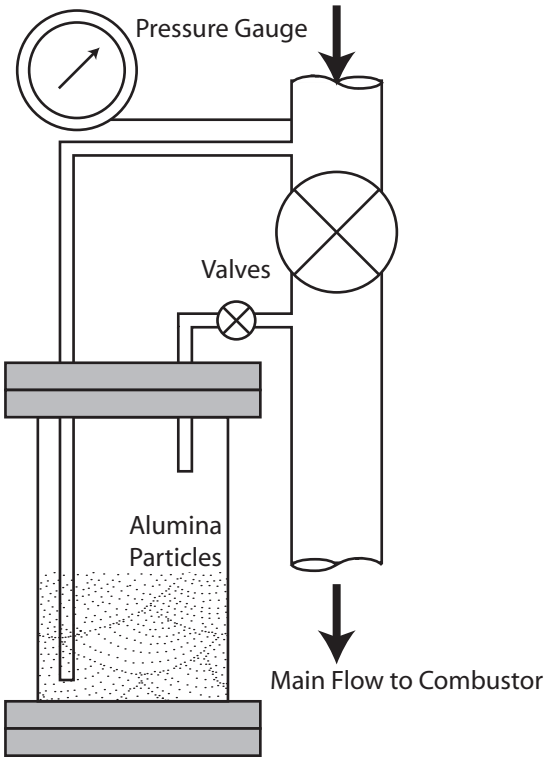

Figure 2.11: Schematic of the seeder arrangement.

from the fact that there will always be instances where particles present in the first frame would have moved out of the window in the second frame. This tends to bias the velocity measurement towards lower values because particles moving at lower velocities have a higher probability of remaining within an interrogation window across the two frames. Raffel et al. (2002) and Westerweel et al. (1997) have computed the RMS uncertainty due to this source from their Monte-Carlo simulations. They find that, for the conditions in the experiments in the current study, the RMS uncertainty is 0.015 pixel. The multi-pass processing used in this study reduces this uncertainty by shifting the second frame of the PIV recording by an appropriate amount. This reduces the number of lost in-plane particle pairs and hence reduces the error arising from uncertainties in peak finding. The value stated above therefore can be taken as a worst case scenario.

Displacement gradients within an interrogation window lead to uncertainties for similar reasons as errors due to uncertainties in peak finding. If a velocity gradient exists within an interrogation window, the computed velocity will underestimate the true average velocity since the higher velocity particles will be less well correlated across the two PIV frames. A worst case gradient would be about 0.05 pixel/pixel. The simulations of Raffel et al. (2002) suggest that this leads to an uncertainty of 0.3 pixel.

Another source of error that was important in this study was perception error due to the out-of-plane motion of particles. The swirling flow in the combustor naturally produces considerable velocities in the out-of-plane direction that could be on the order of the velocities in-plane. It was mentioned earlier that this necessitated a thicker sheet to ensure that there were minimal losses of particle pairs between the two frames. However, due to the optical layout of the imaging system, perspective causes out-of-plane motion to appear as in-plane motion on a two-dimensional image. A worst case scenario can be estimated by assuming a particle at one extreme end of the field of view (located at $y = 35$ mm) moving out-of-plane at 40 m/s (the highest in-plane velocity observed). Since the camera was about 460 mm from the imaged plane, this leads to a perceived in-plane motion of 0.25 pixel. The RMS uncertainties due to the above mentioned errors give a worst case estimate of 0.57 pixel, or about 1.5 m/s. Since the largest source of uncertainty is from displacement gradients, this is a worst case scenario limited to a small region near the Lip Recirculation Zone.

The final source of error that is more difficult to quantify but is significant is the error arising due to the presence of fuel droplets. Mie scattering from unburnt droplets issuing from both the pilot and main annuluses is shown in Fig. 2.12. The algorithms used to compute the vectors rely upon the intensity of the scattered light

to obtain the correlations. Since the droplets are much larger than the seed used, they naturally scatter more light and hence the velocities in those regions will be biased towards the velocities of the fuel droplets. As explained in §2.2.1, smaller particles are needed to accurately track the gradients in the flow and larger particles are ill-suited for the purpose. The images of the Mie scattering show the very largest droplets to be on the order of 3 pixels, suggesting that the droplets are about 500 μm in diameter (from diffraction limited optics). Though this leads to an error in computed gradients, the errors are limited to a very small region (as seen in Fig. 2.12). Furthermore, the vast majority of fuel droplets are considerably smaller (on the order of 100 μm) and are very disperse, such that there will typically be less than one in any interrogation window. Also, PIV results of cases without main combustion show that the gradients are considerably lower in the bulk main flow where the droplets exist. Finally, results of Gopala et al. (2007) indicate that fuel droplets in a cross flow reach 90% of the air velocity within 25 mm downstream of the injectors. This distance is less than the distance between the injectors and the downstream location at which the measurements were taken. Therefore, in the regions where the droplets exist, the velocities will be slightly underestimated.

2.3 Formaldehyde Planar Laser Induced Fluorescence

The identification of the flame front and reaction zone structure is of crucial importance in many experiments. Practically, this is achieved by measuring a quantity that correlates well with either the peak heat-release rate, temperature, or dilatation. Recent chemical measurements of the flame front rely mostly on fluorescing a particular molecule that is either created at the flame front (e.g. OH), destroyed at the flame (e.g. CH_2O), or is quickly created and destroyed at the reaction zone (e.g. CH

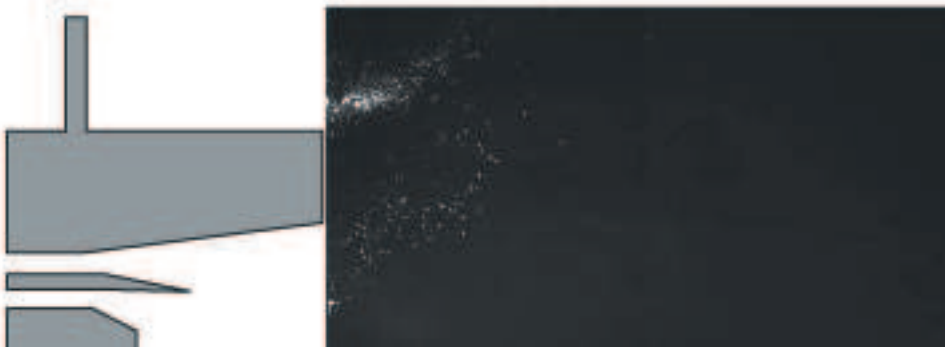

Figure 2.12: Mie scattering from fuel droplets that bias the measured velocities. The flow was not seeded and therefore only the droplets are observed.

or HCO). Other techniques such as chemiluminescence or imaging the disappearance of some tracer (e.g. acetone or particles) provide high SNR but offer a much more ambiguous identification of the flame front. With advances in lasers and intensified cameras, imaging the emissions from LIF of a specific molecule is now possible and provides great insight into the reaction zone structure.

Planar Laser Induced Fluorescence (PLIF) offers a unique and powerful tool for the imaging of the reaction zone. While the LIF signal of a number of important combustion species can be corrected to yield quantitative concentrations of the given specie, qualitative PLIF also provides a valuable diagnostic. This is especially true where only the location of the reaction zone is sought. Details of the physics behind the technique are well detailed in Eckbreth (1996) and Sutton (2005) while Hanson et al. (1990) provides an overview of the diagnostic applied in combustion environments. Qualitative PLIF of the formaldehyde molecule (CH_2O) was used in this study to mark the reaction zone in the Jet-A fuelled flame in the combustor.

Formaldehyde is an important combustion intermediate and marks the initial fuel breakdown (Vandooren et al. (1986)). It is formed primarily in the preheat zone of

premixed combustion and also marks low temperature reactions. One of its primary production pathways is through the methyl radical reacting with O (Vandooren et al. (1986), Smooke et al. (1989), and Peeters and Mahnen (1973)):

$$CH_3 + O \rightharpoonup CH_2O + H. \tag{2.5}$$

Computations were made with the CHEMKIN packages PREMIX and OPPDIFF with GRIMECH 3.0 for a range of equivalence ratios and mixtures and the results are shown in Fig. 2.13. Along with the temperature profile, the concentration of CH, which is a known marker of peak heat release rate (Porter et al. (1966)) provides a reference for understanding the spatial distribution of CH_2O. From the premix cases (Fig. 2.13(a) and (b)), it can be seen that CH_2O is formed throughout the preheat zone and peaks at the point of highest temperature gradient. In diffusion flames, the CH_2O zone is considerably wider than the CH zone and is created considerably upstream of the flame front (Fig. 2.13(c)). To simulate combustor conditions where hot products often mix with the fuel prior to the reaction, computations were made with a mixture of fuel and products reacting with air. The reactants were assumed to be those from a non-premixed jet flame at an axial distance half-way between the base and tip, and therefore consisted of 60.5% CH_4, 28.34% N_2, 3.72% CO_2, and 7.44% H_2O, all by volume. The reactants were also assumed to be at 1305 K while the oxidizer was air at 300 K. The results from this are shown in Fig. 2.13(d) where similar to Fig. 2.13(c), the CH_2O zone is fairly broad. It is clear that on the reactant side, the concentrations of CH_2O are well correlated with temperature. However, it can be seen from Fig. 2.13(d) that the much higher temperatures do not cause a marked increase in the relative CH_2O concentrations. Another scenario that is likely to be encountered in realistic combustors is that of a partially premixed flame

(Fig. 2.13(e)). Here, the reactants were set to $\phi = 2.0$ which is too rich to react and therefore require additional air from the oxidizer stream. As shown, the CH_2O is broader than the premixed case, but is still confined to the preheat zone near the flame front. Preheating the reactants to 500 K as shown in Fig. 2.13(f) does not produce any appreciable differences. In all the cases, the magnitude of the spatial gradient of the CH_2O concentration is also plotted. For all cases, the location of the highest magnitude of the gradient shows exceptional correlation with the location of the flame front. This suggests that with sufficient resolution in the measurement, the gradient of the CH_2O concentration could provide a reliable way to accurately mark the flame front.

In all the computational cases, it was seen that at the point of peak CH concentrations, CH_2O is destroyed and that there is some overlap in the concentrations. This is to be expected since along with thermal decomposition, formaldehyde is consumed by reactions with the O/H radical pool near the reaction zone through the following reactions (Glarborg et al. (2003), Hochgreb and Dryer (1992), and Najm et al. (1998b)):

$$CH_2O + H \rightleftharpoons HCO + H_2 \tag{2.6}$$

$$CH_2O + O \rightleftharpoons HCO + OH \tag{2.7}$$

$$CH_2O + OH \rightleftharpoons HCO + H_2O \tag{2.8}$$

$$CH_2O + HO_2 \rightleftharpoons HCO + H_2O_2 \tag{2.9}$$

Reaction 2.8 has been exploited in the imaging of the reaction rate where the product of the CH_2O and OH LIF signals was used as a surrogate for the reaction rate. The

kinetics and computations suggest that formaldehyde makes a good marker for the reaction zone and that it can be used reliably to detect low temperature combustion and the preheat zone. Also, its product or fuel-lean edge marks the peak heat release rate and important parameters such as wrinkling and flame surface density can be computed from that edge. However, similar to OH PLIF, it suffers from the ambiguity of identifying the product or fuel-lean edge in a highly wrinkled flame.

LIF of formaldehyde in a flame was first demonstrated by Harrington and Smyth (1993) who excited naturally occurring formaldehyde in a methane/air flame. They demonstrated that formaldehyde can be excited in a flame at 355 nm, the third harmonic of an Nd:YAG laser. Since then, formaldehyde PLIF has been used in laminar flames by Brackmann et al. (2003) and Paul and Najm (1998); in engines by Bäuerle et al. (1994) and Richter et al. (2005); in turbulent flames by Böckle et al. (2006) and Joedicke et al. (2005); and in a supersonic combustor by Rasmussen et al. (2007). Of these, Brackmann et al. (2003), Rasmussen et al. (2007), and Bombach and Käppeli (1999) are of note for they successfully excited formaldehyde at 355 nm. A major weakness of this excitation strategy is that this laser line overlaps weak rotational transitions in the 4_0^1 band. However, the high pulse energies available with commercial Nd:YAG lasers help overcome this shortcoming. In fact, the availability of high laser energies allows for signal from polycyclic aromatic hydrocarbons (PAH's) to be blocked out. PAH's are excited broadband in the UV and therefore make the use of low SNR techniques such as CH PLIF very difficult in even mildly sooty environments. Formaldehyde LIF signals though show a linear dependence on laser intensity up to at least several GW/cm^2 as shown by Brackmann et al. (2003) and Harrington and Smyth (1993). This allows one to image the reaction zone in environments where other techniques fail by using higher laser energies to saturate

the PAH signal and not the formaldehyde signal. Higher signals from formaldehyde PLIF have also allowed the use of kHz lasers and high frame rate cameras to obtain time-resolved images of formaldehyde by Olofsson et al. (2006).

2.3.1 Simultaneous CH and Formaldehyde PLIF

While the kinetics of formaldehyde is fairly well understood, ambiguity exists about the information obtained from PLIF images of formaldehyde, especially when excited at 355 nm. Both thin layers and broad zones of formaldehyde have been observed in flames and combustors and it is unclear under which conditions these occur. To help resolve some of these ambiguities, a detailed study was undertaken where simultaneous images of CH and CH_2O in a well characterized turbulent flame were acquired. CH has been a popular marker of the reaction zone primarily because of its existence in thin layers that correspond well with the peak temperature regions of the flame as shown in Fig. 2.13. Allen et al. (1986) first applied CH-PLIF to both premixed and diffusion flames. Since then, it has been applied to turbulent premixed flames (Filatyev et al. (2005)), diffusion flames (Carter et al. (1998)), lifted flames (Watson et al. (1999b) and Watson et al. (2000)), and swirl flames (Weigand et al. (2006) and Ratner et al. (2000)). Unfortunately, due to its low SNR, the diagnostic can only be applied to specialized or doctored laboratory scale flames. PLIF of CH_2O can however be more readily applied to realistic flames and geometries and through this study, an interpretation of CH_2O images was obtained.

2.3.1.1 Simultaneous PLIF Experimental Setup

To calibrate and understand the CH and CH_2O PLIF results, several different unconfined calibration methane/air flames were studied. A GRI burner that was characterized extensively during the University of Michigan/GRI/IFRF Scaling 400

Flame	CH_4 Flow Rate (SLPM)	Air Flow Rate (SLPM)	Re	Co-Flow Velocity (m/s)	ϕ
PF1	7.31	66.6	10100	19	1.0
PF2	8.08	65.9	10100	19	1.2
PF3	9.81	64.0	10100	16	1.5
PPF	13.1	61.3	10100	16	2.0
LF	21.4	60.7	11000	9.5	3.3

Table 2.2: Flame conditions of the calibration burner for which data is presented. The Reynolds number is defined by the exit velocity of the reactants, the center tube diameter, and the mole weighted average kinematic viscosity.

studies (Hsieh et al. (1998)) was picked as the calibration burner. The geometry of the burner is shown in Fig. 2.14. Premixed fuel and air are injected through a central 10 mm tube and coaxial air issues from a 27 mm tube. A movable block swirler allows the swirl number to be varied and all measurements shown here were taken with no swirl. The various flames studied are given in Table 2.2 and a representative visual flame image of each is shown in Fig. 2.15. The first three flames represent turbulent premixed flames ranging from stoichiometric to rich. The fourth flame was partially premixed and required air from the co-flow to combust. Finally a lifted flame was also studied with special attention given to the stabilization mechanism at the base.

The schematic for the PLIF diagnostics is given in Fig. 2.16. Formaldehyde was excited using the third harmonic (λ = 355 nm) of an Nd:YAG laser (Spectra Physics GCR-250). The laser beam was passed through a combination of a -125 mm cylindrical lens and a 1 m spherical lens to create a sheet 40 mm tall and approximately 400 μm thin. Pulse energies of 50 mJ/pulse allowed the formaldehyde diagnostics to be well within the linear regime.

CH was excited by pumping the $Q_1(7.5)$ transition of the $B^2\Sigma^- - X^2\Pi(0,0)$ band of the CH molecule at 390.30 nm as was described by Carter et al. (1998). The resulting emission is detected from the A-X(1,1), A-X(0,0), and B-X(0,1) bands in

the 420-440 nm range. Compared to the fluorescence yield from pumping the A-X and C-X bands, pumping the chosen band results in a higher signal due to the fast electronic energy transfer from the B to the A state (Donbar (1998)). The requisite 390.3 nm beam was produced as shown in Fig. 2.16. The 532 nm beam output of a second Nd:YAG laser (Spectra-Physics LAB-150) was used to pump a dye laser (Sirah CSTR-D-24) running a mix of Rhodamine 610 and Rhodamine 640 dyes. The 616 nm beam output from the dye laser was mixed with the 1064 nm output of the Nd:YAG laser using a KD*P mixing crystal to produce the 390.3 nm beam. The wavelength was verified by a wavelength meter. This beam was combined with the 355 nm beam through a custom dichroic and passed through the same sheet forming optics described above. Due to the closeness of the two wavelengths, the two sheets were nearly identical.

For both PLIF diagnostics, the emissions were collected by separate intensified CCD cameras (Andor iStar DH-734). For CH-PLIF, the camera was fitted with a fast 50 mm/f1.2 lens stopped down to f2.0 to eliminate lens effects visible when fully open. An interference filter with a center wavelength of 430 nm and a FWHM of 10 nm was used to block scattering from the pump beam and flame luminosity. The 1024x1024 pixels of the CCD were binned 3x3 to improve SNR and created a field of view of 60mm x 60mm which resulted in a resolution of 180 μm per pixel. For CH_2O PLIF, a second camera located on the opposite side of the flame was fitted with a 50 mm lens stopped down to f/4. A Schott glass filter (GG-385) was used to block scattering from the pump beam. Although signal from formaldehyde PLIF was sufficiently high, the camera was also binned 3x3 to maintain the same camera readout times for both cameras and therefore allow simultaneous measurements.

2.3.1.2 System Synchronization

Though simultaneous imaging implies no temporal separation between the two measurements, the possibility of cross-talk between the two systems requires that there be a finite separation in time between when the two images are acquired. However, if the time separation in the experiment (Δt) is such that $\Delta t \ll \tau$, where τ is the fluid mechanic time scale, then the flow is essentially "frozen" during that time and the measurement is essentially simultaneous. For the jet flames considered in this study, the characteristic fluid mechanic time scale is

$$\tau = \frac{\Delta x}{U}, \tag{2.10}$$

where Δx is the smallest displacement measurable by the camera and U is the exit velocity of the jet. Since sub-pixel movements cannot be detected by the camera, Δx should equal one-half the camera pixel spacing (90 μm). This gives a $\tau = 5.6\mu s$. By choosing $\Delta t = 500\ ns$ therefore, it was ensured that the flow was "frozen" for the duration of the measurement.

The system was wired as shown in Fig. 2.17. The timing was controlled by a digital delay generator (DDG) (Stanford Systems DG-535) that ensured accurate synchronization of the signal acquisition with their respective laser pulses. The DDG was triggered internally at 10 Hz and the trigger signal (T_0) was used to fire the Lamp of the CH laser (Lab-150). A second output (A) on the DDG was set to $T_0 + 186.5\ \mu s$ and connected to the Q-Sw input of the CH Laser. Output B of the DDG was set to $T_0 + 500\ ns$ and connected to the Lamp input of the formaldehyde laser (GCR-250). Finally, output C of the DDG was set to $B + 186\ \mu s$ and connected to the Q-Sw input of the formaldehyde laser. This ensured that the lasers operated at their native 10 Hz repetition rates and that the delay between the lamp and Q-Sw

firing was as required for maximum power output. Furthermore, the DDG ensured the temporal separation (Δt) between the two laser pulses was 500 ns, as verified by a fast UV sensitive photo-diode connected to an oscilloscope.

The cameras used for the acquisition of the PLIF signals were connected to dedicated computers for each system and were triggered by the software (Andor Solis) on each computer. Therefore, while the lasers fired continuously at 10 Hz, the cameras only acquired the resulting PLIF signal when triggered by their respective computers. A considerable problem with any such multi-camera system is the inability to command the software to begin acquisition simultaneously on both systems. This problem was overcome by utilizing the Output-A trigger output available on the cameras. In this arrangement, the Q-Sw output of the CH laser was connected to the Trigger In of the ICCD used for the acquisition of the CH PLIF signal, coupling the camera to its laser. The Output-A trigger of the CH ICCD was then fed into the ICCD used for the acquisition of the formaldehyde PLIF signal. To initiate the acquisition of the signal, first the formaldehyde computer was commanded to acquire, putting the camera in standby until a trigger was received from the CH ICCD. Then the CH computer was set to acquire, which acquired a CH PLIF signal when it received a trigger from the CH laser. After the acquisition, the CH ICCD outputted a trigger to the formaldehyde ICCD through its Ouput-A output. Upon receiving the trigger, the formaldehyde ICCD acquired the formaldehyde PLIF signal. In this manner, the formaldehyde ICCD was essentially decoupled from its laser, but by setting the delay on the CH ICCD's Output-A accordingly, the acquisition was timed to match the formaldehyde excitation pulse from the laser. The correct timing was verified by a fast photo-diode connected to an oscilloscope. This method is preferable because it removes the need for an external custom timing module as

was used by Sutton (2005).

2.3.1.3 Simultaneous PLIF Results

Premixed Turbulent Flames

Fig. 2.18 shows sample images from the rich premixed flame PF3. The right most column shows the CH and CH_2O images overlaid with the the CH boundaries marked by the white lines and the CH_2O shown with a continuous color spectrum ranging from blue (low) to red (high). All images are shown with the same field of view which is clearly in the potential core of the flame. Therefore, large scale wrinkling from vortices can be seen in the CH images. No small scale wrinkling is seen in the CH images which is a direct effect of the heat release near the flame (Clemens and Paul (1995)).

The CH reaction zones are seen to be thin everywhere as has been previously observed for similar flames. In fact, the thickness of the CH layers remains constant across the entire image. This is in contrast to the formaldehyde images where although layers comparable in thickness to CH layers are seen, there are also distinctly broadened regions of formaldehyde. While some of this broadening may be attributed to the orientation of the laser sheet with the instantaneous flame, the simultaneous CH PLIF image suggests that the broadened zone is normal to the flame. The thin layers of formaldehyde reflect the pre-heat zone suggested by the PREMIX results (Fig. 2.13) with the max signal count likely to be the point of highest temperature gradient. The broadened zones however are too thick to be the pre-heat zone and are therefore pools of pre-heated reactants convected downstream. This is also apparent in the structure seen in the fuel-rich side of the formaldehyde images. Kortschik et al. (2004) report observing temperature increases ahead of the preheat zone caused by

turbulent transport of temperature. Such transport could also lead to the production of formaldehyde ahead of the preheat zone and lead to the broadened zones. The structures suggest a higher degree of flame wrinkling from the turbulence in the reactant jet and will be revisited in §2.3.1.5.

The simultaneous images in Fig. 2.18 indicate that the spatial correlation between the reactant side of the CH and the product side of the CH_2O is excellent. There is always a small overlap between the two zones indicating that the product side of the CH_2O PLIF image marks the reaction zone. Ambiguity about which side is the reactant or product side however exists in the images and it is only the simultaneous CH image that provides the answer. This for example is best exemplified by Fig. 2.18(c) where a small island is seen inside the otherwise cold reactants. From just the CH_2O image, it is unclear whether it is the outer or the inner boundary of the island that marks the reaction zone. Of course, the CH image by itself also fails to clear the ambiguity.

Fig. 2.19 shows sample images from Flame PF1 in which the reactants were at a stoichiometric mixture and had the shortest flame. In Fig. 2.19(b) for example, the flame tip can be seen from both the CH and CH_2O images. Here too, as in Flame PF3, both the CH and formaldehyde appear as thin flamelets everywhere. While regions of broadened formaldehyde appeared in the richer flame however, there are considerably fewer pockets of broadened zones in this flame. Furthermore, the few broad zones that do appear are thinner than the broadened zones in the richer flame. Flame pinching near the tip can be seen in Fig. 2.19(a) where the CH layers have merged and there is a distinct break in the formaldehyde surfaces. While the three-dimensional flame surface may still be connected, it is more likely that the flame has been pinched near the tip leaving an island of flammable reactants. Once again, the

formaldehyde appears on the reactant side and this explains the distinct break in the formaldehyde surfaces while the CH layers have merged. Some degree of flame pinching in fact can also be observed to be occurring in Fig. 2.19(b).

Flame PF2 was at an equivalence ratio of 1.2 and displayed many of the same characteristics of the other premixed flames studied. Fig. 2.20 shows a sample image where the flame tip has been captured and where the flame has been pinched to create an isolated island of reactants above the flame tip. Unlike Fig. 2.19(a), there is a distinct break in the CH surfaces as well. The formaldehyde image shows two islands of unburned reactants along with the central reactant jet. This suggests that the turbulence in such flames causes a high degree of wrinkling that routinely causes breaks in the flame surface. However, all such isolated islands are enclosed by closed CH and CH_2O surfaces and therefore are probably completely burning. The closed surfaces also suggest that the break is caused by the two sides of jet being pinched together until they merge, break from the main central jet, and then convect downstream. While the images were all taken at random times, Fig.'s 2.19(b), 2.19(a), and 2.20 provide an idea of the time history of this process in the order listed.

Rich Partially Premixed Flame

Flame PPF reflects a partially premixed flame where the reactants are outside the flammability limits ($\phi = 2.0$) and must therefore mix with ambient air from the co-flow in order to react. Fig. 2.21 shows a sample image set from Flame PPF. The signal count in the CH images for all images was lower than the signal for the premixed flames. The CH layer thickness though remained thin at all locations and marked the reaction zone similarly to the premixed flames. Formaldehyde on the other hand shows marked differences from the premixed flames. While the CH_2O

layers remained thin for the most part in the premixed flames, they appear as broad diffuse regions in the partially premixed flame. Peak concentrations are no longer concentrated in thin layers but rather are spread over a large region. The chemically long lifetimes of formaldehyde allow it to be produced throughout the reactant pool but be consumed only at the flame front. In the interim, formaldehyde is convected both upstream and towards the flame and therefore is spread over a large region. In all images, it was seen that the fuel-lean side of the formaldehyde lined up very well with the CH layers.

Lifted Flames

Lifted jet flames form an important category of jet flames and a number of practical combustors such as commercial boilers utilize this phenomena. It is also possible that the main premixed component of the TAPS combustor will be a lifted flame. While turbulent lifted jet flames have been studied by many researchers, the underlying physics explaining the flame stabilization is not well understood. Though the purpose of this work was not to conclusively explain the stabilization mechanism, the simultaneous technique does shed some new light on the reaction zone at the base.

Vanquickenborne and van Tiggelen (1966) first proposed a stabilization mechanism based on a premixed flame model where the leading edge of the lifted flame is premixed and that at the base,

$$\overline{U} = S_b, \tag{2.11}$$

where $\overline{U}$ is the reactant velocity at the base and S_b is the local burning velocity, either laminar, or turbulent as suggested by Kalghatgi (1984). Watson et al. (1999b) and Watson et al. (1999a) employed CH PLIF along with simultaneous PIV to understand

the stabilization based on this idea and observed intermittent CH layers that curl toward the outside. They argue that these may be lean premixed structures akin to the lean premixed branch of a tribrachial flame, in agreement with the edge-flame concept proposed by Buckmaster (2002). This theory is based upon the idea of triple flames seen in laminar flames by Phillips (1965). As shown in Fig. 2.22 the edge-flame consists of three branches, the rich premixed branch on the fuel/reactant side, the lean premixed branch on the oxidizer side, and a diffusion branch in the middle. The base of this flame is premixed and is theorized to follow the condition given by Eqn. 2.11.

Fig. 2.23 shows sample image sets from the lifted flame (Flame LF). The CH images are very similar to those seen by previous studies of lifted flames where a continuous vertical structure exists representing the primary diffusion flame. The formaldehyde images however clearly show a triple flame structure at the base of the lifted flame. Similar structures were also seen by Joedicke et al. (2005) through PLIF of CH_2O. The lean premixed branch appears as thin flamelets very similarly to the thin flamelets observed in the premixed flames (Fig.'s 2.18, 2.19, and 2.20) giving proof that the branches are indeed premixed. The edge of the formaldehyde images that lines up with the CH layer shows characteristics that are very similar to the CH_2O zones seen in the partially premixed flame (Fig. 2.21). This too suggests that the CH layers in a lifted flame mark the primary diffusion flame. The rich premixed branch of the triple flame is not so obvious and one can only conjecture that the inner edge of the formaldehyde zones is reacting. An important observation from the formaldehyde images is that the base of the CH layers does not always mark the base of the flame. For example, the left edge of the CH layer in Fig. 2.23(c) suggests that the base of the flame is actually stabilized upstream of the point suggested by

the CH_2O image. This has important implications for computing the flame speed at the base of a lifted flame. Therefore, techniques such as simultaneous PIV/CH_2O PLIF are better suited at assessing models based on the premixed flame theory. Furthermore, the CH image also shows the CH layer curling towards the outside which may suggest that it is part of the lean premixed branch. However, comparison with the simultaneous CH_2O image shows that this curling is really a part of the wrinkled diffusion flame, and that the CH does not show the premixed branch. It is not immediately obvious why the triple flame structure that clearly exists is not observed in the CH PLIF images. It is quite possible that the premixed branches are very weak and that the low concentrations there are only picked up by a technique that provides a stronger signal such as CH_2O PLIF.

2.3.1.4 Local Extinction

Flame blowout is a problem of considerable importance in most practical combustors and especially aviation gas turbine engines. On a smaller scale, when reaction rates decrease, the flame can become extinguished (Bushe and Bilger (1998)) and the combustion ceases in a specific region. This results in localized holes in the flame surface where no reactions take place. While these pockets may reignite, they can also lead to global extinction where no flame exists to sustain combustion. It is important therefore for any diagnostic to correctly identify such local extinction events.

Fig. 2.24 shows a sample image set from Flame PF3 exhibiting local extinction as evidenced from the break in the CH layer. Although it is likely the three-dimensional flame surface is connected, a local hole in this surface exists. Such an event allows for an analysis of the formaldehyde image near a flame hole. While the break in the

flame is apparent in the CH image, it is not immediately obvious in the formaldehyde image. The layers appear to be continuous near the hole. A sharp decrease in the formaldehyde concentration is observed near the flame hole although measurable quantities still exist at the break. Furthermore, the size of the region of reduced concentrations is smaller than break in the CH image. In effect, the longer lifetimes of formaldehyde allow it to exist across a break in the flame surface. It is unlikely therefore, that in isolation, local extinction can be reliably detected from formaldehyde PLIF images.

Local extinction can also be seen in Fig. 2.23(a) where there is a distinct break in the diffusion flame. Watson et al. (1999b) have looked at this phenomena with simultaneous CH/PIV. Their PIV results indicate that there is an outward radial movement of fuel through the opening in the flame surface. This is also evidenced here through the formaldehyde image which suggests that reactants have escaped through the hole and formed a pool outside the main diffusion flame. It is likely that in the absence of an ignition source, this fuel remains unburnt due to the local extinction.

2.3.1.5 Flame Wrinkling in the Calibration Burner

Many LES based simulations of combustors utilize a model first suggested by Marble and Broadwell (1977) where it is assumed that thin reaction zones lead to the general result that

$$\omega_F = V_F \Sigma, \tag{2.12}$$

where ω_F is the local turbulent reaction rate, V_F is the mass of fuel consumed per unit flame sheet area, and Σ is the flame sheet area per unit volume. It is assumed therefore, that since turbulence causes the flame surface to be wrinkled (and thereby

increase the flame sheet area in comparison to a laminar flame), ω_F is locally increased due to the higher surface area in contact with the reactants. The use of Eqn. 2.12 in LES models makes it imperative that the total flame surface area be correctly computed. Fichot et al. (1994) used OH PLIF images to compute Σ while Donbar et al. (2000) used CH PLIF images to compute the same.

The location and broadening of the CH and CH_2O layers, analogous to the turbulent flame brush, can be quantified by computing a probability of finding the respective molecule along the radius at a given downstream location. For this purpose, the images were first converted to a binary image by setting a threshold. Then at a given axial location, the probability of the molecule's occurrence was computed at each radial location. The PDF's of the CH images are shown in Fig. 2.25 while that for CH_2O are given in Fig. 2.26.

The PDF of the CH layers shows that the layers remain nearly straight. This is evidenced in the fact that the peaks of the PDF's at all three downstream locations are at virtually the same radial location on both sides of centerline. Also, the flame brush thickness can be computed from the FWHM of the PDF, and it is seen that at all downstream locations, the brush thickness is about 0.25 jet diameters. This is in sharp contrast to the PDF computed from the formaldehyde images. As expected from the images, the peaks at all axial locations are closer to the centerline (i.e. on the reactant side) than the CH peaks. Large differences in the PDF's are seen at the downstream locations where the merging of the two sides suggests broad zones of formaldehyde nearer to the flame tip. While the probability of finding CH near the centerline is close to zero, there are high occurrences of CH_2O away from the reaction zone, especially as one approaches the flame tip. This could be a result of the formaldehyde layers merging together as the flame closes in on itself near

the tip. Also, as was seen in the images, formaldehyde appears to be convected upstream in the cold reactant jet and the formaldehyde produced upstream is likely to form pools of formaldehyde downstream. Therefore, the PDF's confirm that the formaldehyde is subject to the turbulence in the cold reactant jet and is more likely to be convected toward the centerline near the tip of the flame. Furthermore, as the flame tip is approached, formaldehyde formed upstream but not consumed collects in broad zones of formaldehyde.

The degree of wrinkling of a flame can be also be computed by measuring the perimeter of the reaction zone as marked by both the CH and CH_2O. The wrinkling parameter has been defined as

$$\xi = \frac{s}{d}, \tag{2.13}$$

with s and d defined as shown in Fig. 2.27. Therefore, a perfectly straight flame with no wrinkling (akin to a laminar flame) will have $\xi = 1$. ξ as defined here is analogous to Σ used in Eqn. 2.12. For computing the wrinkling parameter from the formaldehyde images, the broadened zones mandated computing a different perimeter for the product and reactant sides. This also allows the assessment of the idea that the reactant side is more wrinkled than the product side as suggested in §2.3.1.3.

The wrinkling parameter was computed for Flame PF3 and the PDF for CH is shown in Fig. 2.28. For comparison, the PDF was computed separately for the product and reactant sides and for both sides together. As expected, the thinness of the CH layers causes the wrinkling of both the product and reactant sides to be the same. The peak of the PDF suggests that wrinkling from the turbulence causes the flame surface to be about 20% larger than for a laminar flame. The PDF computed from the formaldehyde images is shown in Fig. 2.29. Also shown is the

PDF computed from both the reactant and product sides of the CH layers. The wrinkling parameter from the product side agrees with the CH as expected from the PLIF images. The reactant side however not only peaks at a higher value but also has high probabilities of layers with areas over 1.5 times that of a laminar flame. This shows that the reactant side of the formaldehyde layers is subject to the turbulence in the cold reactants whose characteristics are determined by the initial conditions and Reynolds number. As was shown by Clemens and Paul (1995), the heat release from the reaction zone greatly stabilizes or laminarizes the local turbulence. Yule et al. (1981) suggest that this is due to the lower effective Reynolds number because of the heat release. This has implications for models of premixed combustion that use the turbulent surface area for computing the turbulent reaction rate. While the surface area of the actual reaction zone is that computed from the CH layers, the cold reactants are in contact with a larger area of preheated radicals. Formaldehyde is an intermediate and its presence assists the combustion of the reactants. Therefore, mixing with formaldehyde enhances the reaction rate of the reactants. Thus, a larger turbulent surface area than that computed from the CH layers needs to be used to accurately compute a reaction rate.

2.3.1.6 Conclusions from the Calibration Study

The results from the calibration study have strongly suggested that CH_2O PLIF provides an attractive and practical way to image the reaction zone in turbulent flames and combustors. The product side of the CH_2O has high spatial correlation with the flame front and high signal gradients exist along this edge. These results indicate that the spatial locations of high PLIF signal gradients (as marked by a given contour level) provide a reliable means of marking the flame contour.

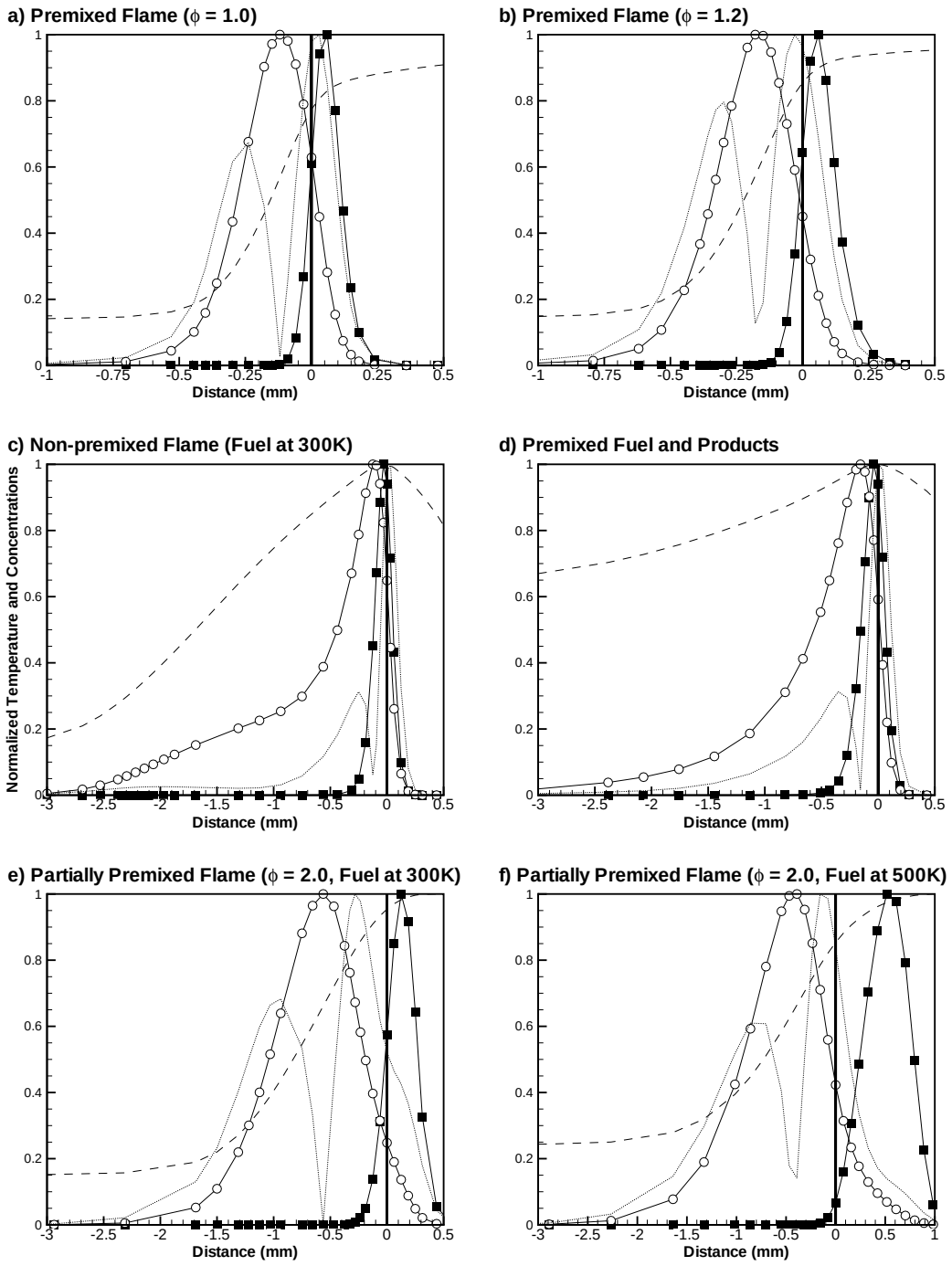

Figure 2.13: Computed profiles from CHEMKIN for a range of conditions. Square: CH, Open Circle: CH_2O, Dashed Line: Temperature, Dotted Line: $|\frac{\mathrm{d}[CH_2O]}{\mathrm{d}x}|$. The flame front is at 0 mm in all sub-figures. The location of the peak gradient of CH_2O lines up well with the flame front. Note how the formaldehyde zone gets narrower with increased premixing.

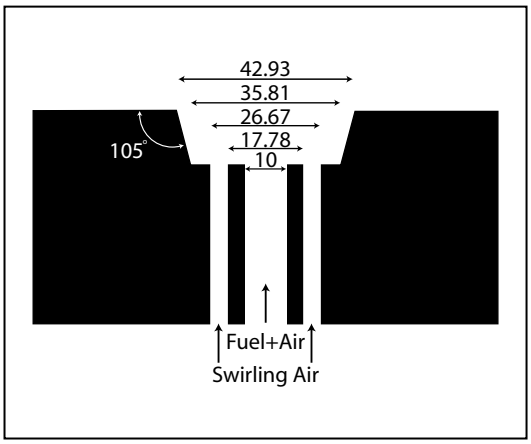

Figure 2.14: Details of the calibration burner. All dimensions are in mm.

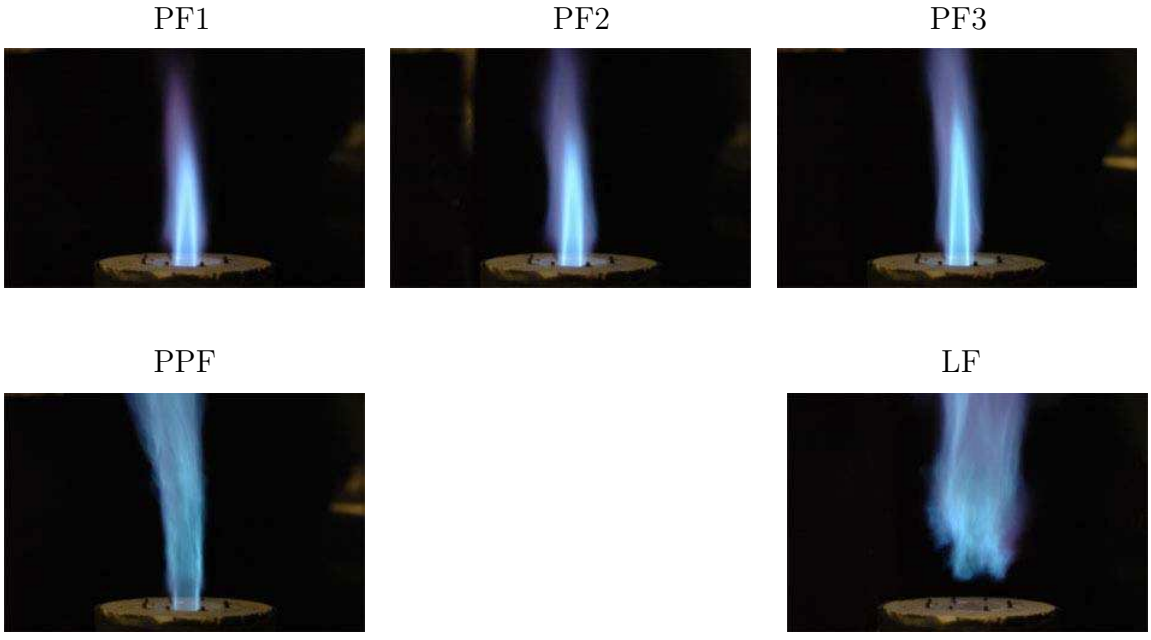

Figure 2.15: Visual images of the flames studied.

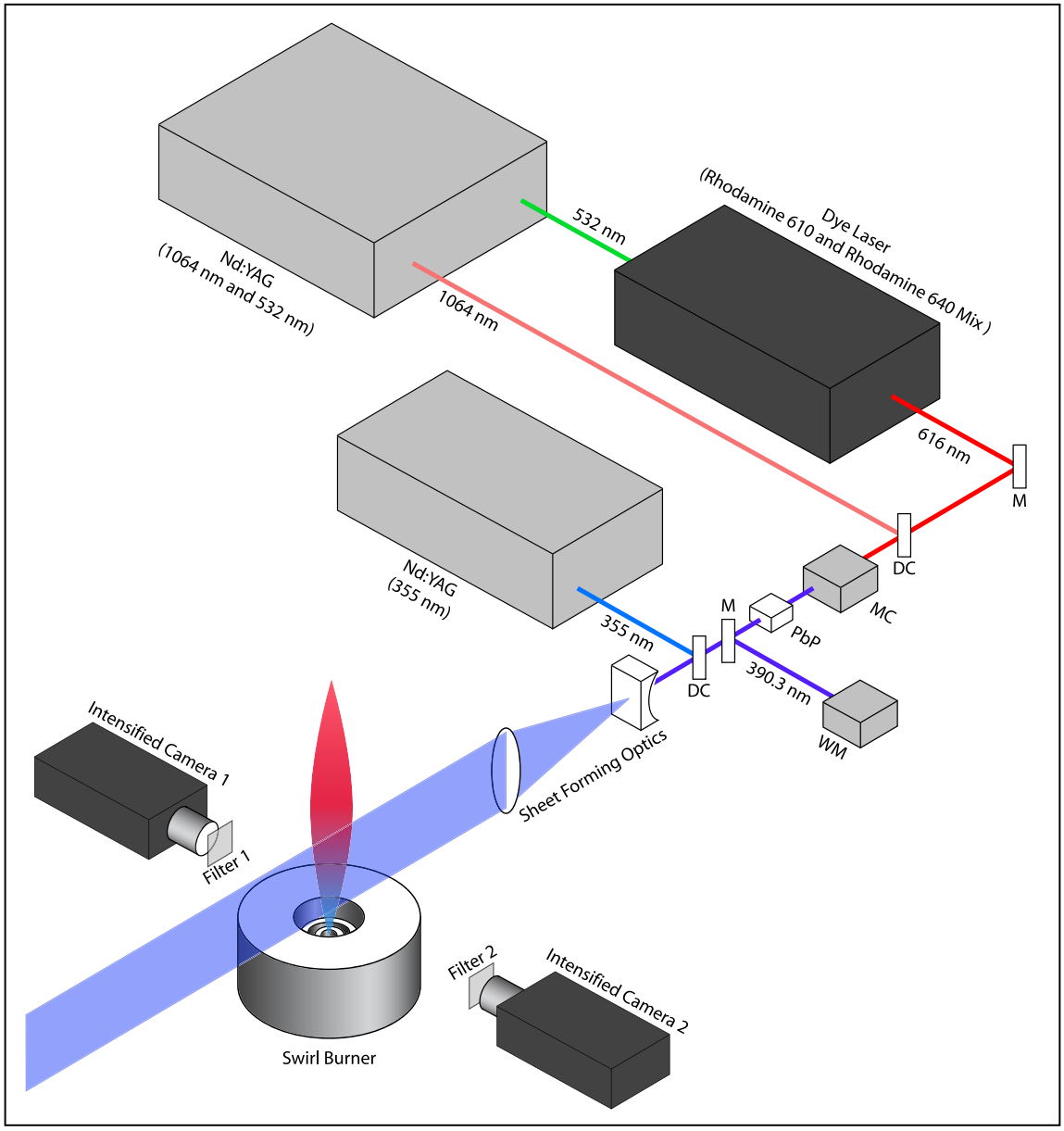

Figure 2.16: The experimental setup. The pellinbroca prism (PbP) bends the beam by 90° but that fact is not shown. Mirror (M), Dichroic (DC), Mixing Crystal (MC), Wavelength Meter (WM).

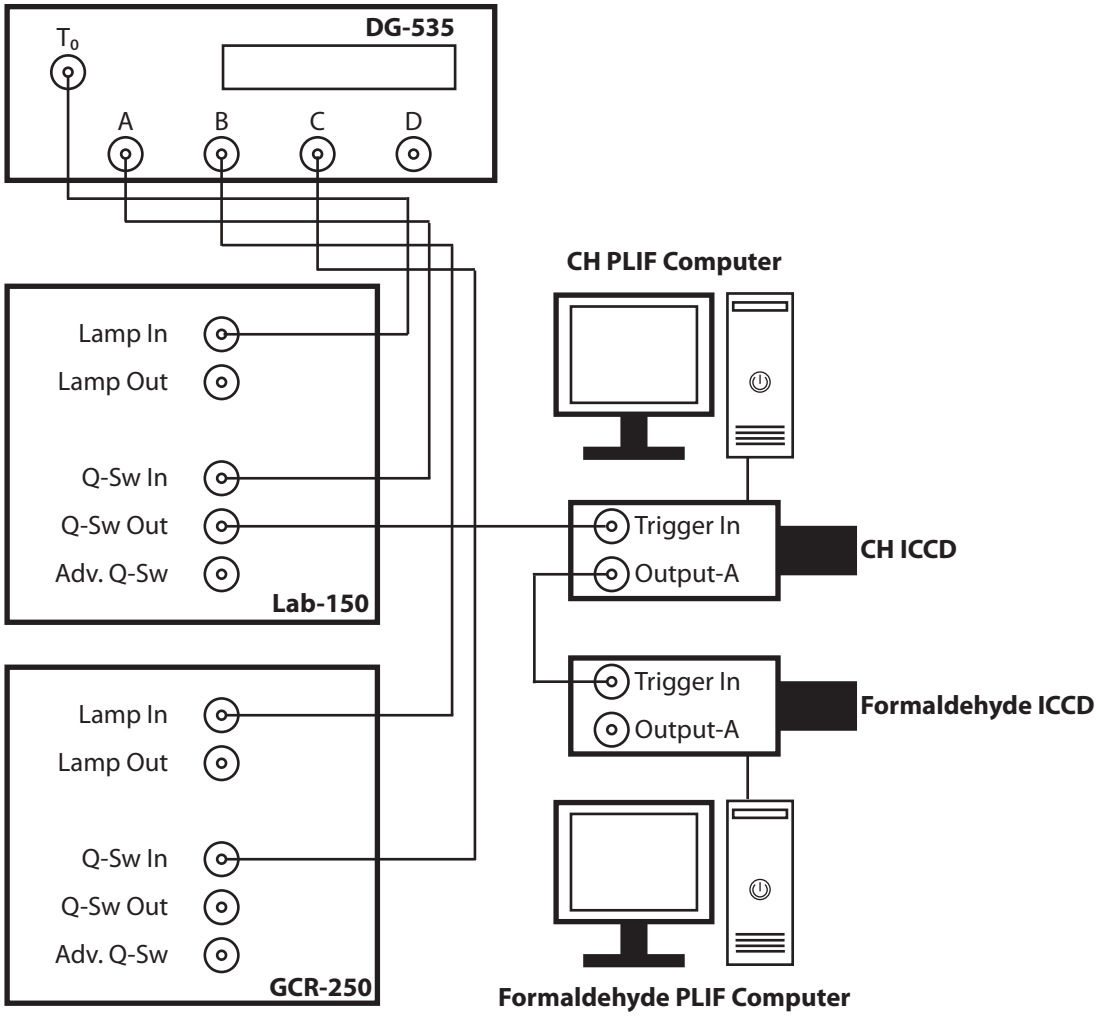

Figure 2.17: Schematic of the wiring used to synchronize the acquisition of the CH and formaldehyde PLIF signals.

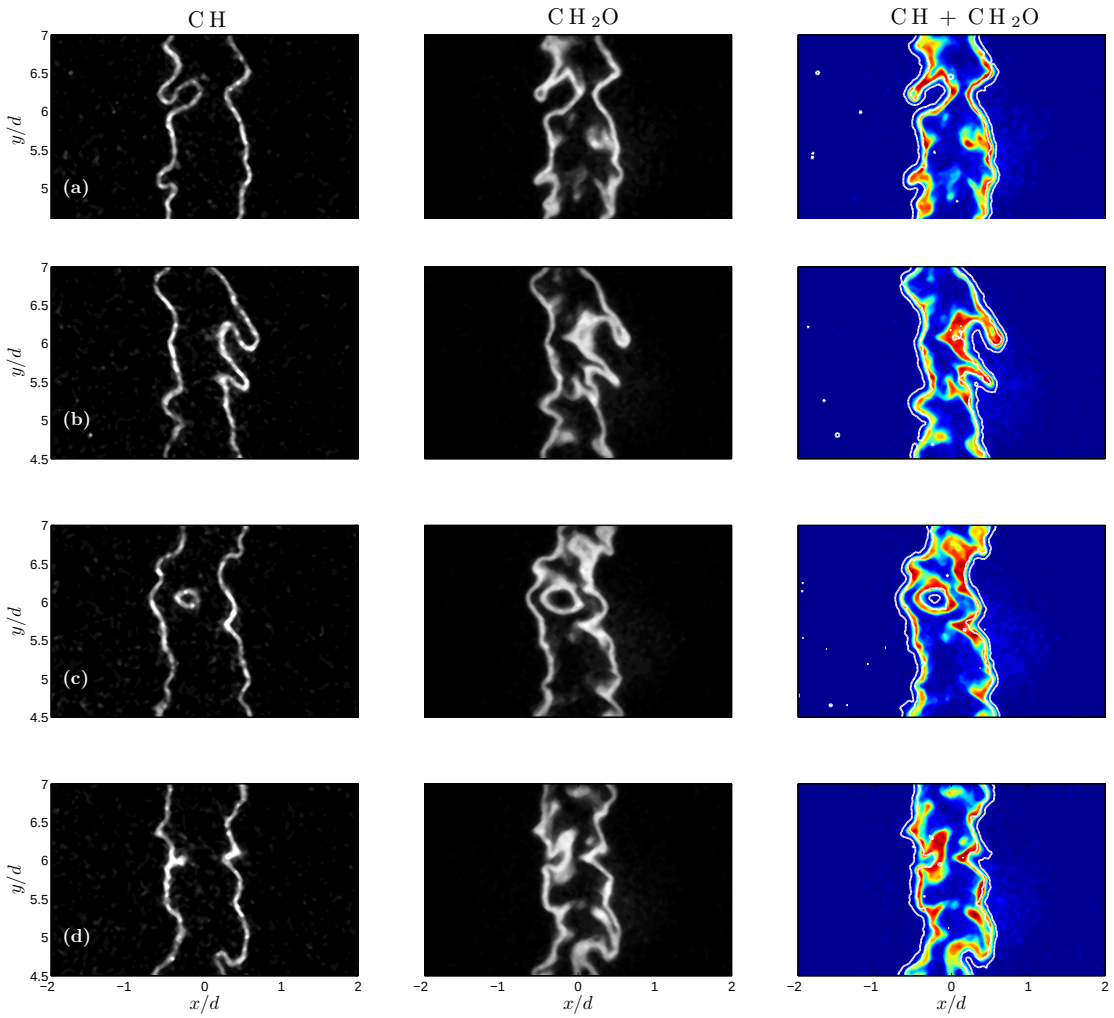

Figure 2.18: Sample instantaneous PLIF images from Flame PF3 ($\phi = 1.5$).

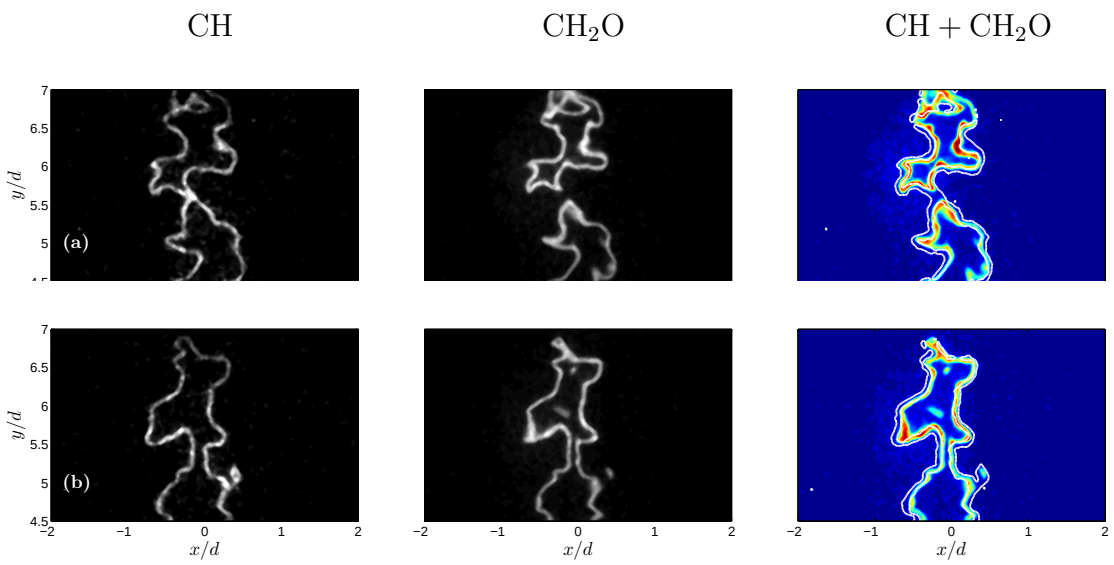

Figure 2.19: Sample images from Flame PF1 ($\phi = 1.0$).

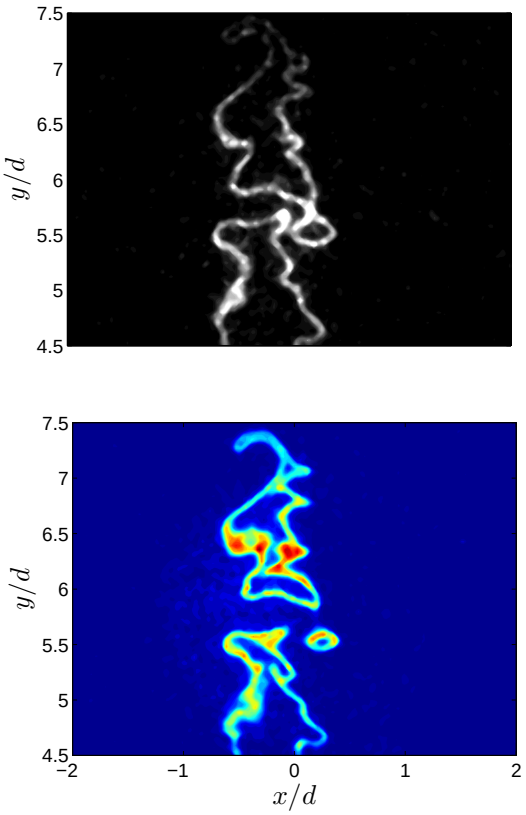

Figure 2.20: A sample image set from Flame PF2 ($\phi = 1.2$). CH, above; CH_2O, below.

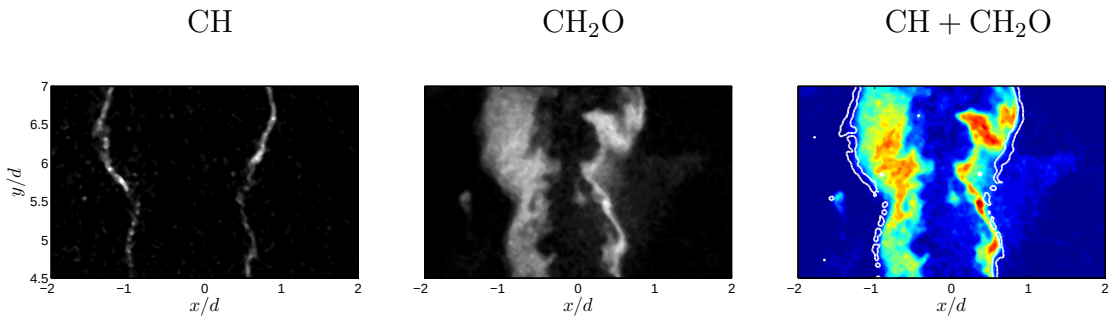

Figure 2.21: A sample image set from the rich partially premixed flame ($\phi = 2.0$).

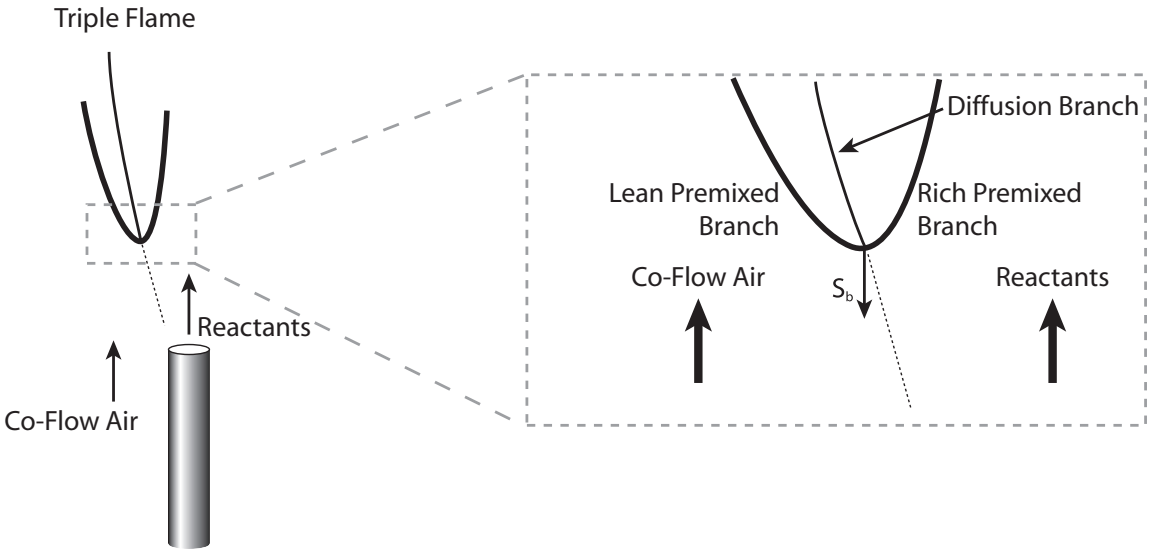

Figure 2.22: Schematic of the edge-flame or triple flame model of lifted flame stabilization.

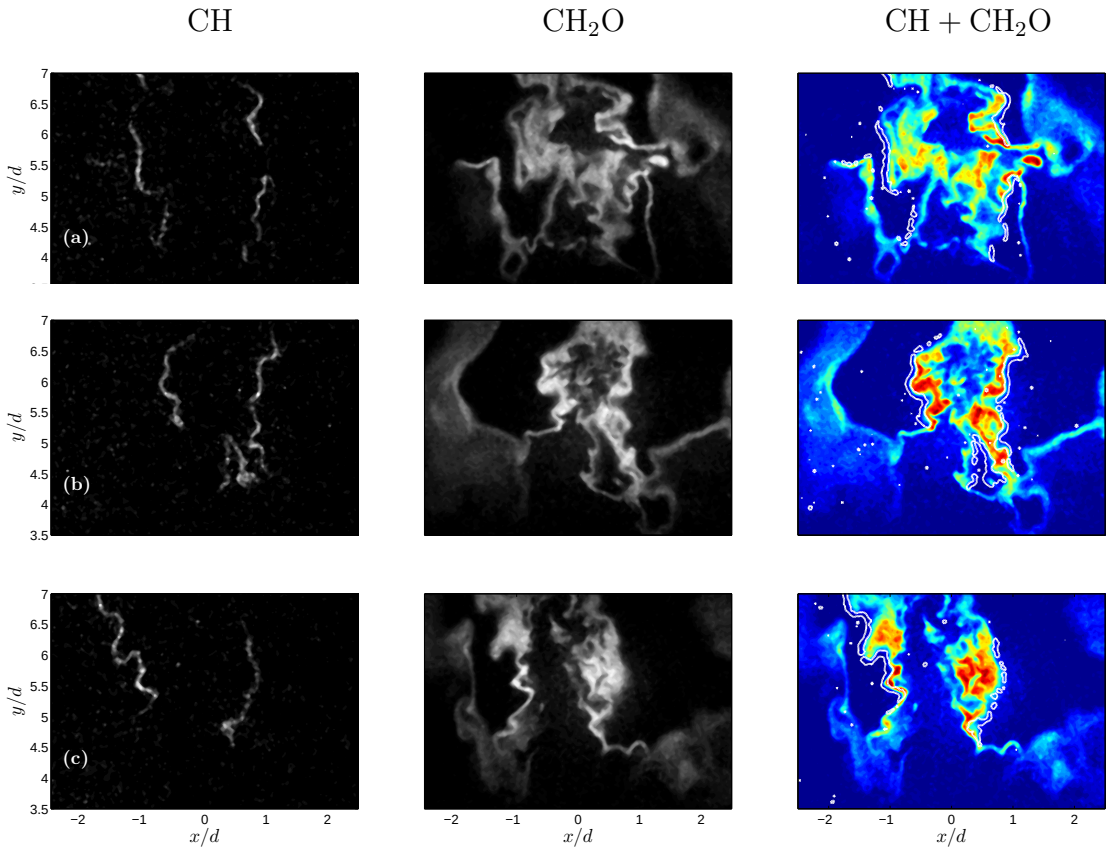

Figure 2.23: Sample images from the lifted jet flame (Flame LF).

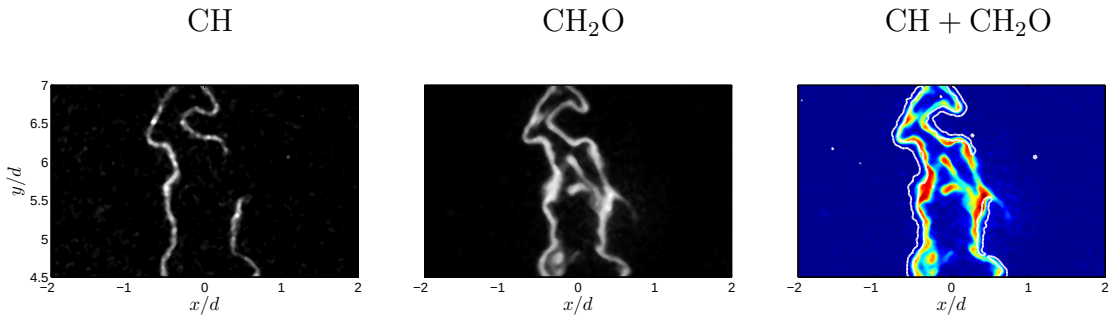

Figure 2.24: A sample image showing local extinction from Flame PF3.

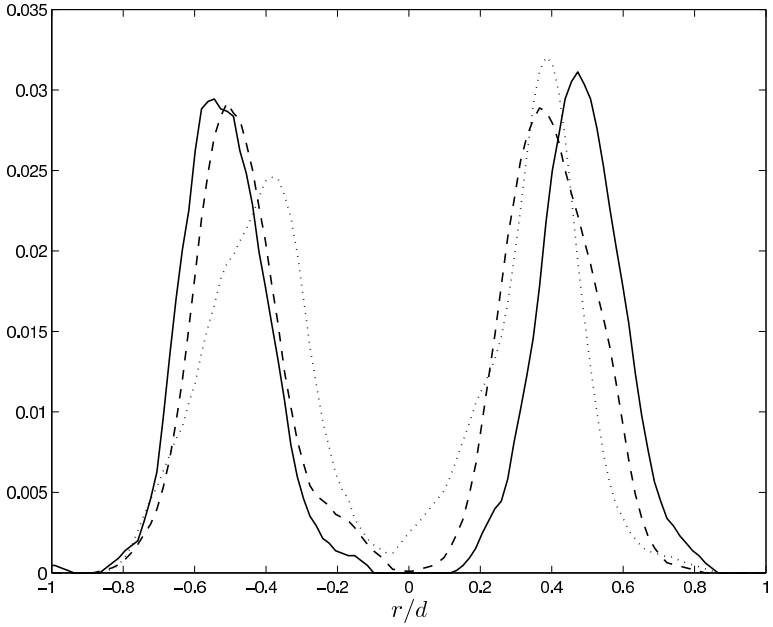

Figure 2.25: PDF of CH signal from Flame PF3 shown for three downstream locations. —: $y/d = 4.5$, - - -: $y/d = 5.5$, $\cdots$: $y/d = 6.5$.

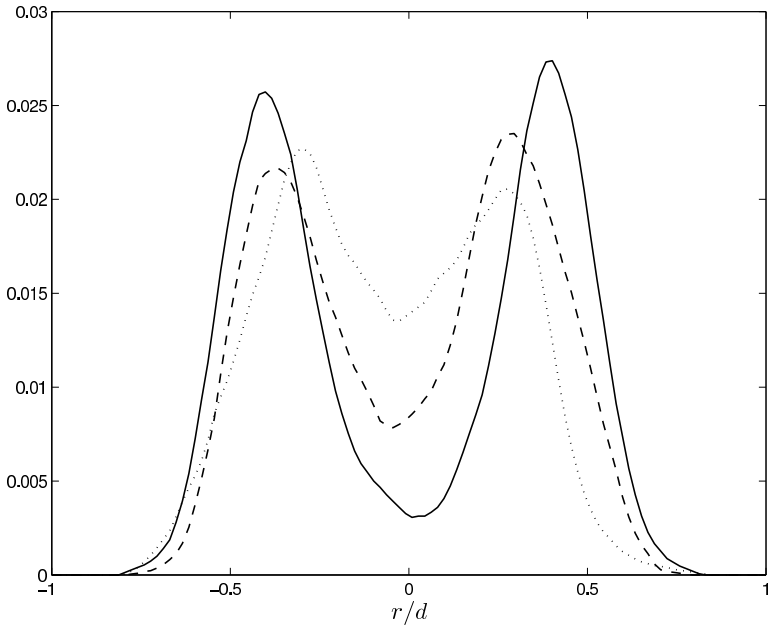

Figure 2.26: PDF of CH_2O signal from Flame PF3 shown for three downstream locations. —: $y/d = 4.5$, - - -: $y/d = 5.5$, $\cdots$: $y/d = 6.5$.

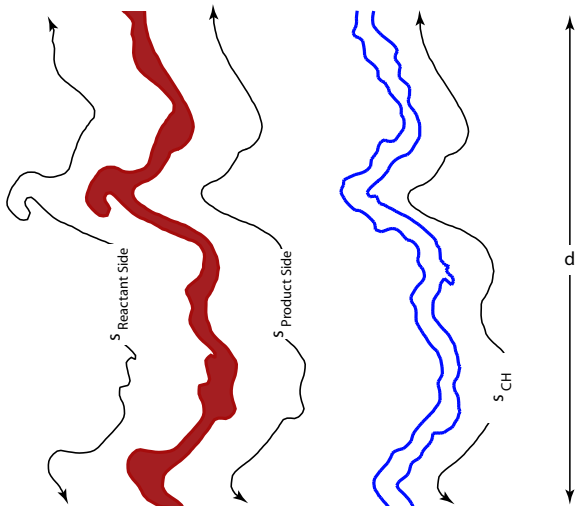

Figure 2.27: Schematic showing the definition of the perimeter used in computing the wrinkling parameter (ξ).

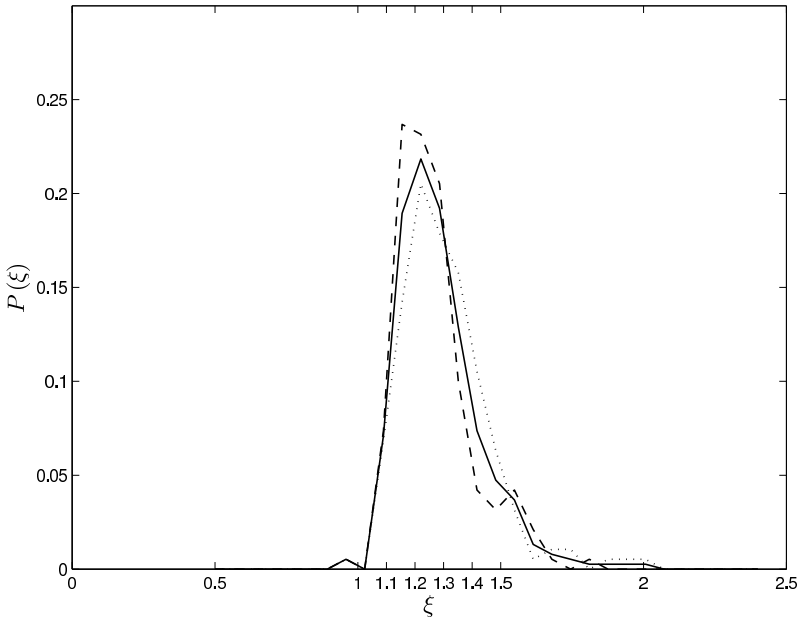

Figure 2.28: PDF of the wrinkling parameter from the reactant sides ($\cdots$), product sides (- - -), and both sides of the CH layers (—).

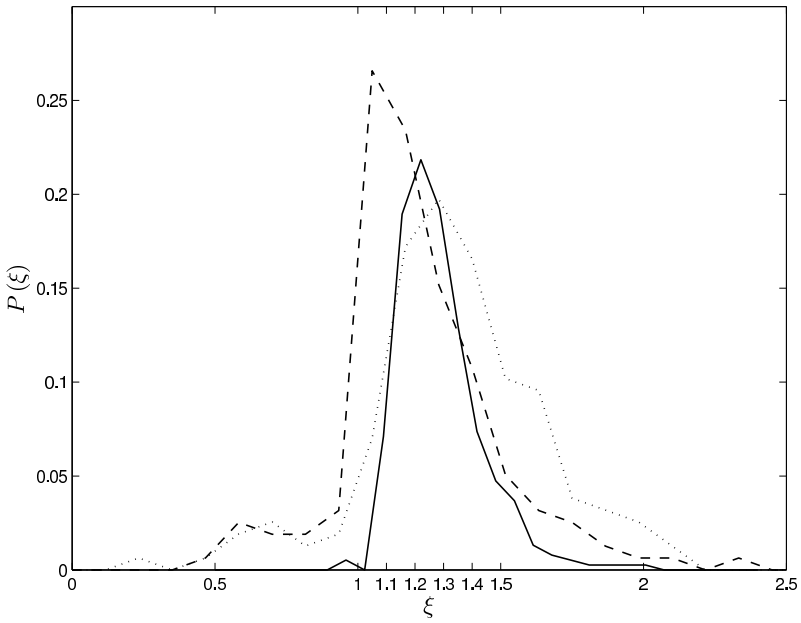

Figure 2.29: PDF of the wrinkling parameter for both the reactant ($\cdots$) and product (- - -) sides of the CH_2O layers. The PDF from the CH layers (—) is also plotted for comparison.

2.3.2 Formaldehyde PLIF of the Flame in the TAPS Combustor

For the reasons noted earlier, PLIF of CH_2O was chosen to image the reaction zones in the combustor. The same equipment and transitions used in the simultaneous CH/CH_2O PLIF experiments with the calibration burner were used to image CH_2O in the TAPS combustor (§2.3.1.1). A schematic of the layout used for CH_2O PLIF in the TAPS combustor is shown in Fig. 2.30. The third harmonic (355 nm) of an Nd:YAG laser (Spectra-Physics GCR-250) was passed through a combination of -100 mm and -500 mm plano-concave lenses to form a sheet 80 mm wide that was passed through the combustor. The average pulse energy was 150 mJ. The ICCD described earlier was mounted vertically to image the resulting emissions from the top window of the combustor. The camera was fitted with a 90 mm (Sigma) lens stopped down to f#4. A combination of Schott glass GG-385 (3 mm) and BG-3 (2 mm) filters was used to block the laser wavelength and flame luminosity. As shown in Fig. 2.31 the GG-385 filter blocks all wavelengths below about 385 nm and the BG-3 filter blocks wavelengths above 500 nm. With this combination, the camera effectively imaged wavelengths between 385-500 nm. The BG-3 filter was necessary because even with the short gate widths (100 ns) of the intensifier, there was sufficient luminosity from the flame to render the image unusable. Along with the filter, a mechanical shutter (Uniblitz VS-25) was used to further block flame luminosity. The shutter ensures that no stray light is allowed onto the CCD during the CCD readout times when the CCD is sensitive to light even with no electronic gating. The timing of the camera and shutter was controlled by a Digital Delay Generator (DG-535) with the Advance Q-Switch of the YAG serving as the master clock. Since the camera was unable to acquire images at the 10 Hz rate of the laser, the delays were set such that only every eighth pulse triggered the camera. The overlap of the

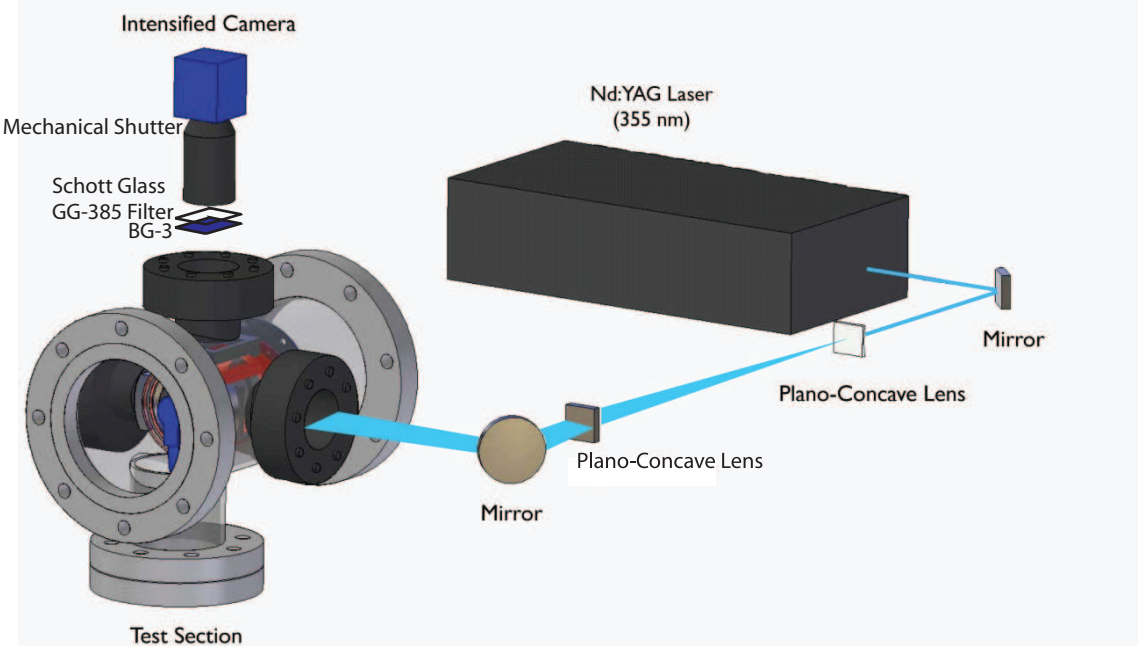

Figure 2.30: Schematic of the CH_2O PLIF setup used for imaging CH_2O in the TAPS combustor.

camera gate and laser pulse was ensured by monitoring both the camera gate output and the output from a fast photo-diode on a digital oscilloscope. The field of view was 75 mm × 75 mm. The 2k×2k CCD of the camera was hardware-binned 2×2 to give a create an array of 1k×1k pixels, giving a final resolution of 148 μm per pixel. Though the signal was sufficiently large, 2k×2k binning of the pixels was necessary to decrease the read-out times.

2.3.3 Image Corrections

The PLIF signal captured by the camera includes contributions from numerous extraneous sources that are not a part of the desired signal and corrections are necessary (Clemens (2002)). Though these corrections are more critical when quantitative measurements are attempted, they also must be made when qualitative images are recorded to allow for accurate comparisons of the images. The total signal recorded

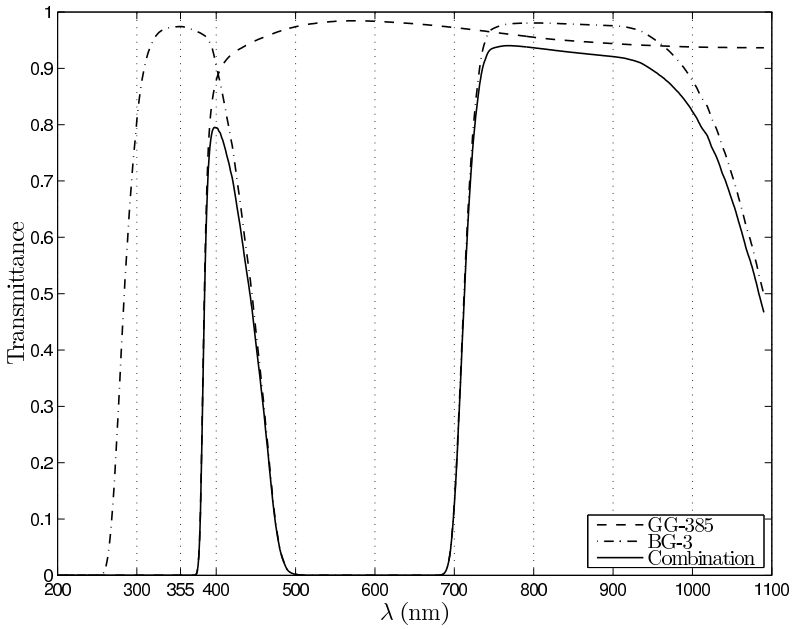

Figure 2.31: The transmittance of the filters used for CH_2O PLIF.

by the camera (S_{TOT}) is:

$$S_{TOT}(x,y) = \omega(x,y)\left[L(x)S_e(x,y) + S_{back}(x,y)\right] + S_{dark}(x,y), \tag{2.14}$$

where S_e is the desired signal, $\omega(x,y)$ is the white-field response function, $L(x)$ is the laser sheet intensity distribution, S_{back} is the background signal, and S_{dark} is the camera's dark noise. Since the pixels on CCD arrays do not have a uniform response to a given source of light, this variability must be taken into account by $\omega(x,y)$. Unless the fluorescence is saturated, the fluorescence signal is directly dependent on the incident laser intensity. Therefore, variations in the laser sheet fluence across the imaged region must be corrected by measuring $L(x)$. S_{back} is the background signal that exists from rogue laser scattering off of windows or walls, flame luminosity, and other extraneous light sources. This is often the largest contributor of noise in a measurement, and it is difficult to account for it completely. Since the two major sources of background signal are internal reflections and flame luminosity,

both cannot be accounted for simultaneously. Essentially, by having both the laser and flame present, the signal measured by the camera will not be S_{back} but will be S_{TOT}. Ideally there should be a background image acquired for each instantaneous image but this is not possible. Fortunately the discrepancy between an instantaneous and average background image is negligible. S_{dark} is the camera's dark field response and is the background signal count that exists with no light source (or with the lens cap on). By rearranging Eqn. 2.14 for the desired signal, it can be seen that S_{dark} is automatically included in the measurement of the background signal:

$$S_e = \frac{S_{TOT} - S_{correction}}{\omega L}, \tag{2.15}$$

where $S_{correction} = \omega S_{back} + S_{dark}$.

In the experiments, $S_{correction}$ was measured by taking an ensemble average of 50 images of just the laser sheet with no flame present. This accounts for laser reflections and non-uniformities in the wall of the combustor that was behind the imaged region, but does not account for the flame luminosity. Noise from the flame luminosity was kept to a minimum by having a short gate time along with the combination of filters and the shutter described earlier. Though one could take a background image separately with the flame present and no laser and add it to the background signal described earlier, this strategy is not very reliable in the presence of an unsteady flame. It is therefore better to attempt to minimize the noise from flame luminosity. To further reduce the background signal counts, the inner combustor wall was repainted with a high temperature black paint before every run. Since the wall is close to the imaged region, it was not possible to sufficiently put it out of focus, and therefore non-uniformities in the surface from chipped/peeled paint and particulate build-up led to considerable noise.

Ideally, the white-field response of the camera ($\omega(x, y)$) must be computed by imaging a back-lit frosted plate as shown in Fig. 2.32. Variations in intensity across the image due to imaging with a circular aperture should then also be taken into account through the equation, $I(\beta)/I(0) = \cos^4 \beta$, with $\beta(x, y)$ as given in Fig. 2.32 (Smith (1990)). In practice however, it is difficult to reliably obtain a perfectly uniformly lit object. The variations in intensity across the image due to the non-uniformities are often greater than the non-uniformities in the CCD's white-field response and produce errors that far outweigh any gains from the correction. Furthermore, since the flames typically encompassed only a portion of the entire CCD, any corrections in the white-field response were considered negligible and therefore not made. The laser sheet intensity distribution was measured by replacing the test section with a dye cell fitted with a fused silica glass window and filled with a high concentration of Rhodamine 590 dye in methanol. This created an "optically thick" concentration of dye such that the laser was entirely absorbed by the dye. The cell was mounted at a 45° angle to the oncoming laser sheet and the resulting fluorescence was imaged by the ICCD as shown in Fig. 2.33. The linearity of the response of the dye cell to laser power was verified as shown in Fig. 2.34. By keeping the camera in the same position as used for the PLIF measurements, the sheet intensity was automatically aligned spatially with the PLIF measurements. The average sheet image and profile in the coordinate system of the actual experiments are shown in Fig. 2.35. As shown in Fig. 2.36, the shot-to-shot variations in the intensity distributions were minor and therefore an ensemble average of 50 measurements was used for $L(x)$ rather than instantaneous sheet corrections.

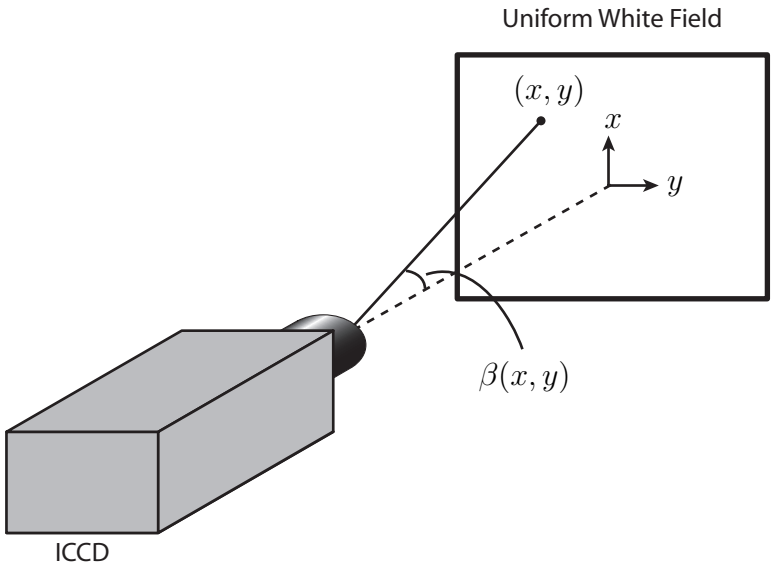

Figure 2.32: Geometry for the measurement of the camera's white-field response function ($\omega(x, y)$).

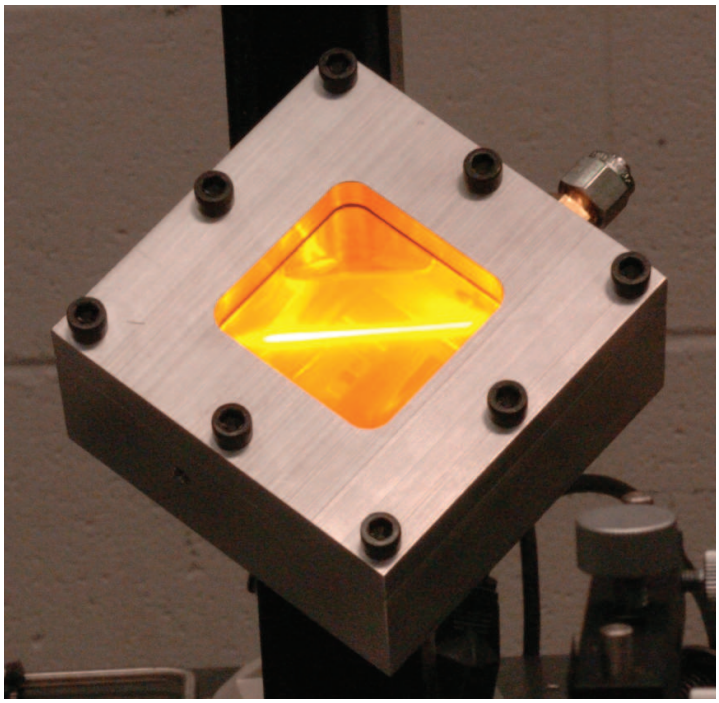

Figure 2.33: The arrangement of the dye cell for the measurement of the average laser intensity distribution ($L(x)$). The laser sheet is visualized from the fluorescence emissions of the dye in the cell.

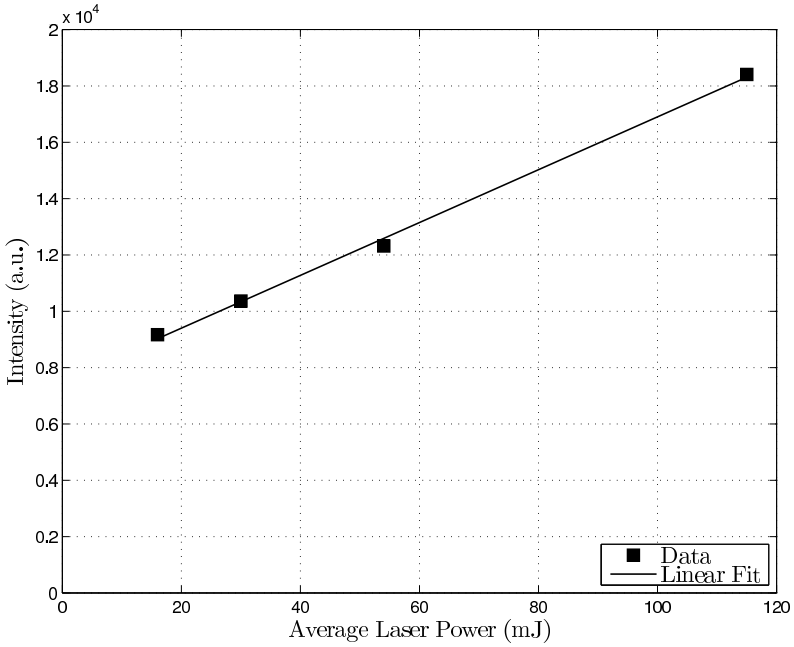

Figure 2.34: The response of the dye cell with laser power.

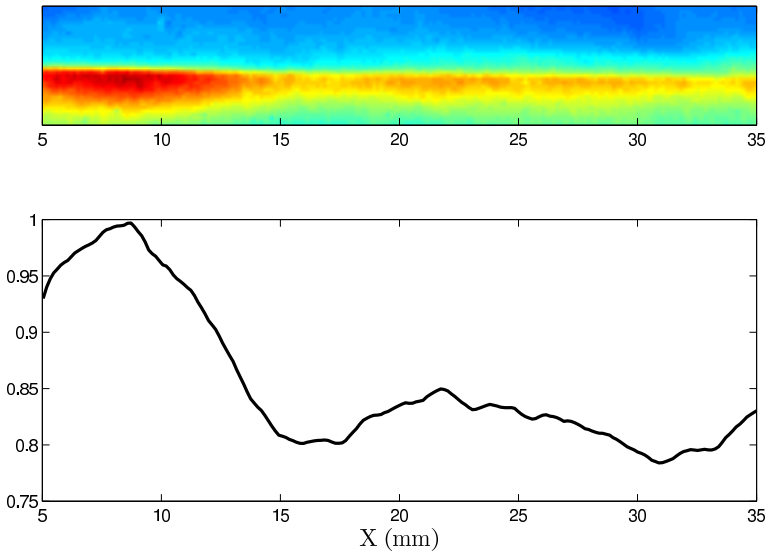

Figure 2.35: The average sheet intensity image on top and its profile in the spatial coordinate system used in the experiments.

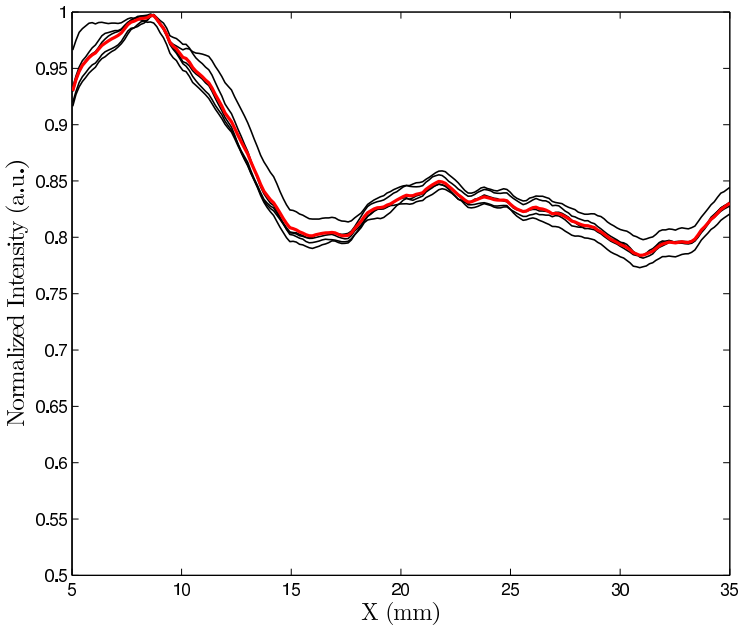

Figure 2.36: Five randomly selected laser intensity distributions along with the average $L(x)$ (shown in red) used for the sheet corrections.

2.3.3.1 Image Filtering

To further reduce experimental noise, the acquired images were spatially filtered after making the corrections described in §2.3.3. Filtering an image has the effect of removing, or "smoothing", out random spikes of noise while typically preserving the signal of interest, leading to enhanced signal to noise ratios. However, this comes at the cost of reduced spatial resolution. One of the most common filters used is a median filter that simply determines the value of each pixel by the median value of all pixels in a given template. Therefore, strong isolated (and spurious) spikes are effectively removed from the final images. Although median filtering is not optimal for removing the randomly distributed shot noise prevalent in all scientific cameras (Clemens (2002)), this is more of a concern when the fine spatial structural detail of a flame is being probed. The purpose of PLIF imaging in this study was to gain an understanding of the general spatial location of the flame(s) and a median

filter provided the optimum balance of enhancing the signal to noise ratio while preserving spatial resolution. All PLIF images were processed by a 3x3 pixel median filter followed by a 2x2 median filter.

The image corrections and filtering techniques described were applied to all instantaneous PLIF images to yield a flame contour. The flame contour was obtained by selecting an appropriate signal threshold that most closely corresponded to the location of highest signal gradients. The typical signal counts near the flame front were 5000 $\pm$ 100, suggesting an uncertainty in the identification of the flame front of 2%.

2.4 Chemiluminescence Imaging

Imaging of the naturally occurring flame chemiluminescence provides a convenient way to qualitatively measure the temporal and spatial distribution of the heat release. Chemical reactions lead to electronically excited species in the flame which then emit radiation known as chemiluminescence (Gaydon and Wolfhard (1979)). Chemiluminescence in lean hydrocarbon flames is primarily due to CH*, OH*, and CO_2^* (Lee and Santavicca (2003)). Of these, CH* and OH* occur at distinct wavelengths with narrow spectral linewidths, with peaks emissions at 431 nm and 309 nm for CH* and OH* respectively (Ikeda et al. (2002)). The emission of CO_2^* however is broadband over 300-600 nm and over the entire range the emission intensity is higher than that from just CH* or OH*. Samaniego et al. (1995) and Najm et al. (1998a) have used detailed numerical analysis to show that there is good correlation between the heat release rate in a flame and chemiluminescence emissions, especially from OH* and CO_2^*. Samaniego et al. (1995) have also shown that the overall emissions intensity is directly proportional to the overall heat release. However, while chemilu-

minescence imaging is useful in marking the locations of heat release, it is necessarily a line-of-sight measurement. Therefore, the two-dimensional measurements are naturally integrated over the entire three-dimensional flame surface. So while other diagnostics such as PLIF are better suited for determining the detailed structure of the flame, chemiluminescence imaging provides convenience and the ability to obtain temporally resolved images of the flame.

2.4.1 Simultaneous High Speed Chemiluminescence Imaging and Pressure Measurements

A high speed CCD camera (Phantom v9.0 s, Vision Research), was used in conjunction with a high speed pressure transducer to obtain simultaneous time resolved measurements of the combustor pressure and heat release. This was done for selected conditions when the combustor became unstable and there were large sinusoidal variations in both chemiluminescence and pressure. The camera was fitted with a 90 mm lens (Sigma, Inc) and set up to look through the combustor at a slight angle. In this manner, the imaged region clearly included the face of the TAPS injector. While this arrangement no longer provides well defined line-of-sight images, it provides a better view of the flame dynamics. The use of a visible (non-UV grade) lens and no filters meant that chemiluminescence emissions were recorded in the wavelength range greater than roughly 400 nm. Therefore, OH* emissions were not captured and the measured emissions intensity was predominantly from CO_2^*.

A pressure transducer (Omega) measured the absolute pressure (p_3) in the combustor upstream of the TAPS injector. The 0-5 V output from the transducer was fed into a Boxcar Integrator (Stanford Research Systems SR 250) that was capable of recording the high frequency voltage data through an external trigger. Both the camera and Boxcar were triggered by a digital delay generator (Stanford Systems

DG-535) that was triggered internally at 1000 Hz. Accurate timing of the two systems was therefore ensured by having the delay generator serve as a reliable master clock. In practice, both the camera and pressure acquisition systems were primed and then the delay generator was activated to initiate the simultaneous acquisition of chemiluminescence and pressure data.

CHAPTER III

Flame Imaging in the TAPS Combustor

An important goal of this study was to identify both the instantaneous and average flame locations. The primary design feature of the TAPS injector is its novel combination of a stable diffusion flame (the pilot) and a primary ideally-premixed flame (the main flame). Since the main flame cannot exist without the pilot flame, focus was placed on understanding the interactions between the two. PLIF of formaldehyde was used to obtain information about the structure and location of both flames for a variety of conditions. Details of the experimental strategy and technique were discussed in §2.3.

Fig. 3.1 shows visual flame images of the pilot and main flames at three different pressures. All images were taken at the same conditions with $\dot{m}_{air} = 0.228$ kg/s, $T_3 = 505$ K, $\dot{m}_{f,m} = 2.40$ g/s, and $\dot{m}_{f,p} = 0.99$ g/s. The combustor pressure (p_3) was varied from 1-3 bar as indicated in the figure. The most striking difference in the images is the drastic increase in flame luminosity and soot radiation from the flame. The "yellowness" of the flame indicates the strong presence of soot particles that form a blackbody radiator in the high temperatures of the flame. While soot formation mechanisms are still a matter of research, it is clear that pressure has a strong effect on soot formation. Researchers have studied the effect of pressure

on soot formation in a variety of laminar flames for ethylene (Flower and Bowman (1988); McCrain and Roberts (2005)), methane (Thomson et al. (2005); McCrain and Roberts (2005)), and propane (Bento et al. (2006)) and found that soot volume fraction has a power law dependence on pressure ([soot] $\propto p^n$). These studies have all shown that irrespective of the fuel used, the volume fraction of soot is approximately proportional to $p^{1.3}$. The results of Bento et al. (2006) also suggest that at lower pressures (between 1-2 bar) the dependence may be even higher and the exponent (n) is 3.3.

While the mechanisms of soot formation is beyond the scope of this study, the influence of pressure on flame luminosity and soot (along with other PAH's) has an important bearing on the study of gas turbine combustors with laser diagnostics. As was described in §2.3, fluorescence from soot and PAH's in the UV wavelength range interfere with the PLIF signal. Furthermore, flame luminosity also leads to increased background signal that can only be subtracted on an average basis. This reduces the overall signal to noise ratio (SNR) of the measurement and poses substantial problems for accurately imaging the flame at higher pressures. For this reason, PLIF measurements were made at a combustor pressure of 1 and 2 bars. PLIF images were recorded at 3 bars but the SNR was not acceptable. The best signal to noise ratios were obtained for a combustor pressure of 1 bar. Analysis of the flame therefore was done with results from the 1 bar cases while the 2 bar case provides an understanding of the flame location at elevated pressures.

3.1 Flame Images at 1 bar

A number of flames were tested with the combustor at a pressure of 1 bar. Of course, gas turbine combustors never operate at atmospheric pressure and even at

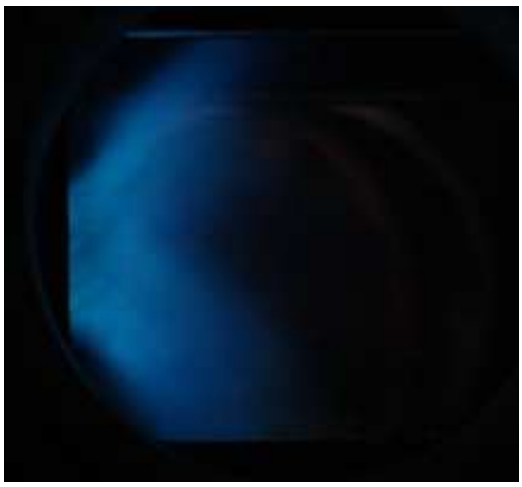

(a) 1 bar

(b) 2 bars

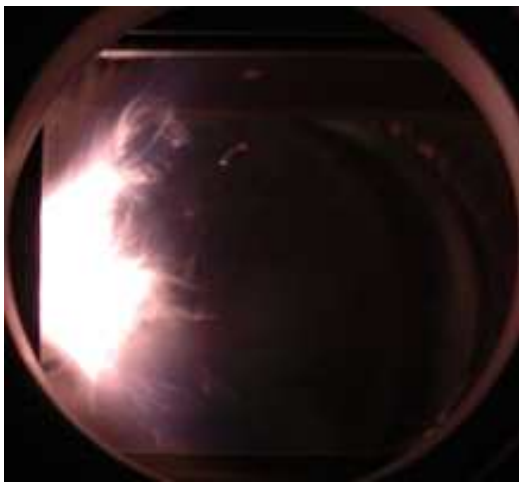

(c) 3 bars

Figure 3.1: Visual images of the pilot and main flames at different pressures. The air and fuel mass flowrates and combustor temperature were constant in all cases. All images were taken with the same exposure settings on the camera.

Case	Pilot Fuel Flowrate $\dot{m}_{f,p}$ (g/s)	Main Fuel Flowrate $\dot{m}_{f,m}$ (g/s)
1Pt1	1.17	0
1Pt2	1.52	0
1Pt3	1.87	0
1Main	1.17	2.49

Table 3.1: Flame conditions for the 1 bar case. For all cases, $\dot{m}_{air} = 0.228$ kg/s, $T_3 = 505$ K, $p_3 = 1.0$ bar.

cruise altitudes would typically operate at pressures around 6 bar (assuming a compression ratio of 30). However, experimental results at atmospheric pressure serve as a useful test for simulations as they represent a relatively simpler condition for models to attain. The conditions for the flames are given in Table 3.1.

3.1.1 Pilot Flames

The mean formaldehyde PLIF signal for the three pilot cases (Cases 1Pt1, 1Pt2, and 1Pt3) are shown in Figs. 3.2, 3.3, and 3.4. All three mean images have been shown with the same linear color scale and colormap ranging from blue (low) to red (high). Since the flame is axisymmetric, only one half of the combustor is shown. While it is important to recognize that the signal intensities do not represent actual formaldehyde concentrations, comparisons can nevertheless be made between the signal intensities across the images. In all three pilot cases, the pilot flame is a curve that encloses the fuel-rich gases that issue from the central pilot injector. In all cases therefore, the pilot flame is a hollow conical flame with reactions occurring on both the inner side (near centerline) and outer side (near the main annulus) of the fuel-rich spray region. The key difference between the three pilot cases is the length of the flame. The flame length will be discussed in more detail in §3.1.1.1.

Instantaneous PLIF images help shed light on the instantaneous flame structure

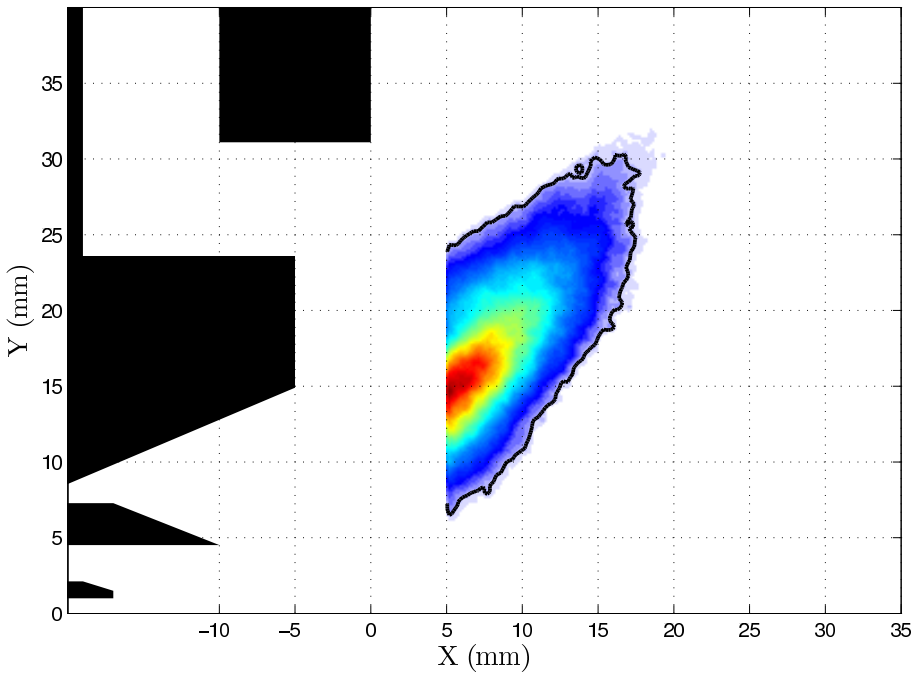

Figure 3.2: Average CH_2O PLIF image for Case 1Pt1. The TAPS injector is shown in black. The pilot injector is at the center surrounded by the two pilot annuluses. The main annulus is between $y = 23.4$ mm and $y = 31.1$ mm. The solid black line marks the flame contour.

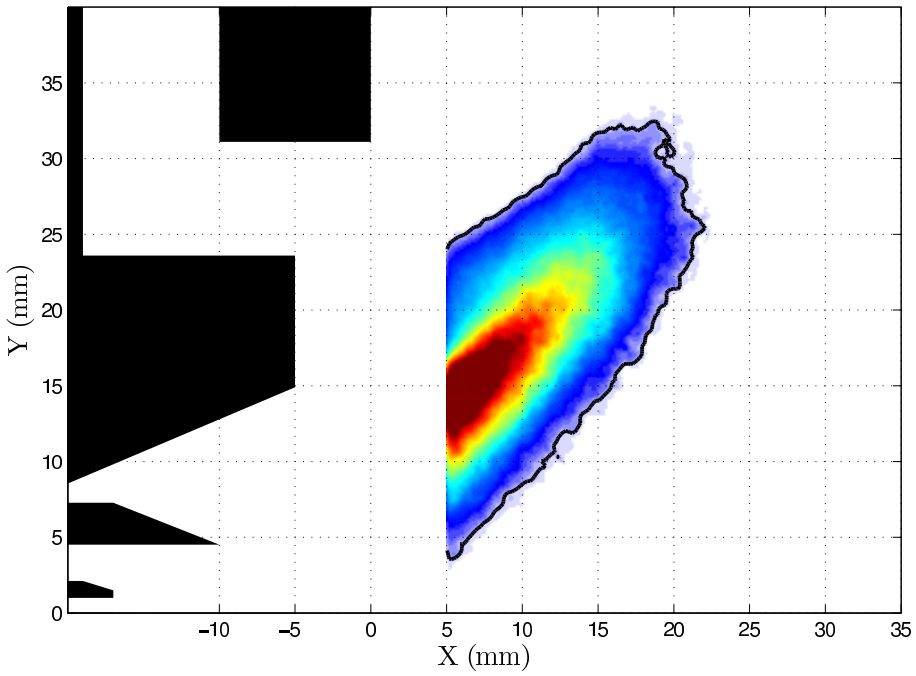

Figure 3.3: Average CH_2O PLIF image for Case 1Pt2. The solid black line marks the flame contour.

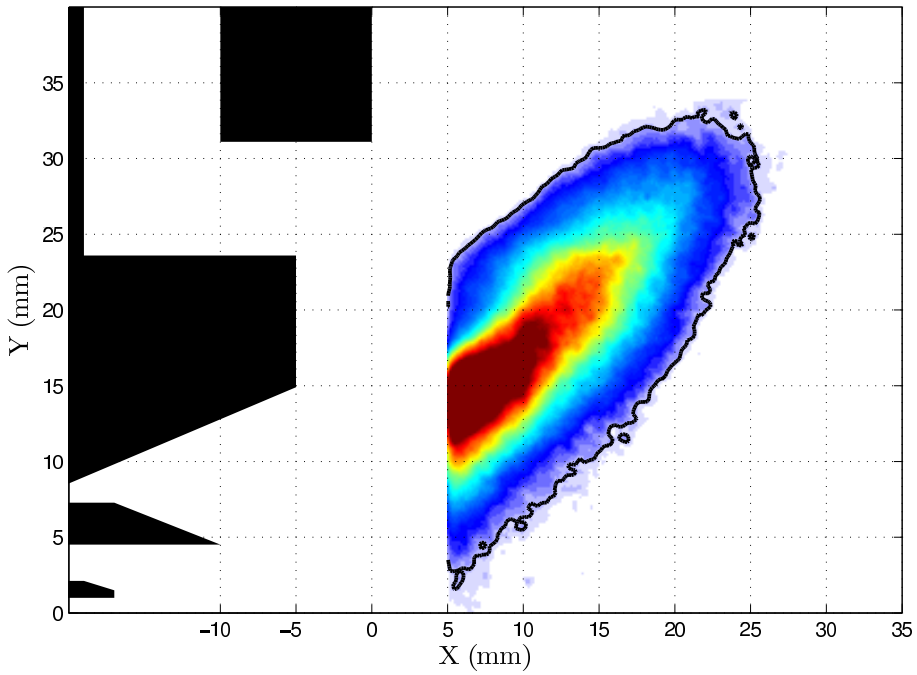

Figure 3.4: Average CH_2O PLIF image for Case 1Pt3. The solid black line marks the flame contour.

and are shown in Fig. 3.5. The instantaneous images are for Case 1Pt2 and are representative of all three pilot cases. Overlayed on the PLIF images is the flame contour (shown as a black line) that was obtained by plotting the contour line of the appropriate CH_2O signal level. The CHEMKIN results of Fig. 2.13 indicated that the location of the peak gradient of formaldehyde concentration is well correlated with the location of the flame front. Therefore, the contour level that was selected is the one that corresponds to the peak gradient in the PLIF signal. Sufficient noise existed in the images (even after filtering) that make is impossible to directly compute the CH_2O signal gradient at each location and use it to identify the flame boundary. Instead, the appropriate contour level was chosen that best identified the peak gradient location in the images.

Isolated islands of signal are seen as small dots that are scattered around the flame due to Mie scattering off unvaporized fuel droplets. All instantaneous images show

a very high degree of flame wrinkling that is absent in the mean PLIF images. None of the images show reduced signal between the two edges of the flame indicating that formaldehyde is spread out over the entire fuel jet. This is not surprising considering the broad zones of formaldehyde seen in both the CHEMKIN simulations (2.13c,d) and PLIF results in a turbulent partially premixed flame (2.21). Both of these results showed that the formaldehyde can easily exist over a spatial range of 4-8 mm from the flame front, which agrees with the range seen in the PLIF images of Fig. 3.5. It is interesting to note however that the peak signal does not always appear to be next to the flame front as predicted by the CHEMKIN simulations. In the simulations, the partially premixed cases (Fig. 2.13e,f) had the greatest separation between the flame front and peak formaldehyde concentrations of about 0.5-0.75 mm. In the instantaneous PLIF results, Figs. 3.5a (outer edge) and 3.5b (outer edge) show the peak signal existing immediately adjacent to the flame surface. In Figs. 3.5c (inner edge) and 3.5d (inner edge) however, the separation between the peak signal and the flame front is on the order of 1 mm. These results confirm that the pilot flame in the TAPS is subject to both partial premixing and turbulent transport of temperature from the vigorous mixing induced by the pilot swirl annuluses. In a number of images, the pilot flame appeared as in Fig. 3.5d where both the overall signal was lower and the pilot flame was considerably thinner ($\sim$ 5 mm vs. $\sim$ 10 mm). Such instances were however fairly uncommon and are probably a localized thinning of the flame in the plane of the laser sheet. Another feature seen in a few instantaneous images was breaks in the flame surface such as that in Fig. 3.5f where a small island of fuel appears downstream of the bulk flame tip. This is analogous to the flame pinching and separation seen in the turbulent flames studied earlier (Fig. 2.20). The pinching of the flame to create such an island suggests that the pilot flame is subject to high

strain rates present in the shear layer near the main annulus.

3.1.1.1 Flame Length

A number of important flame parameters were computed from the instantaneous PLIF images of the flame. These parameters not only provide a better understanding of the flame dynamics but also provide a useful set of parameters for model validation. Fig. 3.6 shows how the flame length and flame cone angle (α) were computed from the instantaneous flame contours. To define the flame length and angle, the origin of the coordinate system was located at the exit of the pilot injector. Since the pilot flame is expected to be anchored to the injector, this is a natural coordinate system to use to define the flame length. For each flame surface contour (such as the one shown in Fig. 3.6), points along the contour were identified. The distance from the pilot injector to a given point was then computed as $d = \sqrt{x^2 + y^2}$. The maximum distance then was defined as the instantaneous flame length. The location of the maximum distance is the flame tip and was recorded as (x_{max}, y_{max}) as denoted in Fig. 3.6.

The mean and standard deviation of the flame lengths vs. pilot mass flowrate ($\dot{m}_{f,p}$) for the three pilot cases is shown in Fig. 3.7. The flame length increases with fuel flowrate though there does not appear to be a clear linear relationship. In general, increasing the fuel flowrate is expected to cause a proportional increase in the flame length if the fuel-air mixing rate remained constant. However, the mass entrainment of air into the pilot flame may not remain constant. As the flame lengthens, it extends into the flow that issues from the main annulus where the turbulence levels are relatively large. This would increase the mass entrainment of air into the pilot flame and would explain the decrease of the slope of the curve in Fig. 3.7. The

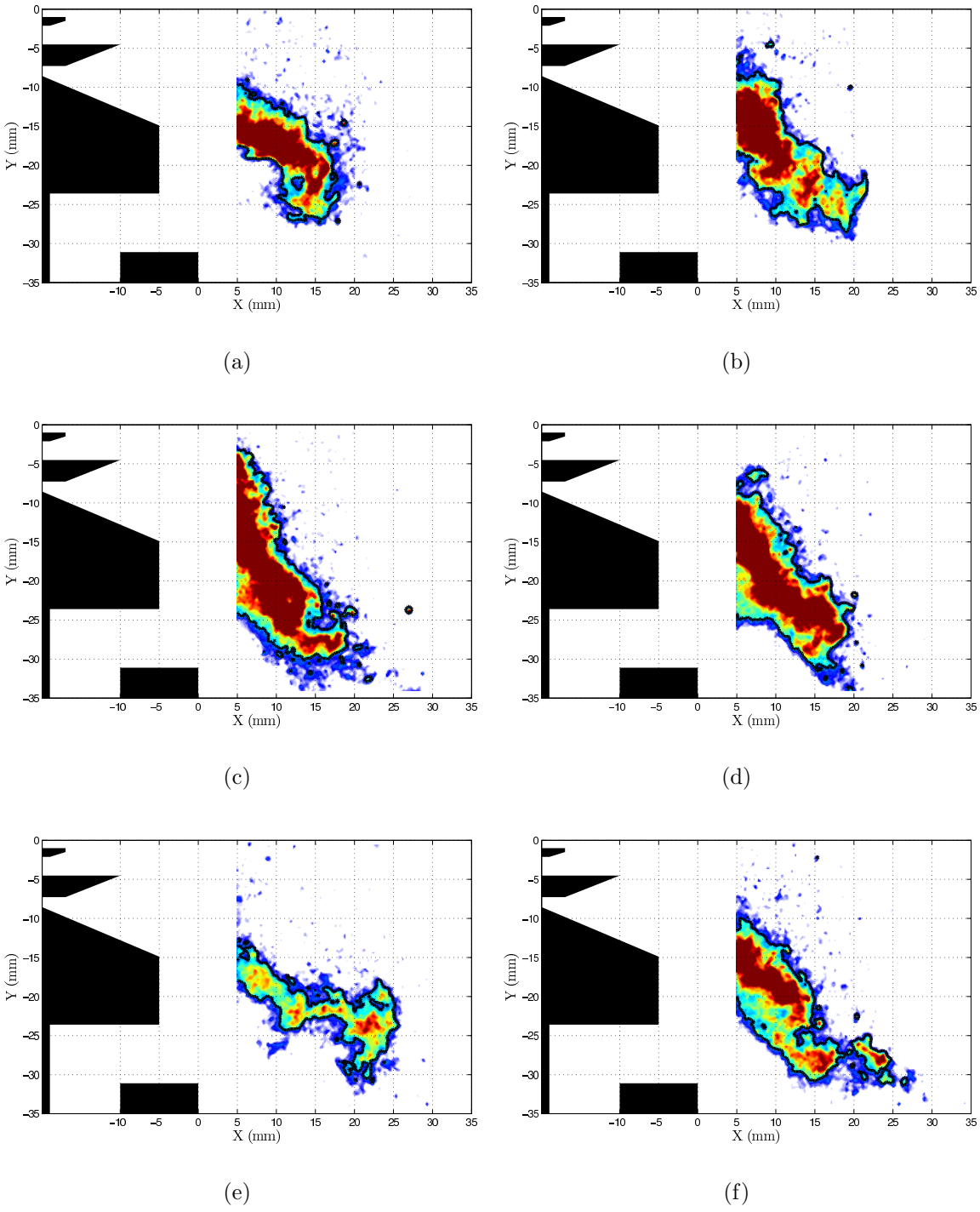

Figure 3.5: Randomly selected PLIF images of Case 1Pt2. The black line is the flame contour obtained by setting an appropriate threshold.

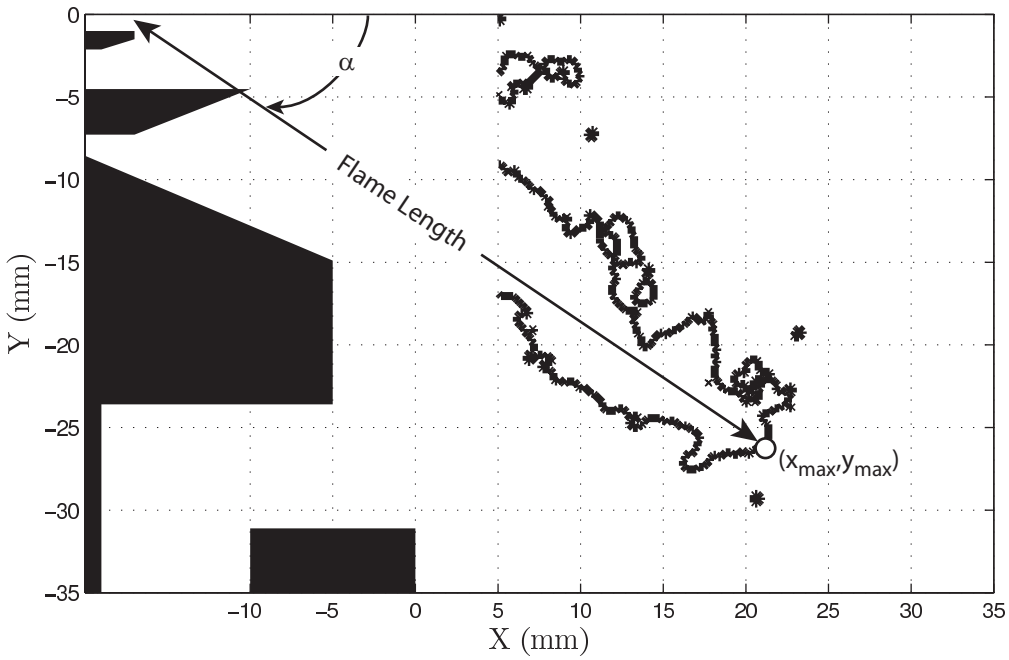

Figure 3.6: Schematic showing how the flame length and flame tip coordinates were computed from the instantaneous images.

extension of the flame into the main flow also helps to explain the observation that the standard deviation of the flame length too increases with fuel flowrate as seen in Fig. 3.7. Vortices shed from the injector along with high velocity fluctuations in these regions would cause large scale perturbations in the length of the flame. The PDF of the flame length for the three pilot cases is shown in Fig. 3.8. It is clear that the basic shape of the PDF for all three cases is the same and that almost all the statistics of the flame length can be described by the mean and standard deviation alone. This is better illustrated by the PDF of the flame length normalized by its mean and standard deviation as shown in Fig. 3.9. The solid curve also drawn in the figure is that of a normal distribution with a mean of zero and standard deviation of one. For the most part the data collapses onto the normal distribution. There is slight discrepancy in the results for Case 1Pt3 where mean values of the flame length occur with higher probabilities than suggested by the Gaussian curve. This along

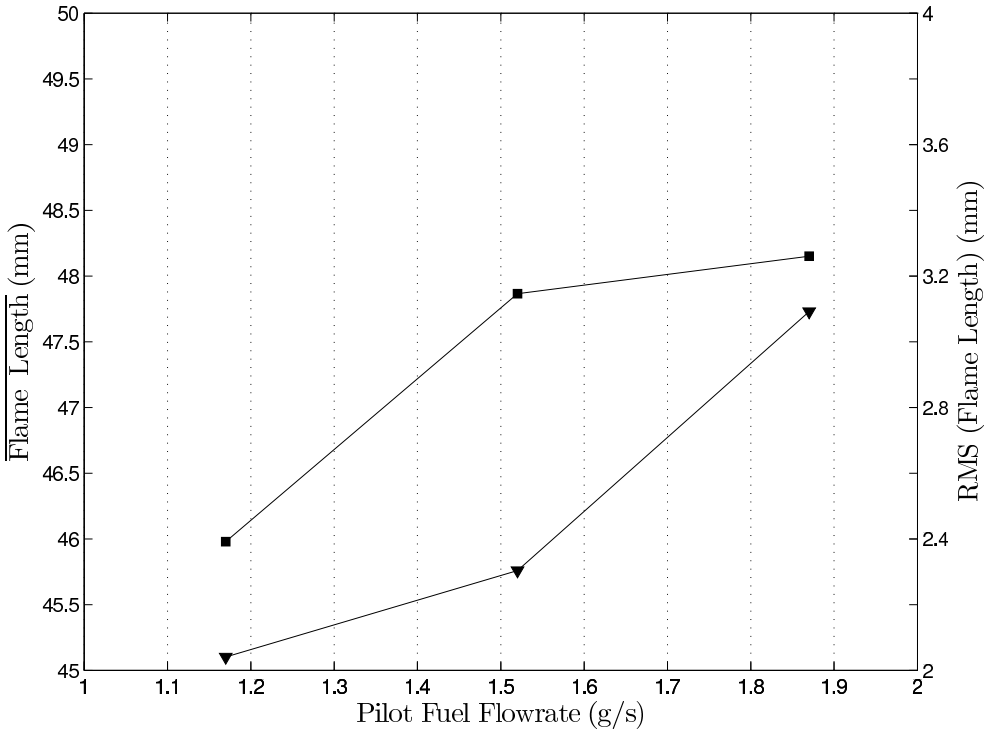

Figure 3.7: The mean and standard deviation of the flame length for the three pilot cases (1Pt1, 1Pt2, and 1Pt3). The square markers are the flame length and the triangles are the RMS.

with the higher standard deviation suggests that there are isolated events where the flame length in this case is much higher than the mean.

3.1.1.2 Flame Cone Angle

Like all swirl combustors, the flow and therefore the flame, issues at an angle to the centerline. This is the reason that the flame exists as a hollow conical flame as was seen in both the average and instantaneous PLIF images. The angle the flame issues at is of crucial importance to understanding the interaction of the flame and the flow. In addition, the flame cone angle and its statistics serve as a useful assessment of models. The flame angle (α) was defined as the cone angle as shown in Fig. 3.6. It was computed for each instantaneous image from the measured (x_{max}, y_{max}) using the relation $\alpha = \arctan(y_{max}/x_{max})$. This method therefore only takes into account

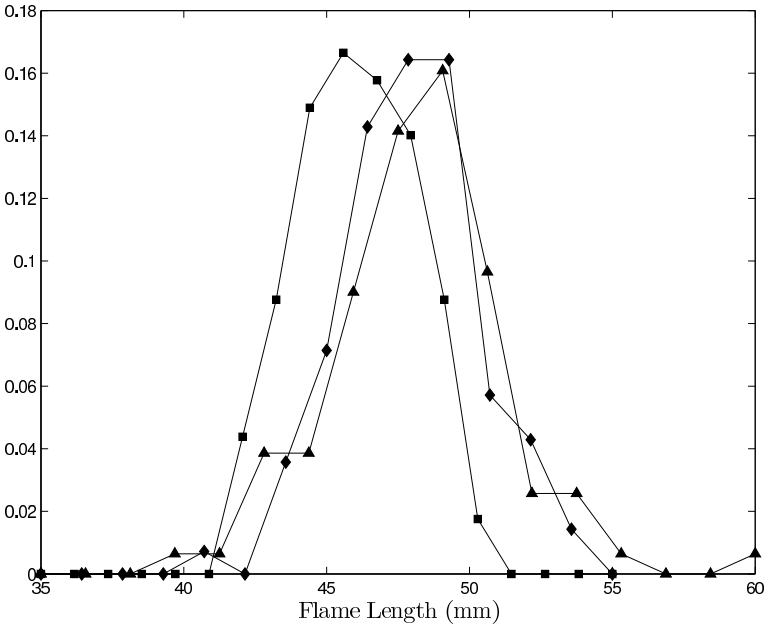

Figure 3.8: PDF of the flame length for the three pilot cases. Square markers: Case 1Pt1, Diamonds: Case 1Pt2, Triangles: Case 1Pt3.

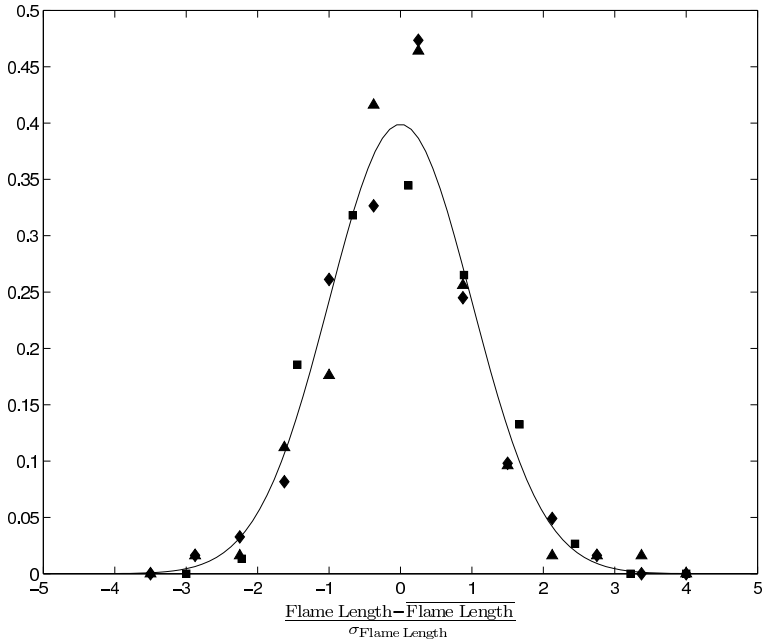

Figure 3.9: PDF of the flame length normalized by its first two moments as given in the title of the abscissa. Square markers: Case 1Pt1, Diamonds: Case 1Pt2, Triangles: Case 1Pt3.

Case	Average Flame Cone Half-Angle $\overline{\alpha}$ (degrees)	RMS of Flame Cone Half Angle σ_α (degrees)
1Pt1	32.6	2.0
1Pt2	31.5	2.0
1Pt3	30.9	2.4

Table 3.2: The mean and standard deviation of the flame cone angle for the three pilot cases studied.

the location of the flame tip relative to the injector exit. As such, the instantaneous flame cone angle measurement is susceptible to some error if the flame tip turns significantly away from the bulk flame (such as in Fig. 3.5a). However, only a few instantaneous images showed any significant deviations of the flame tip and the vast majority of the images were similar to Fig. 3.5b-f where the flame tip was in line with the flame. More importantly, there is no reason to expect the flame tip to preferentially turn one way or another with respect to the flame and therefore the mean should be insensitive to this methodology. Lastly, any measurement of the flame cone angle is inherently an averaged measurement over the entire flame surface and therefore it is sensitive to the method used.

The mean and standard deviation of the flame cone angle for all three pilot cases were about the same and are listed in Table 3.2. The results show that the flame angle is independent of the fuel flowrates. This is to be expected since the flame cone exists as a result of the swirling flow which is created by the geometry of the combustor and is a function of the swirl number. In the TAPS combustor, the swirl number is defined by the angle(s) of the swirl vanes and is therefore constant for all three flames. This leads to a near uniform flame cone angle.

The PDF of the flame cone angle for the three pilot cases is shown in Fig. 3.10. A more illustrative way of plotting the PDF for the three cases is shown in Fig. 3.11. As

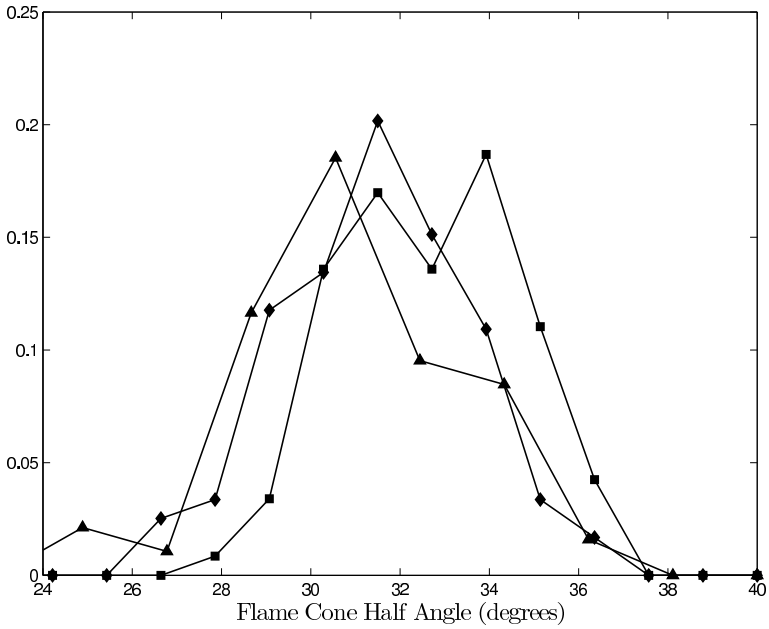

Figure 3.10: PDF of the flame cone angle (α) for the three pilot cases. Square markers: Case 1Pt1, Diamonds: Case 1Pt2, Triangles: Case 1Pt3.

was done for Fig. 3.9, the angles have been normalized by their mean and standard deviation as $(\alpha - \overline{\alpha})/\sigma_\alpha$. Also plotted by the solid line is a normal distribution with a mean of zero and standard deviation of one. The measured PDFs of all three cases collapse onto a single curve that is well described by the normal distribution. This indicates that the first two moments of the PDF adequately describe the statistics of the flame cone angle. This confirms that the flame cone angle is primarily determined by the geometry of the swirl vanes.

3.1.1.3 Flame Surface Density and Flame Brush

The flame surface density (Σ) is defined as the average amount of flame surface area per unit volume within a small interrogation box at one location in the flow field. It is an important parameter in models of turbulent combustion. Most models of turbulent combustion assume that the turbulent burning velocity increases linearly with the increase in the wrinkled flame surface area, which is described by Σ. The

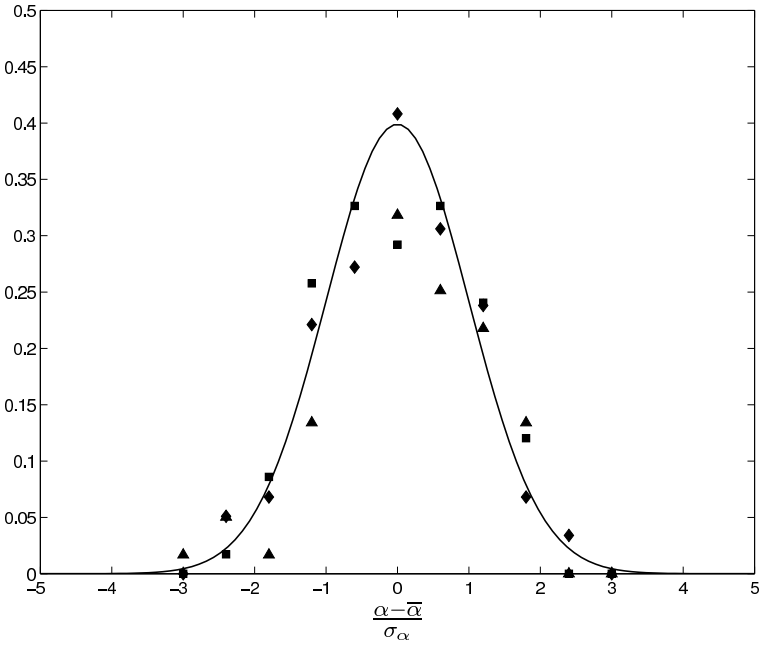

Figure 3.11: PDF of the flame cone angle (α) normalized by its first two moments ($\overline{\alpha}$ and σ_α). Square markers: Case 1Pt1, Diamonds: Case 1Pt2, Triangles: Case 1Pt3.

flame surface density of the pilot flames was computed in a manner similar to that by Filatyev et al. (2005) and Bell et al. (2007). Since only a two-dimensional cut of the flame is available in the experimental data, it was assumed that the flame surface area per unit volume is equal to the flame surface perimeter per unit area. DNS results of Bell et al. (2007) show that this assumption is valid to within an uncertainty of $\pm 10\%$. Therefore, the flame is wrinkled by the same amount in the third dimension as it is in the two dimensions that are captured by the PLIF technique. Since the flame is axisymmetric, Σ defined in this manner is not underestimated or overestimated. The instantaneous flame contours from the PLIF images were used and the image was broken up into interrogation windows of 7 pixels $\times$ 7 pixels, which corresponds to a spatial dimension of 1.04 mm. Filatyev et al. (2005) have shown that the measured Σ is independent of the interrogation box size since the increased box area cancels out with the increased flame perimeter within the box. The length of the flame contour

within each interrogation box was measured by counting the number of "pixels" of the contour line within each box and dividing by the thickness of the contour line (one "pixel"). The length of the flame within each box was then divided by the area of the interrogation box to yield Σ.

A contour plot of Σ is shown in Fig. 3.12 for Case 1Pt2. What is noteworthy is that Σ is not the same on the inner and outer edges of the flame. While the flame surface density is symmetric about the axis of a jet flame, the surface density is clearly larger on the outer edge than the inner edge of the pilot flame. Profiles of Σ taken at a number of downstream locations are shown in Fig. 3.13. At $x = 5.86$ mm for example, the surface density of the outer edge is twice that of the inner edge. Therefore, there must be some flow feature that causes one edge to have considerably more wrinkled surface than another. It will be shown in (§4.3.1) that the lack of symmetry in what is otherwise a jet flame issuing at an angle can be ascribed to distinct flow features present in the TAPS combustor. This asymmetry continues to about $x = 13$ mm after which point the contour plot resembles contours of Σ in a jet flame. The profile becomes almost flat across the flame indicating a uniform amount of wrinkling as also indicated by the contour plot of Fig. 3.12. Note also that the center of the profiles move radially outward with increasing downstream/axial distance. This is simply a result of the angle of the flame (§3.1.1.2).

Along with the flame surface density, another quantitative measurement that is useful for model development and validation is the wrinkling factor (Ω). The wrinkling factor provides a measure of the degree of wrinkling at an axial location and it was shown by Bray (1990) and Candel and Poinsot (1990) that it can be

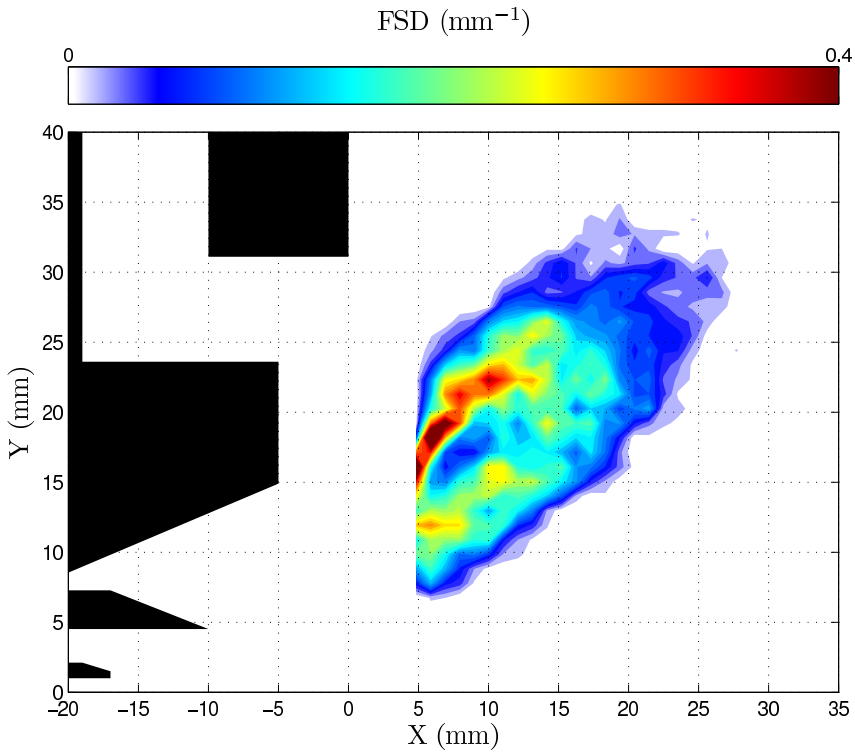

Figure 3.12: Contour plot of the flame surface density (Σ) for Case 1Pt2.

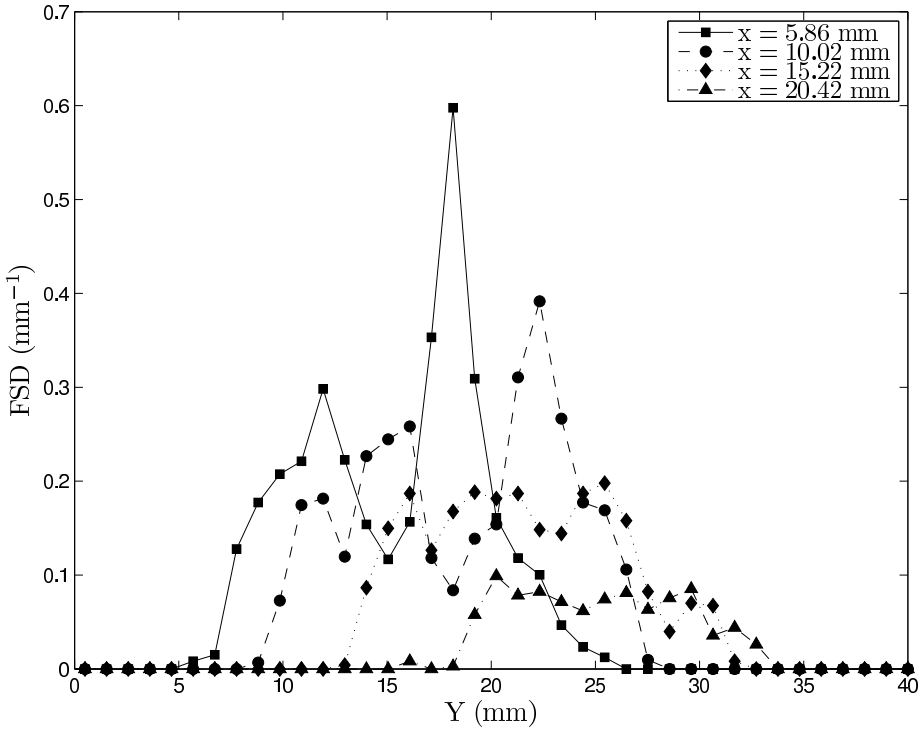

Figure 3.13: Profiles of Σ for Case 1Pt2 taken at select downstream locations.

defined as:

$$\Omega = \int_0^\infty \Sigma \, \mathrm{d}y. \tag{3.1}$$

Ω is plotted versus downstream distance (X) for the three pilot cases in Fig. 3.14. The points are plotted at every 1.04 mm which is the size of the interrogation window used for calculating Σ. Ω remains roughly uniform for a short distance before it decreases to zero through the flame. The profiles reach zero at different values of downstream distance due to the different flame lengths (Fig. 3.7) of all three cases. It should also be noted that the wrinkling factor is constant for about the same distance that the asymmetry exists in the flame surface density. The decrease in the wrinkling factor through the flame suggests that the flame is subject to more vortices of higher strength near the base and that it proceeds to "laminarize" as the tip is approached.

The flame brush shown in Fig. 3.15 provides an idea of the spatial distribution of the flame. The flame brush was generated by plotting randomly selected instantaneous flame contours. As can be seen from the figure, the brush exists uniformly on either side of the average flame contour. At all points it is typically within 5 mm of the average flame contour. This result indicates that the average flame contour is a reliable marker of the flame surface at any instance of time. This is useful in this study because simultaneous velocity measurements were not made with the PLIF measurements. Therefore, we can use the average flame contour to study the interaction of the flame with the flow.

3.1.2 Main Flame

The main flame (Case 1Main) studied provides a good representation of the stable operation of the combustor with both pilot and main flames. It was not possible to

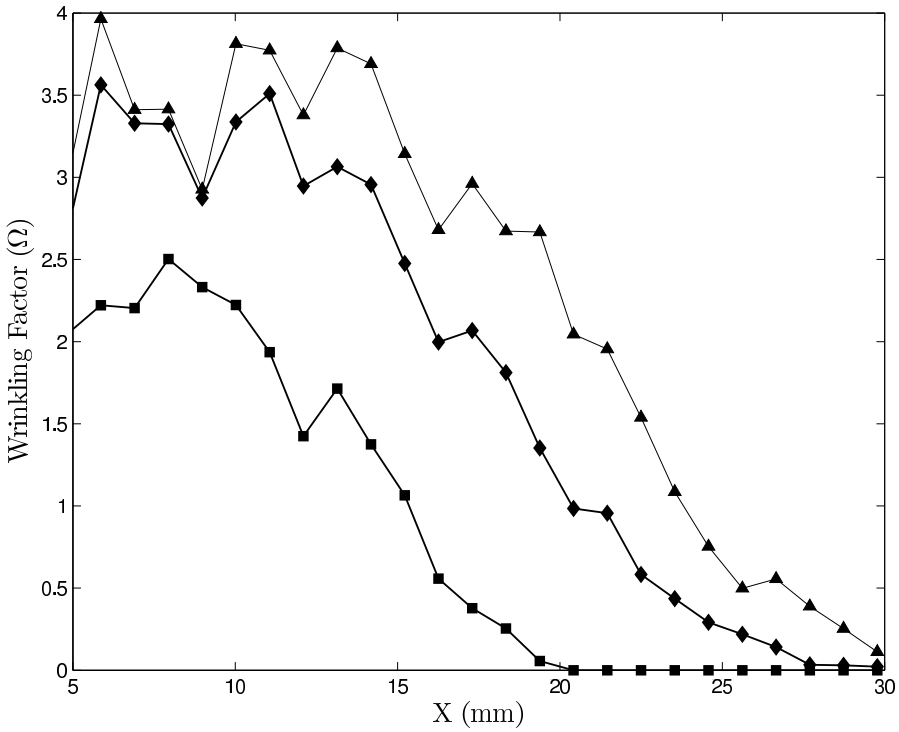

Figure 3.14: Profiles of the wrinkling factor for the three pilot cases. Square markers: Case 1Pt1, Diamonds: Case 1Pt2, Triangles: Case 1Pt3.

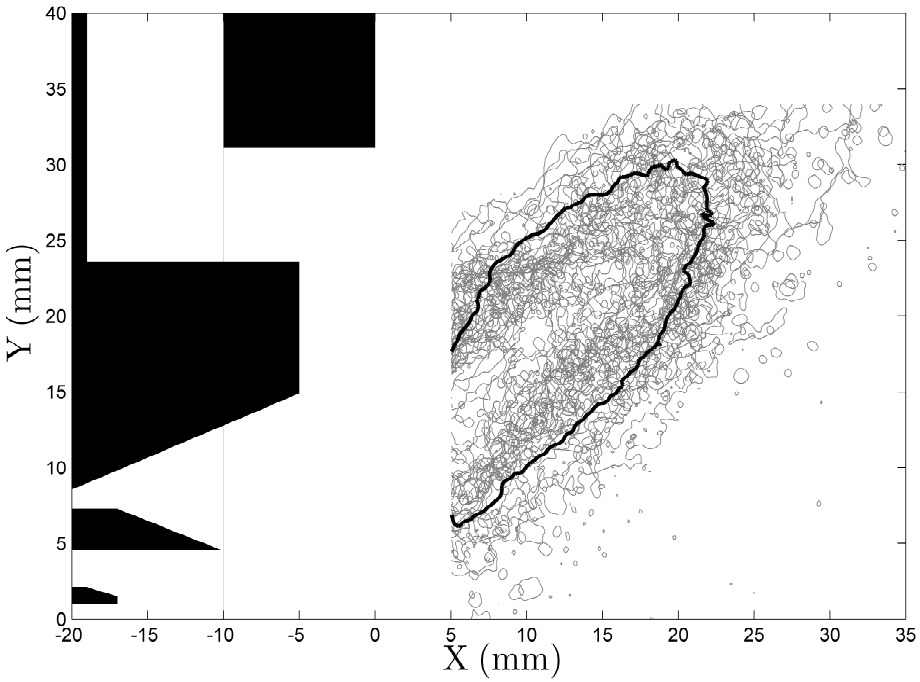

Figure 3.15: The flame brush of Case 1Pt3 illustrated by plotting 25 randomly selected instantaneous flame contours. The average flame contour is also overlayed and shown in black.

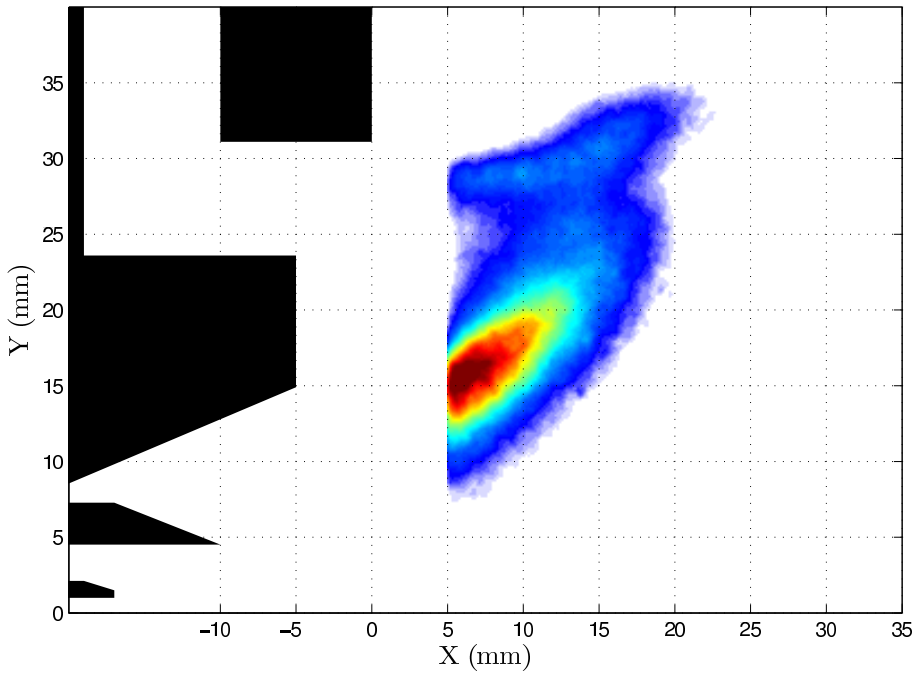

Figure 3.16: Average CH_2O PLIF image for Case 1Main.

ignite or maintain a main flame without the presence of a pilot flame. The unstable operation of the combustor will be discussed in detail in Chapter V. Fig. 3.16 shows the average PLIF signal for Case1Main. Though the pilot fuel flowrate in this case is identical to the flowrate in Case 1Pt1, there are differences between the two pilot flames as evidenced by comparing Fig. 3.2 and Fig. 3.16. It should be noted that the color scale is different for the two images. The biggest difference in the pilot flame is in the outer edge. With only a pilot flame, the average PLIF signal near the outer edge is more radially spread out, i. e. the radial gradient of the signal is smaller. With the presence of the main flame, the outer edge is pushed radially inwards towards the center of the pilot flame. The length and location of the flame however appears to be largely unaffected.

The main flame appears as a separate flame issuing from the main annulus. The base of the main flame was not captured as locations at $x < 5$ mm could not be

imaged due to a lack of optical access there. Therefore, no conclusions can be drawn about whether the main flame is lifted or attached to the main injectors. A small region between 20 mm $< y <$ 27 mm and 5 mm $< x <$ 7 mm exists where there is no measurable formaldehyde. This region is likely to be filled with hot products from the pilot flame. It was seen from the velocity results that a recirculation zone exists in this region and has been termed the Lip Recirculation Zone (LRZ). The existence of this region also confirms that the main flame is stabilized upstream of the point where the pilot flame impinges upon the main flame. Since the main flame could not exist without the pilot flame, the hot products being recirculated in this region must be critical to the operation of the main flame. This fact also suggests that the main flame is unlikely to be attached to the main injectors since then it would not be dependent on the presence of a flame (the pilot) considerably downstream. There is a distinct change in the angle of the main flame around $(x, y) = (12, 31)$ mm. This location also corresponds to around where the pilot flame impinges upon the main flame. As will be seen from the velocity results, the heat release from the pilot flame causes the flow from the main annulus to be deflected radially outward near this region. Though the fuel flowrate of the main was over twice the flowrate of the pilot, the average PLIF signal is lower in the main flame than in the pilot flame. This difference may be due to the expectation that the main flame is of a premixed nature while the pilot flame is a nonpremixed flame. In addition, the main fuel is spread out over a larger area than the pilot fuel since it is injected at larger radial distance away from the centerline. A final cause for the reduced signal is also the fact (as will be seen in §4.4.3 and §3.2) that some of the fuel injected in the main annulus actually reacts in the pilot flame cone.

The combustion of the main flame is no doubt affected by the spray characteristics

of the TAPS combustor. Spray and droplet formation in a crossflow such as that employed for the main injectors in the TAPS was discussed in §1.2.2. Unfortunately, full details of the GE TAPS spray distribution is not known. The Weber number defined in Eqn. 1.1 can be computed by estimating the diameter of the fuel injectors. The study of sprays in crossflows by Tambe et al. (2005) was conducted by the same group that is partly responsible for the development of the TAPS, so it was assumed that their injector diameter (500 μm) is approximately that of the TAPS. For a combustor pressure of 1 bar and air preheat temperature of 500 K, $U_\infty = 40$ m/s, and the fuel surface tension $\sigma_{Jet-A} = 28 \times 10^{-3}$ N/m (the room temperature value), the Weber number is estimated to be $We \approx 20$.

Fig. 3.17 shows some selected instantaneous PLIF images for Case 1Main. The same color scale has been used in all the images and was selected to highlight the main flame. In none of the instantaneous images was the base of the main flame visible in the available field of view. The instantaneous images show a highly irregular main flame issuing from the main annulus with varying levels of interaction with the pilot flame. For example, in Fig. 3.17a and b, the pilot flame tip does not reach the main flame and the two flames appear to be independent of one another. In Fig. 3.17c and d however, the pilot flame clearly impinges upon the main flame that is anchored upstream of the point that the two flames meet. At certain times, the main flame appears as an extension of the pilot flame as shown in Fig. 3.17f. In all the instantaneous images, the width of the flame main is considerably smaller than the pilot flame and therefore the heat release from the main flame is localized in a small region.

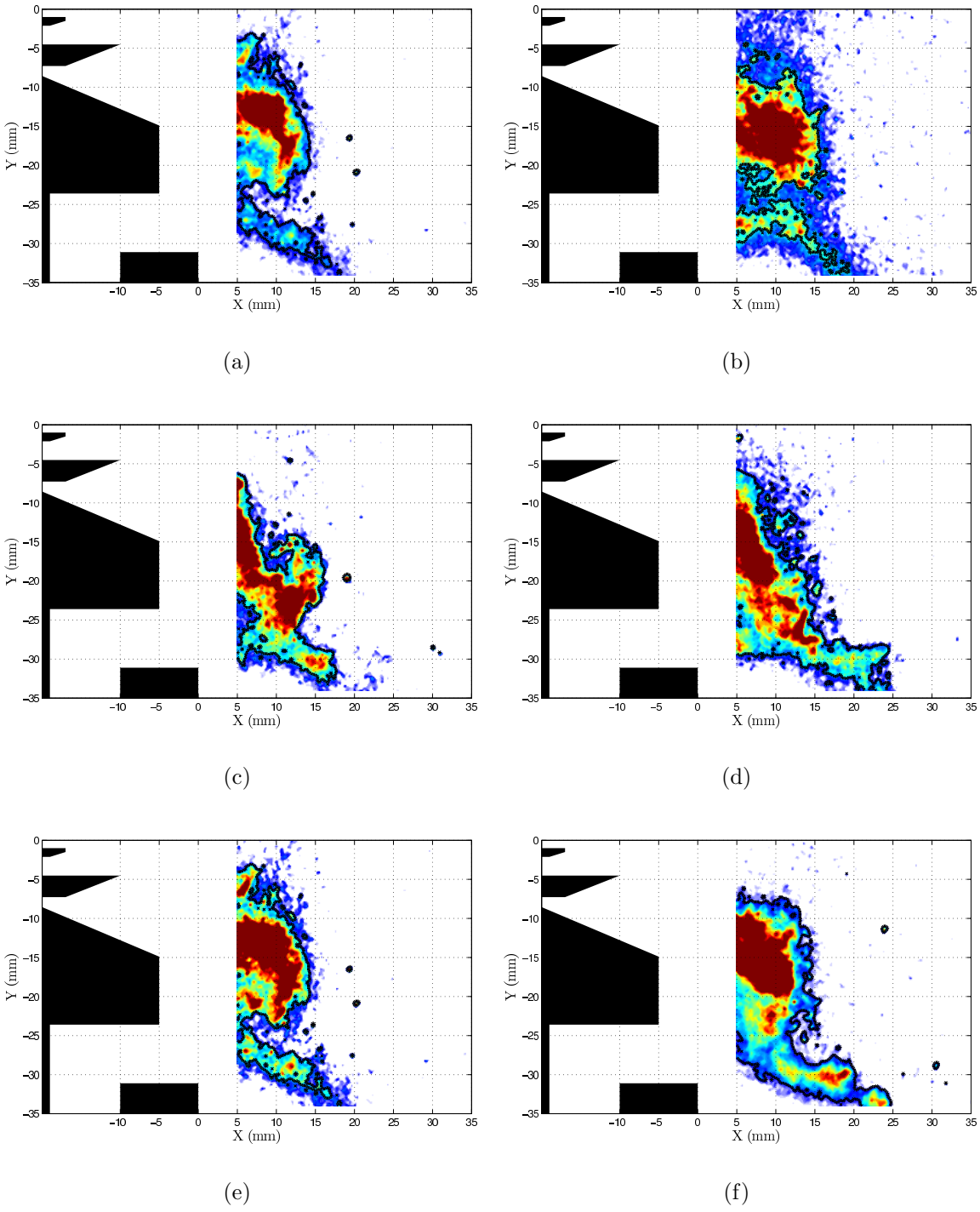

Figure 3.17: Select instantaneous PLIF images for Case 1Main. The black line is the flame contour obtained by setting an appropriate threshold.

Case	Pilot Fuel Flowrate $\dot{m}_{f,p}$ (g/s)	Main Fuel Flowrate $\dot{m}_{f,m}$ (g/s)
2Pt	0.99	0
2Main	0.99	2.40

Table 3.3: Flame conditions for the 2 bars case. For all cases, $\dot{m}_{air} = 0.228$ kg/s, $T_3 = 505$ K, $p_3 = 2.0$ bars.

3.2 Flame Images at 2 bars

Gas turbine combustors operate at high pressures and it is important to understand the effect of pressure on the flame. It was not possible to operate the PLIF or PIV diagnostics at realistic combustor pressures in the current study. Instead a baseline case of 2 bars was chosen to apply PLIF and PIV at an elevated pressure. For the two bars cases, the air mass flowrate was $\dot{m}_{air} = 0.228$ kg/s and $T_3 = 505$ K, which are identical to the 1 bar cases. Both pilot only and pilot and main cases were studied with $p_3 = 2$ bars. The fuel flowrates for the two cases are given in Table 3.3.

Fig. 3.18 shows the average PLIF signal for Case 2Pt. The average PLIF signal at 2 bars looks virtually identical to the PLIF signal at 1 bar for Case 1Pt1 (Fig. 3.2). The pilot flame has the same shape and angle as the the flame at 1 bar. The average image therefore suggests that the flame at 2 bars behaves in the same manner as the flame at 1 bar. Therefore, while there are marked differences in the concentrations of soot and PAHs between the two flames (Fig. 3.1) the actual flame is unaffected. This is not surprising since it is known that pressure typically only has a weak affect on combustion. Even in hydrogen-air flames, where the chemistry is relatively simple, there are many chain branching and terminating reactions that have greatly varying dependencies on pressure (Law (2006)). This typically has the net result that the flame speed does not vary monotonically with pressure. In fact, with gaseous fuels,

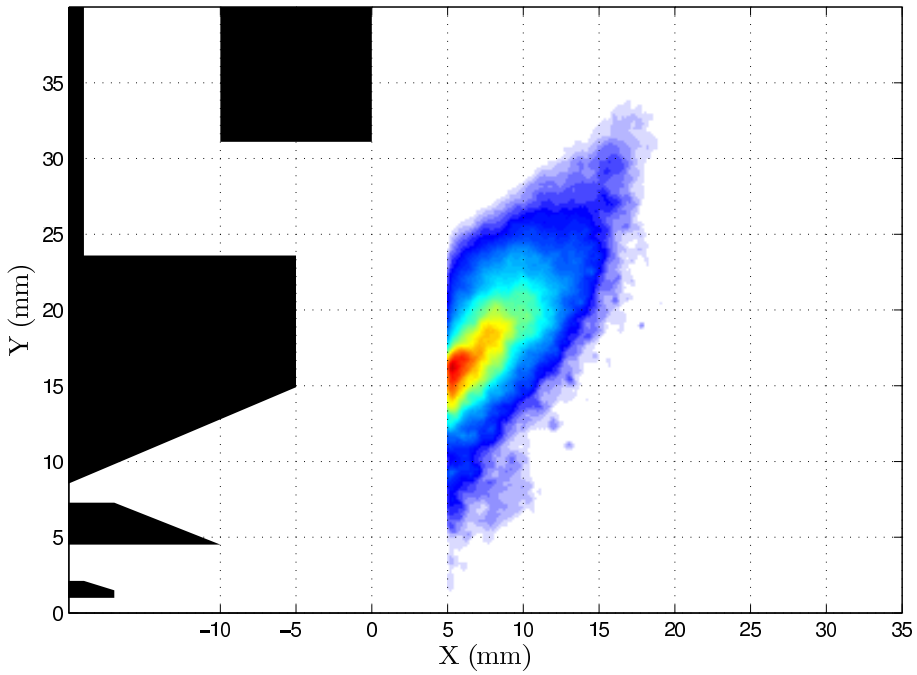

Figure 3.18: Average PLIF image for Case 2Pt.

the primary effect of pressure is felt through a corresponding change in the gas density (Law (2006)), something which does not happen with the liquid fuel used here. More importantly, the effects of pressure are typically not felt until considerably higher pressures and doubling the pressure, as in this case, should have negligible affects on the chemistry. As will be seen in the velocity results, the primary affect of pressure in fact is on the velocity.

The change in the combustor pressure does not affect the combustion of the main either as seen in the average PLIF image of Case 2Main shown in Fig. 3.19. Similar to the main case of 1 bar, a jet like main flame issues from the main annulus with the pilot flame largely unaffected. The region between the pilot and main flames where there is no formaldehyde appears smaller in the 2 bars case, but is still apparent around 25 mm $< y <$ 27 mm and 5 mm $< x <$ 7 mm. In this case too, the base of the main flame could not be observed in the available field of view and therefore the

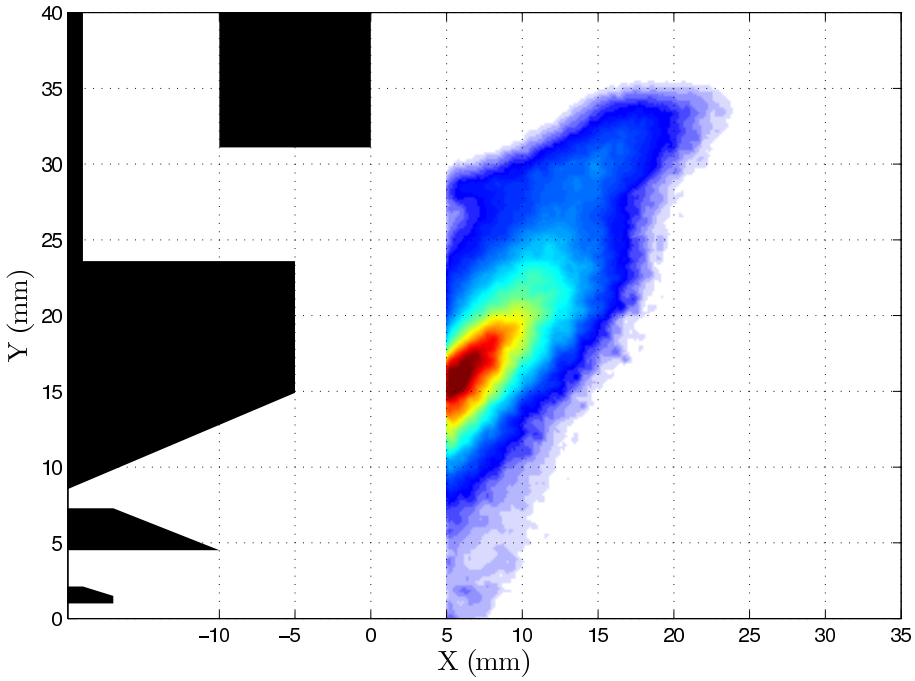

Figure 3.19: Average PLIF image for Case 2Main.

main flame was never observed to be lifted to $x \geq 5$ mm. The change in the main flame cone angle that appeared in Case 1Main also appears in Case 2Main where the pilot flame impinges upon the main flame.

To better understand the main flame, the average PLIF signal for Case 2Pt was subtracted from the average PLIF signal for Case 2Main. The result is shown in Fig. 3.20. The structure of the main flame is more clearly visible from this figure. The highest concentrations of formaldehyde are in the center of the main jet flame and they uniformly decay as the flame edges and tip are approached. It is also clear from this image that the base of the flame extends upstream of $x = 5$ mm and possibly into the injector. Another interesting point to note is the increased PLIF signal in the pilot flame. While the PLIF signal is a function of many parameters, including formaldehyde concentration, the same average laser power and sheet were used to image both Case 2Pt and Case 2Main. Clearly therefore, some fuel from

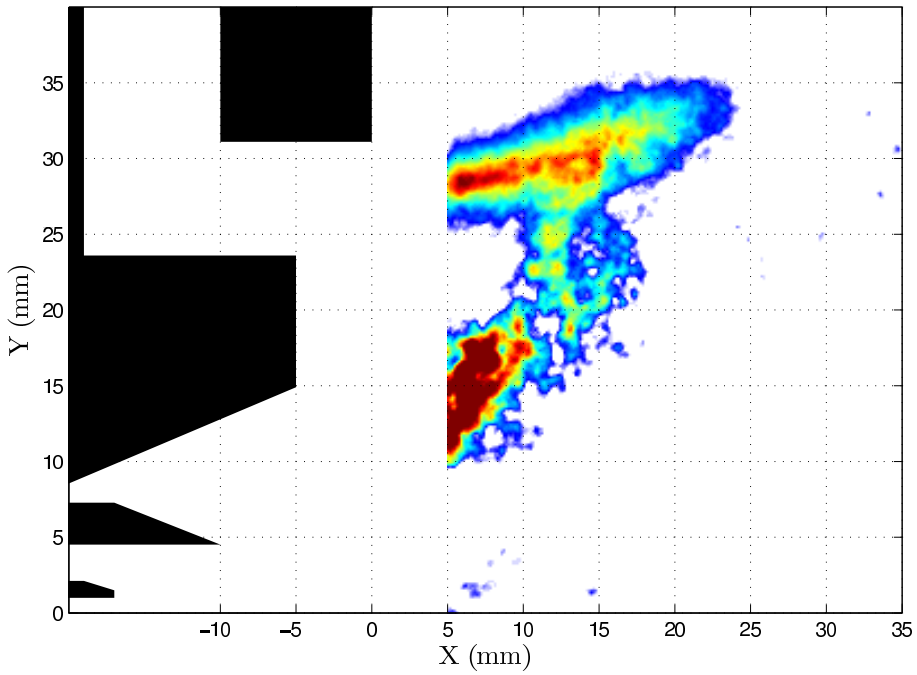

Figure 3.20: The average PLIF signal for Case 2Pt (Fig. 3.18) subtracted from the average PLIF signal for Case 2Main (Fig. 3.19).

the main does make its way into the pilot flame through both the LRZ and possibly out-of-plane swirl. Evidence of the main fuel enhancing the pilot flame was also seen in the blowout results that will be presented in §5.1.

3.3 Flame Images at 3 bars

Attempts were made to image the flame at a pressure of 3 bars though they were unsuccessful. The higher soot and PAH concentrations present in the flames at higher pressures led to significant emissions from molecules other than formaldehyde. Even with increased laser power, it was not possible to saturate these signals and clearly identify the flame using the methods in §2.3. The results for a combustor pressure of 3 bars are shown in Fig. 3.21. Emissions from excited PAHs and flame luminosity throughout the flame cone mask any discernible signal from CH_2O PLIF.

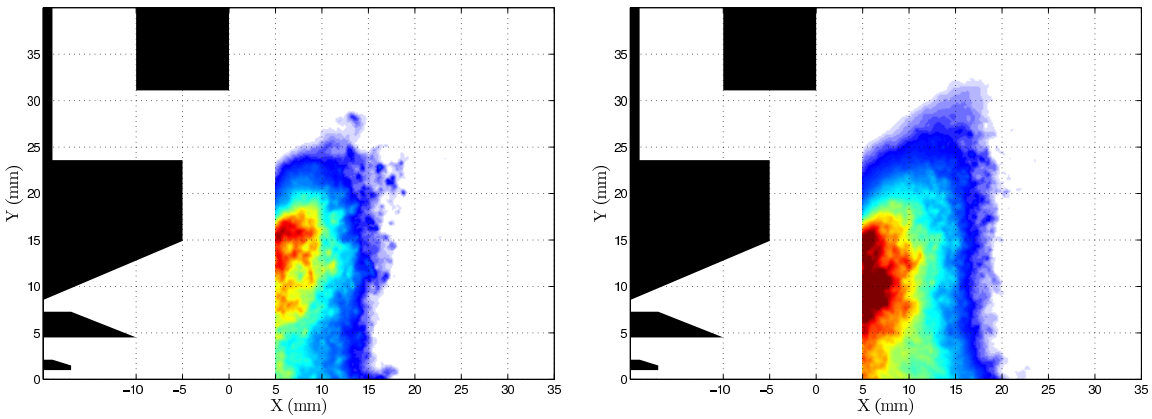

(a) Pilot Only

(b) Pilot and Main

Figure 3.21: The average PLIF signal at a combustor pressure of 3 bars.

CHAPTER IV

Flow Field

The flow field was measured by the use of PIV for a range of conditions, both non-reacting and reacting (for both pilot and pilot and main fuelling cases). These conditions are listed in Table 4.1. This section has been divided into two major sections. The first discusses the effects of heat release on the flow field and compares the non-reacting and reacting results. The second section then investigates the effects of heat release from the main flame by comparing a pilot flame only to both pilot and main fuelling. A parameter known as swirling strength was used in studying the instantaneous flow field and this parameter will be developed first. This chapter concludes with a discussion of the symmetry of the geometry and flow.

4.1 Swirling Strength

One of the the greatest advantages of a tool such as PIV is its ability to capture instantaneous flow structures, especially vortices. While these vortices must be identified unambiguously, a big problem with the identification of a vortex lies with the fact that a clear definition of a vortex is lacking. A definition that is probably the most commonly accepted one is offered by Robinson et al. (1989) where they state: "A vortex exists when instantaneous streamlines mapped onto a plane normal

Case	Air Mass Flowrate $\dot{m}_{air,tot}(kg/s)$	Preheat Temperature T_3 (K)	Combustor Pressure p_3 (bar)	Pilot Fuel Flowrate $\dot{m}_{f,p}$ (g/s)	Main Fuel Flowrate $\dot{m}_{f,m}$ (g/s)	Fuel Air Ratio F/A
1NR	0.216	422	2.5	0	0	-
1R	0.216	422	2.5	1.8	0	0.0083
2NR	0.260	445	3.1	0	0	-
2R	0.262	444	3.1	1.95	0	0.0074
3NR	0.377	503	4.5	0	0	-
3R	0.379	498	4.5	2.78	0	0.0073
4P	0.230	505	2	0.99	0	0.0043
4M	0.230	505	2	0.99	2.40	0.015

Table 4.1: Conditions for the PIV data. The F/A has been computed based on the total fuel injected divided by the total mass flowrate of air going through the combustor (as given in the second column). Cases 1R, 2R, and 3R represent cases on the engine operating line. Note that Cases 4P and 4M are identical conditions to Cases 2Pt and 2Main given in Table 3.3

to the core exhibit a roughly circular or spiral pattern, when viewed in a reference frame moving with the center of the vortex core". Traditionally, contours of vorticity have been used to identify vortices in the flow and cohesive packets of vorticity over a certain threshold have been deemed to be the only vortices in a flow. There are however two problems with such an approach. First, vorticity can exist without the existence of a distinct vortex. For example, strong shear layers also lead to large values of vorticity and these strong shearing motions will mask vorticity from a vortex. Also, the above definition of a vortex requires that the vortex be viewed from the reference frame of the vortex and therefore one needs to a priori know the convection velocity of the vortex Adrian et al. (2000). Therefore, while vorticity contours, whether applied to the original field or a Reynolds decomposed field, work well in a simple flow, it is not as effective in many practical situations. This necessitates another tool that can identify vortices even amidst strong shear layers and one that does not require the pain-staking process of trying a range of convection velocities to isolate a vortex.

Critical point analysis of the local velocity gradient tensor and its corresponding eigenvalues have been identified by Chong et al. (1990), Dallman et al. (1991), and Zhou et al. (1999) as a tool to extract vortices from a velocity fields. These researchers present the full three-dimensional analysis which can easily be simplified for the two-dimensional data returned by PIV. A set of first-order differential equations can be written as

$$\begin{bmatrix} \dot{x_1} \\ \dot{x_2} \end{bmatrix} = \begin{bmatrix} d_{11} & d_{12} \\ d_{21} & d_{22} \end{bmatrix} \begin{bmatrix} x_1 \\ x_2 \end{bmatrix} \quad \text{or} \quad \dot{\mathbf{x}} = \mathbf{D} \cdot \mathbf{x}. \tag{4.1}$$

In the case of flow, $\dot{\mathbf{x}}$ is the velocity and $\mathbf{D}$ is simply the rate-of-deformation tensor:

$$\mathbf{D} = \frac{\partial u_i}{\partial x_j} = \begin{bmatrix} \frac{\partial u}{\partial x} & \frac{\partial u}{\partial y} \\ \frac{\partial v}{\partial x} & \frac{\partial v}{\partial y} \end{bmatrix}. \tag{4.2}$$

The gradient tensor can be decomposed into a symmetric part and an antisymmetric part, $D_{ij} = S_{ij} + R_{ij}$, where

$$S_{ij} = \frac{1}{2}\left(\frac{\partial u_i}{\partial x_j} + \frac{\partial u_j}{\partial x_i}\right) \quad \text{and} \quad R_{ij} = \frac{1}{2}\left(\frac{\partial u_i}{\partial x_j} - \frac{\partial u_j}{\partial x_i}\right). \tag{4.3}$$

S_{ij} and R_{ij} are the strain rate tensor and rotation tensor respectively. Decomposing the deformation tensor in this manner gives,

$$\mathbf{D} = \begin{bmatrix} S_{11} & S_{12} + R_{12} \\ S_{21} + R_{21} & S_{22} \end{bmatrix}. \tag{4.4}$$

The invariants of this tensor are then

$$\begin{aligned} P &= \text{tr}(\mathbf{D}) = S_{11} + S_{22} \\ Q &= \det(\mathbf{D}) = S_{11}S_{22} - S_{12}^2 + R_{12}^2. \end{aligned} \tag{4.5}$$

In terms of these invariants, the characteristic equation for the eigenvalues is

$$\lambda^2 - P\lambda + Q = 0, \tag{4.6}$$

and the eigenvalues themselves are given simply by

$$\lambda = \frac{1}{2}\left(P \pm \sqrt{P^2 - 4Q}\right). \tag{4.7}$$

The discriminant of the characteristic equation, $\Delta = P^2 - 4Q = 0$, along with the lines $Q = 0$ and $P = 0$ form the boundaries for trajectories of the critical points of the gradient tensor (Cantwell (1981)) as shown in Fig. 4.1.

For the purposes of identifying the vortices, only the shaded region where $Q > \frac{1}{4}P^2$ is important. In this region, the eigenvalues of the gradient tensor are a pair of complex

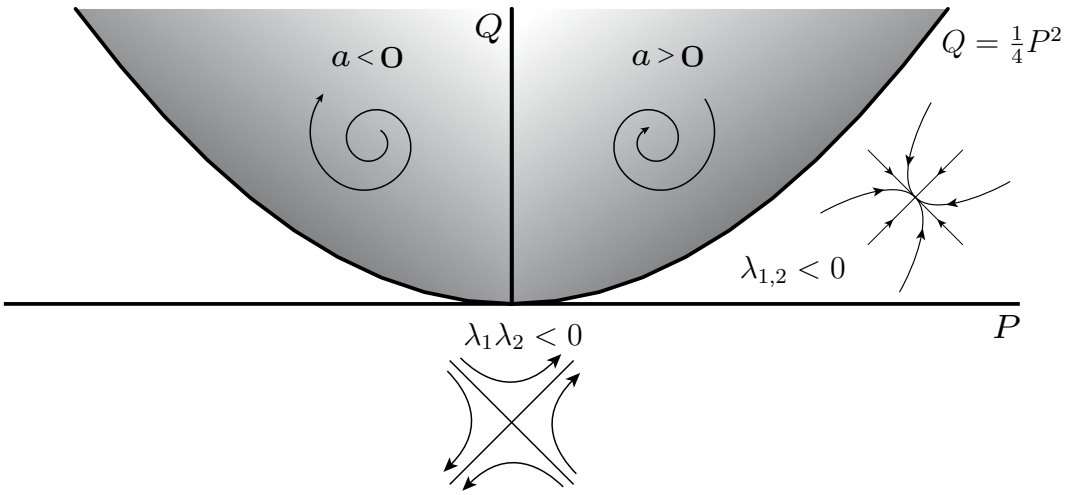

Figure 4.1: Flow trajectories in the PQ space. Adapted from Cantwell (1981).

conjugates, $\lambda_{1,2} = a \pm ib$, where $a = Re(\lambda) = P/2$, and $b = Im(\lambda) = \sqrt{4Q - P^2}/2$. Since the solution to the original differential equation (Eqn. 4.1) is of the form $\mathbf{x}(t) = c_1 e^{\lambda_1 t}\mathbf{v_1} + c_2 e^{\lambda_2 t}\mathbf{v_2}$ (where $\mathbf{v_{1,2}}$ are the eigenvectors) the real part of the solution gives the trajectory in the eigenspace as:

$$x_1(t) = C_1 e^{at}\left(\cos(bt) + \sin(bt)\right) \tag{4.8}$$

$$x_2(t) = C_2 e^{at}\left(\cos(bt) - \sin(bt)\right) \tag{4.9}$$

with C_1 and C_2 being real constants. These trajectories lead to spirals as shown in Fig. 4.1 and describe precisely the definition of a vortex given earlier. Note that the real part of the eigenvalue only affects whether the streamlines spiral out ($a > 0$) or in ($a < 0$) and do not affect the rotation. For example, this is shown for an artificial deformation rate tensor with complex eigenvalues as shown in Fig. 4.2 where the velocity vectors and streamlines clearly indicate a vortex. This analysis leads to the interesting observation that the eigenvalues of the rate-of-deformation tensor can be used to potentially identify vortices. Since wherever there exists a vortex and therefore spiralling trajectories there exist complex eigenvalues, one can compute

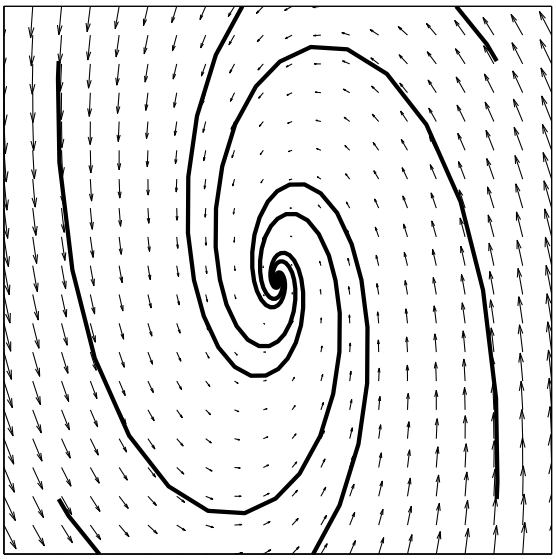

Figure 4.2: An example of velocity vectors and corresponding streamlines in a region where the eigenvalues of the deformation rate tensor are complex.

the eigenvalues everywhere and plot contours of iso-b values.

The validity of this technique can be further demonstrated by seeing that when the eigenvalues are complex the rate of rotation tensor dominates the strain-rate tensor. Since one of the biggest shortcomings of vorticity contour plots is in identifying vortices amongst strong shear, the ability of this technique to pick out strong rotation over strain makes it especially successful. As discussed earlier, complex eigenvalues require the discriminant to be negative ($\Delta < 0$). Substituting in from Eqn. 4.5 gives

$$\begin{aligned} Q &> \frac{P}{4} \\ R_{12}^2 &> \frac{1}{4}\left(S_{11}^2 + S_{22}^2\right) + S_{12}^2 - \frac{1}{2}S_{11}S_{22}. \end{aligned} \tag{4.10}$$

Since $R_{12}^2 = \omega_z^2/4$ it can be seen that the vorticity dominates the strain wherever $b \neq 0$. Thus, vortices do imply high vorticity values but high vorticity values such as those caused by shear do not imply vortices.

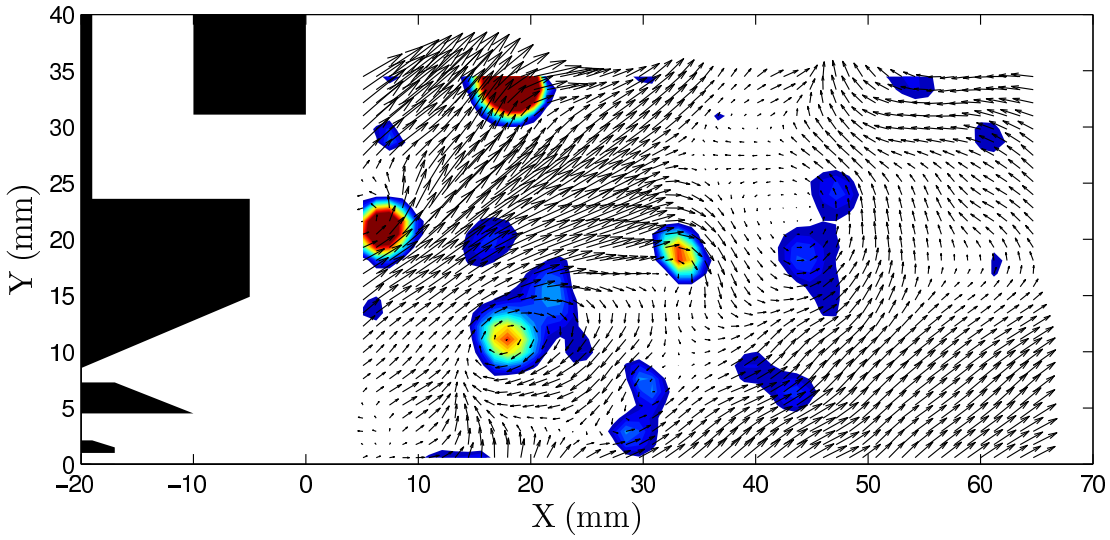

Figure 4.3: A sample contour plot of swirling strength for an instantaneous PIV data of a reacting flow field. Superimposed are the velocity vectors (undecomposed).

While the theory suggests that simply plotting regions where the imaginary part of the eigenvalue is non-trivial should highlight vortices, it is slightly different in practice. Due to experimental noise and finite resolution, better results are obtained if instead contours of b^2 are plotted. The square of the imaginary part has been termed the swirling strength by Zhou et al. (1999) and has been considered analogous to enstrophy. Although the imaginary component cannot be directly related back to enstrophy, it is dimensionally the same. This analysis has been applied to the PIV data from the GE combustor and the result from a sample instantaneous field is shown in Fig. 4.3. Overlayed on the contours of swirling strength are the velocity vectors. Each cohesive packet of swirling strength implies a separate vortex. Regions where the velocity vectors distinctly show a vortex, such as at $(x, y) = (18, 10)$ mm and at $(x, y) = (7, 20)$ mm have high values of swirling strength. Other vortices indicated by the contours only show the vortices when they are observed at their respective convection velocity, i. e. when viewed in the reference frame of the vortex.

Critical point analysis of the type done here to identify vortices has been done and utilized by other researchers with their PIV (Adrian et al. (2000) and Geers et al. (2005)), or DNS (Taylor et al. (2005)) data. However, the trajectories shown in Fig. 4.1 suggest further use of the eigenvalues for more than just identifying vortices. For example, the trajectories below the line $P = 0$ are those of a stagnation point. If they occur on a flame front, then the flame will experience conditions similar to an opposed-diffusion flame. Once again, identifying flow features such as these can be difficult since it will be masked by the overall convection. Computing and subsequently plotting regions where the two eigenvalues have opposite signs will easily highlight areas with opposed flow. This is a tool that has not been really utilized to its full potential in the combustion literature.

4.2 Non-Reacting Flow Field

Cases 1NR, 2NR, and 3NR represent three different conditions for which the flow was quantified without the presence of a flame. No fuel was injected through any of the injectors and it was assumed that the effect of the fuel spray on the flow is negligible. In general it was seen that the flow fields for all three cases were very similar and therefore Case 3NR will be used as a representative case for discussing the non-reacting results. This case represents the highest flowrates, temperatures, and combustor pressures, and thus is higher on the engine operating line than the other cases.

4.2.1 Mean Flow Field

Fig. 4.4 shows contour plots of the average axial velocity ($\overline{U}$) and radial velocity ($\overline{V}$) for Case 3NR. The boundary of the recirculation zone is marked by the boundary of negative axial velocities and is shown by the solid black lines. The contours of

$\overline{U}$ indicate that a recirculation zone exists along the centerline from the injector all the way downstream to the available field of view. While the azimuthal velocity was not measured, the results indicate that vortex breakdown has occurred and that the recirculation zones from the wake of the injector and from vortex breakdown have merged to form one Primary Recirculation Zone (PRZ). The rear stagnation point was not in the field of view but the results discussed in §1.2.1 suggest that one exists due to the area contraction at the exit of the combustor (Fig. 2.2). Flow from the pilot annulus can be seen to issue around $y = 15$ mm near the maximum radial location of the pilot annulus. Flow from the inner pilot annulus at $y = 3$ mm presumably merges with the outer pilot annulus within the injector and issues as one bulk stream into the combustor. The pilot flow pushes the PRZ radially inward until the pilot flow merges with the flow from the main annulus, leading to the kink in the PRZ at $(x, y) = (18, 20)$ mm. The highest velocities are in the main flow as would be expected. The mean radial velocity also is as expected for a swirling flow with high radial velocities in the pilot and main flows and a near zero value at the centerline. The flow from both annuluses is seen to issue at the same angle as confirmed by the velocity vectors and the ratio of axial to radial velocities. The points made above are supported by profiles of $\overline{U}$ and $\overline{V}$ at select axial locations shown in Fig. 4.5. Profiles as shown here are useful for comparisons with any future simulations and can also help highlight key features of the flow. The profiles of both $\overline{U}$ and $\overline{V}$ at $x = 14$ mm show that the pilot flow has mostly merged with the flow from the main annulus that continues to move radially out of the field of view. A much smaller recirculation zone is seen near the lip of the injector at $(x, y) = (5, 24)$ mm and will be referred to as the Lip Recirculation Zone (LRZ). Unlike the PRZ, the LRZ is caused by the wake of the lip of the injector and causes the pilot flow to slow down (and even reverse

direction) before it merges with the main flow.

A number of pertinent gradients and turbulence quantities were computed from the measured velocity data. The Reynolds stresses $(u'v')$[1] can be computed from the measured two components of velocity and its contours are shown in Fig. 4.6a. The Reynolds stress plays an important role in turbulence modelling and especially RANS based models utilize approximations to model the Reynolds stress and "close" the equations of motion. Measurements of the Reynolds stress therefore provide a direct way to compare the assumptions of a particular model to measured results. The overall magnitudes of the Reynolds stress are similar to the values reported for isothermal conditions in other swirl combustors. In general, the PRZ has low to trivial values of Reynolds stress indicating that the PRZ can successfully be modelled as being isotropic. The peak values as one would expect are in the flow from the two annuluses. Due to the angle at which the flow is issuing, $\overline{u'v'}$ is necessarily positive since there is significant transport of the axial momentum in the radial direction. There is a small region of negative stresses near the exit of the main annulus, between the pilot and main flows. This region is where the pilot flow turns around the LRZ before merging with the main flow. The slowing down of the axial velocity while still maintaining positive radial velocity leads to negative correlations in the two fluctuating velocity components.

The turbulence intensity (q) was defined as

$$q = \frac{1}{2}\sqrt{u'^2 + v'^2}. \tag{4.11}$$

Note that the turbulence intensity defined in this manner can be related back to the

[1]The Reynolds stress tensor is actually $= \rho\overline{u_i' u_j'}$ but for the purposes of this study the density has been ignored for plotting the Reynolds stress.

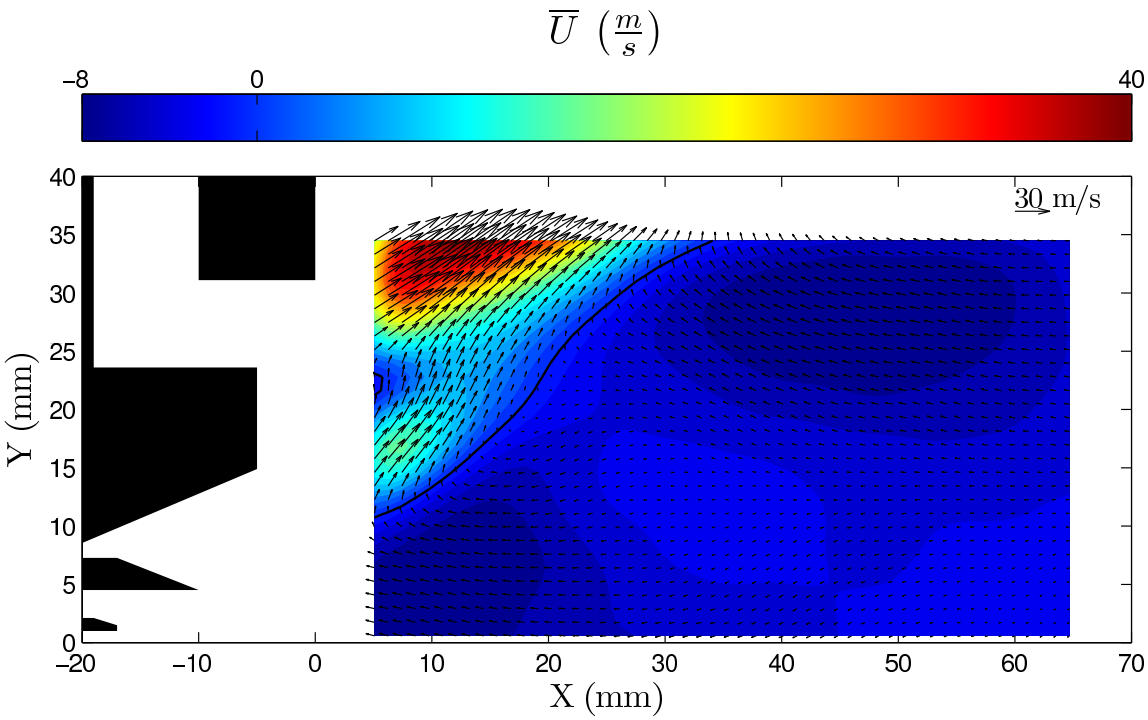

(a) Contours of mean axial velocity. The solid black line is the contour line of zero axial velocity and serves to demarcate the recirculation zone.

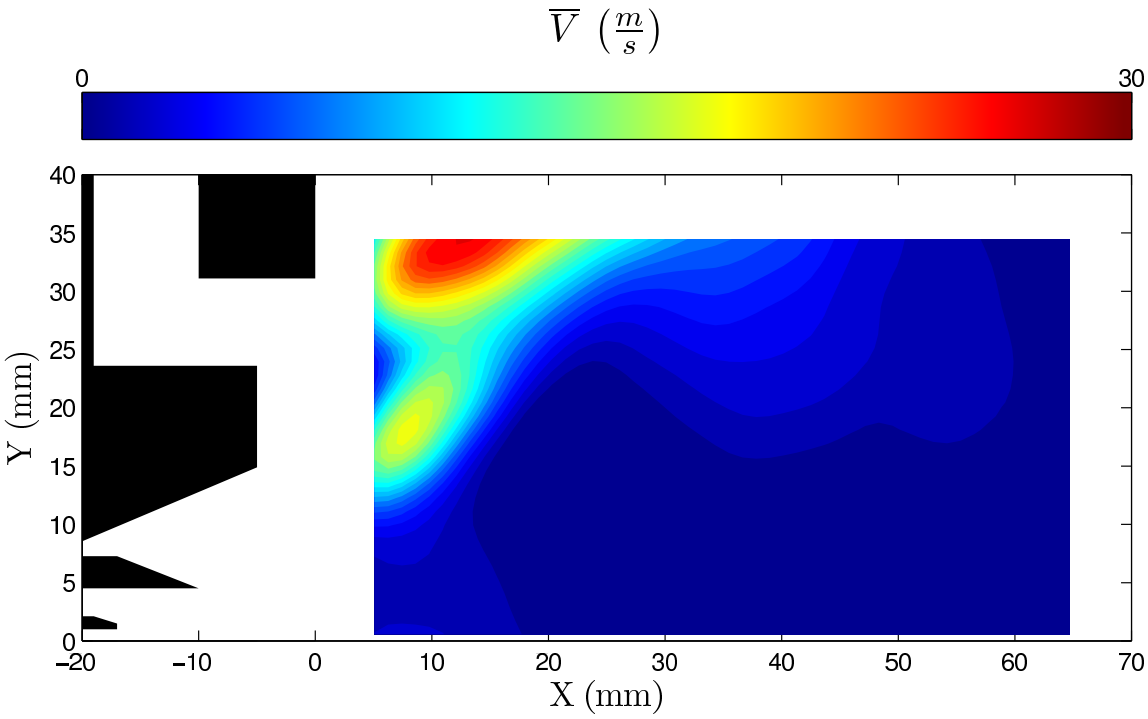

(b) Contours of mean radial velocity.

Figure 4.4: The mean flow field of the non-reacting case (Case 3NR). The velocity vectors are overlayed on contours of the mean axial velocity ($\overline{U}$). This flow field is representative of all the non-reacting cases.

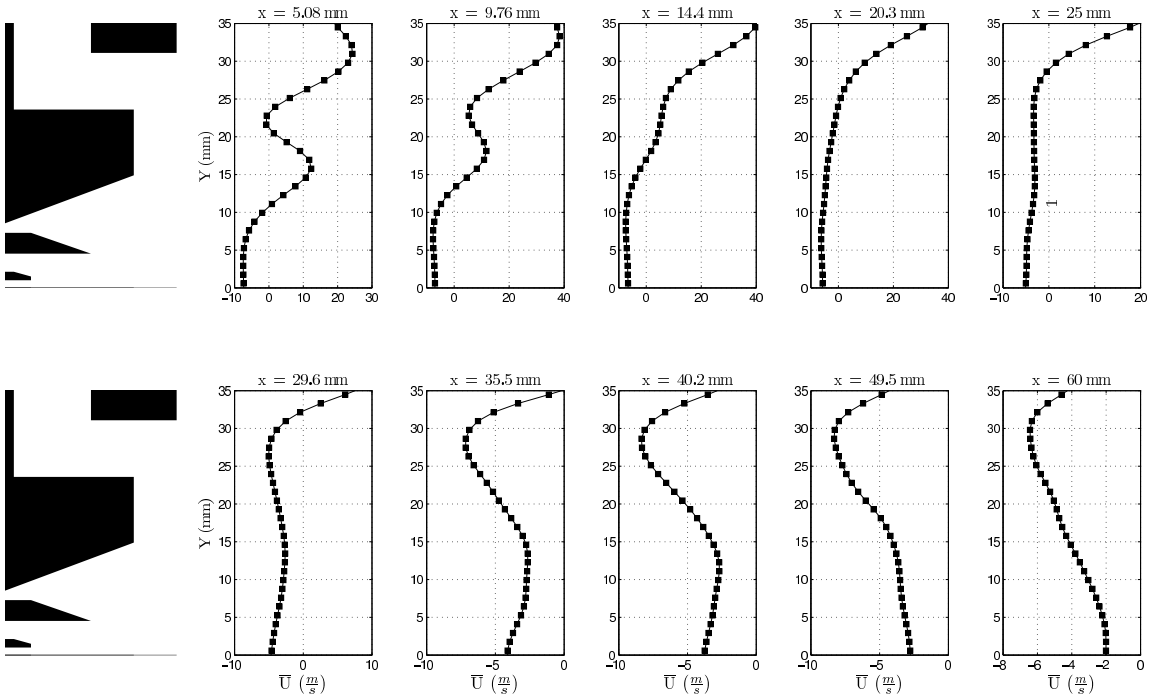

(a)

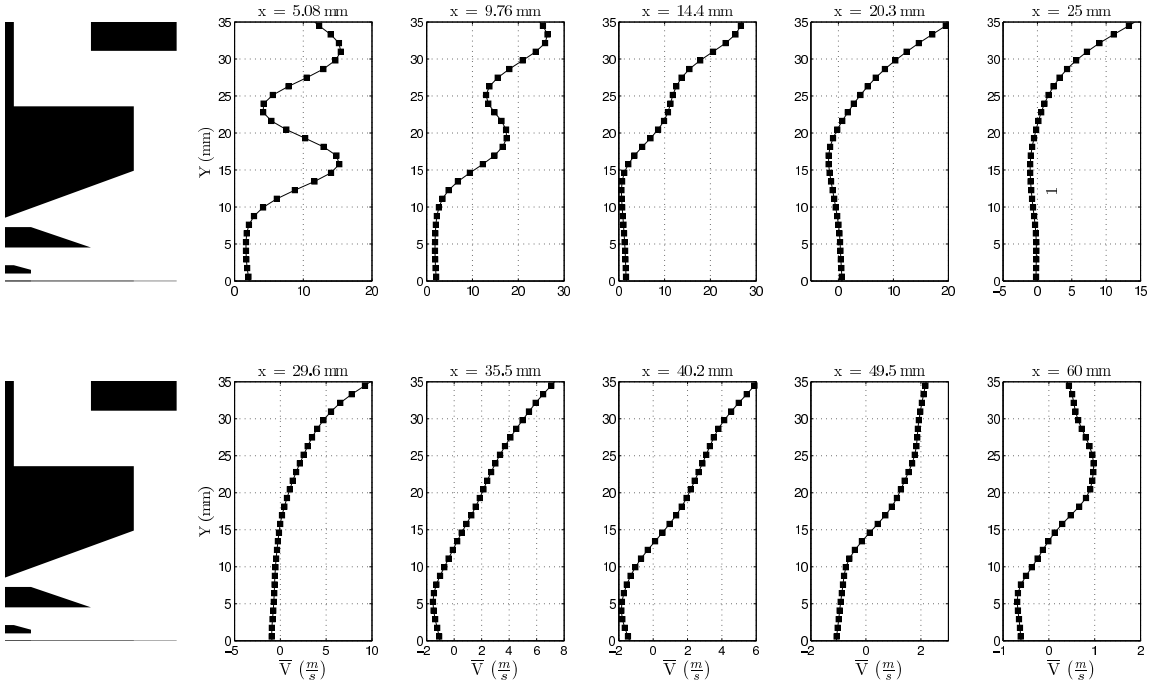

(b)

Figure 4.5: Profiles of $\overline{U}$ and $\overline{V}$ at select downstream locations for the non-reacting case (Case 3NR). The square markers are the experimental data points.

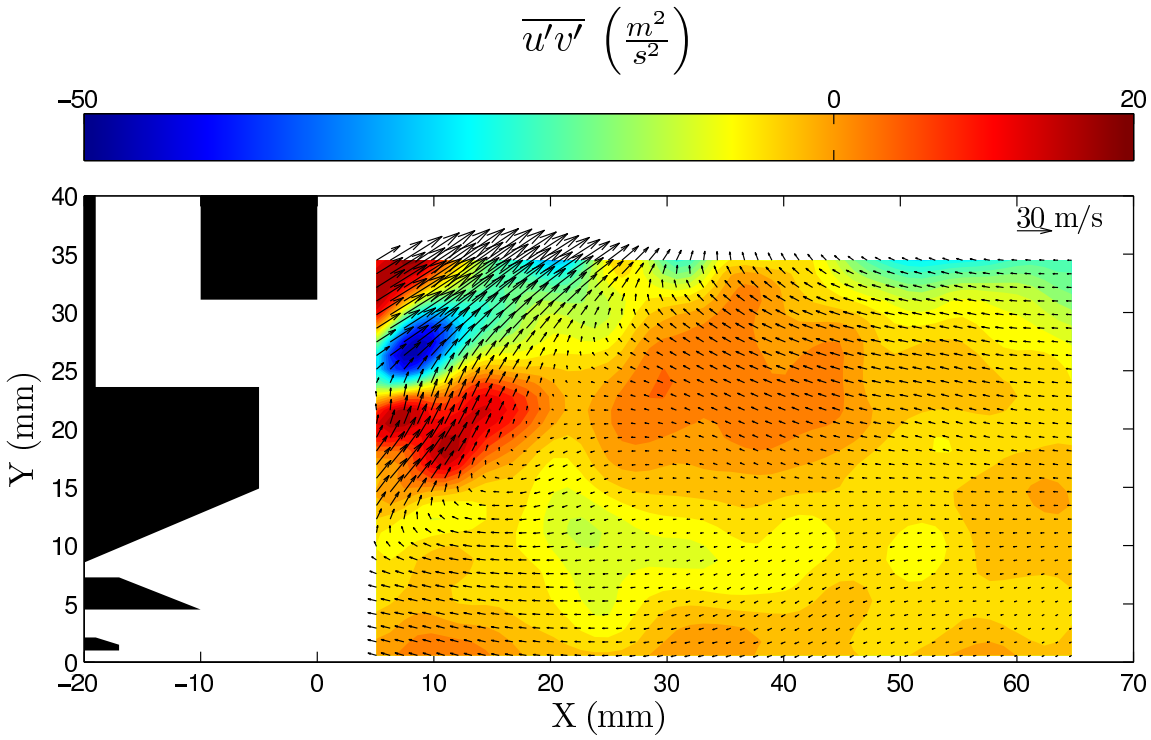

(a)

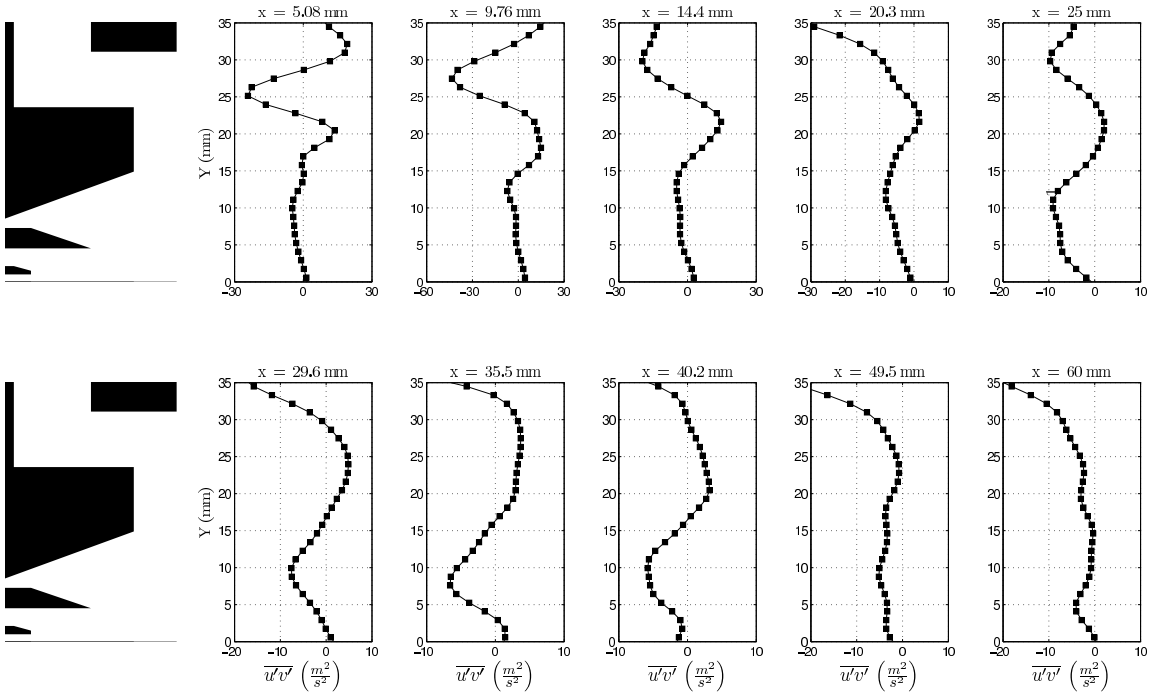

(b)

Figure 4.6: Contour plot and profiles of the Reynolds stress for the non-reacting flow field (Case 3NR).

two-component turbulent kinetic energy (TKE) as

$$TKE = \frac{1}{2}\left(u'^2 + v'^2\right) = 2q^2. \tag{4.12}$$

A contour plot and profiles of q for the non-reacting case are shown in Fig. 4.7. In the non-reacting case, the highest kinetic energies are in the flows from the two annuluses. The PRZ meanwhile has a near uniform value of $q \approx 4$ m/s.

The out-of-plane component of vorticity (ω_z) was computed from the two measured components of velocity as

$$\omega_z = \frac{\partial v}{\partial x} - \frac{\partial u}{\partial y}. \tag{4.13}$$

This is the only component of vorticity that can be resolved with standard 2-D PIV. It is interesting to note that the measurement of the third component of velocity, through Stereo-PIV, is still unable to yield any more components of vorticity since gradients in the third direction (z) are not measured. The contour plot and profiles of $\overline{\omega_z}$ are shown in Fig. 4.8. The boundary of the recirculation zones have been repeated here because the vorticity plays a dominant role near the edge of the zones. As can be seen from the figure, the regions of high vorticity line up very well with the edges of both the PRZ and the LRZ. As also indicated by the profile at $x = 5.08$ mm, four distinct peaks with alternating sign exist at the exit of the injector and main swirler. Starting from the peak closest to the centerline, this region of vorticity is created from flow issuing into the pilot flow from the PRZ as opposed to the pilot flow issuing into the PRZ. This is confirmed from the velocity vectors in Fig. 4.4a. This pattern exists throughout the edge of the PRZ. The second peak is from the pilot flow turning around the LRZ with the sign of the vorticity peak confirming the direction of motion. The third peak is from the pilot flow merging with the main flow. This region of negative vorticity continues downstream and marks the edge of

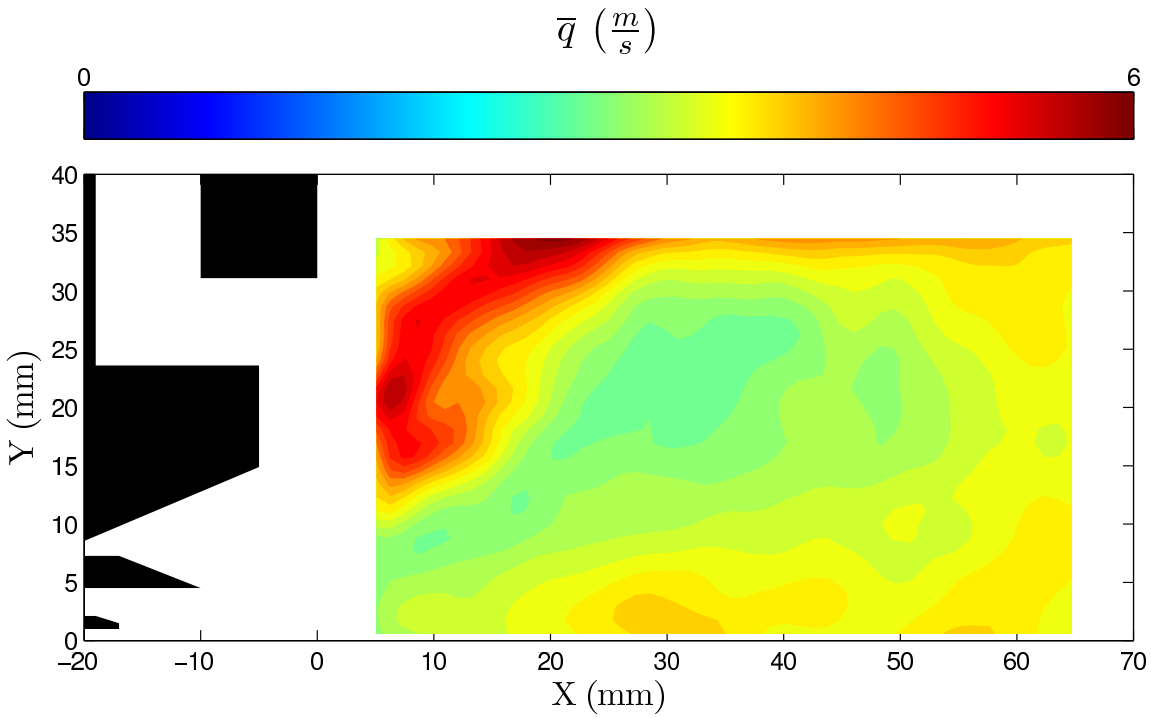

(a)

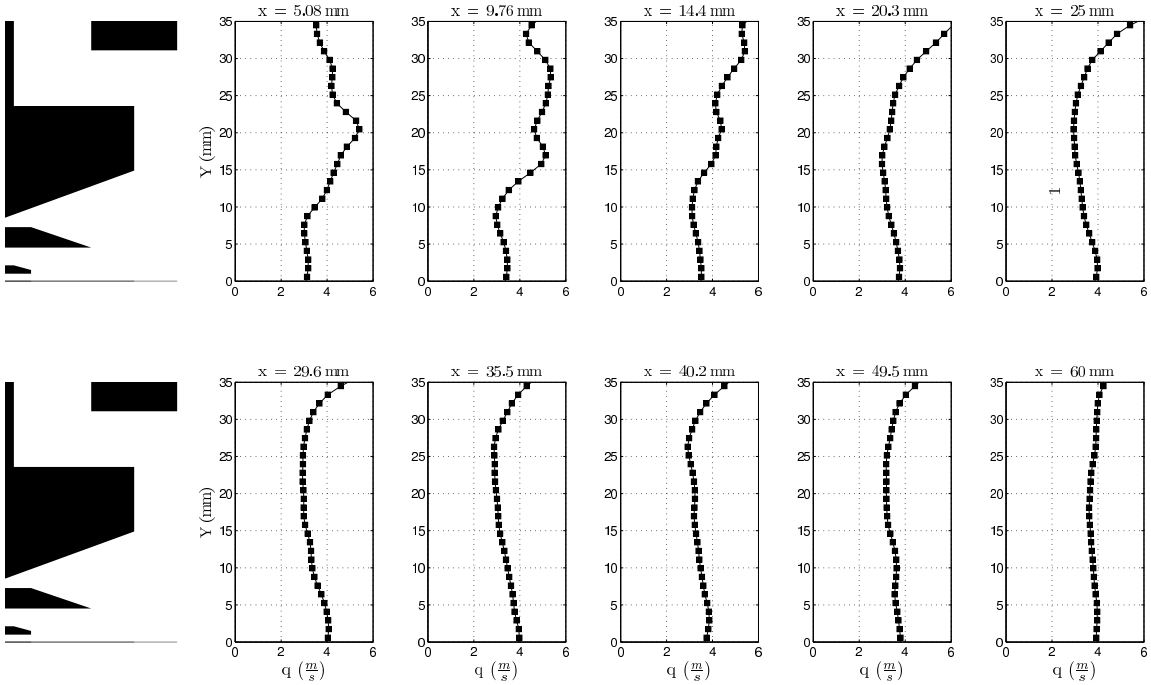

(b)

Figure 4.7: Contour plot and profiles of the turbulence intensity for the non-reacting flow field (Case 3NR).

the PRZ. The fourth peak was not captured entirely but shows regions of positive vorticity in the main flow as it turns radial outward upon issuing from the main annulus. Within the PRZ, the mean vorticity values are close to zero everywhere. As will be shown, this apparent trivial result is an illusion and the result of many vortices with opposite signs cancelling each other out in the ensemble average.

Another gradient quantity relevant to turbulent flows in general and combustion in particular is the shear strain rate, defined as

$$\varepsilon_{xy} = \frac{\partial u}{\partial y} + \frac{\partial v}{\partial x} = \varepsilon_{yx}. \tag{4.14}$$

Of course, from the two measured components of velocity, one can also compute ε_{xx} and ε_{yy}, giving three out of the six independent components of the strain rate tensor. However, emphasis will be placed on the off-diagonal component as it is the dominant component in this flow, as it is in most turbulent flows. As can be seen from the contour plot and profiles shown in Fig. 4.9, the highest strain rates are in the main flow. High strain rates (of an opposite sign) also exist in the pilot flow although their magnitudes are only about half of the strain rates of the main flow. The PRZ again has negligible gradients, confirming the idea that the PRZ is isotropic on the mean, since shear causes departure from isotropy.

As a final comparison, the mean locations of all three non-reacting cases (Cases 1NR, 2NR, and 3NR) are shown in Fig. 4.10. As shown, the mean location and shape of the PRZ is virtually identical for all three cases. This is an expected result from earlier studies of vortex breakdown that have shown that the phenomenon has a very weak dependence on the Reynolds number and is almost entirely governed by the geometry (i. e. the swirl number and downstream constriction). Since the swirl number does not change between cases, negligible changes are seen in the PRZ.

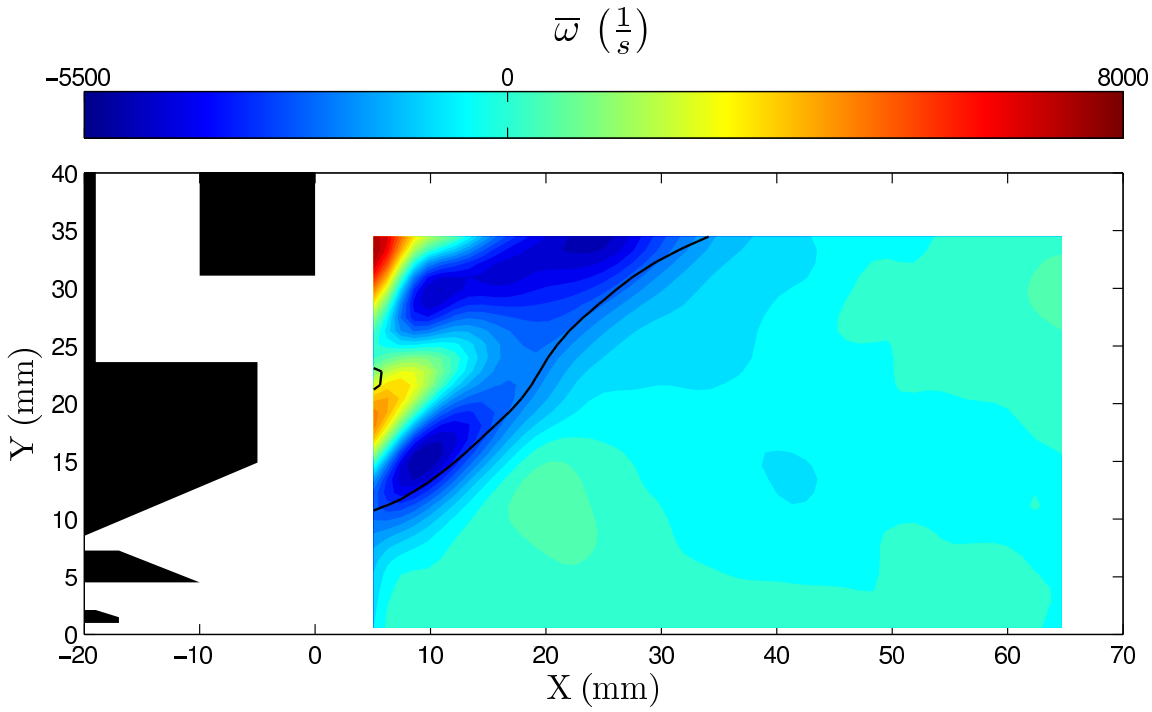

(a)

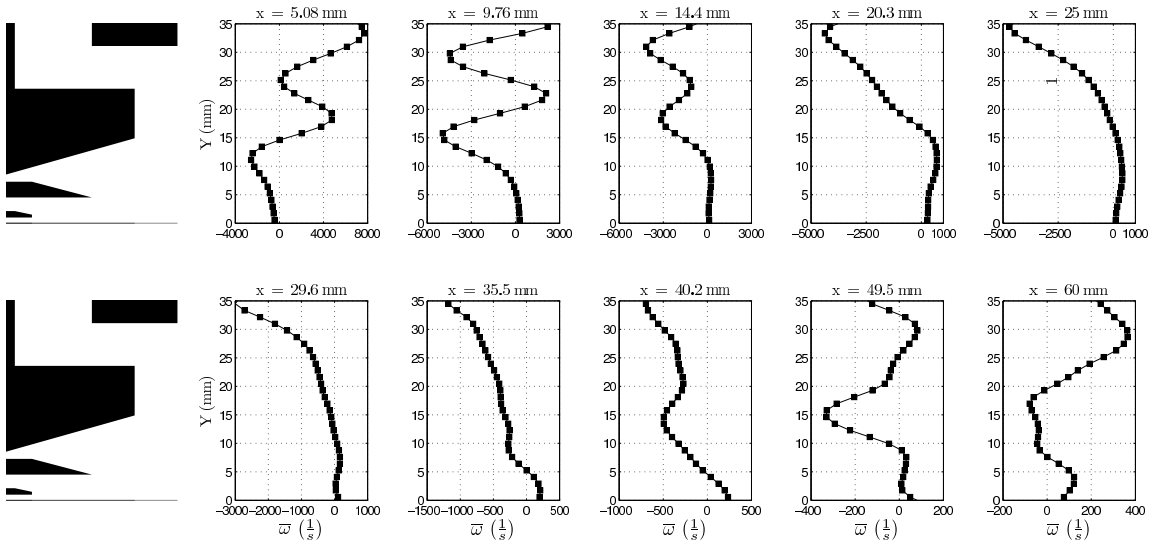

(b)

Figure 4.8: Contour plot and profiles of vorticity for the non-reacting flow field (Case 3NR).

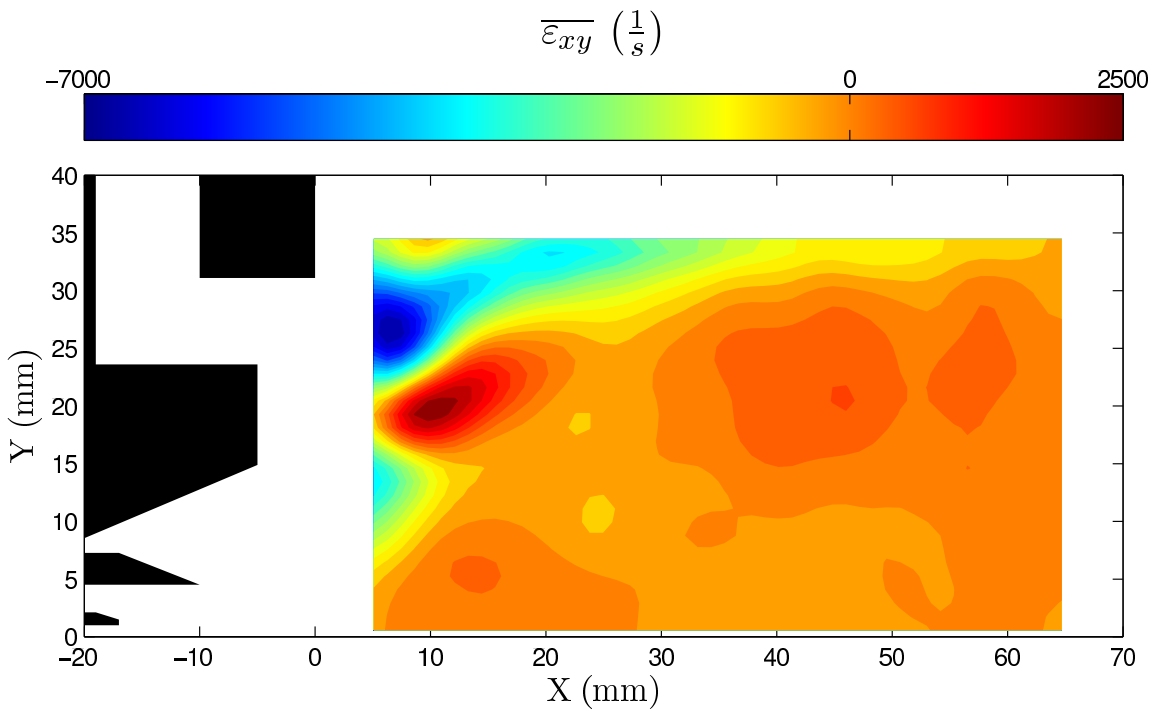

(a)

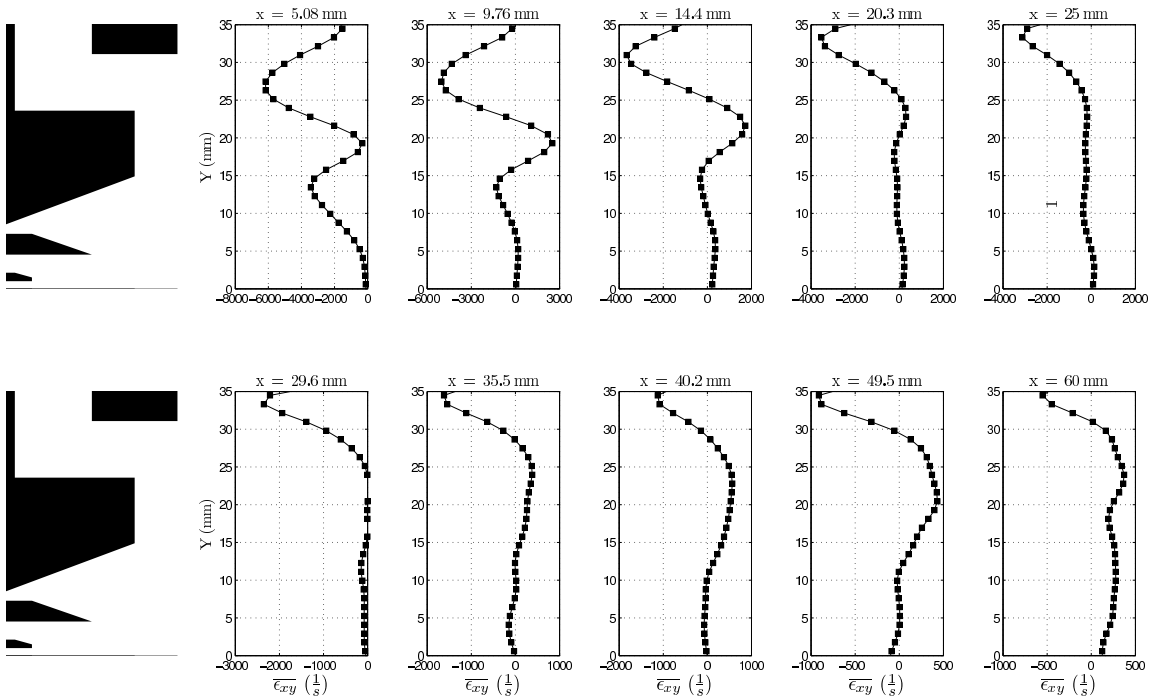

(b)

Figure 4.9: Contour plot and profiles of the shear strain rate for the non-reacting flow field (Case 3NR).

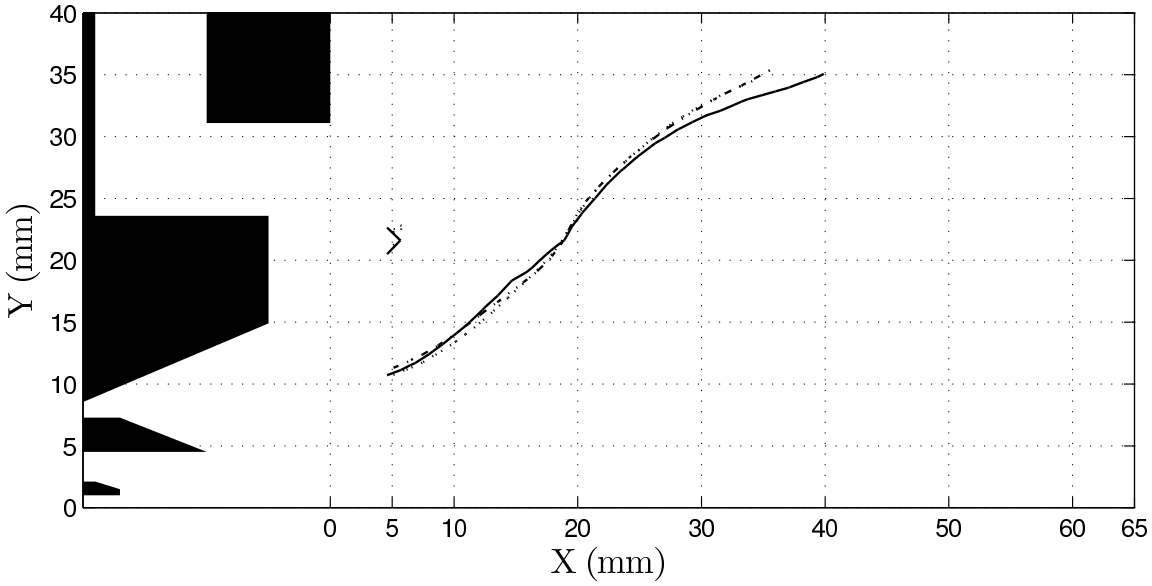

Figure 4.10: The mean recirculation edge(s) of all three non-reacting cases studied. —: Case 1NR, -·-: Case 2NR, · · ·: Case 3NR.

4.2.2 Instantaneous Flow Field

The previous results for the non-reacting flow field showed the mean of the velocity components and other pertinent computed quantities. The instantaneous flow field however is extremely important since in actuality the flow within the combustor is described by the instantaneous features. The instantaneous velocity vectors overlayed on contours of the swirling strength for four randomly selected fields are shown in Fig. 4.11. As described in §4.1, the swirling strength provides a more unambiguous measure of the individual eddies than contour plots of vorticity. As seen in the instantaneous flow fields, numerous vortices are seen to issue from the injector. These eddies roll around the edge of the PRZ and are responsible for the large scale transport of momentum between the fluid in the PRZ and the fluid issuing from the pilot and main annuluses. The instantaneous images also show that there is considerable transport from the pilot and main flows into the PRZ near the injector. This

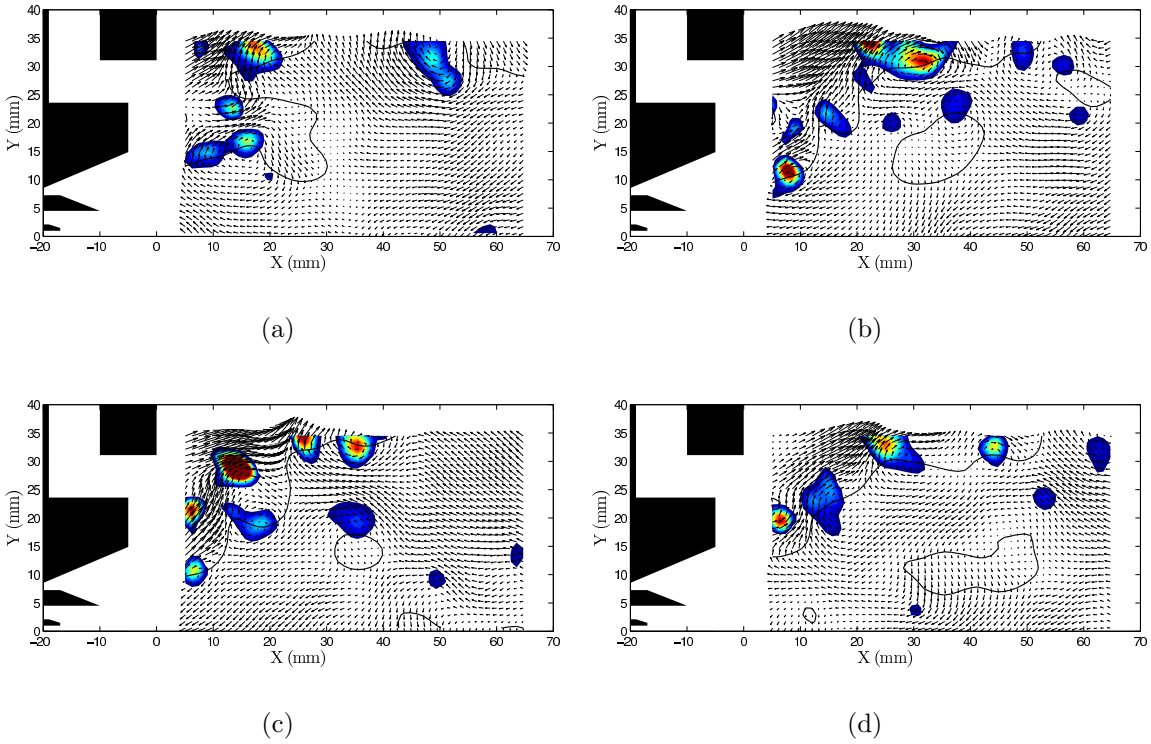

Figure 4.11: Four randomly selected instantaneous representative velocity fields for the non-reacting case (Case 3NR). Overlayed on each image are contours of the swirling strength and the instantaneous recirculation zone boundary shown by the solid black line.

is in contrast to the mean velocity field which suggested that there is only flow from the PRZ into the pilot and main flows and not vice versa. Also, it can be seen that instantaneously there is considerable spatial variation in the location of the edge of the PRZ. These results highlight the highly unsteady nature of the isothermal flow within the TAPS combustor. Crucially, the mean flow results presented §4.2.1 mask some important structural detail of the actual flow.

4.3 Reacting Flow Field - Pilot Only

Similar to the non-reacting flow fields, the reacting fields for Cases 1R, 2R, and 3R all were very similar. In fact, it was seen that the profiles of the mean axial velocity could be made to collapse onto one universal curve by using an appropriate

scale. It was assumed that simple continuity defines the magnitudes of the axial velocity and the geometry defines the shape of the profiles. Since the geometry of the injector or combustor does not change between cases, scaling the velocities by the mass flow rate should lead to a universal curve. Continuity gives $\dot{m} = \rho U A$, therefore a new velocity (U^*) was defined as $U^* = \dot{m}/(\rho_3 A)$. The density (ρ) was computed assuming an ideal gas using the inlet temperatures (T_3) and pressures (p_3) given in Table 4.1 for Cases 1R, 2R, and 3R. The mass flow rate ($\dot{m}$) was set to the total mass flow rate also given in Table 4.1. The mean axial velocity scaled by U^* for Cases 1R, 2R, and 3R is shown in Fig. 4.12. The level of collapse at all downstream locations is excellent for three cases that span a range of mass flow rates, temperatures, and pressures. The collapse also confirms the hypothesis that the specific geometry of the combustor defines the mean flow field. This fact can now be used to predict the velocities in the combustor for any given condition through the simple scaling provided by U^*.

The similarity in the flow field is also confirmed by plotting the edges of the recirculation zones for Cases 1R, 2R, and 3R as shown in Fig. 4.13. All three recirculation zones are very similar in shape and size and at most spatial locations the discrepancy in the location of the RZ edge is on the order of one interrogation window. These results prove the validity of using one of the conditions, Case 3R in this case, as a representative condition for the reacting flow with only a pilot flame.

4.3.1 Mean Flow Field

The mean velocity field for Case 3R is shown in Fig's. 4.14 (mean axial velocity), 4.15 (mean radial velocity), and 4.16 (profiles of $\overline{U}$ and $\overline{V}$). Similar to Fig. 4.4a, the recirculation zones have been demarcated by the contour of zero axial velocity.

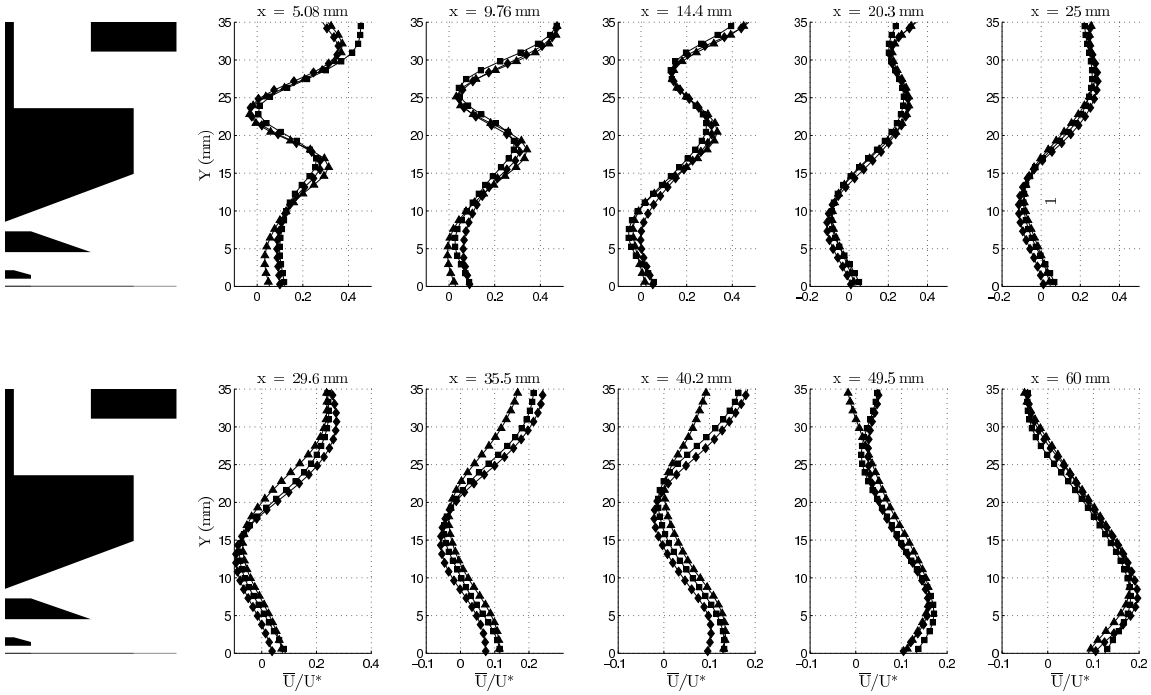

Figure 4.12: Average axial velocities scaled by $U^* = \dot{m}/(\rho_3 A)$. Conditions at three different air mass flowrates, temperatures, and pressures are seen to collapse onto one universal curve. ■: Case 1R, ♦: Case 2R, ▲: Case 3R.

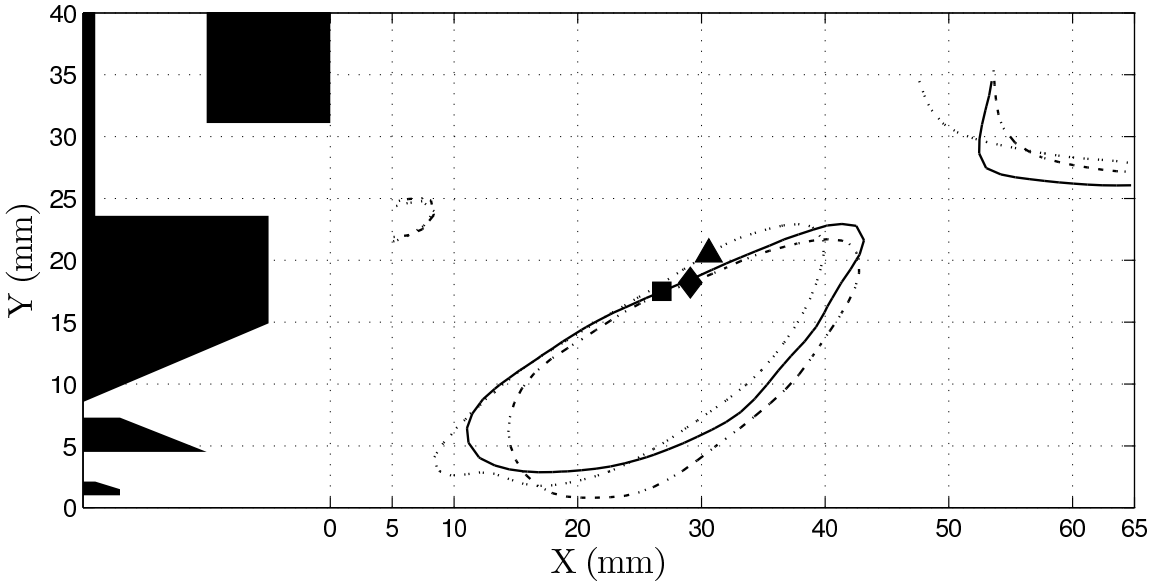

Figure 4.13: The average recirculation zones for Cases 1R, 2R, and 3R. Very little variation between the size, shape, and location is seen between the three different operating cases. The markers (■: Case 1R, ♦: Case 2R, ▲: Case 3R) denote the center of the mean vortex on the edge of the PRZ as described in Fig. 4.14 and §4.3.1.

Also, in Fig. 4.14, the mean flame contour from Fig. 3.4 has been plotted as a solid red line. Though the flow conditions including the pilot fuel flowrate were different for Case 3R than for Case 1Pt3 (the case shown), the flame contour does provide a good idea of the location of the mean flame front.

The single biggest difference observed from the mean axial velocity is the drastic reduction in the size of the recirculation zone. The PRZ is seen to reduce to an oval shaped toroidal recirculation zone that is no longer attached to the injector and has its rear stagnation point well within the field of view. Also, the toroidal shape means that the mean velocity on the centerline is positive. A smaller recirculation zone is also seen in the top right of the image. The instantaneous images suggest that this zone is a part of the PRZ and only a small region with low positive axial

velocities breaks the PRZ into two separate lobes. It is entirely possible that a break of this nature is not axisymmetric and only exists on the plane of measurement. In this case, it would be akin to a hole in the PRZ. The LRZ exists in the same location as it did for the non-reacting case, giving credence to the idea that it is the wake of the injector and not vortex breakdown. The drastic change in the size of the PRZ has been observed by multiple other researchers (Heitor and Moreira (1992), Weber and Dugue (1992), and Ji and Gore (2002) amongst others) and can be explained by vortex breakdown. As was explained in §1.2.1, continuity requires that the gas expansion from the heat release in the flame lead to positive axial velocities. The increase in axial velocities causes a transition from a subcritical state to a supercritical state. Also, the high heat release from the flame has the same effect as a large contraction, in that it pushes the rear stagnation point upstream enough such that no reversed flow exists on the centerline. In fact, with combustion providing the transition to a supercritical state, a contraction is not needed to create the favorable pressure gradient. Any contraction of course causes a small amount of drag and is undesirable. This result shows that the extension of a non-reacting result to an actual combustor can lead to inefficient designs.

Another key difference from the non-reacting condition is the flow between the PRZ and pilot flow. In the non-reacting case, it was noted that the mean velocity vectors all suggested mass flow from the PRZ into the pilot flow and not vice versa. Of course, it was seen that instantaneously there was mass flow in both directions. In the reacting conditions, a large vortex exists between the pilot flow and the PRZ. The center of this vortex was identified in Fig. 4.13 for Cases 1R, 2R, and 3R. This vortex can be seen in Fig. 4.14 with its center at $(x, y) = (30.6, 20.5)$ mm. This vortex lies near the flame tip and carries hot products from the flame into the PRZ.

Of course, these hot products are then convected upstream along the length of the flame. The pilot flame exists almost entirely in the pilot flow as would be expected. The PRZ can be seen to be radially inside the pilot flame cone as required for the flame stability. The PRZ is critical to the operation of a stable pilot flame since it recirculates hot products from the length of the flame down to the base. In fact this key aspect of swirl combustors makes them a popular choice for practical gas turbine combustors.

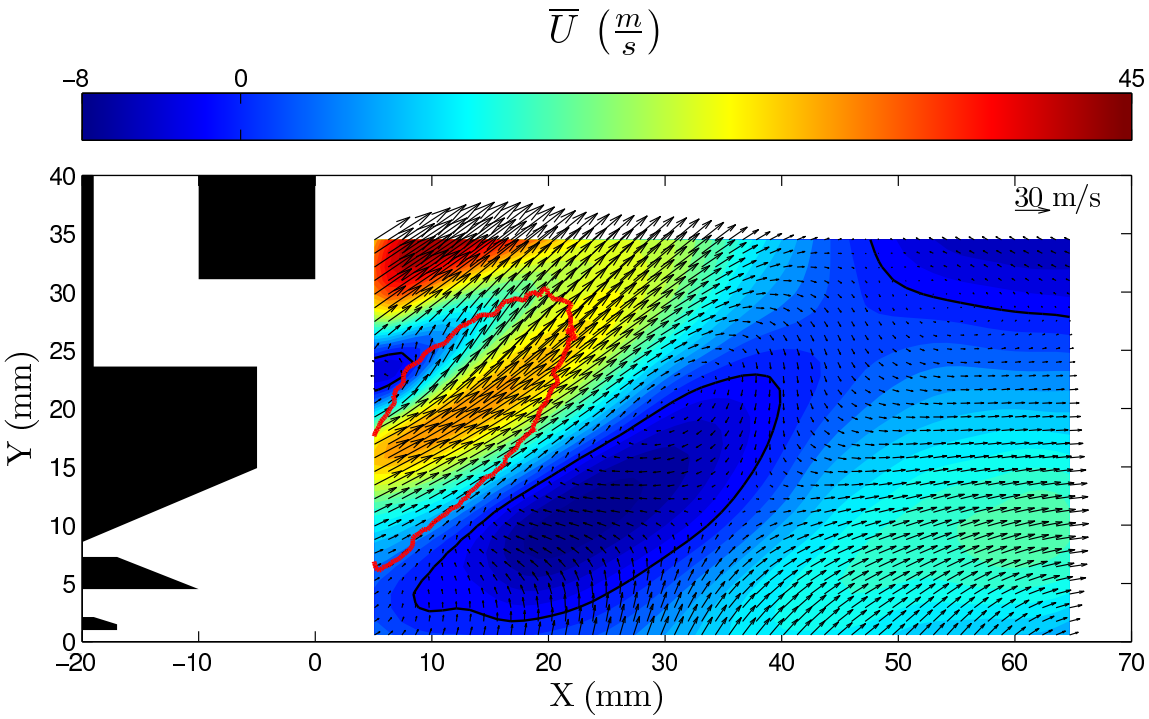

Figure 4.14: Mean velocity vectors overlayed on contours of mean axial velocity for the reacting case (Case 3R). The solid black line is the contour line of zero axial velocity and serves to demarcate the recirculation zone. The mean flame contour from Fig. 3.4 has been plotted in red. This flow field is representative of all the non-reacting cases.

Contours and profiles of the Reynolds stress shown in Fig. 4.17 show a very different correlation from the non-reacting condition. Clearly, the pilot flame leads to large increases in both the axial and radial velocities that cause high Reynolds

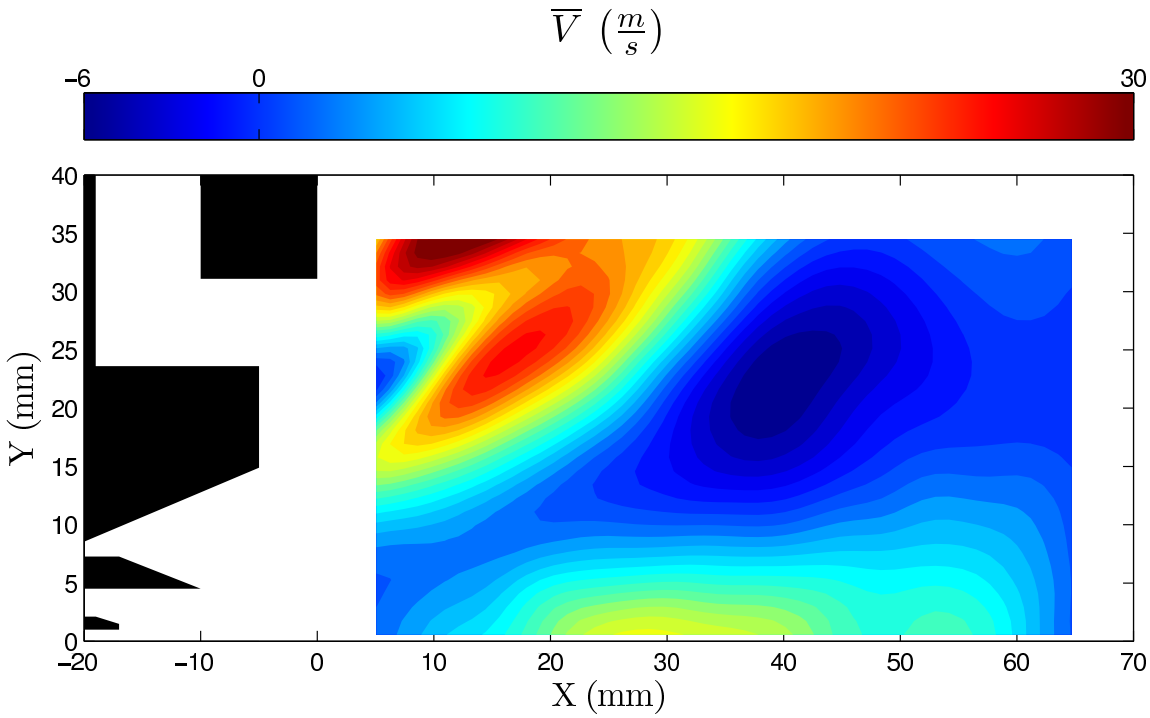

Figure 4.15: Contours of mean radial velocity for the reacting case (Case 3R).

stresses. Since the pilot fuel flowrate for Case 3R was higher than for the flame contour shown, it can be hypothesized that the actual flame in Case 3R is longer than the flame shown (see Fig. 3.7). There are two zones of high stresses visible in the contour. The first zone (clearly visible in Fig. 4.17b at $x = 9.76$ mm and $x = 14.4$ mm) is between the flame and the main flow. The second zone is near the flame tip and the heat release from the flame at these locations drives high positive fluctuations in the velocity. Interestingly, there is no corresponding zone of high Reynolds stress near the inner edge of the flame. Quite possibly, the PRZ at this location helps to dampen the fluctuations by efficiently transporting a lot of the hot accelerated products.

Contours and profiles of q (Eqn. 4.11) for the reacting case are shown in Fig. 4.18. Compared to the non-reacting condition, there is a large increase in the turbulence

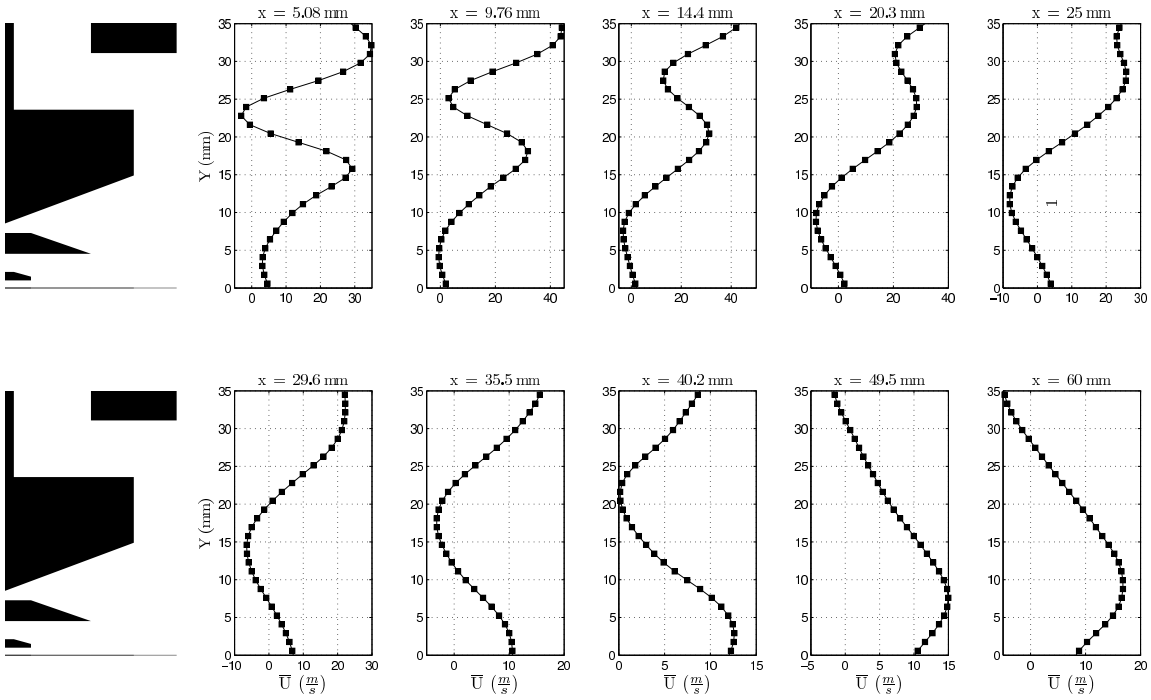

(a)

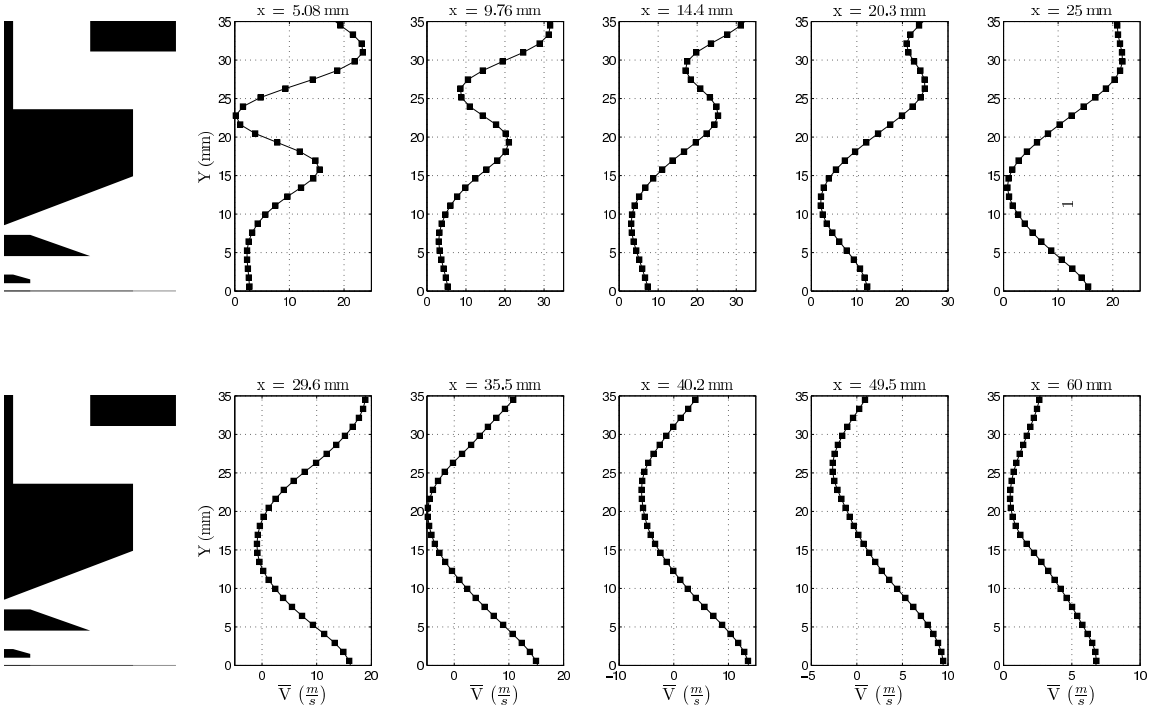

(b)

Figure 4.16: Profiles of $\overline{U}$ and $\overline{V}$ at select downstream locations for the reacting case (Case 3R). The square markers are the experimental data points.

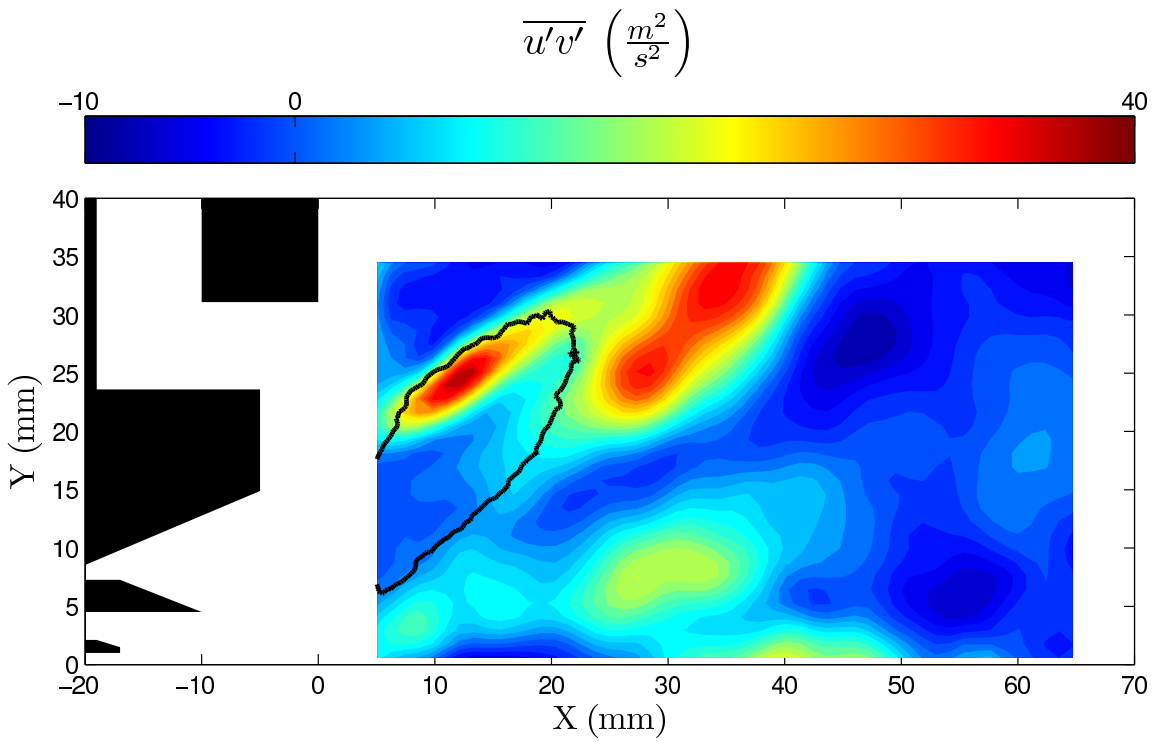

(a)

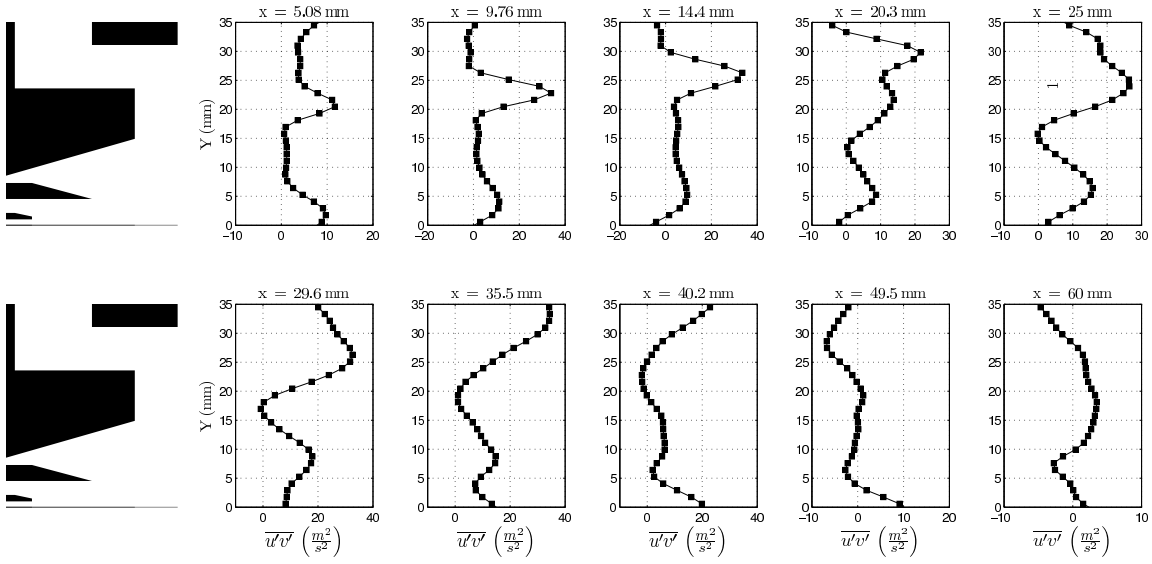

(b)

Figure 4.17: Contour plot and profiles of the Reynolds stress for the reacting flow field (Case 3R). The average flame contour is overlayed in black in (a).

intensity on the centerline. This result is to be expected from the mean axial velocities. The heat release from the pilot cone clearly causes large fluctuations in the axial velocity especially along the centerline where a large proportion of the hot products issue out of the combustor from. The two zones of high q at $y > 15$ mm correspond with the high Reynolds stresses at the same locations. The same process that causes the high stresses naturally leads to high turbulence intensities. The turbulence intensities of the incoming pilot and main flows are markedly lower than their counterparts in the non-reacting condition. The presence of the flame in the combustor effectively poses a fluid mechanical obstruction to the incoming flow. This obstruction has the effect of damping the large fluctuations that are otherwise present in the incoming flow. Of course, these reduced intensities are beneficial for flame stability.

Gradient quantities such as vorticity and shear strain rate highlight key structural details of the flow and are important in understanding the underlying turbulence field. Since the local turbulence is defined by the global gradient fields measured here, these quantities assist in the development of gas turbine combustors in a number of ways. First, they can be used as a check on simulation results, especially LES. LES requires modelling the small unresolved scales which has a direct effect on the resolved large scales. The measurements here require no assumptions of the small scales and therefore reflect the correct role of the inner scales on the measured outer scales. Another possible application of these measurements is that they can be used as the starting point for a simulation or model that would use the measured large scales along with the universality of the small scales to predict the effect of small eddies on a flame. The self-similarity of the flow suggests that the results presented here can be extended with some measure of confidence to more realistic gas turbine

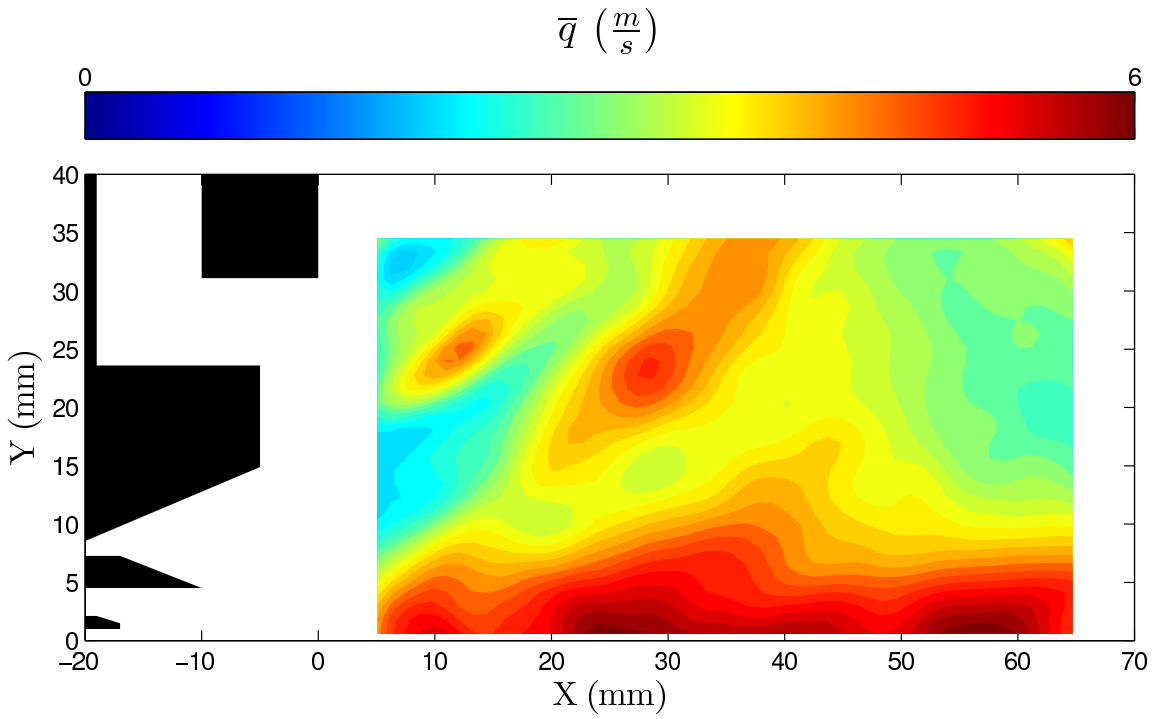

(a)

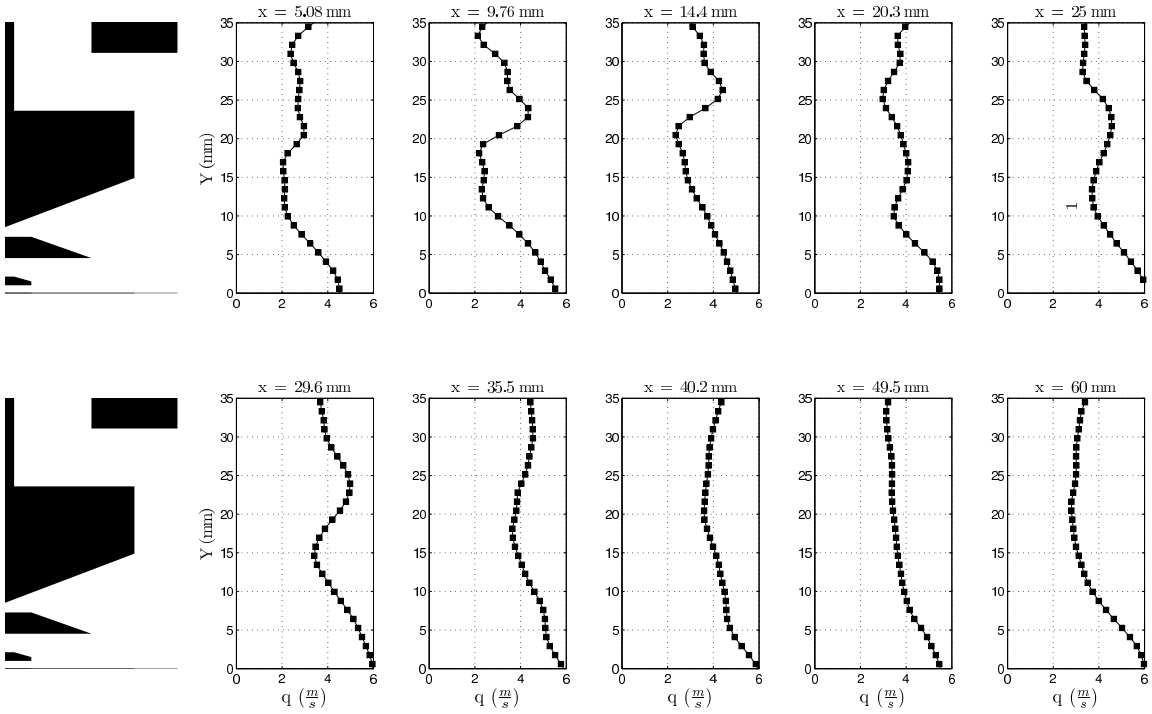

(b)

Figure 4.18: Contour plot and profiles of the turbulence intensity for the reacting flow field (Case 3R).

conditions.

Contours and profiles of vorticity and shear strain rate are presented in Fig. 4.19 and Fig. 4.20 respectively. The overall structure of the vorticity field is very similar in both the non-reacting and reacting cases with only small differences that one would expect with the change in the size and shape of the PRZ. The single biggest difference is the zone of high positive vorticity issuing from the inner edge of the lip of the TAPS injector (starting at $(x, y) \approx (5, 17)$ mm). Both zones of positive and negative vorticity on either side of the lip are from the vortices that are shed from the lip. Since the mean vorticity field is obtained from an ensemble average of the instantaneous vorticity fields, it can be said that the vortices that are shed from the injector mostly travel down the same spatial path in a Karman vortex street like pattern. The vortices of negative sign from the outer edge and of positive sign from the inner edge both issue and convect at an angle due to the swirl.

The shedding of vortices and the presence of shear layers between the recirculation zones and annulus flows leads to high shear strain rates in these regions. The region of high positive strain near the flame is higher in magnitude than the non-reacting case and is over a larger spatial domain corresponding with the length of the flame. The high strain rates and values of Reynolds stress near the injector and along the flame suggest significant departures from isotropy in these regions.

4.3.1.1 The Primary Mixing Layer

Fig. 4.14 showed that a number of shear layers exists in the reacting flow near the PRZ and the LRZ. The shear layer between the pilot flow and the PRZ in fact shows large similarities between the flow over a cavity. Here the PRZ is akin to the cavity and the pilot flow is akin to the free-stream over the cavity. The flow in the TAPS in

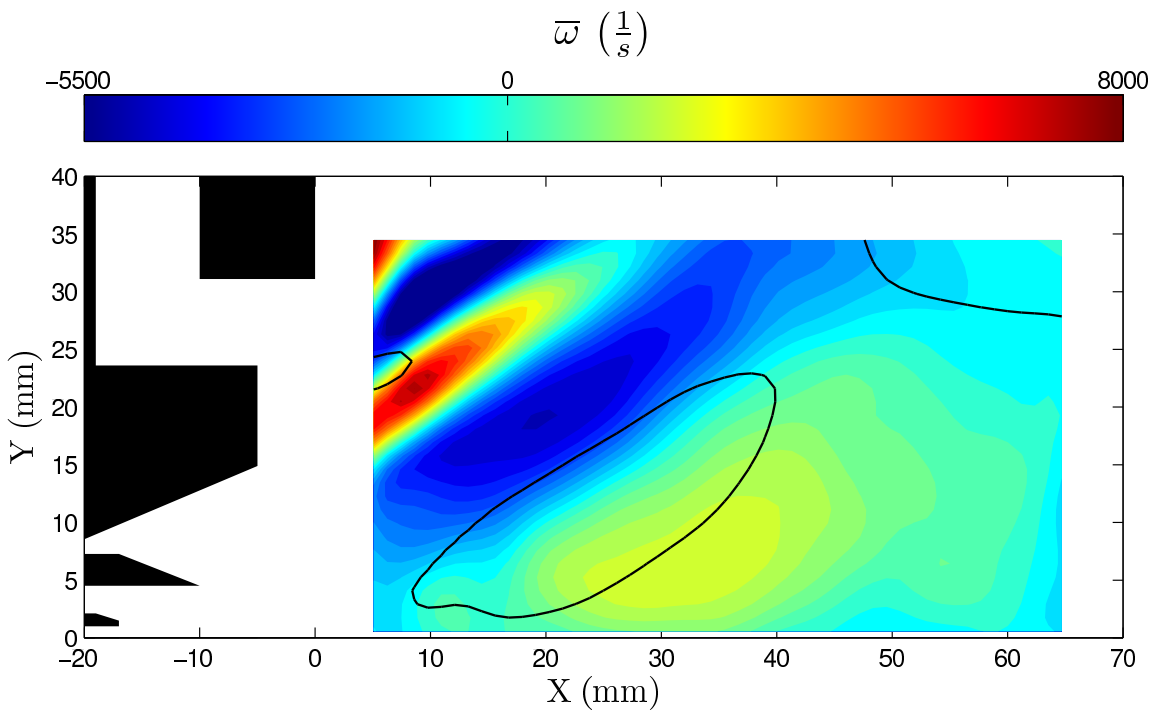

(a)

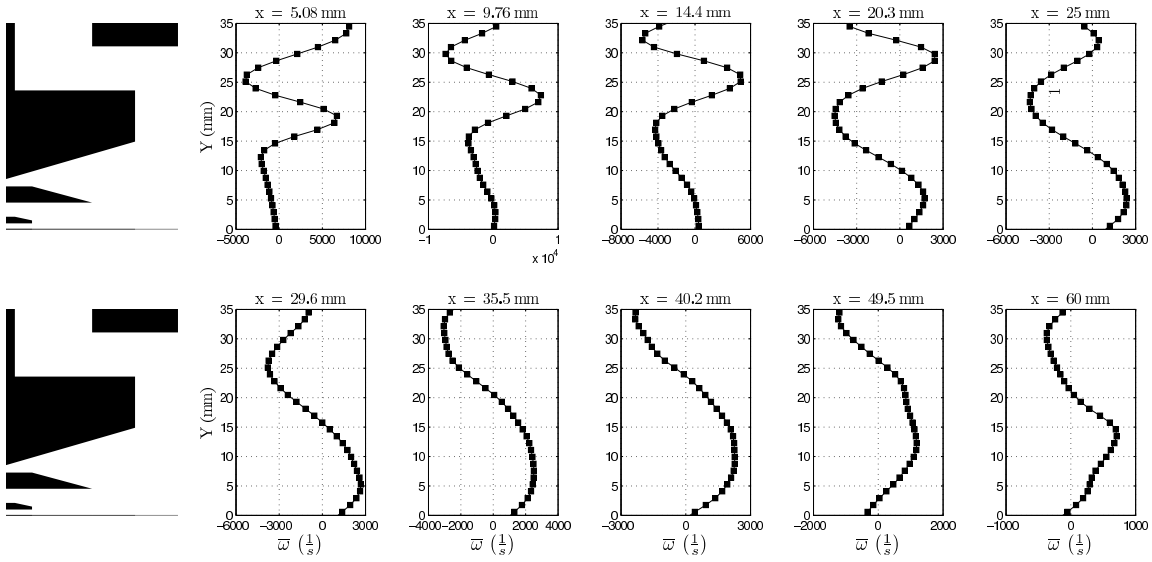

(b)

Figure 4.19: Contour plot and profiles of vorticity for the reacting flow field (Case 3R).

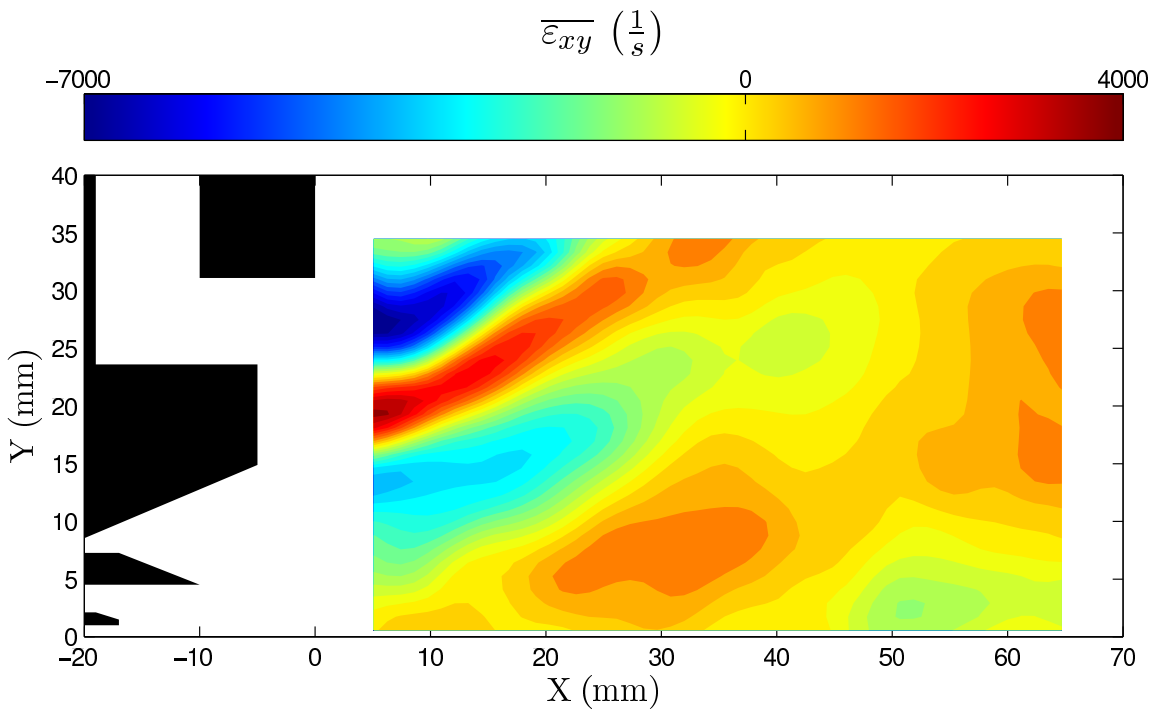

(a)

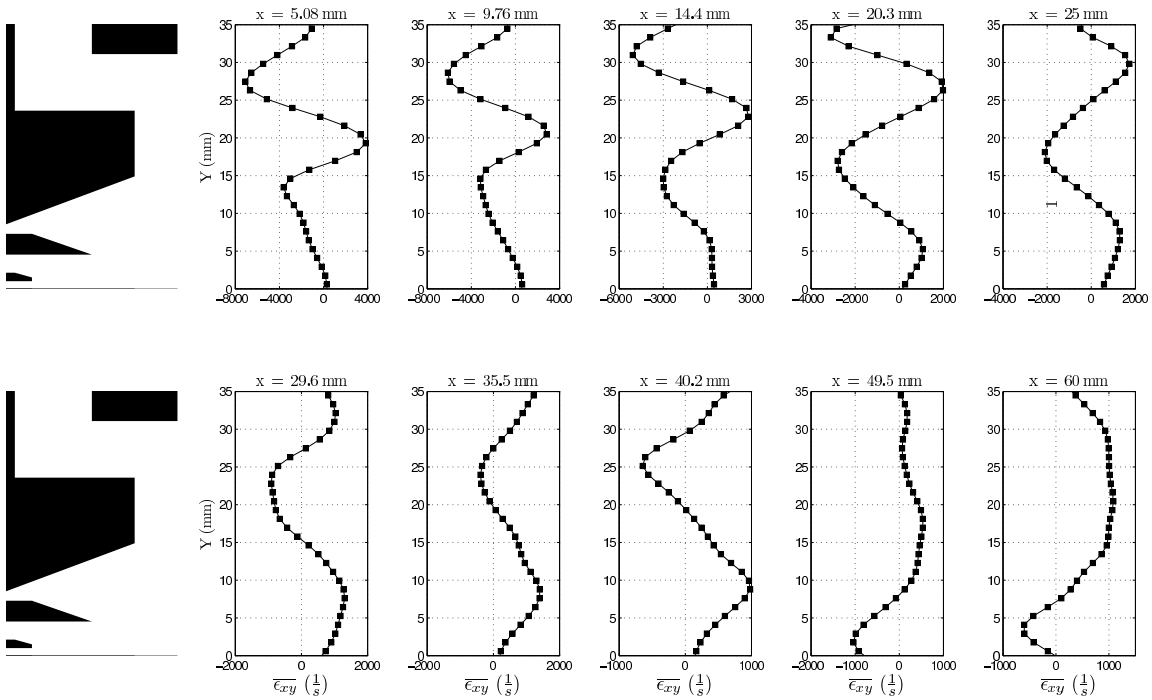

(b)

Figure 4.20: Contour plot and profiles of the shear strain rate for the reacting flow field (Case 3R).

this region shows strong similarity to flows over cavities (Lin and Rockwell (2001), Ukeiley and Murray (2005), Ashcroft and Zhang (2005), and Rasmussen (2006)) with one central vortex and upstream flow in the lower half of the cavity. It is also known that the flow over a cavity resembles a classical mixing layer where two streams of differing velocities merge to form an unconfined shear layer.

For obtaining a first order insight into the complicated flow field present in the TAPS combustor, classical theories of mixing layer growth were applied to the small region between the pilot flow and PRZ. For the purposes of this analysis, it was assumed that the pilot flow represents a constant velocity free-stream and the PRZ represents a cavity (or the second stream in a mixing layer) with a velocity equal to zero. First, the coordinates were rotated as shown in Fig. 4.21a such that $v \approx 0$ in the free-stream and that $\partial u/\partial x' \gg \partial u/\partial y'$. This rotation also places the geometry in the reference frame of a classic mixing layer. As can be seen, some errors are introduced from the fact that the pilot flow does not issue at a constant angle and therefore no one angle of rotation works throughout the mixing layer. Nevertheless, since the purpose of this analysis is to obtain an understanding through classic understandings of a canonical flow, this fact can be ignored. As shown in Fig. 4.21b, the velocity profiles at select downstream locations bear strong resemblance to the velocity profiles in a mixing layer.

The thickness of the mixing layer was defined as

$$\delta_\omega = \frac{U_1 - U_2}{\left(\frac{\partial U}{\partial y}\right)_{max}}, \tag{4.15}$$

following Brown and Roshko (1974). This thickness avoids an arbitrary definition of the edge of the layer (as would be done for δ of a jet) and is commonly referred to as the vorticity thickness. From this, the growth rate of the mixing layer is also

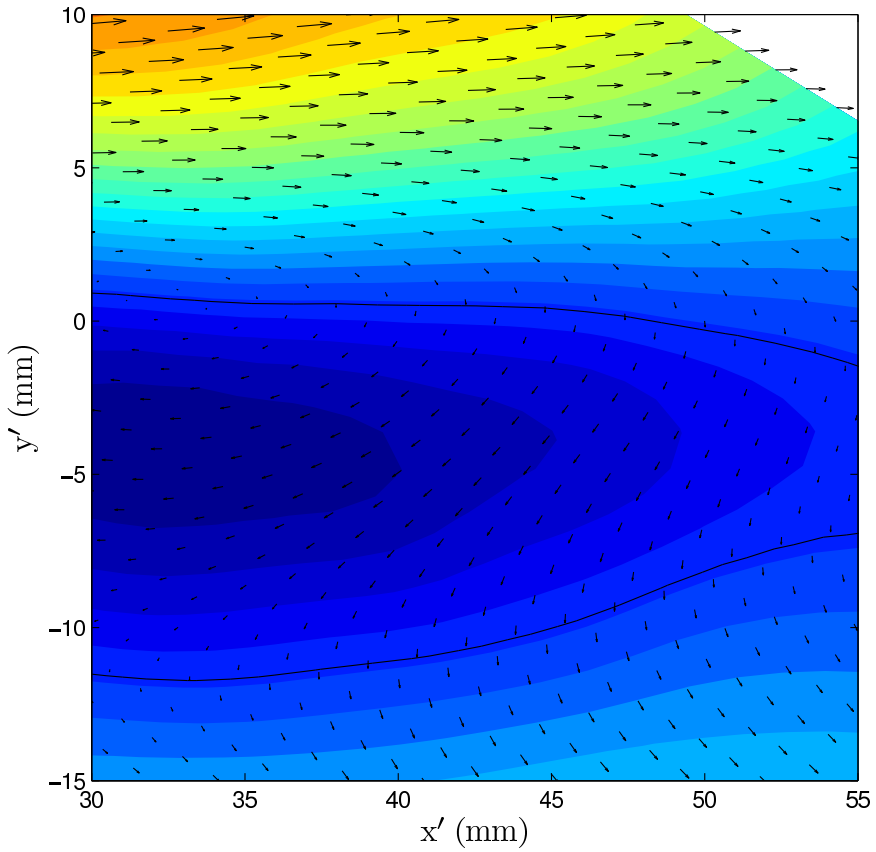

(a) Contours of $\overline{U}$ for Case 1R in the rotated reference frame.

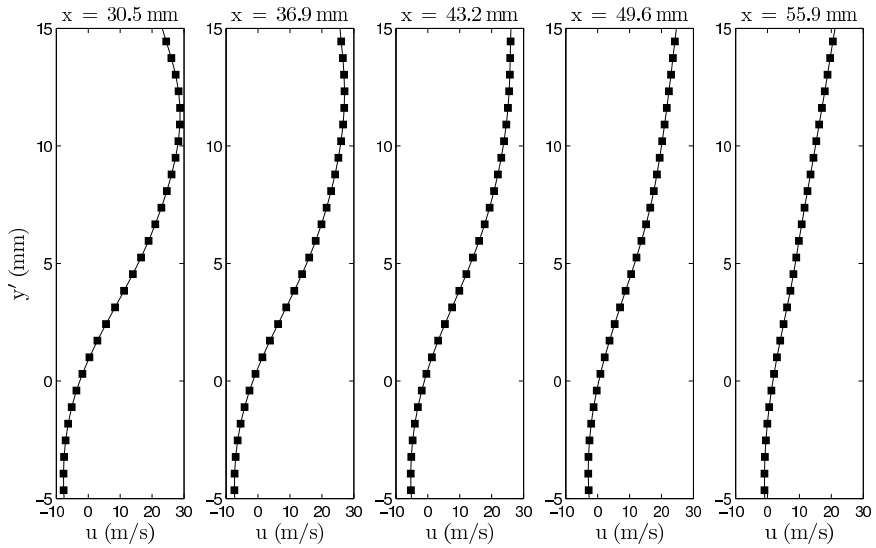

(b) Profiles of axial velocity at select x' locations.

Figure 4.21: The mean velocity field for Case 1R in the rotated reference frame. The profiles of velocity show the mixing layer between the pilot flow and PRZ.

computed as

$$\delta'_{\omega} = \frac{d\,\delta_{\omega}}{d\,x}. \tag{4.16}$$

Dimotakis (1986) gives the growth rate as a function of the density ratio ($s = \rho_2/\rho_1$) and the velocity ratio ($r = U_2/U_1$) by

$$\delta'_{\omega} = C_{\delta}\left(\frac{1-r}{1+r\sqrt{s}}\right)\left[\left(1+\sqrt{s}\right) - \frac{1-\sqrt{s}}{1+2.9\,(1+r)\,/\,(1-r)}\right], \tag{4.17}$$

where C_{δ} is an empirically determined constant. Slessor et al. (2000) suggest a value of $C_{\delta} = 0.18$ that successfully collapses the data from a number of researchers. For flow over a cavity, and the flow here, $U_2 = 0$ and therefore $r = 0$.

The vorticity thickness of the mixing layer in the region shown in Fig. 4.21a is given in Fig. 4.22 for Case 1R. From Eqn. 4.17 it can be seen that for constant density and velocity ratios, the thickness should increase linearly (δ'_{ω} = constant). Clearly, the mixing layer between the pilot and the PRZ does not grow linearly as also evidenced by Fig. 4.23. There is a near constant growth rate from about $x' = 30$ mm to $x' = 45$ mm, after which point the growth rate increases. This non-constant growth rate can be explained by the erroneous assumption that the density ratio (s) is constant across the streamwise direction. In the reacting case shown here, a flame exists in the pilot flow and hot products from the pilot are entrained into the PRZ. These hot products travel upstream and are cooled along the process. Due to the streamwise change in temperature, the assumption of a constant density ratio is erroneous. In fact, using the data shown in Fig. 4.23 and Eqn. 4.17, the density ratio can be backed out. Shown in Fig. 4.24 is the density ratio computed from Eqn. 4.17. It can be seen from the figure that the density ratio near the tip of the flame is around six, which is typical of densities across flame fronts. Closer to the base of the flame, the density ratio is less than one, indicating that the free-stream is hotter

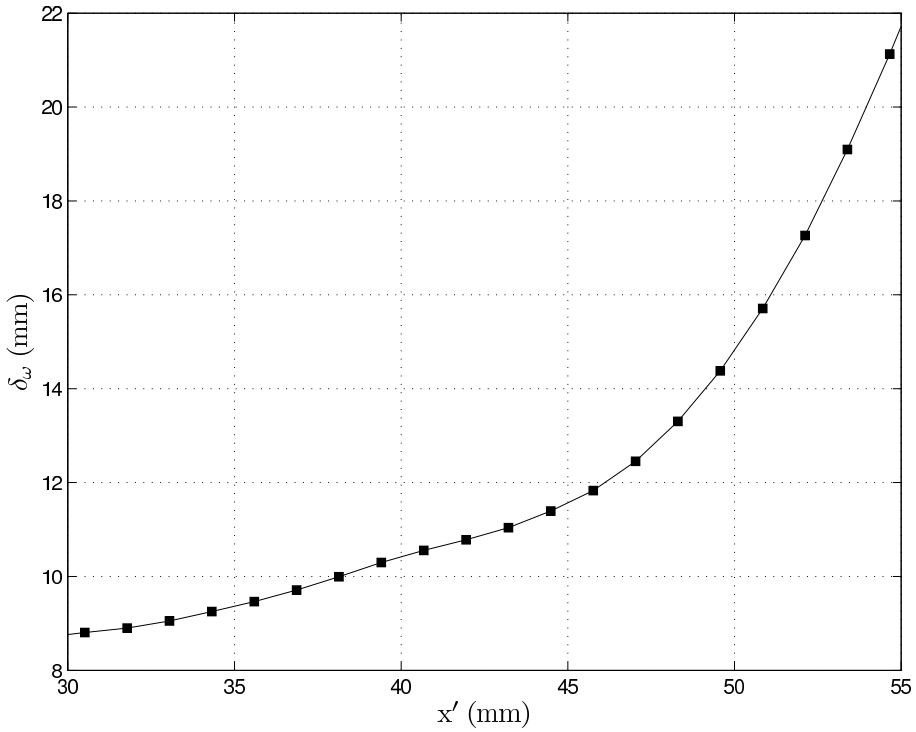

Figure 4.22: The vorticity thickness of the mixing layer.

than the fluid in the PRZ. This too is valid since the free-stream contains the pilot flame while the fluid in the second stream is a mixture of fresh air and hot products that have cooled. It must be stressed that a number of assumptions have been made in this analysis starting from the assumption that a shear layer in a complicated gas turbine combustor can be modelled as a classical mixing layer.

Clearly, there are errors associated with all the assumptions, however, the analysis done here is meant to provide a means of understanding what is otherwise a very complex flow field. By modelling an important feature in the combustor as a canonical turbulent shear flow, we see that a number of important concepts do carry over. The growth of the shear layer is consistent with simpler mixing layers if corrections are made for the varying density. Though the final profile of the density ratio shown in Fig. 4.24 is no better than an empirical curve fit, the numbers are consis-

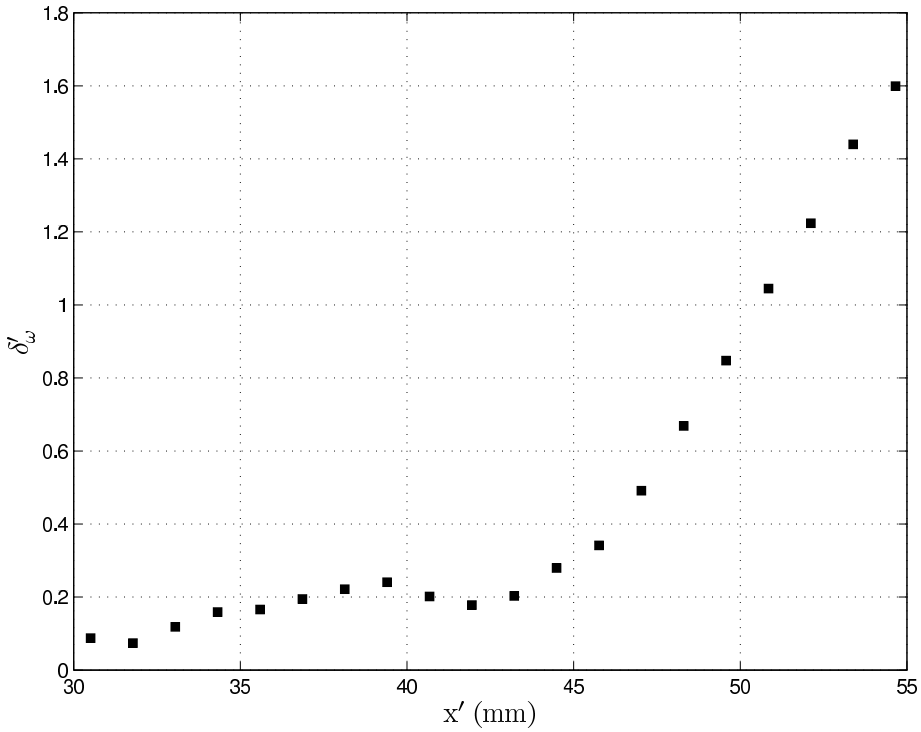

Figure 4.23: The growth of the mixing layer.

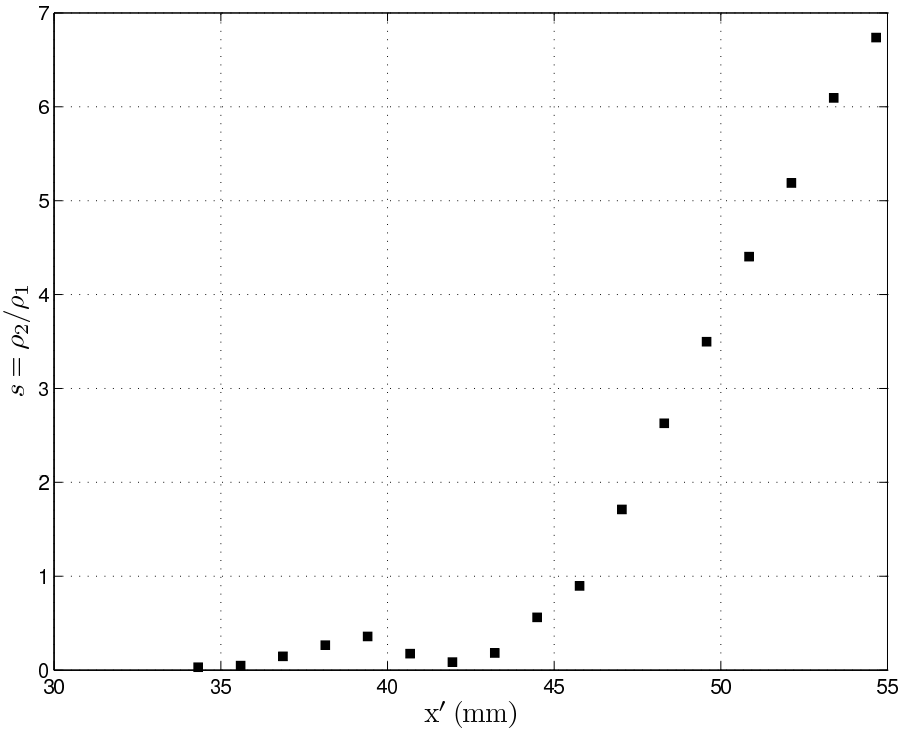

Figure 4.24: The density ratio across the mixing layer.

tent with expectations. This suggests that this model can be used to extend other well known results from mixing layers or flow over cavities to the TAPS combustor. For example, the mass entrainment into the mixing layer is well understood (Brown and Roshko (1974) and Dimotakis (1986)) and can be used to understand the mass entrainment of products into the PRZ. Also, combustor instabilities continue to be a major problem for all LPP combustors (see §1.2.3) and periodic vortex shedding and vortex flame interactions are some of the most dominant mechanisms of acoustic instabilities. The analysis here suggests that the oscillations observed over cavities (Rockwell and Naudascher (1978) and Howe (1997)) can be used as a first order approximation for the frequency of acoustic instabilities in combustors.

4.3.2 Instantaneous Flow Field

An important finding of this study has been the fact that there is considerable structure in the flow that is masked in the average results shown earlier (§4.3.1). Shown in Fig's. 4.25-4.28 are four randomly selected vector plots of the reacting case. To better highlight the structures, the mean flow has been subtracted from the instantaneous velocity measurements in the top panel (a) in all figures. In this manner, the average bulk convection velocity has been subtracted which allows for individual features to be visualized independently. The average flame contour is also overlayed on all the vector plots to provide an idea of the location of the pilot flame. It must be stressed that simultaneous measurements of velocity and flame location are needed for an accurate understanding of turbulence-chemistry interactions. Nevertheless, the location of the average flame contour does provide for some idea of the flow in the vicinity of the flame.

Immediately apparent from all four images is the level of detail present in the

instantaneous images that is not present in the average. Two important types of flow structures, namely vortices and stagnation points, are observed. The vortices appear as distinct regions of swirling flow where the streamlines spiral into or out of one coordinate. This is best seen for example at $(x, y) = (15, 20)$ mm in Fig. 4.27a where a vortex rotating CCW exists in the middle of the flame. Similarly, in Fig. 4.28a a number of vortices of both positive and negative vorticity exist on either side of the flame contour. These vortices transport hot products and fresh reactants and aid in the stability of the flame. These vortices also lead to an enhanced flame surface area due to their ability to stretch and wrinkle the flame surface. The other type of structure observed was a stagnation point or opposed flow. This type of flow as seen for example at $(x, y) = (12, 10)$ mm in Fig. 4.26a is similar to a classic opposed diffusion flame. Correctly modelling the associated strain rates therefore becomes important in aiding our understanding of local extinction and flame blowout in such complex geometries. Structural details such as these are also seen away from the flame in the PRZ and other regions in all four images. Also, at any instant in time, the flow around the inner edge of the flame is seen to be either issuing into the flame (Fig. 4.25a) or away from it (Fig. 4.27a).

The level of detail is also obvious from the vorticity contours of the selected snapshots as shown in Fig's. 4.25b-4.28b. The color scale has been set to the same color scale used for the average vorticity plot (Fig. 4.19) to allow comparison between the average and instantaneous results. The instantaneous vortices are not only higher in number but also in magnitude. In the region in and downstream of the PRZ, the average contours and profiles suggest an almost trivial value of vorticity. The instantaneous images however show that in fact there exist many individual eddies of opposite sign. These eddies convect at the local velocity and therefore over a

sufficient number of samples cancel each other out, leading to a trivial result for $\overline{\omega_z}$. This fact presents a problem to average based models such as RANS where only the mean quantities are computed. Any such model would erroneously conclude that the flow field has negligible vorticity and structure.

4.3.2.1 Instantaneous Recirculation Zone

The above results suggest that the average recirculation zones are also possibly misleading. To assess this, the area of the the recirculation zones was computed by measuring the area of the field of view in which the axial velocities are negative. Since PIV data is naturally discretized by the interrogation windows, this task was accomplished by counting the number of interrogation windows that had $U < 0$. This was done for all the instantaneous images and separately for the average image. The PDF of the recirculation zone area is shown in Fig. 4.29 with the data shown by the solid markers. A Gaussian distribution with the same mean and standard deviation has also been fit to the data. The mean from the instantaneous images is seen to be 619 mm^2 while the area computed from the average image is only 456 mm^2, which is almost one standard deviation less than the actual mean value. As the PRZ is a critical feature in swirl combustors and is important in the stability of the flame, its area is a vital parameter in the combustor's design. It was shown by Gouldin et al. (1985) that the mass that is recirculated by the PRZ is directly proportional to its size. This means that an inaccurate prediction of the PRZ size would also lead to an erroneous result for the total mass of hot products being recirculated, leading to discrepancies in the prediction of the flame behavior. Since the average shape and size of the recirculation zones were obtained by averaging the velocities (and not the areas), this discrepancy can be attributed to the instantaneous values of velocity

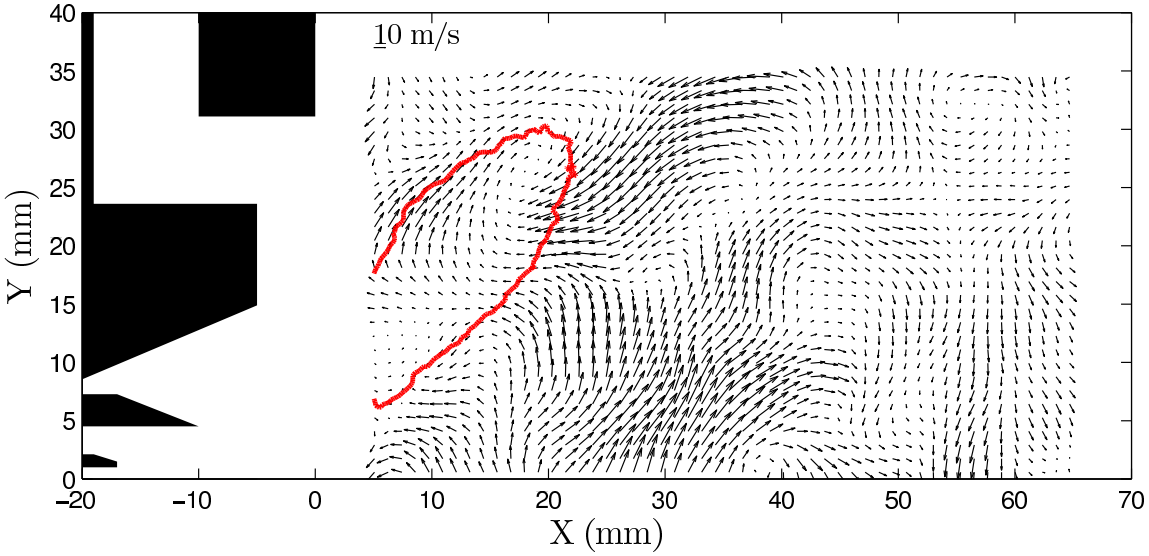

(a) An instantaneous fluctuating velocity field with the average flame contour overlayed.

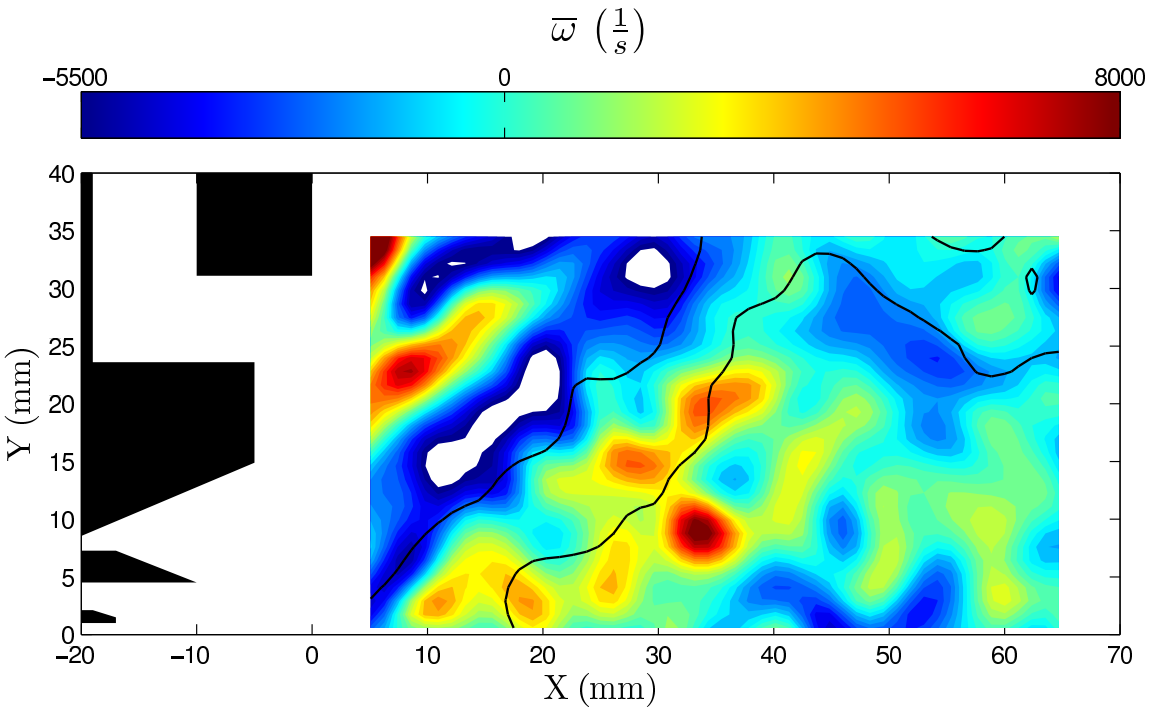

(b) Contours of the instantaneous vorticity field with the edge of the instantaneous recirculation zones overlayed for the same instance shown in (a)

Figure 4.25: A randomly selected instantaneous velocity field for the reacting case (Case 3R).

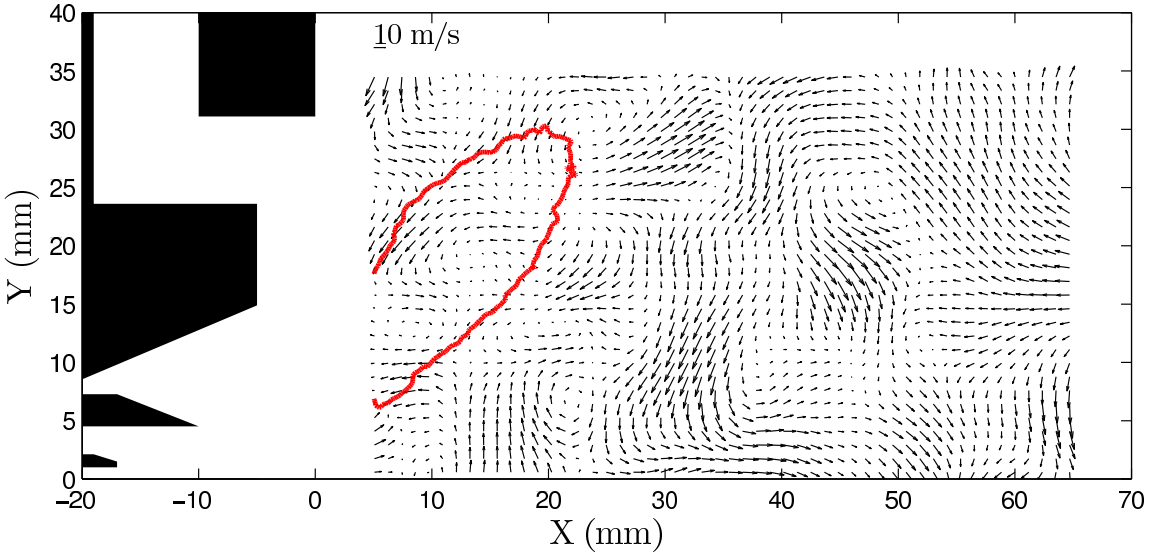

(a) An instantaneous fluctuating velocity field with the average flame contour overlayed.

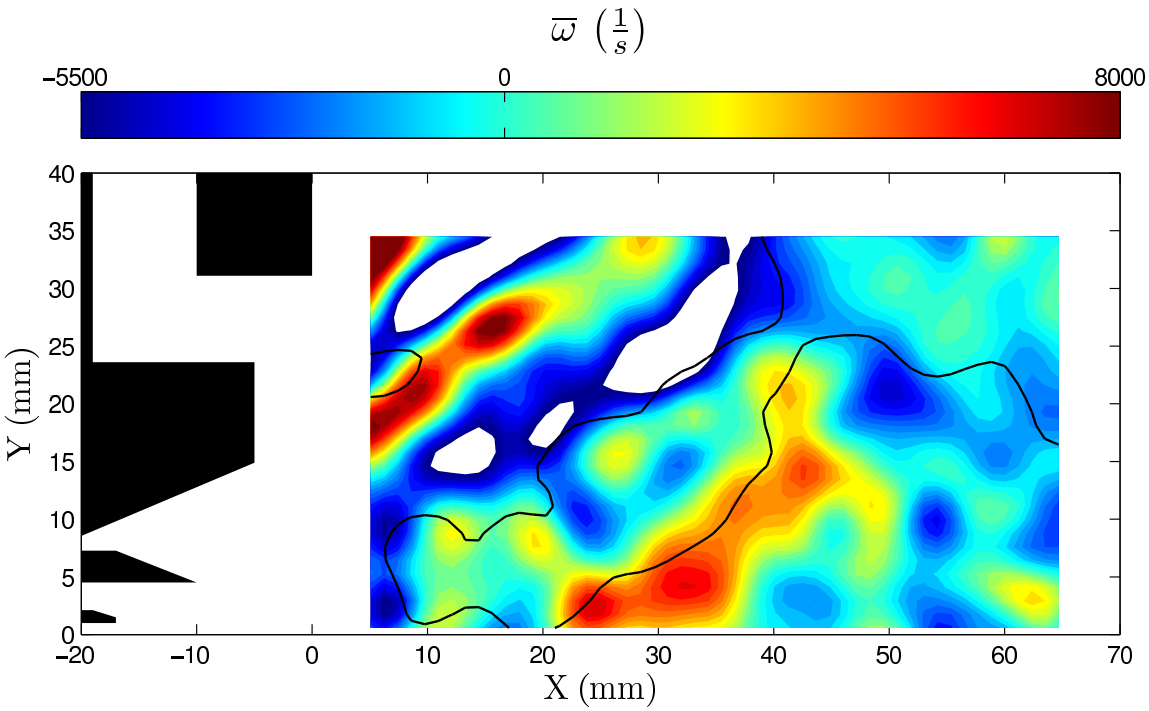

(b) Contours of the instantaneous vorticity field with the edge of the instantaneous recirculation zones overlayed for the same instance shown in (a)

Figure 4.26: A randomly selected instantaneous velocity field for the reacting case (Case 3R).

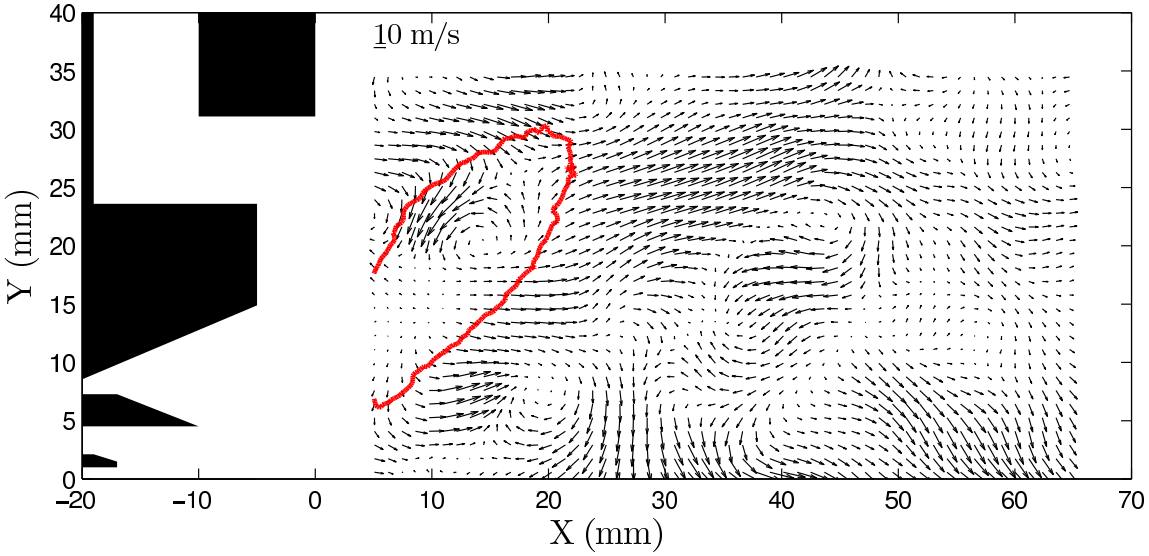

(a) An instantaneous fluctuating velocity field with the average flame contour overlayed.

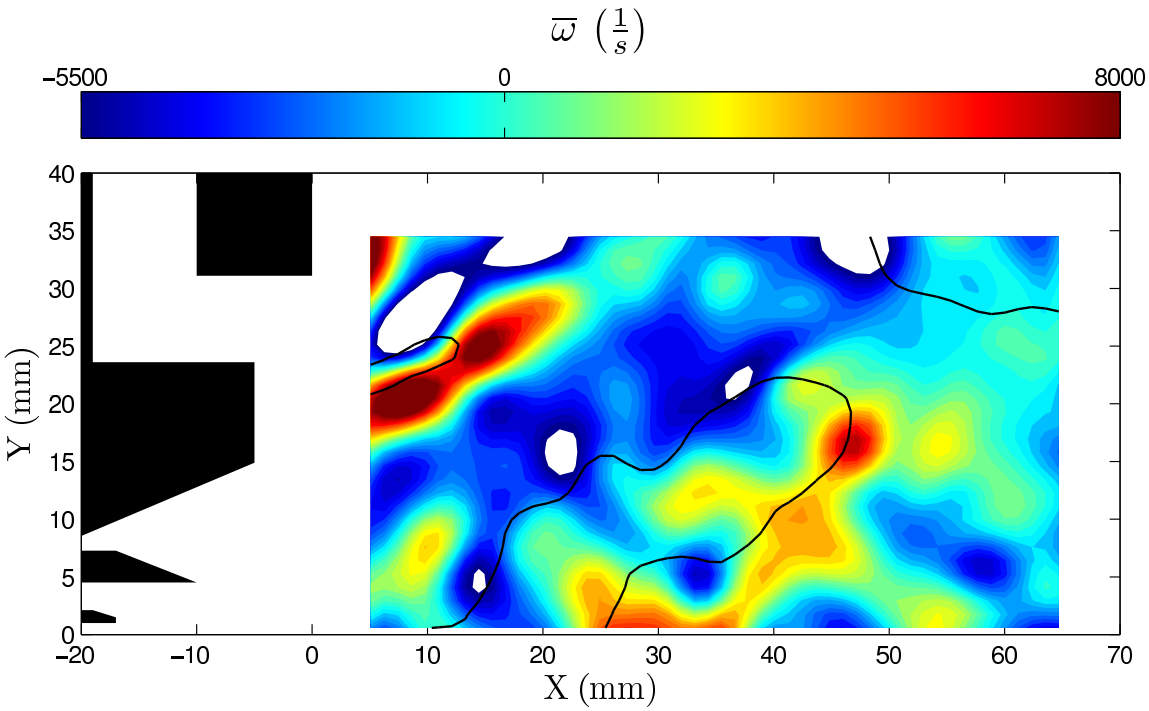

(b) Contours of the instantaneous vorticity field with the edge of the instantaneous recirculation zones overlayed for the same instance shown in (a)

Figure 4.27: A randomly selected instantaneous velocity field for the reacting case (Case 3R).

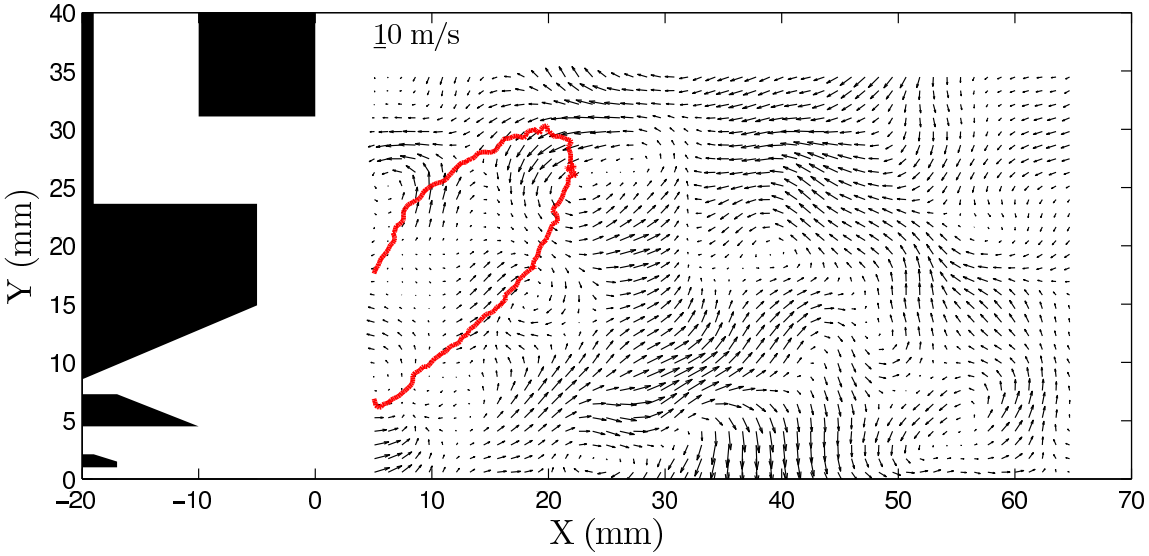

(a) An instantaneous fluctuating velocity field with the average flame contour overlayed.

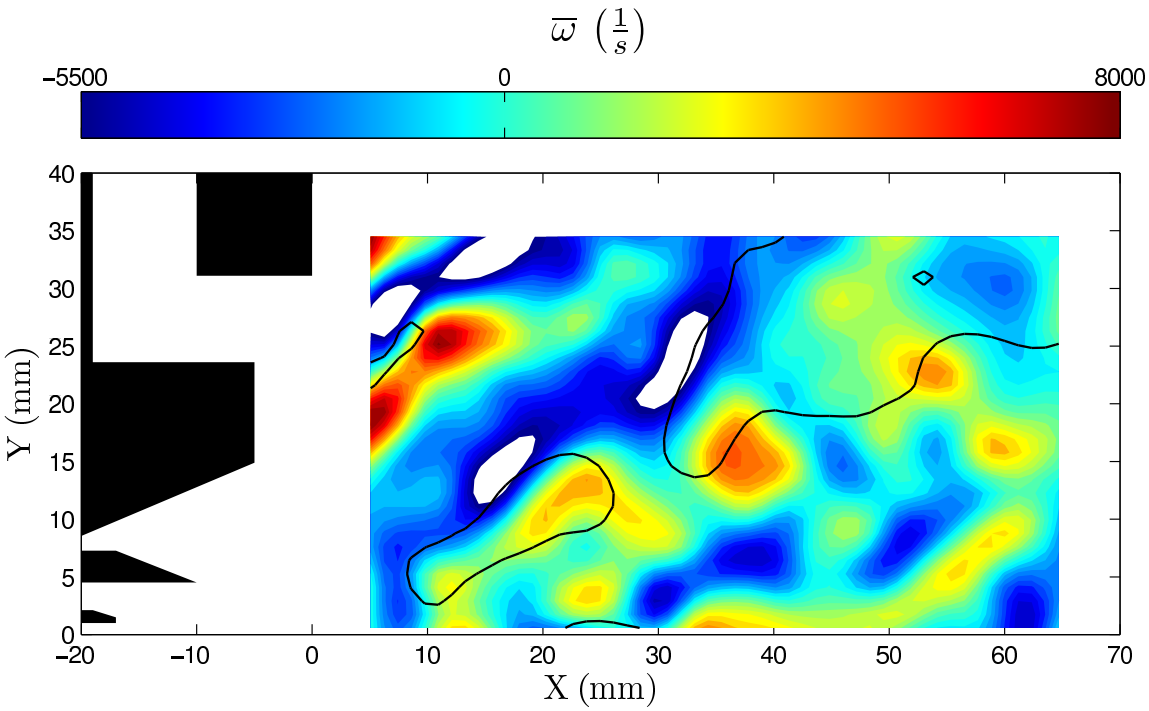

(b) Contours of the instantaneous vorticity field with the edge of the instantaneous recirculation zones overlayed for the same instance shown in (a)

Figure 4.28: A randomly selected instantaneous velocity field for the reacting case (Case 3R).

around the PRZ.

A discrepancy in the area would arise if the axial velocities around the edge(s) of the recirculation zones have a higher magnitude when they are positive than when they are negative. Therefore, on average, the velocity at a point may be positive whereas there may be many instances when the axial velocity at that location is indeed negative. This behavior would lead to a skewness in the PDF of the axial velocity. A skewness should physically be expected since there exists a mechanism that drives high positive axial velocities but not vice versa. It was shown that the heat release from the flame causes an acceleration of the gases. Therefore, fluctuations in the heat release from the flame would drive large positive fluctuations in the axial velocity. As the flame relaxes, the velocity would relax to some steady value, however it would not relax to as high a negative velocity. This mechanism would naturally lead to a difference in the magnitudes of the positive and negative velocities, causing a skewness in the PDF of U. The instantaneous axial velocities were probed at four locations on the border of the average PRZ. These locations are denoted by the solid markers in the top of Fig. 4.30. The PDF of the axial velocity at these four locations are shown in the bottom panel of Fig. 4.30 along with their coordinates. As can be seen from the Gaussian fits to the data, a normal distribution appears to be a close fit to the data but naturally does not capture the skewness present in the PDF's. The third moment, or skewness, of the PDF at each location is listed below the corresponding PDF and is positive at all four representative locations. This means that there are instances of high positive axial velocity (without a corresponding instance of high negative axial velocity) that skew the average results towards a smaller recirculation zone than actually present. This result further illustrates that models relying upon averaged quantities will fail at accurately representing the physics of

a swirl combustor. Furthermore, these results also suggest that Gaussian statistics may not be the best choice for describing certain flow features. It is suggested that accurately predicting the skewness in the velocity is an important parameter for any model. The skewness in the PDFs leads to the particular result for the recirculation zone area shown in Fig. 4.29 and captures the unsteady acceleration of the flow from heat release.

4.4 Reacting Flow Field - Pilot and Main

Case 4 listed in Table 4.1 does not fall on the engine operating line and was chosen as a representative case for the stable operation of both a pilot and a main flame. The flowrates, temperature, and pressure were the same as Cases 2Pt and 2Main listed in Table 3.3 to allow the mean flame contour to be directly applicable to the mean flow field presented in this section.

4.4.1 Pilot Only Mean Flow Field

In general, the flow field of Case 4P was very similar to the other pilot only reacting cases that have been discussed earlier. As shown in Fig. 4.31, a few differences exist between the mean flow field shown in Fig. 4.14 and the mean flow field of Case 4P. The biggest difference is in the size and shape of the PRZ where it now appears to be one large toroidal zone instead of having one small oval shaped zone and another zone in the top right of the field of view. The two zones previously were separated by a region of low positive axial velocities which effectively broke the PRZ. With the reduced heat release (Case 4P had the lowest pilot fuel flowrate), the PRZ is no longer broken up. However, the positive axial velocities along the centerline are still present and the effect of the heat release on vortex breakdown is still apparent. The other mean gradient and turbulence quantities of interest are very similar to the

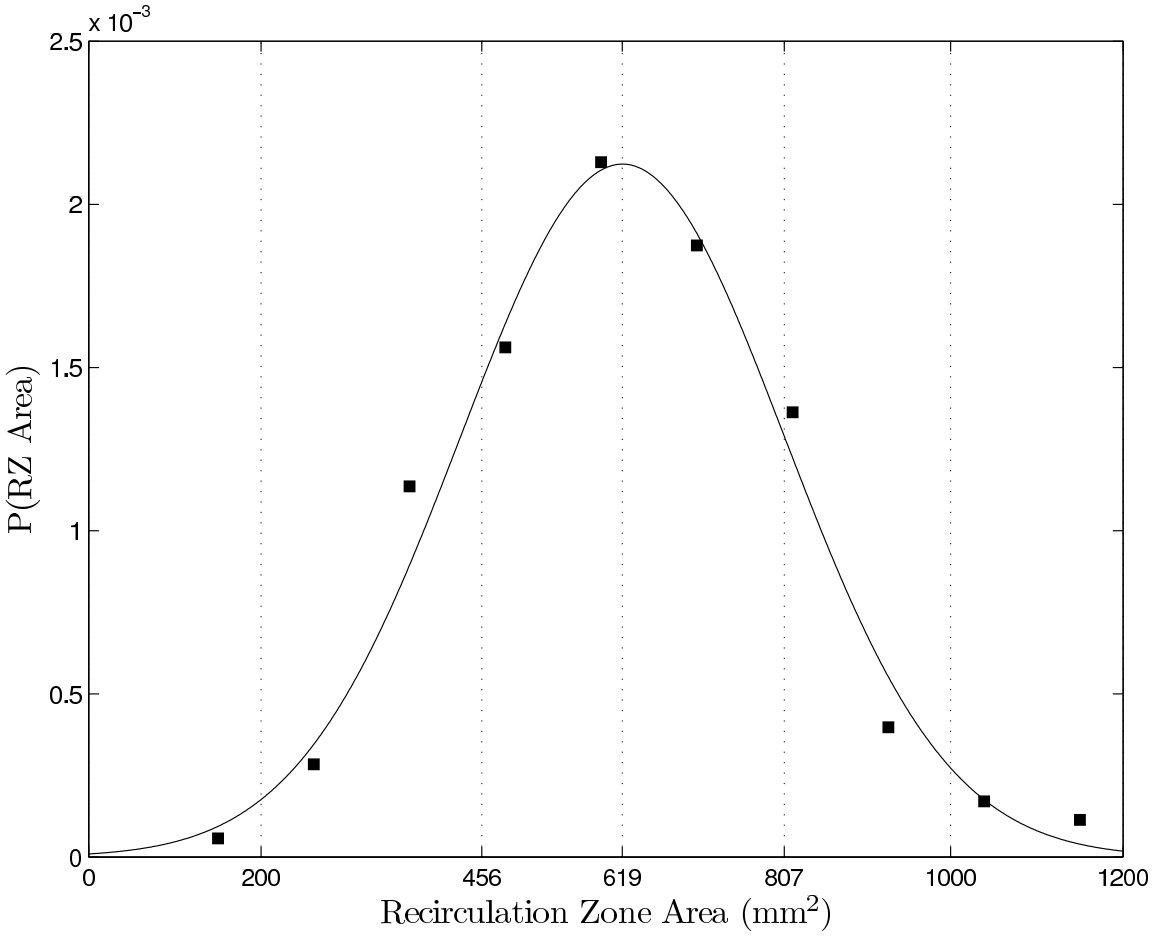

Figure 4.29: PDF of the area of the recirculation zone(s) in $x \in (5, 66), y \in (-5, 36)$ shown by the solid markers. The mean of the instantaneous areas is 619 mm^2 while the recirculation zone area of the average flow field is 456 mm^2. The line is a normal (Gaussian) distribution with the same mean and standard deviation (188 mm^2) as the data.

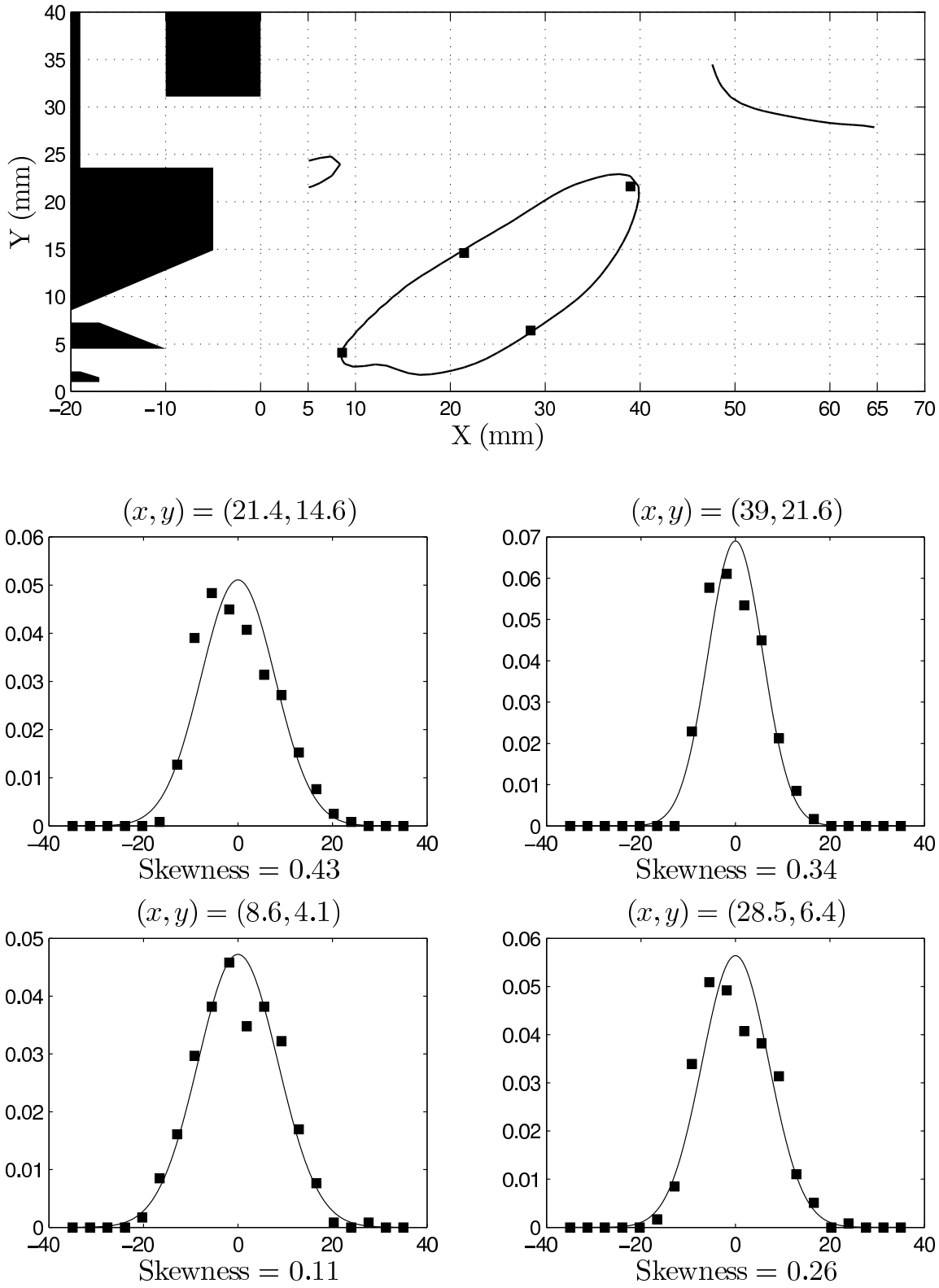

Figure 4.30: PDF of the axial velocity at select locations around the PRZ as marked by the symbols in top. The lines are Gaussian fits to the data. The third moment (skewness) at each location is given below each plot in bottom.

results presented earlier for the reacting case and therefore are not presented here.

4.4.2 Pilot and Main Mean Flow Field

Shown in Fig. 4.32 are the mean flow field results for Case 4M which had both pilot and main combustion. This case was chosen to study the effects of heat release in the main annulus. As was seen in §3.1.2 and §3.2, the main flame has large similarities to a jet flame issuing from the main annulus. Due to the proximity of the pilot flame, the pilot and main flames merge to form what is effectively a longer pilot flame. This effect is apparent in the mean flow field where there are only minor differences between the flow field shown in Fig. 4.31 for Case 4P and the flow field shown in Fig. 4.32 for Case 4M. The PRZ is largely unaffected by the presence of the main flame suggesting that the PRZ is defined by the swirl geometry and location of heat release only. The total fuel flowrate (the sum of pilot and main fuel flowrates) in the combustor at Case 4M was the highest amongst all cases studied. Yet, even with the increased fuel flowrates, the PRZ is virtually unchanged when main fuel is added. This result implies that the PRZ is largely a function of only the location of the pilot flame and the localized gas expansion caused by the pilot flame. The high radial velocities in the main flow quickly convect the hot gases generated by the main flame out of the present field of view. It is expected that the heat release from the main flame affects the flow in the regions of the combustor not captured due to the limited field of view. For example, the heat release from the main flame is likely to affect the Corner Recirculation Zone (CRZ) in the combustor and possibly even the rear stagnation point of the PRZ.

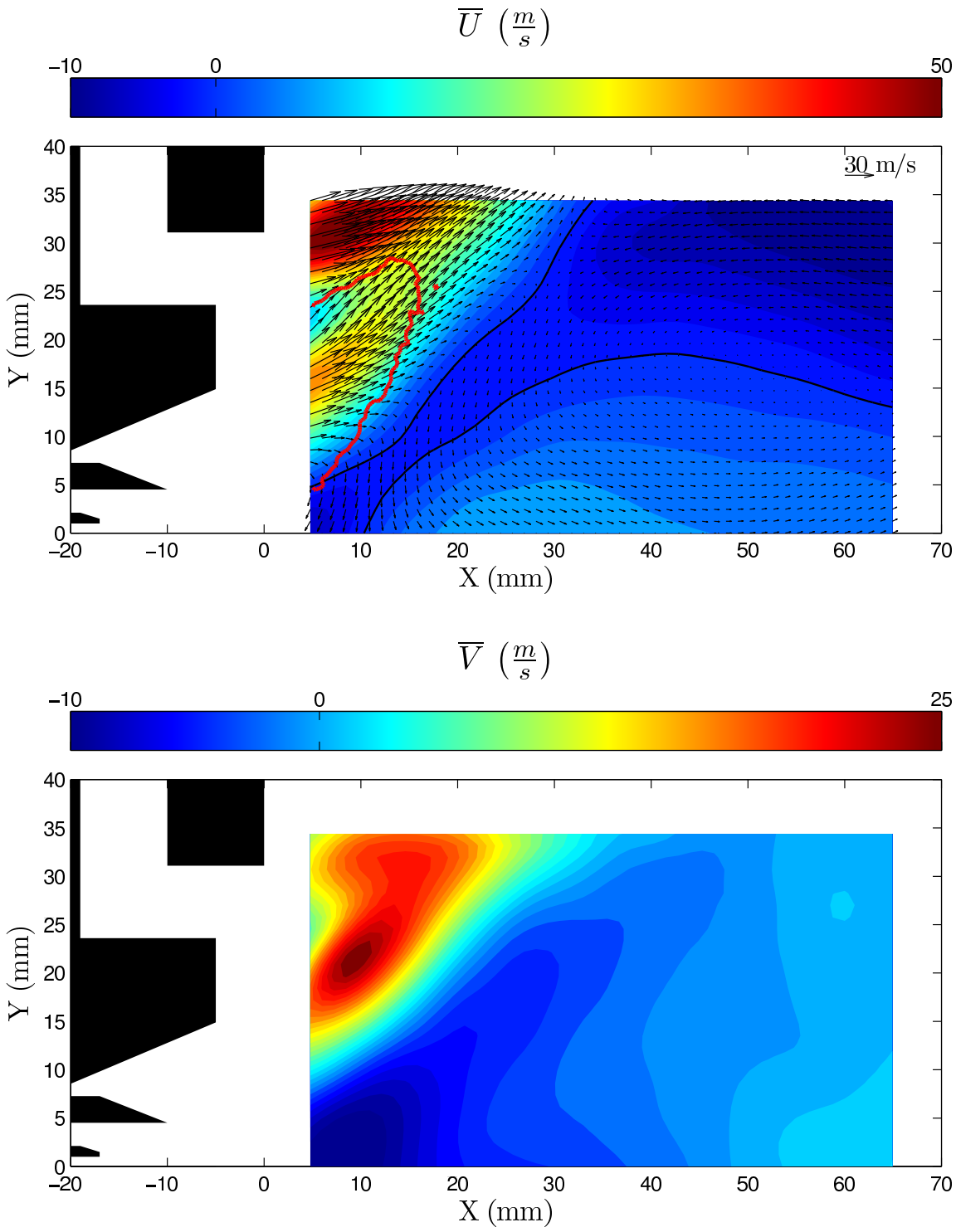

Figure 4.31: Mean flow field of Case 4P. The velocity vectors are overlayed on contours of axial velocity (top). The black lines indicate the edge of the recirculation zone and the solid red line shows the average flame contour from Case 2Pt.

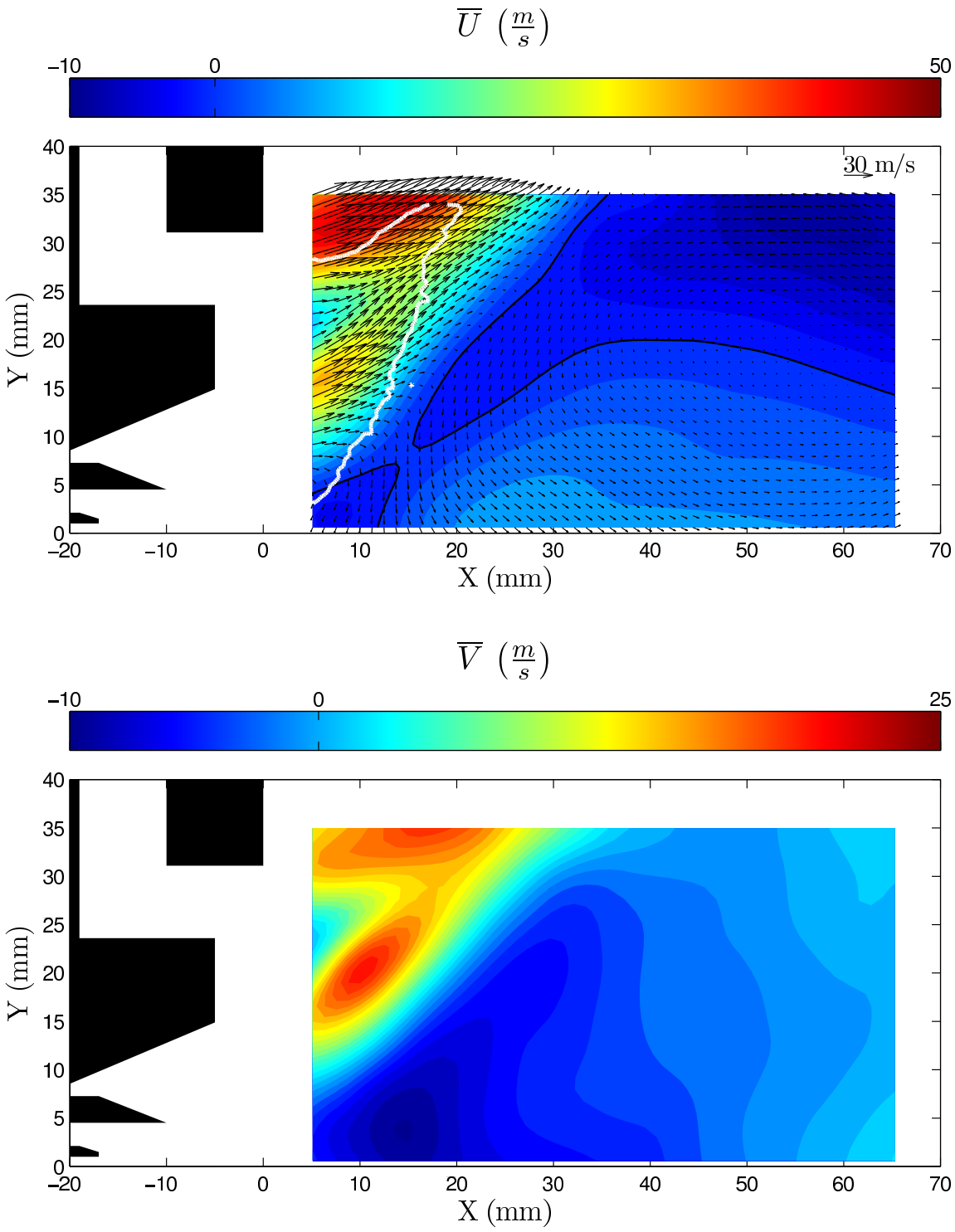

Figure 4.32: Mean flow field of Case 4M. The velocity vectors are overlayed on contours of axial velocity (top). The black lines indicate the edge of the recirculation zone and the solid white line shows the average flame contour from Case 2Main.

4.4.2.1 Turbulence Quantities

The biggest differences between Case 4P and Case 4M are in the turbulence quantities near the main flame. It was seen in the reacting case that the flame reduces both the turbulence intensity and the Reynolds stresses in the vicinity of the flame. The same effect is seen in the main annulus due to the main flame. Shown in Fig. 4.33 are contour plots of $\overline{q}$ for both the pilot only (Case 4P) and pilot and main flames (Case 4M). While the turbulence intensities along the centerline and pilot flame remain unchanged, the turbulence is considerably lower in the main flow. The same is seen in the mean Reynolds stress shown in Fig. 4.34 where the stresses are lower in magnitude in the main flow. This is an important result since both the fuel-air mixing in the main annulus and the stability of the main flame are highly dependent on the turbulence in this region. Though the main flame was not observed to be lifted, these results can be extended to a condition where the main flame would be lifted. Therefore, it can be postulated that the base of a lifted main flame would be anchored in a region of significantly reduced turbulence. This also means that the flame speed at the base of the lifted main flame would be lower and closer to the laminar flame speed.

4.4.3 Instantaneous Flow Field

The mean flow fields presented above hide a number of pertinent details that are important in our understanding of the interactions between the pilot and main flames. A number of different types of interactions were observed in the instantaneous images and will be discussed in this section. First, it was noted in §4.4.2.1 that the turbulence levels in the main flow are very low. This is further demonstrated in the instantaneous images where no major eddies were observed in the main flow. Two

representative instantaneous flow field are shown in Fig. 4.35 where the contours of swirling strength overlaid on top of the velocity vectors highlight the individual vortices in the flow. Similar to the instantaneous images of the non-reacting case (Fig. 4.11), the vortices are at the edges of the recirculation zone and no vortices are observed in the flow issuing from the main annulus. This further supports the hypothesis that any lifted main flame would exist in a fairly uniform flow with low turbulence levels and few interactions with large scale vortices. The main flame however is influenced by interactions with the pilot flame.

Fluid exchange between the pilot and main flames is a vital part of the TAPS combustor and an inherent component of its stable operation. These exchanges are clearly visible when the mean flow field shown in Fig. 4.32 is subtracted from the instantaneous images, leaving a vector plot of the fluctuating velocities. While there were certainly instances as shown in Fig. 4.36 where there was no clear interaction between the pilot and main flows, such instances were rare. In the vast number of images, there was a clear exchange of fluid between the two annuluses. For example, as shown in Fig. 4.37, small eddies often exist near the LRZ (near $(x, y) = (5, 25)$ mm) that convect hot products between the pilot flame and the upstream part of the main flame. Such eddies are undoubtedly important in the stability of the main flame as they provide the high temperatures needed to anchor the main flame. Similarly, Fig. 4.38 shows two sample images where a larger region of flow moving from the pilot into the main flame is visible again near the upstream portion of the main flame.

While flow from the pilot annulus into the main were seen to be commonplace, another important flow motion was present in a large number of images. Here, as shown in Figs. 4.39 and 4.40, there was a large volume of flow from the main annulus

into the pilot. As seen in all four instantaneous images, fluid originating in the main annulus turned towards the centerline to merge with the flow from the pilot annulus. Any flow originating in the main annulus would also carry with it fuel from the main injectors and therefore this fuel would react as part of the pilot flame. This explains the PLIF image seen in Fig. 3.20 where there was evidence of an enhanced pilot flame due to the presence of a main flame. In §5.1, it will be shown that the blowout of the pilot flame is affected by main fuel injection. The instantaneous images shown here confirm that a percentage of fuel injected in the main actually reacts in the pilot flame cone. This result means that there is some percentage of fuel that is otherwise expected to react in a premixed fashion actually reacts as a diffusion flame. This clearly has implications for the total emissions of the combustor along the inherent assumptions regarding the LPP nature of the combustor.

4.5 Flow Asymmetries

The results presented in this thesis for the flow field and flame locations were taken on one half of the combustor plane and assumed an axi-symmetric flow. While the combustor was designed to be nominally axi-symmetric, measurements on both sides of the center plane (both $y > 0$ mm and $y < 0$ mm) indicated marked asymmetries in the measured quantities. These asymmetries can be accredited mostly to the asymmetries in the geometry of the TAPS injector and to a lesser degree the asymmetry in the actual combustor due to the location of the windows. Asymmetries in the flow within the combustor can also be due to non-uniformities in the incoming flow. Since these non-uniformities would lead to artificial asymmetries, care was taken to ensure a symmetric inlet flow field. This was accomplished through the flow conditioning section upstream of the combustor as described in §2.1.1.

The symmetry of the inlet flow was validated with the use of PIV. The TAPS injector and swirl cup were removed, leaving the inner combustor can with a 62.2 mm diameter hole at its inlet. Since the combustor can was not removed, any asymmetries caused by the lack of a fourth window or non-uniformities in the distribution of the cooling air holes were also captured. The inlet conditions were kept constant at $\dot{m} = 0.216$ kg/s, $T_3 = 285$ K, and $p_3 = 1$ bar. The contour plots of the ensemble averaged (of 80 measurements) axial velocity ($\overline{U}$) and radial velocity ($\overline{V}$) are shown in Fig. 4.41 and Fig. 4.42 respectively.

Profiles of the axial velocity taken at select downstream axial locations confirm that the inlet flow is indeed symmetric. Cuts from the field shown in Fig. 4.41 are shown in Fig. 4.43. Direct comparison of the flow on both sides of the centerline is shown in Fig. 4.44 where the axial velocity at one downstream location is shown as a function of the radius from centerline. While there is a slight difference in the velocities at the higher radii, the bulk of the flow agrees very well on both sides. These results indicate that not only is the inlet flow symmetric, but that the effect of non-uniformities in the geometry of the combustor can is negligible. Therefore, any asymmetries in the measured flow are due to the geometry of the TAPS injector.

Though the TAPS injector was designed to be axi-symmetric, the plumbing of the fuel lines and the attachment of the injector to the combustor can necessitated extensions to the injector that spoil the symmetry. As shown in Fig. 4.45, there are three extensions from the injector that go over the swirl cup. The first is the bottom sting that contains the fuel lines. The fuel inlet is at the end of the sting and the fuel lines are plumbed internally to the pilot and main fuel injectors. The other two extensions were welded on to the injector and serve as "arms" that serve the dual purpose of affixing the injector and swirl cup to the combustor can. Since these

extensions go over the swirl cup, they impede the flow of air through the vanes that are covered by the extensions. Therefore, because of the blockage, the flow through all the swirl vanes is not equal. While none of the extensions are over the center plane that the measurements were taken in, they affect the flow in the center plane because of the non-zero azimuthal component of velocity. Since the bulk of the air entering the combustor enters through the swirl cup, this blockage in non-trivial and explains the asymmetries seen in the measurements. While the asymmetry does not alter the physics, thereby allowing measurements to be made on only one half of the combustor, it does pose difficulties for modelling the combustor. If the combustor is modelled as a two-dimensional axi-symmetric geometry (clearly the simpler alternative), making quantitative comparisons to the experiments is not possible. To make direct comparisons, the combustor must be modelled as a full three-dimensional geometry taking into account the blockages caused by the extensions to the injector. Unfortunately, any twin annular configuration with a central pilot such as the TAPS injector will require a fuel sting that will naturally lead to asymmetries in the flow.

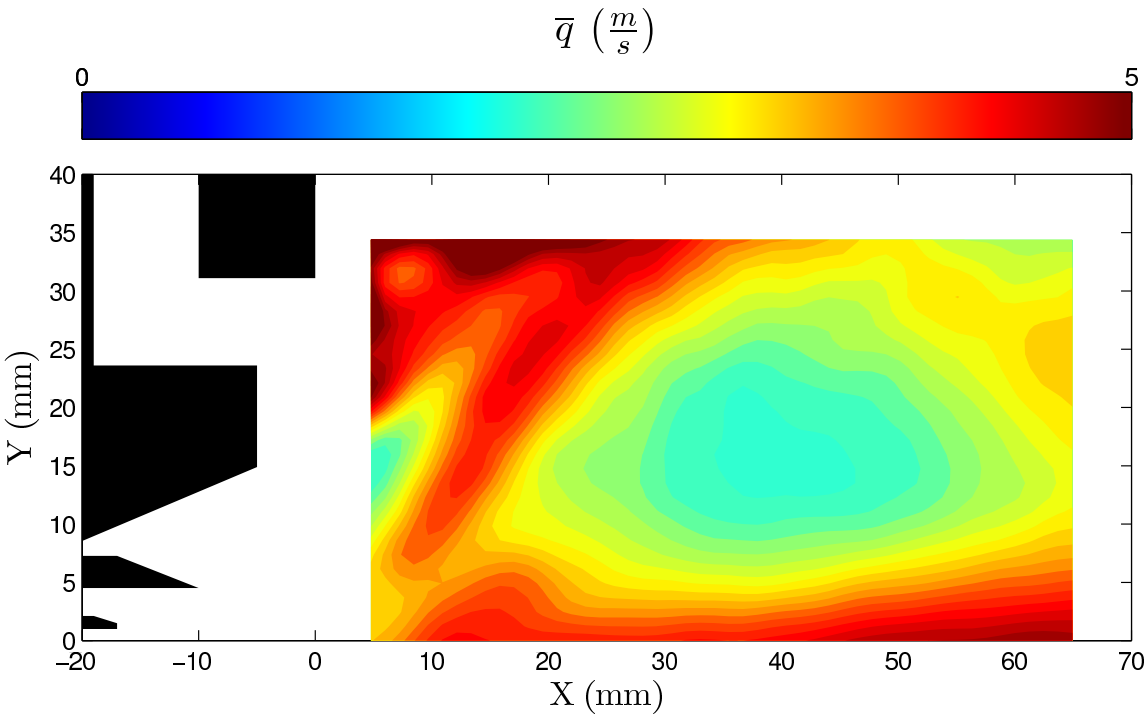

(a) Case 4P

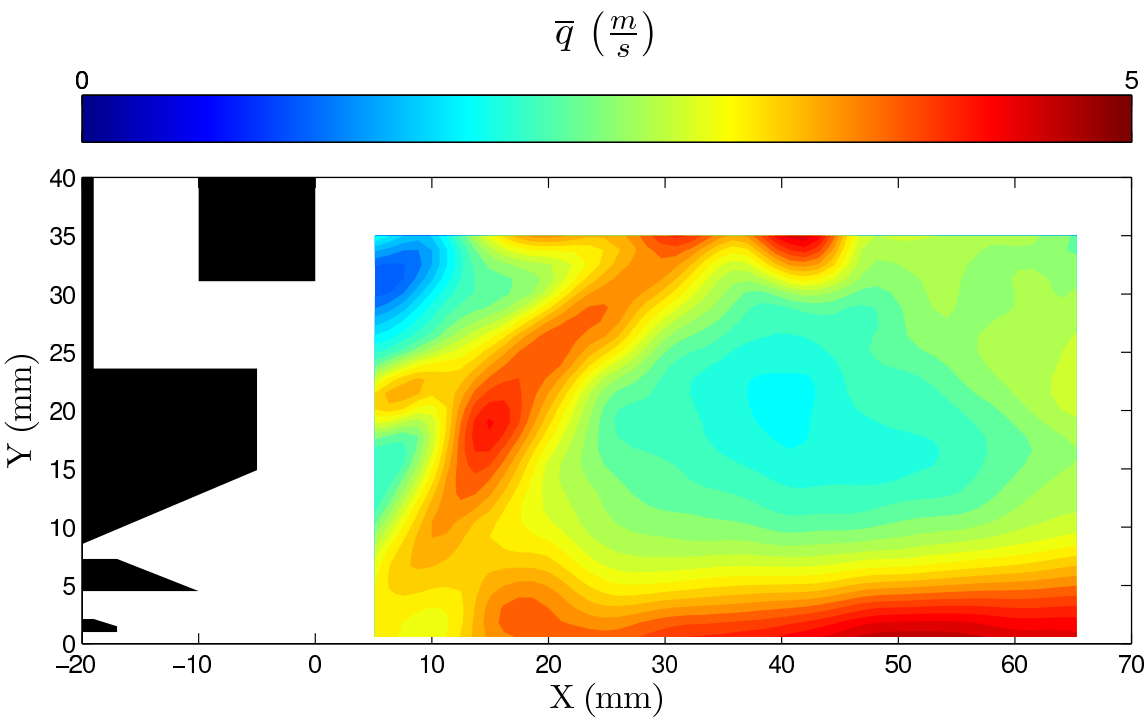

(b) Case 4M

Figure 4.33: Contour plots of the mean turbulence intensity for Case 4P and Case 4M.

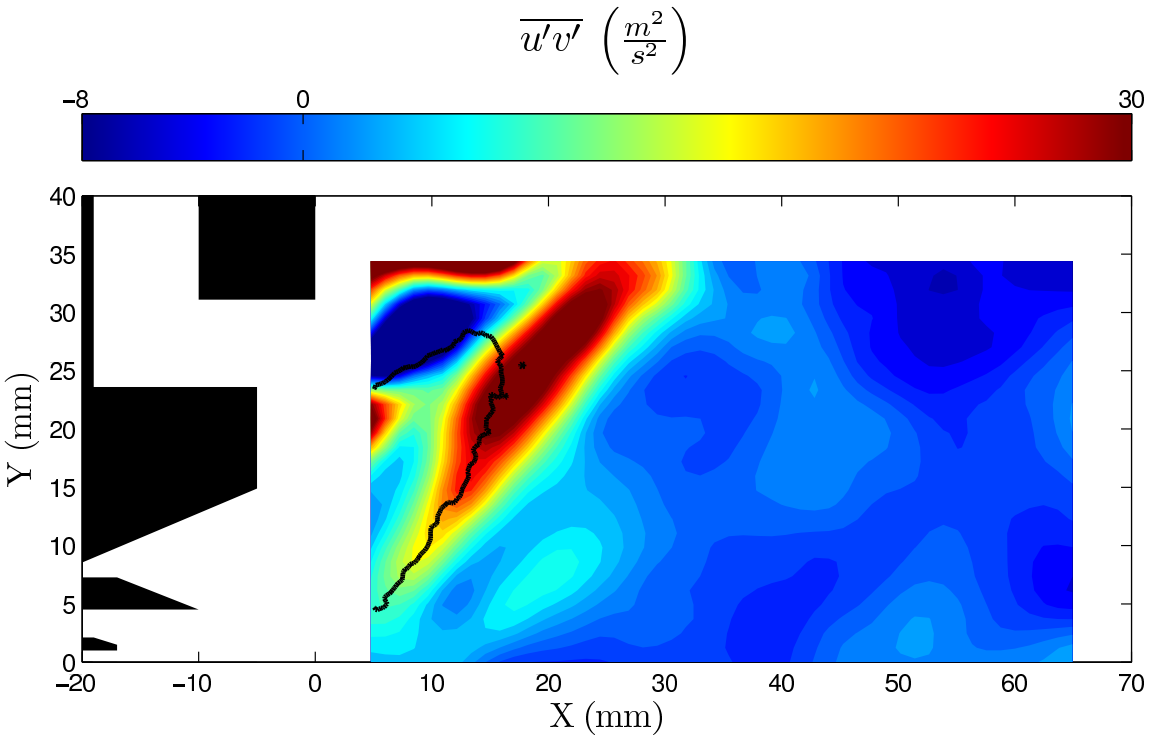

(a) Case 4P

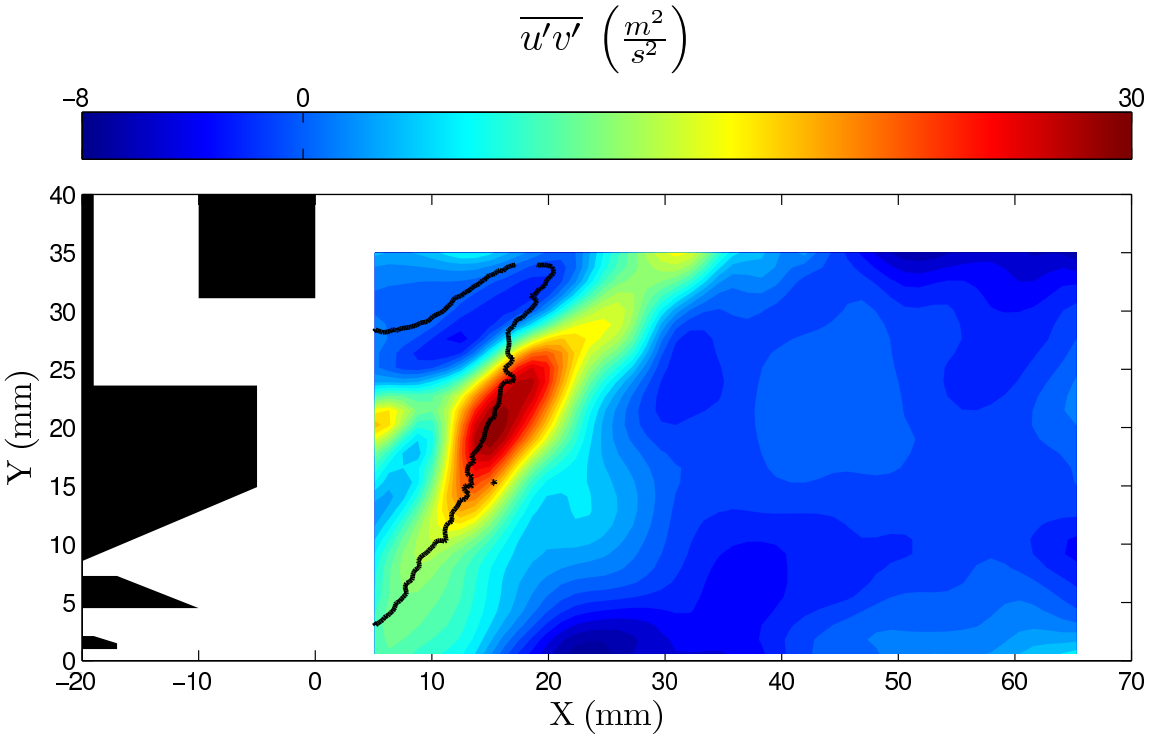

(b) Case 4M

Figure 4.34: Contour plots of the mean Reynolds stress for Case 4P and Case 4M.

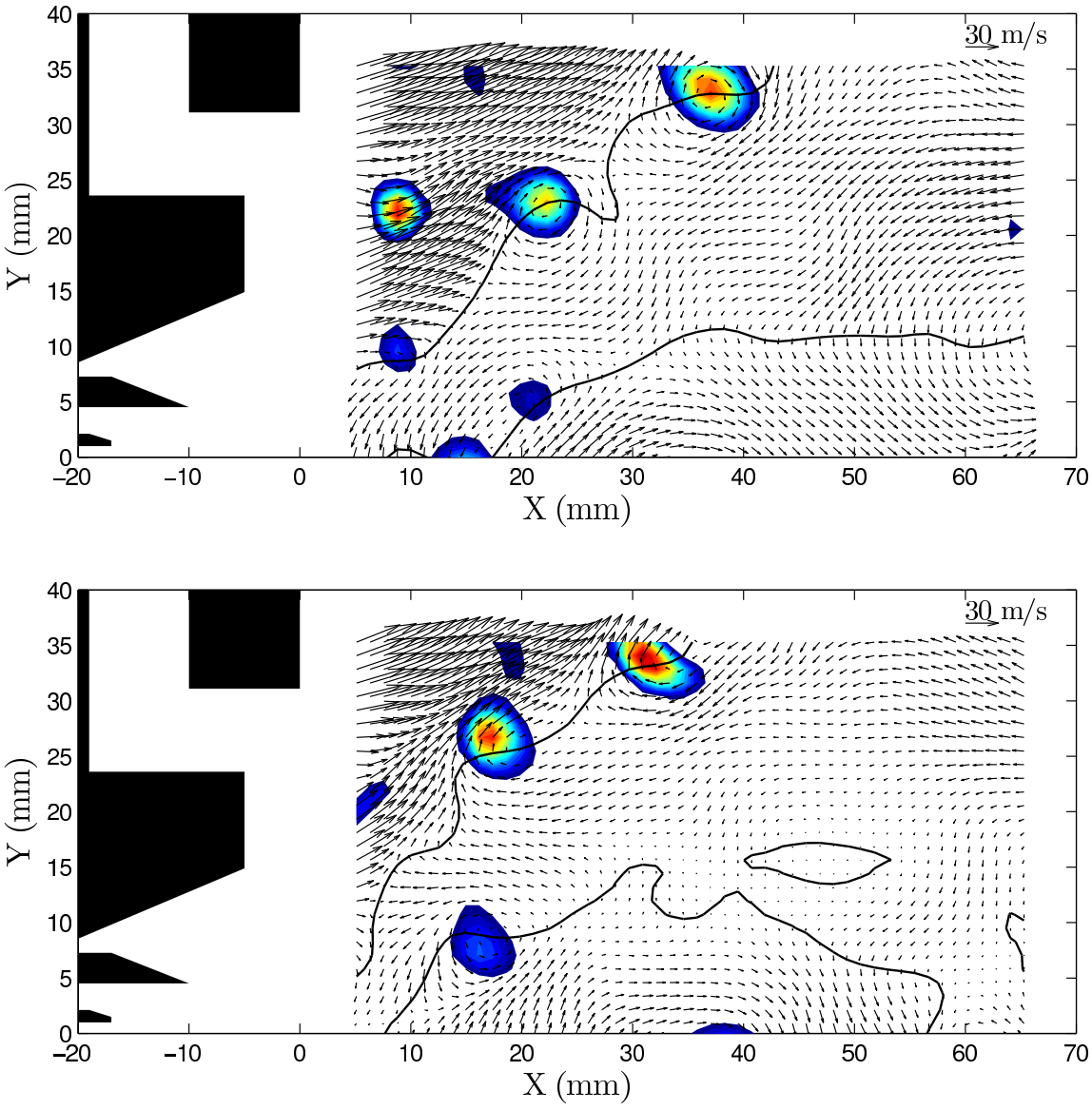

Figure 4.35: Representative images of the instantaneous flow field for Case 4M. Overlaid on the velocity vectors are contours of the swirling strength.

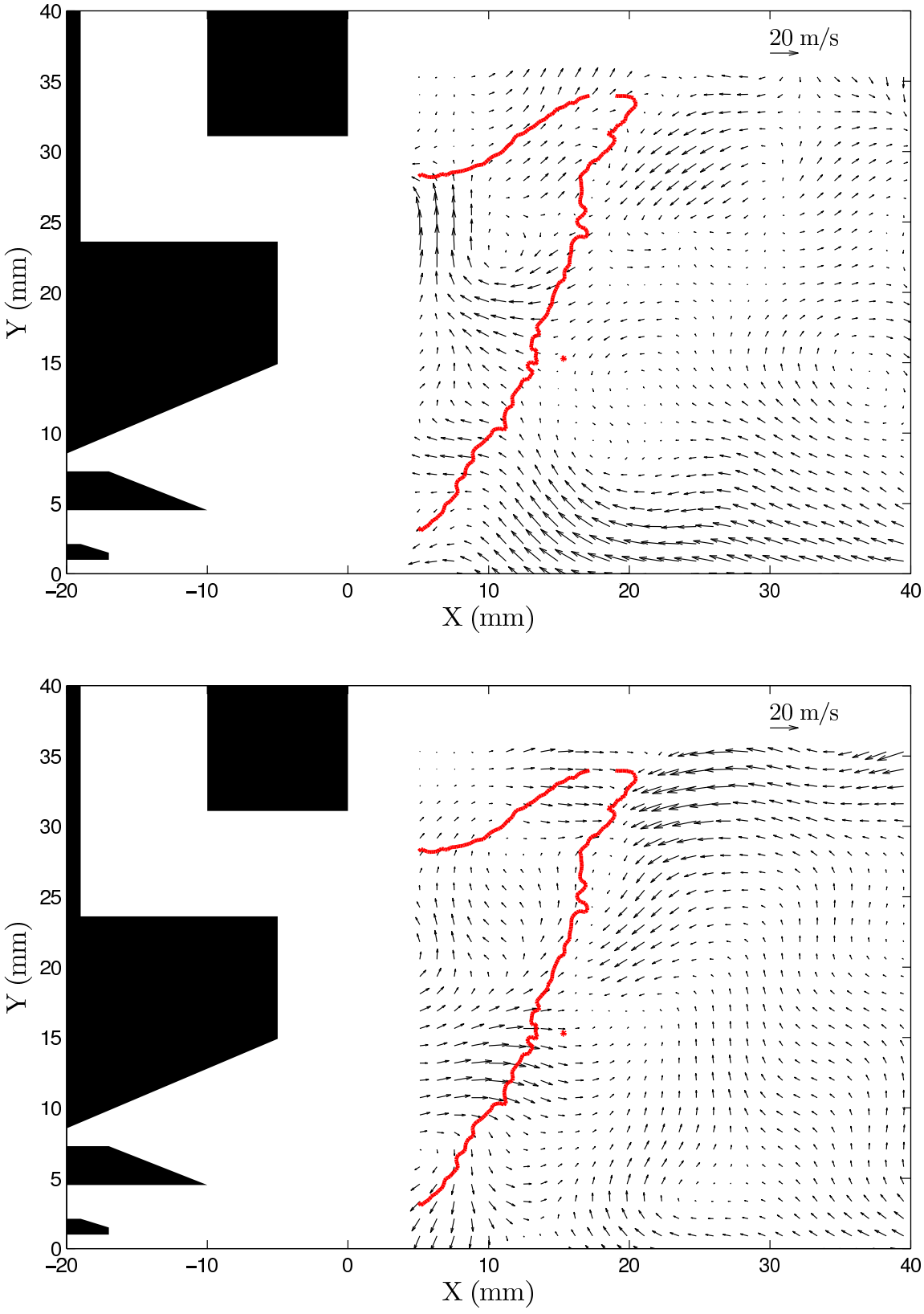

Figure 4.36: Representative images of the instantaneous flow field for Case 4M showing little to no interaction between the pilot and main. The mean velocity has been subtracted from the instantaneous velocity.

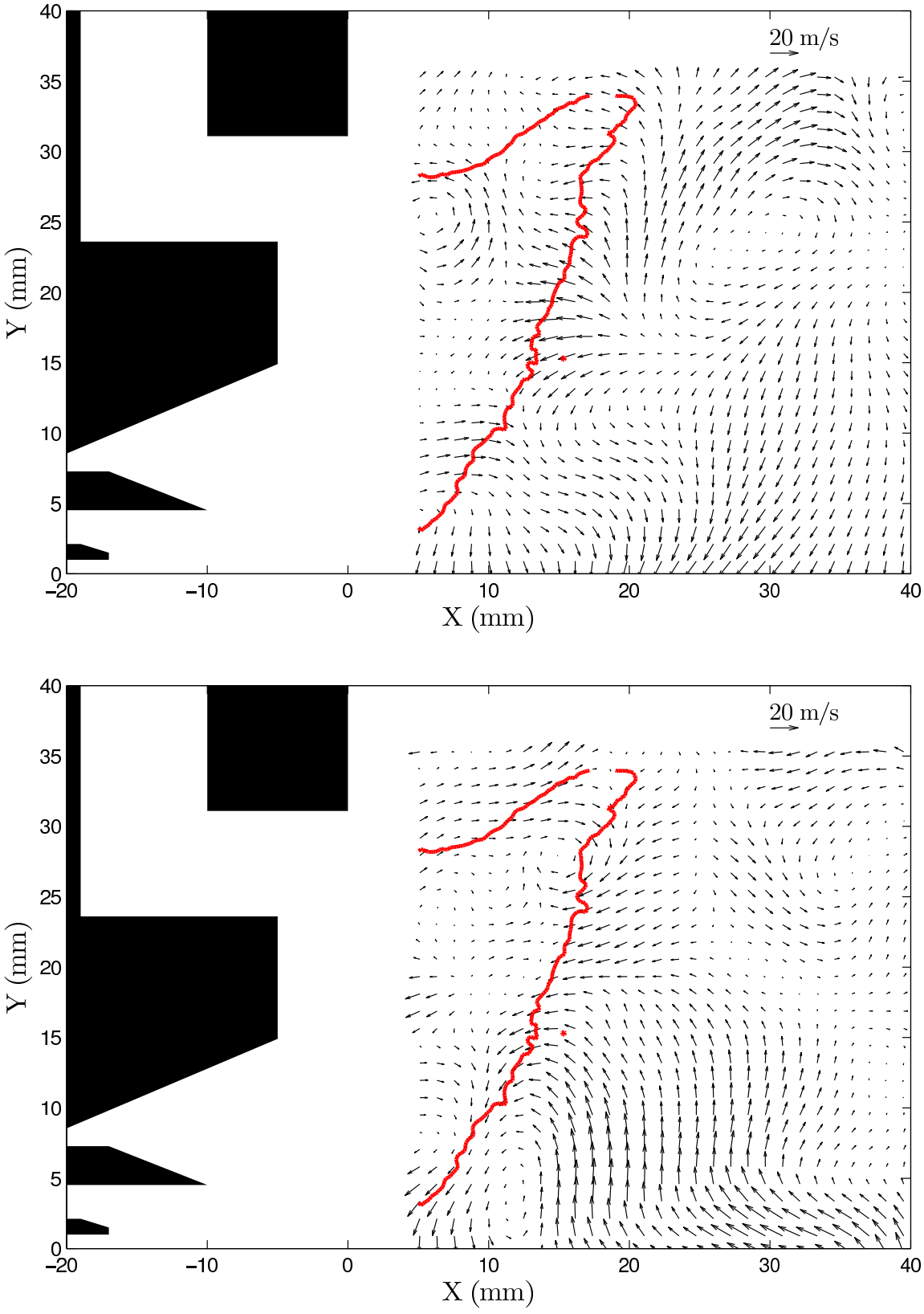

Figure 4.37: Representative images of the instantaneous flow field for Case 4M showing a localized region of flow exchange near the upstream section of the main flame. The mean velocity has been subtracted from the instantaneous velocity.

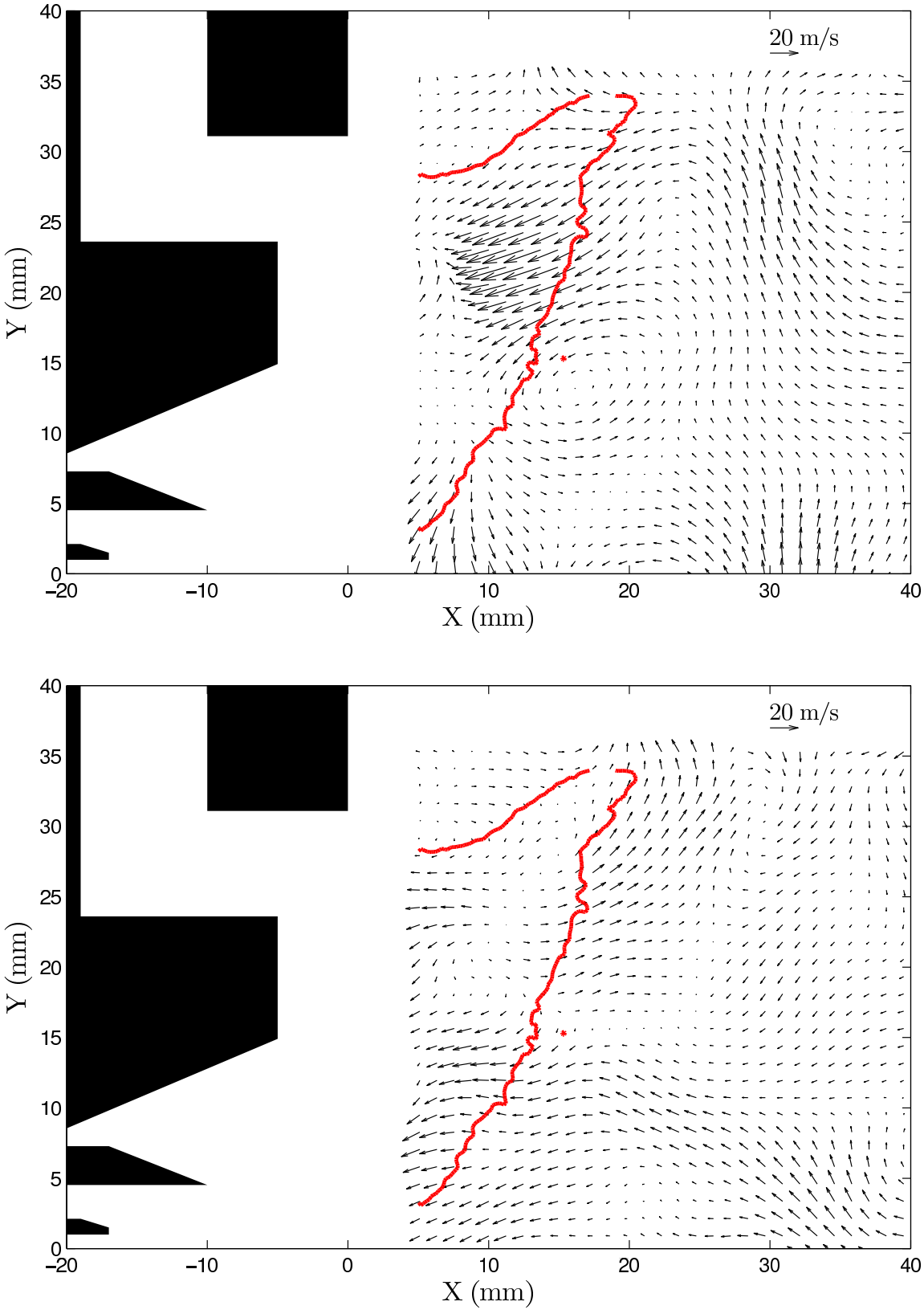

Figure 4.38: Representative images of the instantaneous flow field for Case 4M showing flow from the pilot into the main. The mean velocity has been subtracted from the instantaneous velocity.

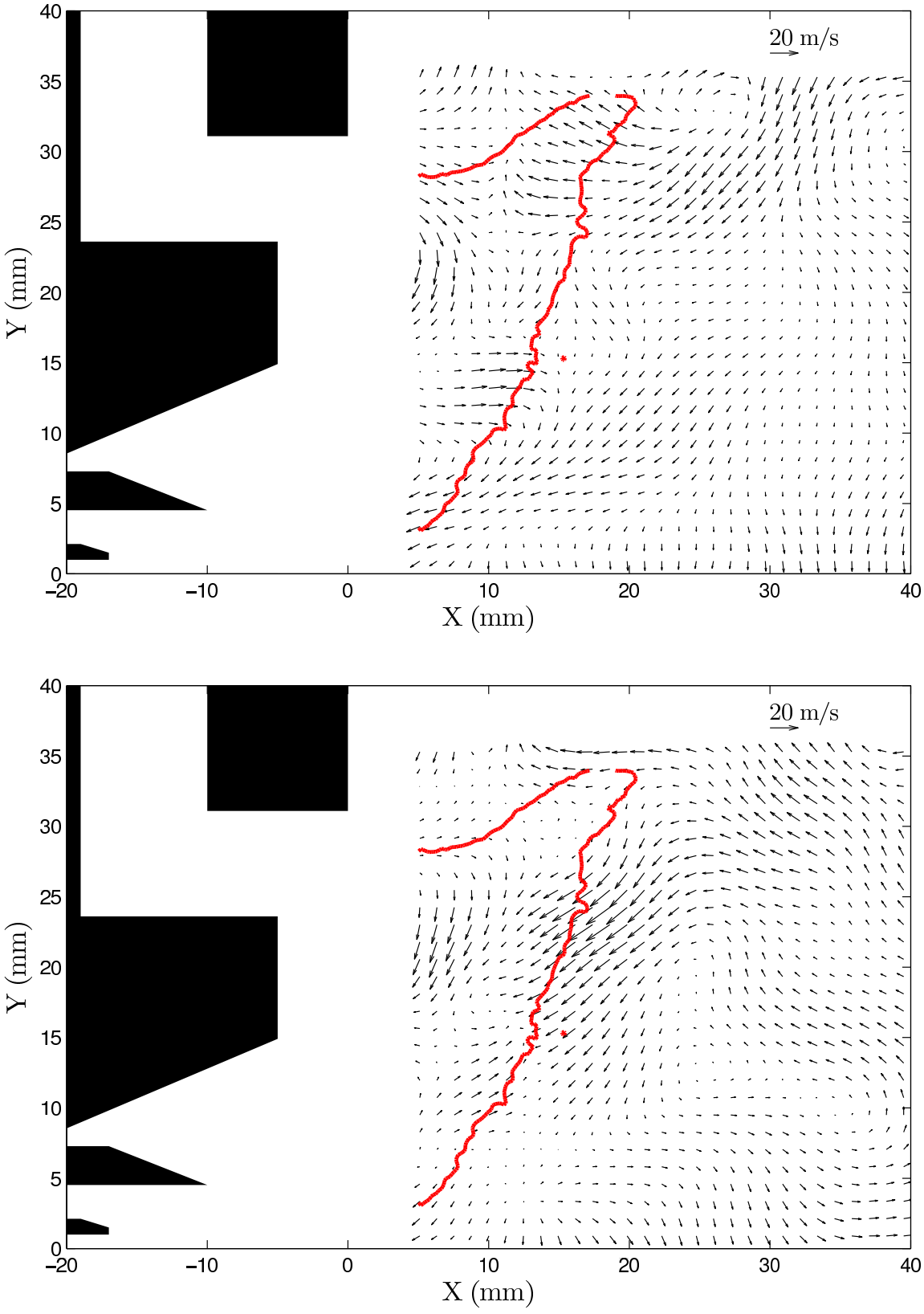

Figure 4.39: Representative images of the instantaneous flow field for Case 4M showing flow from the main into the pilot. The mean velocity has been subtracted from the instantaneous velocity.

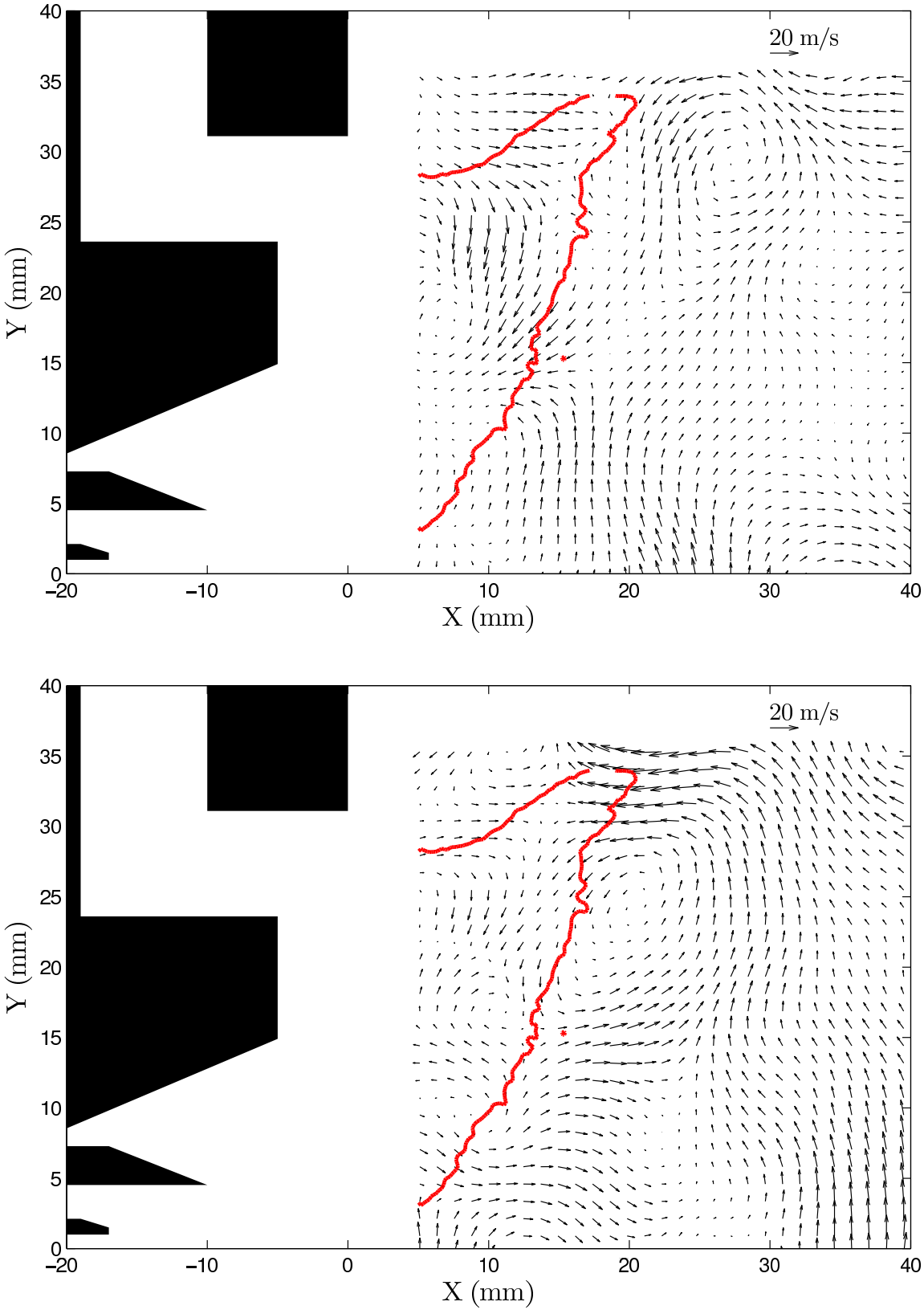

Figure 4.40: Representative images of the instantaneous flow field for Case 4M showing flow from the main into the pilot. The mean velocity has been subtracted from the instantaneous velocity.

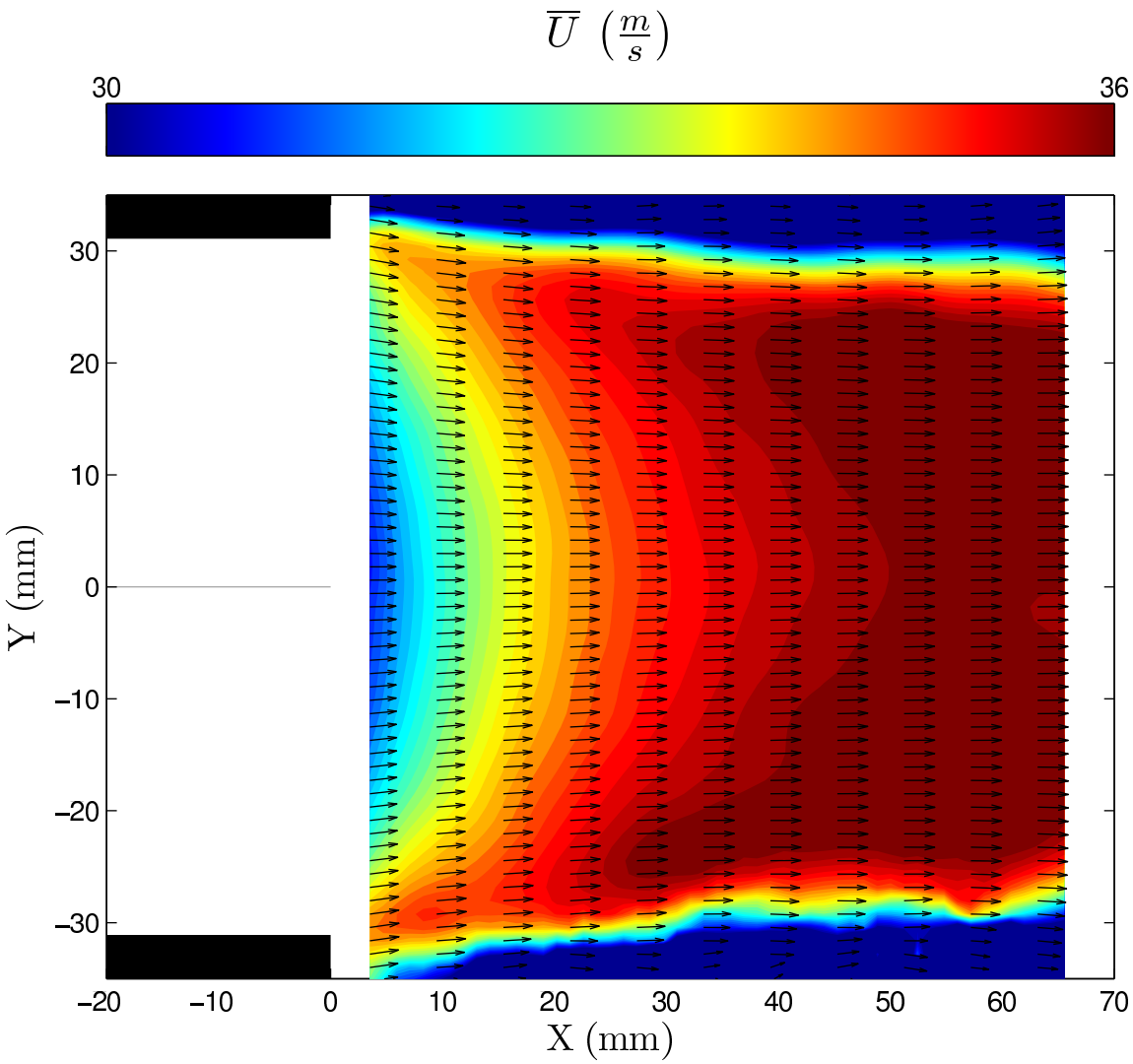

Figure 4.41: Contour plot of the axial velocity taken without the TAPS injector and swirl cup.

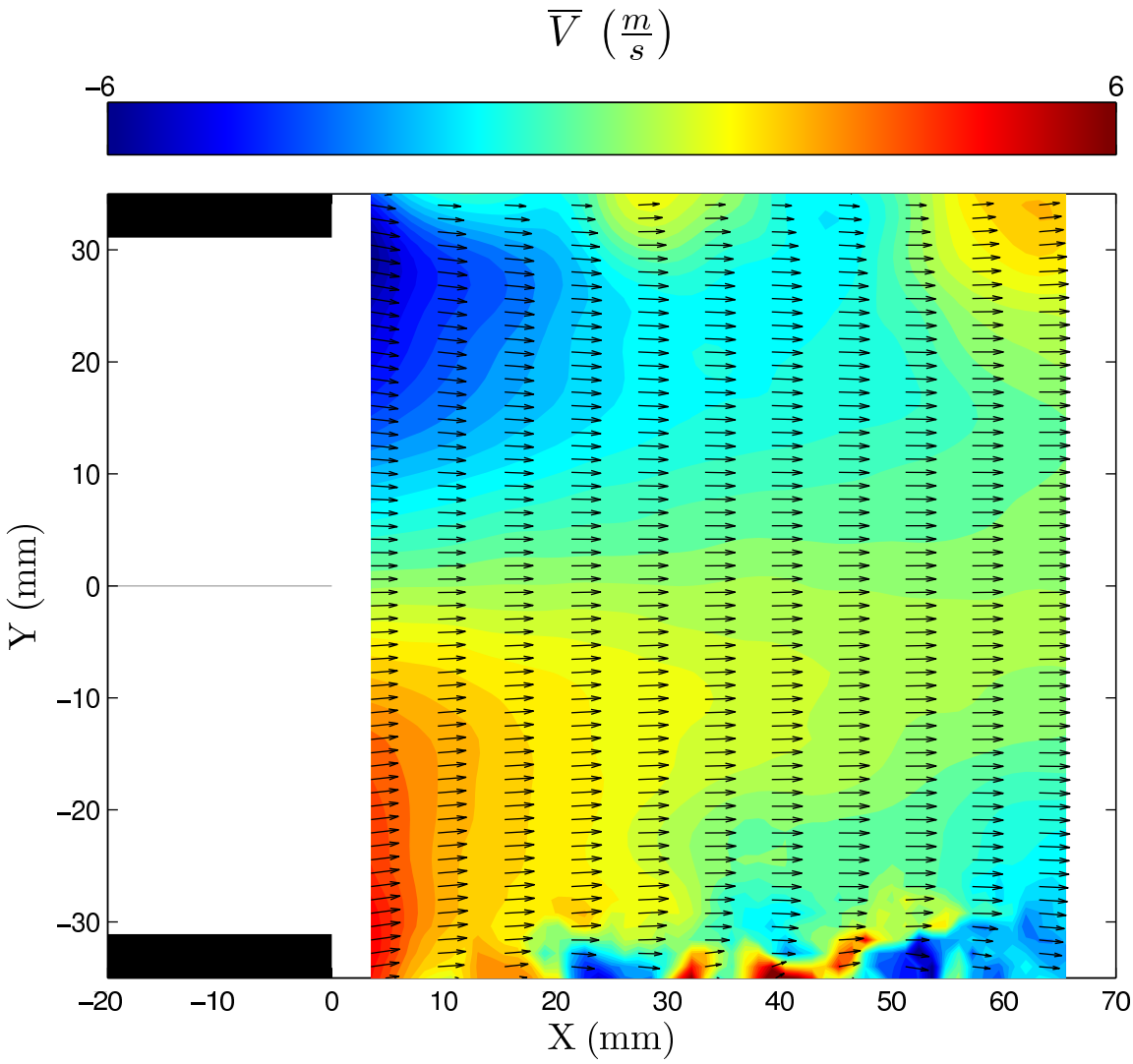

Figure 4.42: Contour plot of the radial velocity taken without the TAPS injector and swirl cup.

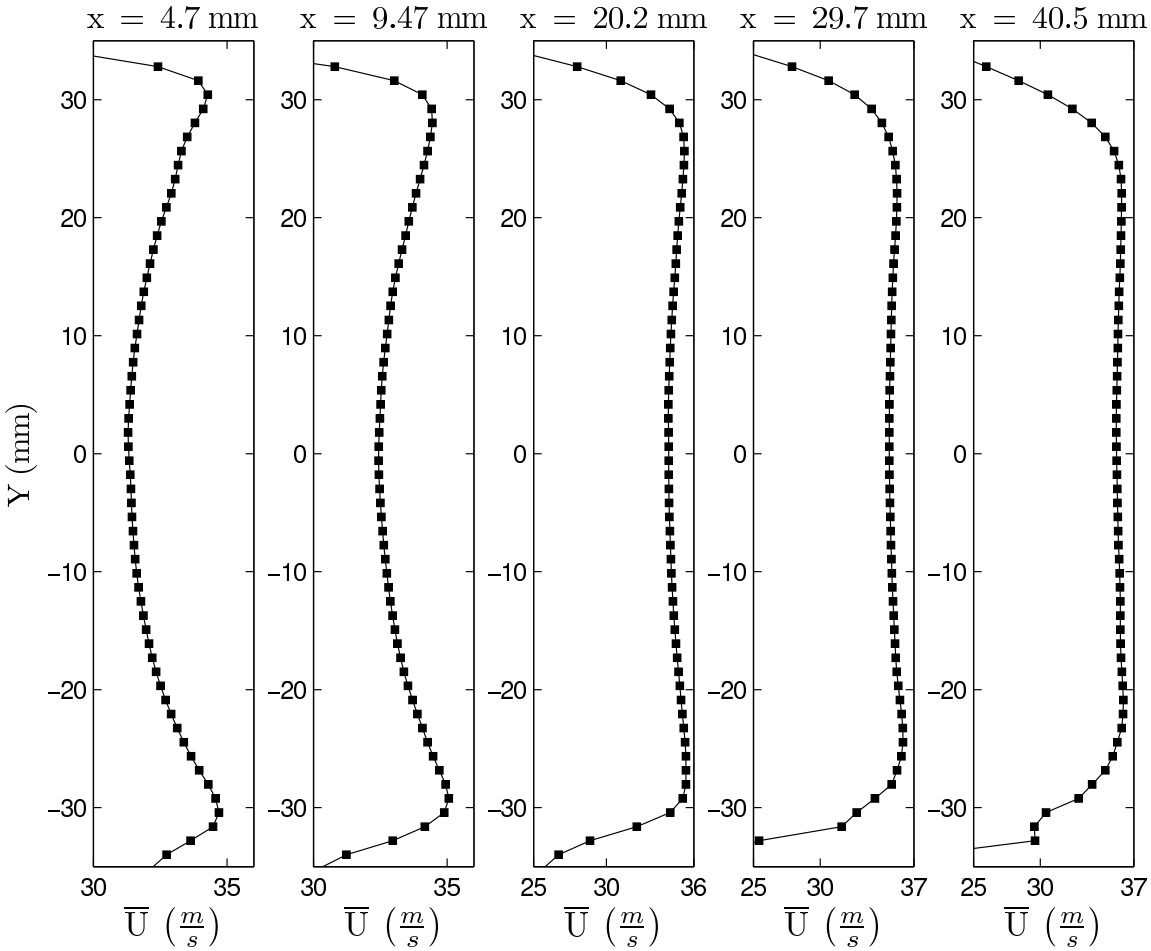

Figure 4.43: Profiles of the axial velocity taken at five axial locations.

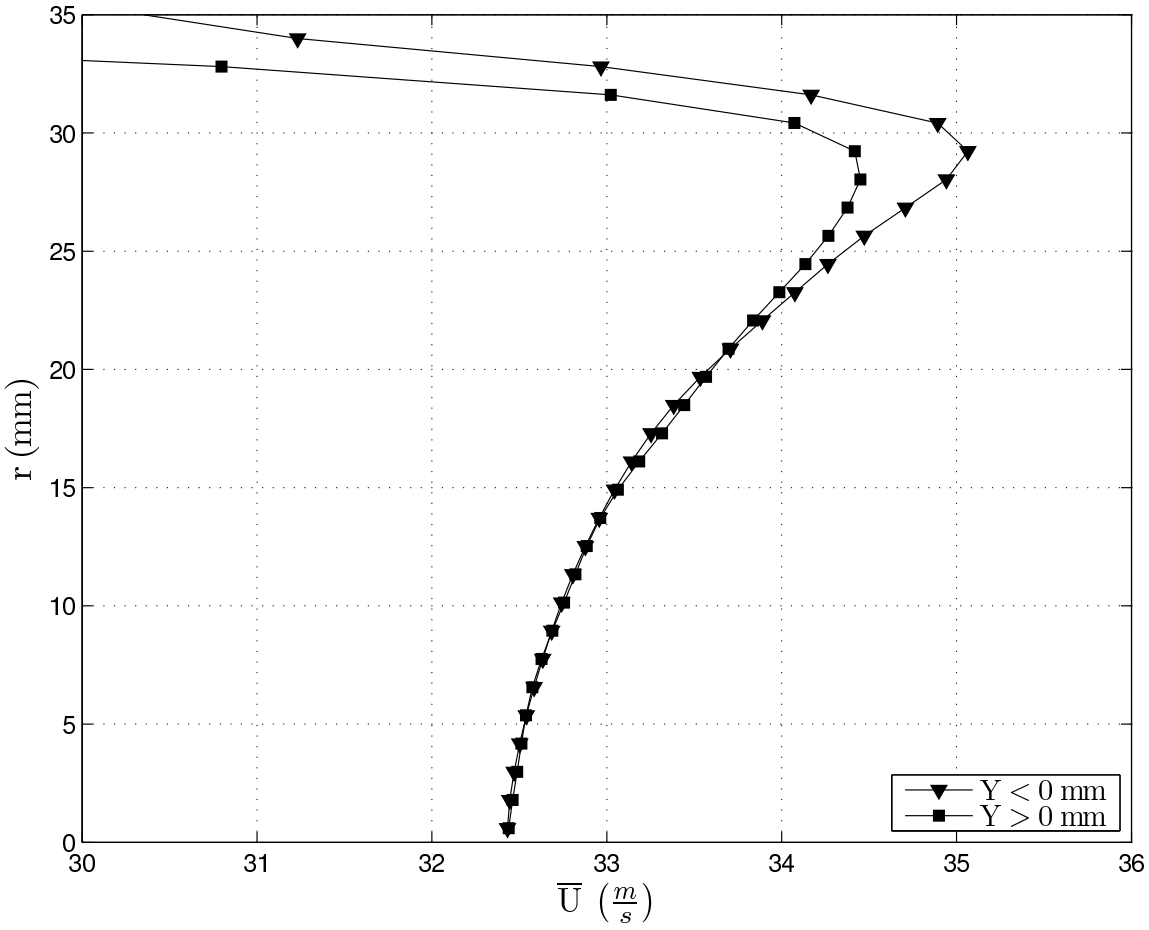

Figure 4.44: Axial velocity at $x = 9.5$ mm as a function of the radius from centerline.

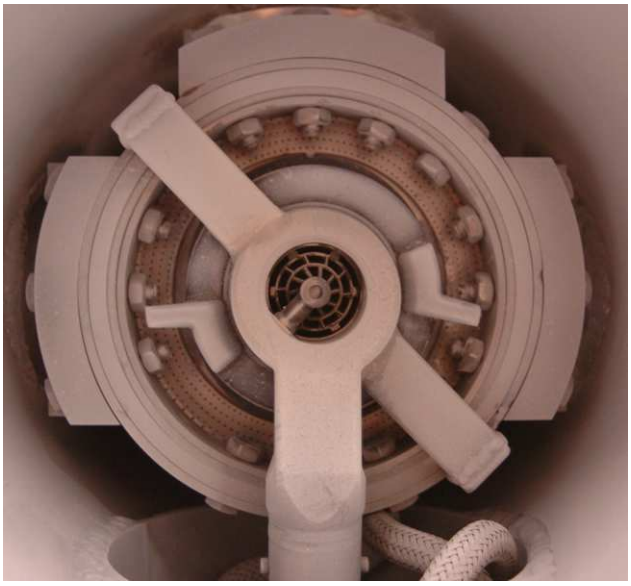

Figure 4.45: Asymmetries in the TAPS injector body. The central fuel sting runs down from the center of the TAPS injector to the fuel connections below. This sting covers a part of the swirl cup with no analogous covering of the swirl cup near the top.

CHAPTER V

Combustor Instabilities

While Lean Premixed Prevaporized (LPP) combustors offer the most promise for meeting the emissions regulations discussed in the Introduction (§I), they are prone to instabilities that can limit their range of operating conditions. The GE TAPS combustor used in this study too was found to be unstable under certain conditions. As discussed in §1.2.3, typically flame dynamics in gas turbines are due to acoustic instabilities. These are usually marked by high frequency oscillations in both the combustor pressure and heat release. In this study, the flame dynamics were not due to acoustic instabilities and were marked by low frequencies caused by flashback oscillations. While the previous chapters have focused on the combustor's stable operation, it is also important to study the mechanisms that cause the instabilities. A better understanding of the factors driving instabilities in the TAPS combustor not only aids in the design of the next generation TAPS injector, but potentially all LPP combustors.

In general the combustor was observed to be unstable at different fuelling flowrates of the pilot and main flames which were a function of the global velocity gradient (U/d) issuing from the main annulus. The global velocity gradient was defined as the average velocity issuing from the main annulus (U) divided by the annulus height

(d = 7.5 mm). It was hypothesized that the critical parameter governing the stability of the combustor is a global velocity gradient in a similar manner to that of a Bunsen flame since the main flame is designed to be premixed. As was seen in Section (§4.3) and Fig. 4.12, the flow in the combustor is self-similar and altering the combustor pressure changes the air density and therefore the velocity through continuity. Since pressure, especially in the range tested in this study, has a negligible effect on the combustion, altering the pressure provides a unique means of changing the velocity issuing from the main annulus without altering the mass flowrate. For the purposes of studying the instabilities, the total air mass flowrate and temperature were held constant at $\dot{m}_{air,total} = 0.228$ kg/s and $T_3 = 505$ K respectively. The combustor pressures and corresponding global velocity gradients are listed in Table 5.1.

Combustor Pressure (p_3) atm	$\bar{U}$ (m/s)	d (mm)	Global Velocity Gradient (U/d) s^{-1}
1	37	7.5	4900
2	22	7.5	2900
3	16	7.5	2100

Table 5.1: The three global velocity gradients tested by altering the combustor pressure. $\dot{m}_{air,total} = 0.228$ kg/s and $T_3 = 505$ K

5.1 Flame Blowout

The lean blowout (BO) of the pilot flame was measured and was seen to be a function of U/d as shown in Fig. 5.1. As the pilot fuelling rate was gradually decreased, the pilot flame decreased in length until it completely blew out at the flowrates shown. The pilot blowout points also were measured with a non-trivial main fuelling rate. In this case, it was seen that regardless of the main fuelling rate the pilot flame blew out at a lower fuelling rate for $U/d = 4900$ and $U/d = 2900$. Fuel

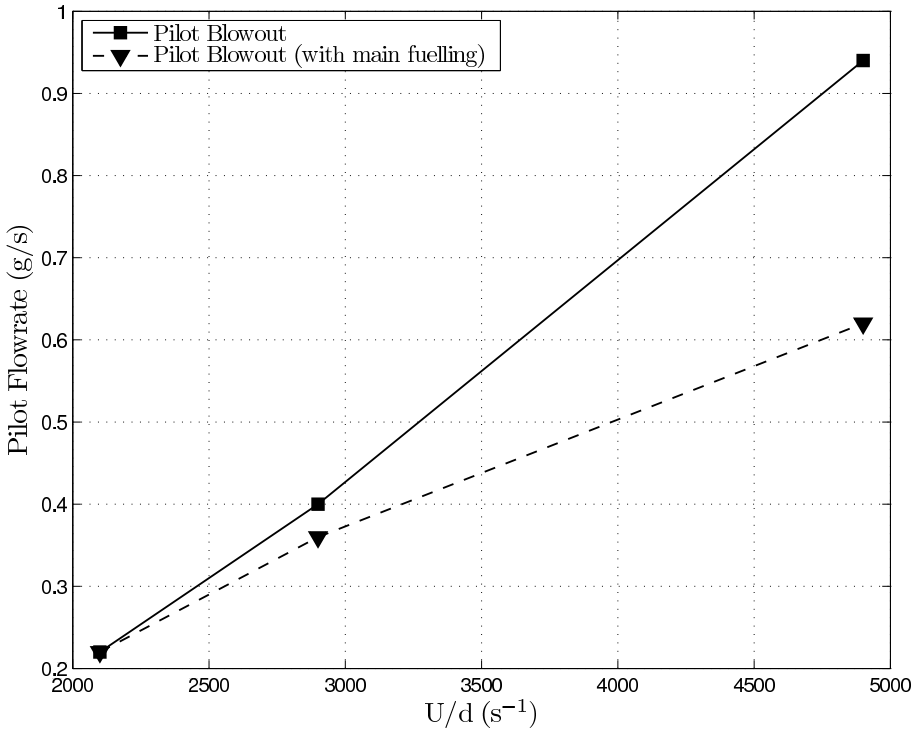

Figure 5.1: The pilot flowrates at which blowout of the flame occurred at different global velocity gradients. The square symbols mark the BO points with only pilot fuelling. The inverted triangles mark the BO points when fuel was also injected through the main.

issuing from the main injectors had no effect on the blowout limit for $U/d = 2100$. This means that at the higher gradients, some main fuel is entrained into the pilot flame and allows for the pilot flame to exist even when the pilot fuelling rate is too low to sustain a flame otherwise. The amount of main fuel entrained is a function of U/d and presumably no fuel is entrained when $U/d = 2100$. Interestingly, the total amount of fuel issuing from the main has no effect on the BO point. This suggests that a constant amount of fuel is always entrained into the pilot with the exact amount given by the difference in the two curves in Fig. 5.1. It is safe to assume that this behavior is not limited to operation near blowout and that at high velocities, a limited amount of main fuel burns as a diffusion flame in the pilot.

5.2 Stability Limits

The stability limits of the combustor are shown in Fig. 5.2 for the three different U/d. The lines mark the sharp boundary between the stable and unstable operation of the combustor. They were obtained by setting the pilot fuel flowrate to some constant (between 1 and 2 g/s) and increasing the main fuel flowrate (from zero). For moderate ratios of main to pilot fuel flowrates, the flames were steady. However, as the main fuel flowrate was increased further, large unsteadiness and oscillations were visually observed. In general, the instabilities were marked by a loud low frequency (4-20 Hz) thumping and a matching variation in the chemiluminescence intensity. The unsteadiness was never acoustically coupled with the combustor and therefore the high frequencies associated with acoustic instabilities Najm and Ghoniem (1994) were never observed, based on the following argument. Acoustic instabilities occur when standing waves are formed inside the combustor with the quarter or half-wavelength of the standing wave matching some integral length of the combustor (L). The frequency of the instabilities are then

$$f = \frac{a}{L}, \tag{5.1}$$

where a is the speed of sound ($a = \sqrt{\gamma RT}$). Since the highest frequencies observed were on the order of 10 Hz, this would correspond to a quarter-wavelength of roughly 10 m for any standing wave. This dimension exceeds any physical length available for the wave. Furthermore, with heat addition in the combustor, the speed of sound would increase, further increasing the integral length required. Therefore, the instabilities observed were not acoustic instabilities, but rather flashback oscillations (Coats (1980)).

The mass based fuel air ratios (F/A) and equivalence ratios in Fig. 5.2 were

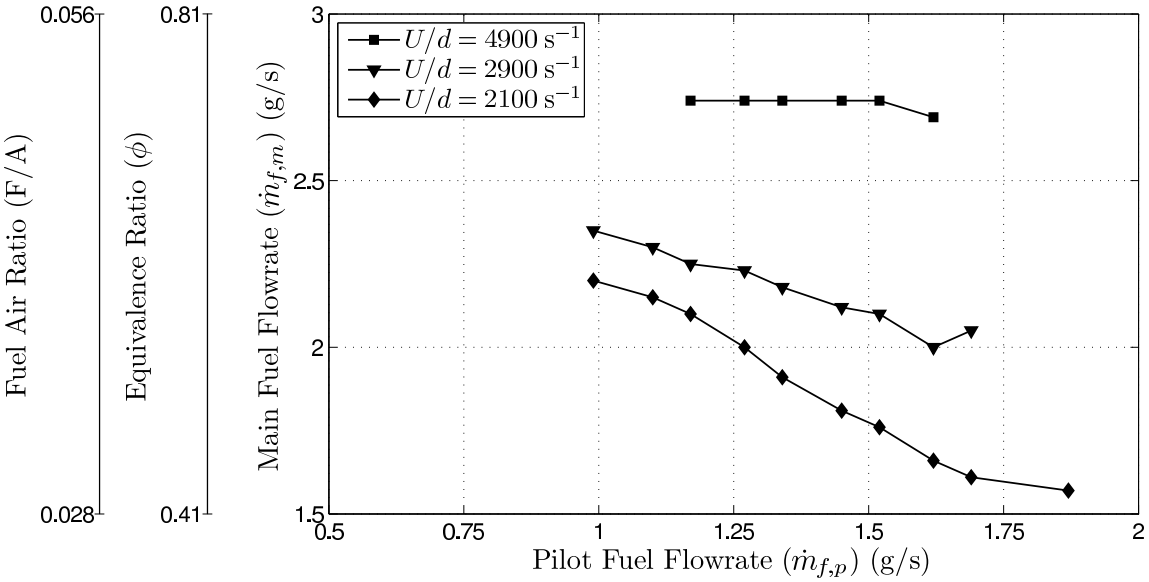

Figure 5.2: The stability limits of the combustor for the three different global velocity gradients. For flowrates of main fuel below the lines, the combustor is stable while in the region above it is unstable.

computed by integrating the velocity measurements from PIV to obtain the air mass flowrate issuing from the main annulus. Computing an equivalence ratio necessitates assuming a perfectly premixed main annulus. The Jet-A fuel used was assumed to be decane ($C_{10}H_{22}$) which has a stoichiometric F/A of 0.069. Immediately apparent from the figure is the effect that U/d has on the stability limits. As the velocity gradient is decreased, the combustor goes unstable at a lower main fuel flowrate and therefore at a leaner mixture. Another difference between the three cases is in the slope of the stability curves. At low velocity gradients, there is a negative slope in the curves indicating that the combustor is less stable with higher pilot fuelling rates (longer pilot flames). At $U/d = 4900\ s^{-1}$ however, there is virtually no slope further illustrating that the combustor is more stable at higher values of the global velocity gradient.

Similar results have been observed by other researchers studying non-acoustic

low frequency instabilities in GT combustors but a clear mechanism explaining the behavior is lacking. De Zilwa et al. (2000) identified a sharp boundary between stable and unstable operation of their dump combustor near the lean blowout point. Lee and Santavicca (2003) describe an increase in flame instability with decreasing velocity while the geometry was fixed. Bernier et al. (2004) defined the sharp boundary between stable and unstable operation of their LPP combustor in terms of a critical velocity (v_{cr}) and found that instabilities occurred when the flow velocity was lower than the critical velocity. Furthermore, they found that the critical velocity was a function of the equivalence ratio with v_{cr} increasing with increasing equivalence ratio. These results along with the trends observed in this study allow for a clearer explanation of the mechanism governing the instabilities.

While the flow within a modern gas turbine combustor such as this one is highly complex, analogies can be drawn between its stability and classic models of premixed flame stability. Plotted in Fig. 5.3 are classic flashback data from a Bunsen burner with ethylene (Grumer et al. (1955)) and methane (Grumer and Harris (1952)). Also shown by square markers are the points at which the LPP combustor goes unstable at one pilot fuel mass flowrate. It can be seen from the methane and ethylene data that the flashback curves are dependent on the specific fuel. Similarly, we can hypothesize a similar curve for the LPP combustor. Therefore, at a given value for a global U/d, as the overall equivalence ratio is increased, the flame reaches a point where it will flashback. At this point, the main flame cannot exist at its stable location and will drive the unsteadiness in the combustor. It is important to note that the dashed curve in Fig. 5.3 is hypothetical and is not the curve for Jet-A in the manner that the flashback curves are for methane and ethylene. Flashback of the LPP combustor depends on other parameters such as the pilot fuelling rate and the geometry.

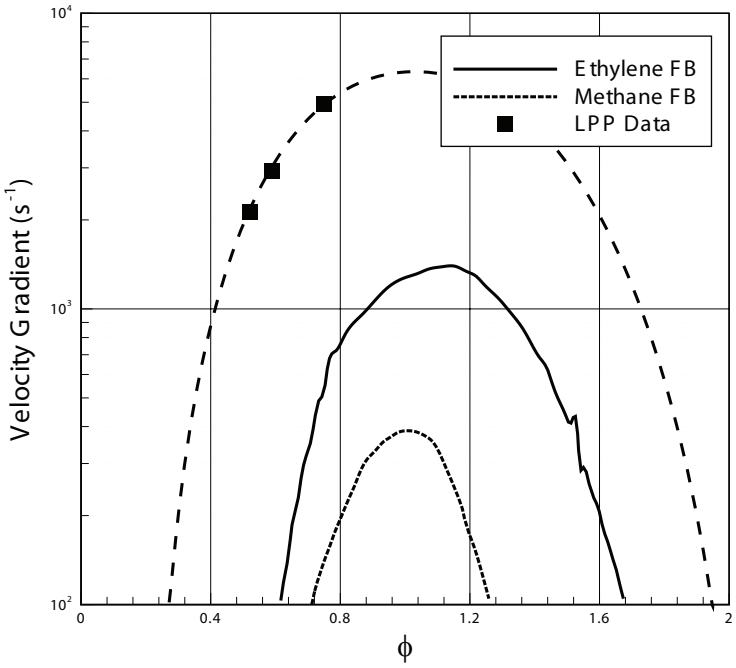

Figure 5.3: Critical velocity gradient measured for the LPP gas turbine combustor with preheated air (solid symbols). For comparison, flashback limits for ethylene (Grumer et al. (1955)) and methane (Grumer and Harris (1952)) Bunsen flames are also plotted.

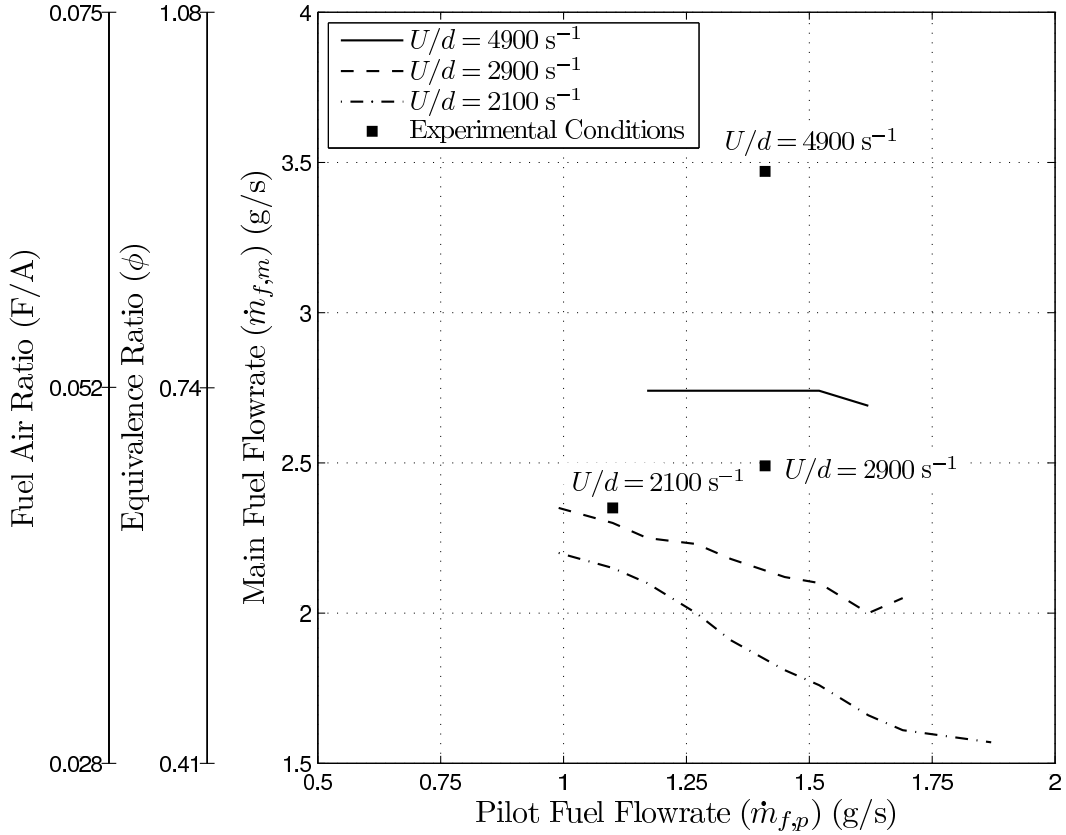

Figure 5.4: The pilot and main fuel flowrates of the three cases presented denoted by the solid square markers. Overlayed is also the stability limits of the combustor at the three global velocity gradients.

5.3 Pressure and Chemiluminescence Results

The equipment and setup described in §2.4.1 was used to simultaneously image the chemiluminescence emissions and measure the pressure at high speeds at the three different global velocity gradients listed in Table 5.1. The fuel flowrates for the three conditions are shown in Fig. 5.4 and will be referred to by the global velocity gradients at which they were taken.

5.3.1 Unstable Operation at U/d = 2900 s^{-1}

Fig. 5.5 shows a sample sequence of chemiluminescence images and combustor pressure for $U/d = 2900$ s^{-1}, which will be used as a representative case. The

sequence of images shows a conical pilot flame in the center that is always present but varies greatly in intensity. The pilot flame gradually increases in intensity (images 7-10) before there is a dramatic rise in both the size of the flame and the overall heat release (image 11). This is followed by a relatively short process where the heat release is at a maximum and the flame extends to the walls of the combustor and into the corners (images 12 and 4). It is clear that combustion is occurring over a larger region than just the pilot since the heat release is not confined to the pilot cone. This process is brief and the flame quickly returns to its quasi-steady-state of just a pilot flame (images 13 and 5). This process is seen to repeat in the exact manner depicted in Fig. 5.5 and described above. An important observation is that the main flame is never visible in any of the images. While a reason for this might be the fact that the main flame is in general less luminous than the pilot (and that the camera exposure has been optimized for the pilot), traces of the main flame should be visible. This is especially true in images where the chemiluminescence from the pilot is also low (e.g. images 14 and 15). This suggests that during the instability process, the main flame fails to stabilize in the mixing layer and does not burn as it does during the combustor's stable operation (Fig. 3.19).

The combustor pressure is seen to also go through a similar oscillation. The rise in the pressure (and subsequent decline) is caused by variations in the heat release in the combustor. With heat addition, the volume of the gas in the combustor rises which presents a fluid mechanical blockage to the incoming flow and raises its pressure. It is clear however that there is a lag in the pressure. Between images 7 through 9 (t = 690-740 ms) for example, the heat release in the pilot increases while the pressure decreases, or relaxes. The pressure is seen to peak only after the flashback phenomena has been completed. This is shown more clearly in Fig. 5.6 where the

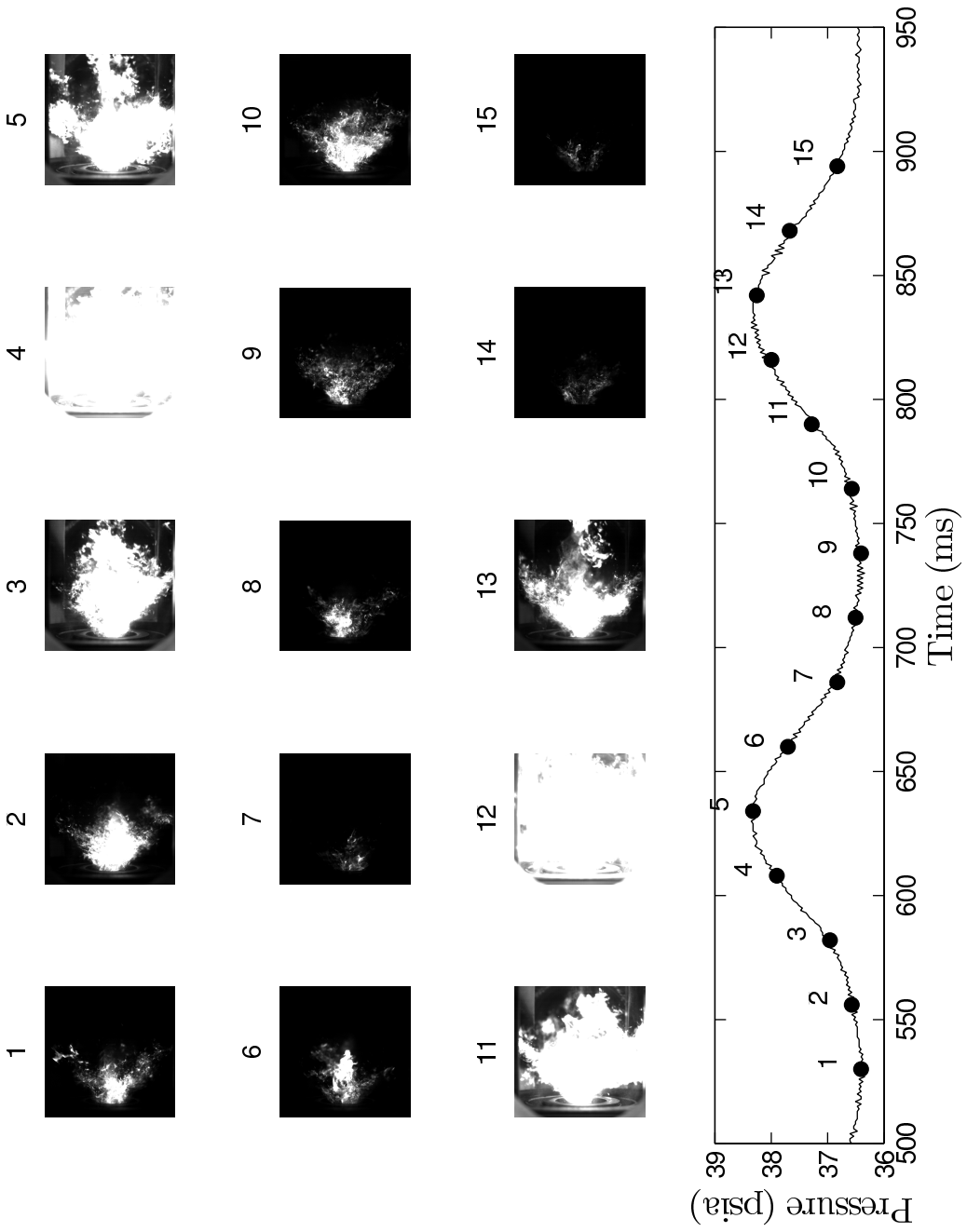

Figure 5.5: Simultaneously acquired chemiluminescence images and pressure measurements for $U/d = 2900\ \mathrm{s}^{-1}$. The images are shown for two periods of the combustion instability.

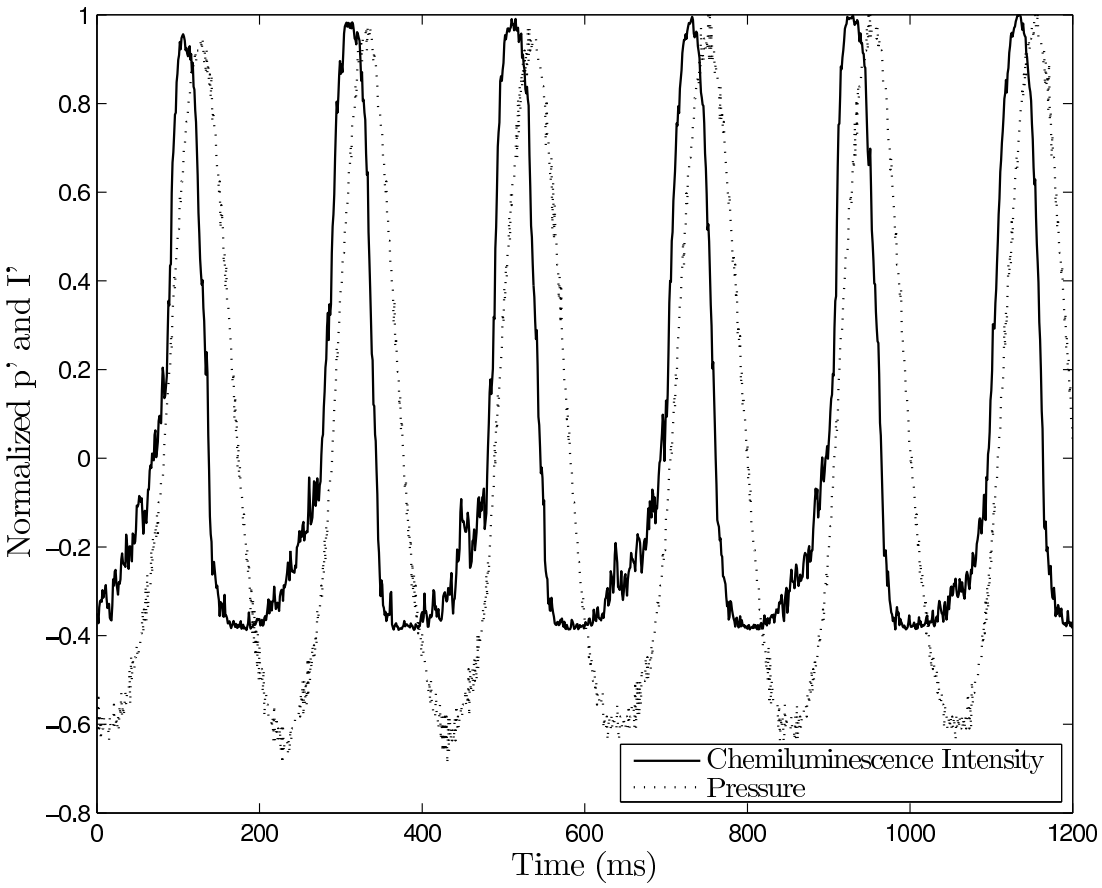

Figure 5.6: The fluctuating pressure and overall chemiluminescence intensity plotted over multiple periods for $U/d = 2900\ \mathrm{s}^{-1}$. It is clear that the combustor pressure lags the heat release in the combustor.

fluctuating pressure and overall chemiluminescence intensities are plotted. The two-dimensional chemiluminescence intensity distribution from each instantaneous image was averaged to yield one value of intensity (I) at each instance in time. The gradual increase in heat release from the pilot flame is seen from the intensity trace and lasts for approximately 100 ms. The sudden rise in heat release (a process lasting about 30 ms) is also apparent. The pressure however lags by 21 ms, which corresponds to a phase angle of 37°. This result is identical to the finding of Venkataraman et al. (1999) where they see the pressure lagging the heat release by a phase angle of 36° at roughly the same ϕ as the case presented here.

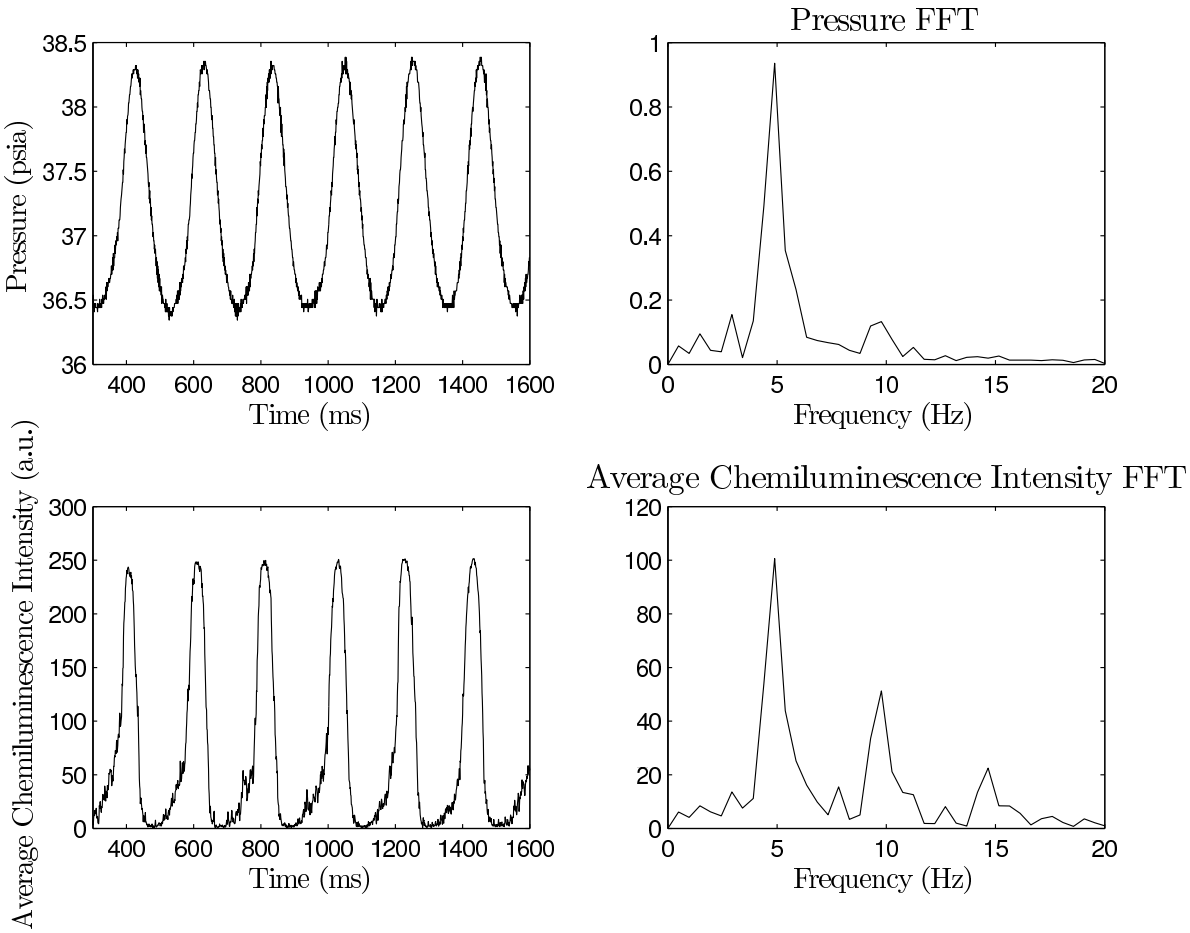

Figure 5.7: The absolute pressure and overall chemiluminescence intensity for $U/d = 2900\ \mathrm{s}^{-1}$. Also plotted are the power spectra. The spectra for both signals show a dominant peak at 4.89 Hz.

The frequency of the instability for $U/d = 2900$ s^{-1} is 4.89 Hz as evidenced by the sharp peak at that frequency in the power spectra for both pressure and average chemiluminescence intensity (Fig. 5.7). Both traces of pressure and intensity indicate a very repeatable process. The peak to peak fluctuations in pressure are 1.91 psia which is 5% of the average combustor pressure. Fig. 5.8 shows the phase space of the instability with each marker marking one instantaneous measurement of pressure and chemiluminescence intensity. The curve is parameterized by time and the arrows denote the direction of time. The phase space provides a novel depiction of the instability process and elucidates a phenomena not obvious in the previous figures. Three branches are present in the phase space. In the first, corresponding to the flashback process, the intensity and pressure are well correlated and increase simultaneously. This is followed by an almost iso-baric relaxation of the chemiluminescence during which the combustor returns to its quasi-steady-state. The third branch is the relaxation of the pressure with near constant heat release from the quasi-steady pilot. Fig. 5.8 not only shows the manner in which the combustor pressure and overall heat release relax but also hints at the phase difference in the two quantities. It is clear through the phase space that the instability is marked by three distinct processes. The use of a phase space in understanding gas turbine instabilities provides a powerful tool that has not been exploited by previous studies of combustor instabilities.

5.3.1.1 Pressure Heat Release Correlation

Rayleigh (1994) proposed that combustor instabilities are amplified when the heat release and pressure are in phase. This has led to the development of the Rayleigh

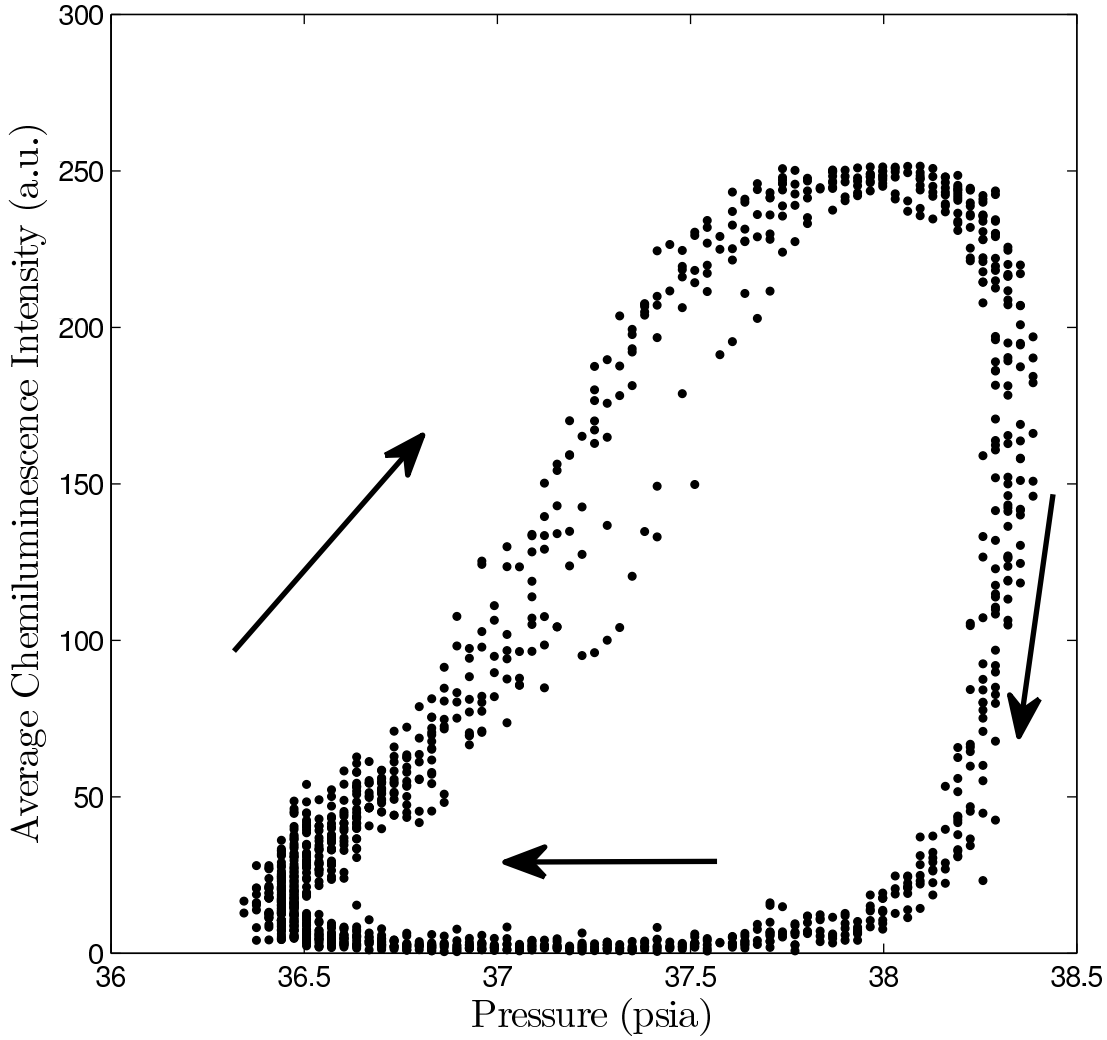

Figure 5.8: Phase space of the instantaneous pressure and overall luminescence intensity for $U/d = 2900\ \mathrm{s}^{-1}$. Each marker marks one instantaneous measurement and the arrows mark the direction of time. The three main phases of the instability are clearly visible.

index (Lee and Santavicca (2003)), given by:

$$R(x,y) = \frac{1}{T}\int_T p'(x,y,t)q'(x,y,t)\,\mathrm{d}t, \tag{5.2}$$

where T is the period of the oscillation, q' is the local heat release fluctuation, and p' is the pressure fluctuation. $q'(x,y,t)$ is obtained from the instantaneous chemiluminescence images and $T = 1/f$. It can be assumed that $p'(x,y,t) = p'(t)$ since the wavelength of the pressure wave is much larger than the typical flame length and therefore the pressure is effectively constant across the flame. Although the Rayleigh index has been developed and used for acoustic instabilities, Eqn. 5.2 effectively provides a two-dimensional correlation between the pressure and local heat release. Therefore, while the instabilities observed were not acoustic, the Rayleigh index will be used to obtain the pressure heat release correlation. A positive index means that the two are in phase and therefore amplify each other and a negative index suggests that the heat release dampens the pressure fluctuation. The two dimensional map can therefore be used to detect regions where the instability is amplified and likewise where it is dampened.

Fig. 5.9 shows the Rayleigh index distribution for $U/d = 2900$ s^{-1}. There is no region in the combustor that has a negative Rayleigh index and the overall Rayleigh index is positive. As expected, the region with the lowest index is the pilot cone since the pilot is largely a diffusion flame anchored to the injector. The regions with the highest (positive) indices are in the outer periphery of the flame cone (near the main annulus) and in the corner recirculation zone. This is consistent with the observation from Fig. 5.8 that the phase with the high correlation between pressure and heat release is at the time when the flame flashes back through the corner recirculation zone. There is also a region with a high index in the center of the combustor where

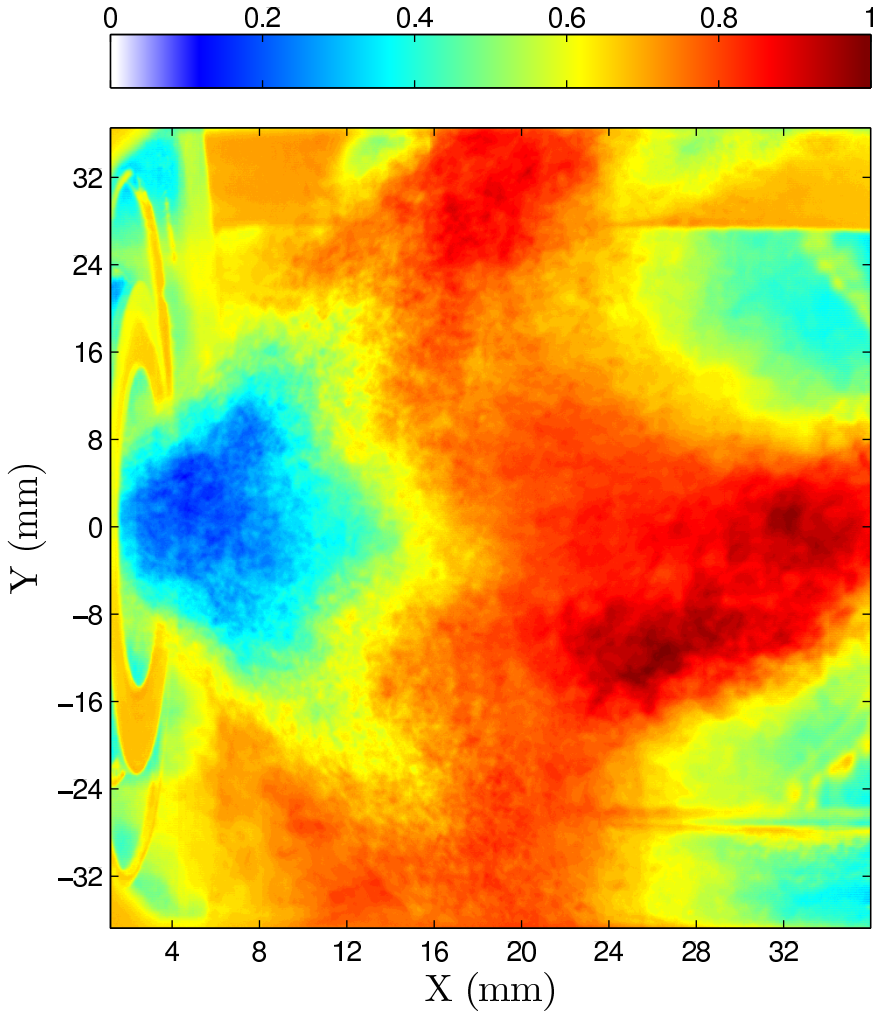

Figure 5.9: Rayleigh index distribution of $U/d = 2900$ s^{-1}.

hot products from the combustion are accelerated out.

5.3.2 Unstable Operation at U/d = 4900 s^{-1} and U/d = 2100 s^{-1}

The other two conditions tested, namely $U/d = 4900$ s^{-1} and $U/d = 2100$ s^{-1}, exhibited much the same behavior as $U/d = 2900$ s^{-1} albeit at difference frequencies and phase angles. A sample sequence of chemiluminescence images from $U/d = 4900$ s^{-1} is shown in Fig. 5.10. Due to the reduced luminosity of the flame at lower pressures the quasi-steady-state phase of the combustor in between the flashback phenomena is not apparent in the images. However, the flashback process is clearly

visible (images 3-4 and 14-15) and is marked by a drastic increase in heat release and change in flame structure. During this brief phenomena, reactions occur in the corner recirculation zone (image 3 top left corner and image 14 bottom left corner) and along the windows (image 4 and 15).

Fig. 5.11 shows the relationship between the heat release and pressure more clearly. The gradual rise in heat release from the pilot seen for $U/d = 2900$ s^{-1} is not apparent from the figure because the camera exposure was optimized to capture the structural detail of the flame during the flashback process. Since the chemiluminescence from the pilot flame was considerably lower, the CCD was unable to capture any changes in the heat release. The intensity trace shows the primary heat release fluctuation to be from the flashback process lasting 23 ms. Once again, the pressure lags the heat release with a phase angle of 62°. As seen in Fig. 5.12, the instability is less uniform than for $U/d = 2900$ s^{-1} and there are cycle-to-cycle variations in both the heat release and pressure. Nevertheless, the power spectra clearly shows a dominant peak at 17.11 Hz and there are no other underlying frequencies suggesting that the variations are random. Though the frequency is higher for this case, the oscillations are less energetic as evidenced by the reduced peak to peak fluctuations in pressure. The magnitude of the fluctuations is 0.48 psi, corresponding to 1.9% of the average. Fig. 5.13 shows the phase space of the instability and while there is considerably more scatter in the data, the same three phases of the instability are obvious. Once again, there is the main flashback of the flame through the corner recirculation zone indicated by the increase in both pressure and heat release. This is followed by a relaxation of the heat release and pressure almost independently of each other. Fig. 5.14 shows the Rayleigh index distribution for $U/d = 4900$ s^{-1}. The distribution is virtually identical to the distribution for $U/d = 2900$ s^{-1} with a

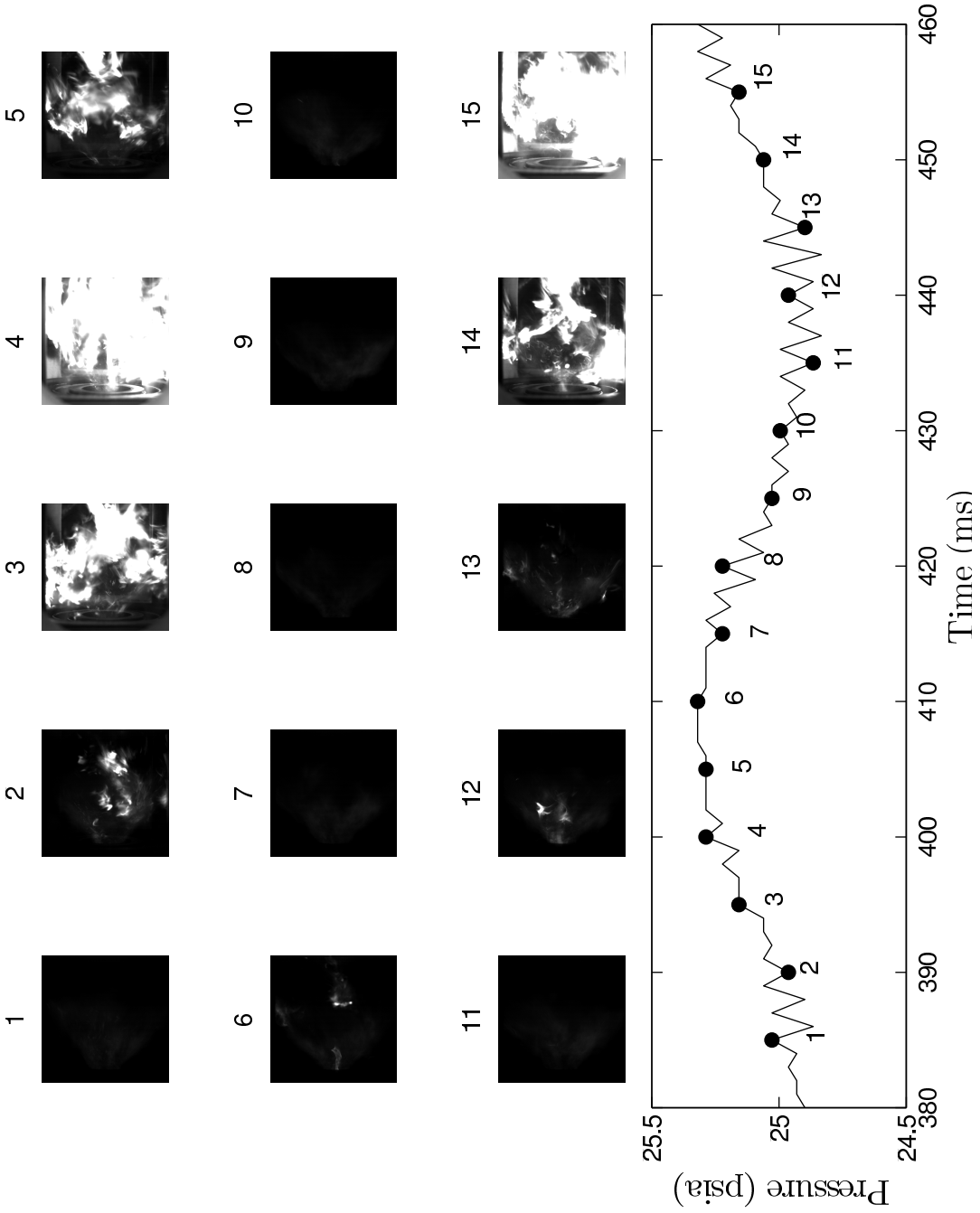

Figure 5.10: Simultaneously acquired chemiluminescence images and pressure measurements for $U/d = 4900\ \mathrm{s}^{-1}$. The images are show two occurrences of the flashback process.

reduced index in the central pilot and the highest values in the corners and periphery of the flame cone.

Fig. 5.15 shows a sample sequence of chemiluminescence images acquired by the high speed camera simultaneously with pressure measurements for $U/d = 2100$ s^{-1}. Unfortunately, as the instability involved the flame flashing back into the corners and along the windows, there was considerable build up of soot on the windows. As can be seen in the images, the soot greatly obscures the image but the general features of the instability can still be ascertained. Equally importantly, the relative magnitude of the heat release can still be computed since the blockage of emissions due to soot is limited to the same region in all images. The primary flashback phenomena is obvious in this sequence of images. For example, in images 3-5, a flame kernel at the bottom can be seen propagating into the corner. Similarly, in image 15 there is reaction clearly occurring in the corners of the combustor.

The fluctuating pressure and chemiluminescence intensities are plotted in Fig. 5.16. While there is the gradual increase in heat release seen for $U/d = 2900$ s^{-1}, the rise in the heat release from the flashback process for $U/d = 2100$ s^{-1} is not as sudden or dramatic. At this condition, the pressure lags the heat release by a phase angle of 42°. The lowest velocity gradient case had the lowest frequency of oscillations as shown in Fig. 5.17. Similar to $U/d = 2900$ s^{-1}, the instability process is very repeatable both in terms of pressure and in terms of the overall heat release. This is indicated by the sharp peak in the power spectra at 3.91 Hz. The peak to peak pressure fluctuations are 0.39 psi which is 0.8% of the average. The phase space of $U/d = 2100$ s^{-1} is given in Fig. 5.18. The phase space has the same features and three primary phases of the instabilities as in the other two conditions. Their is a slight difference however in that both the relaxation of pressure and the subsequent

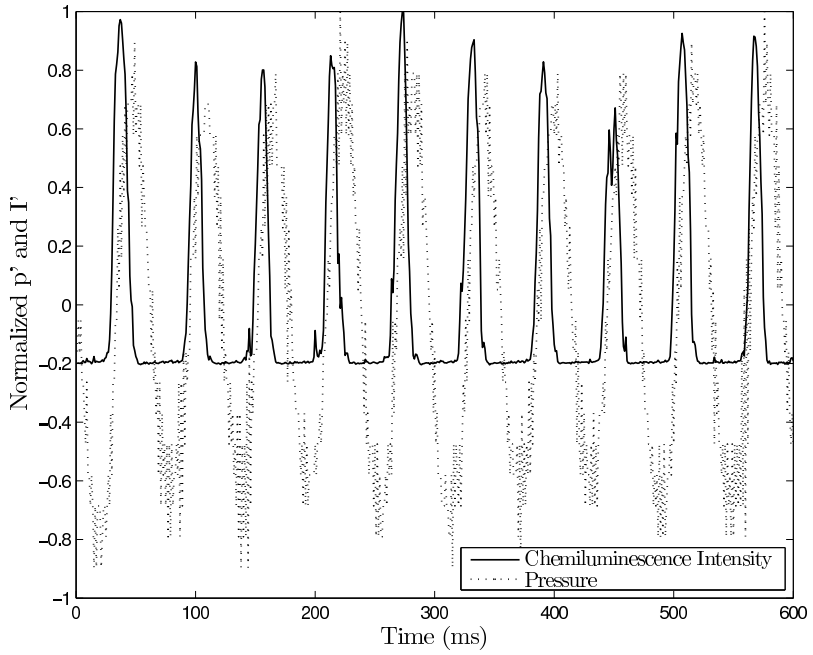

(a)

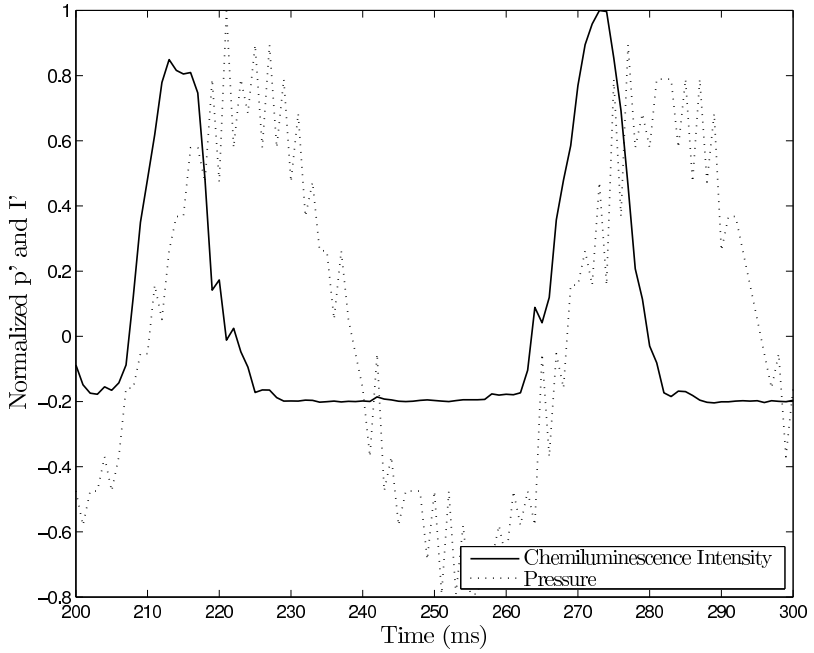

(b)

Figure 5.11: The fluctuating pressure and overall chemiluminescence intensity plotted over multiple periods (a) for $U/d = 4900$ s^{-1}. Shown in (b) is a close-up of the trace in (a).

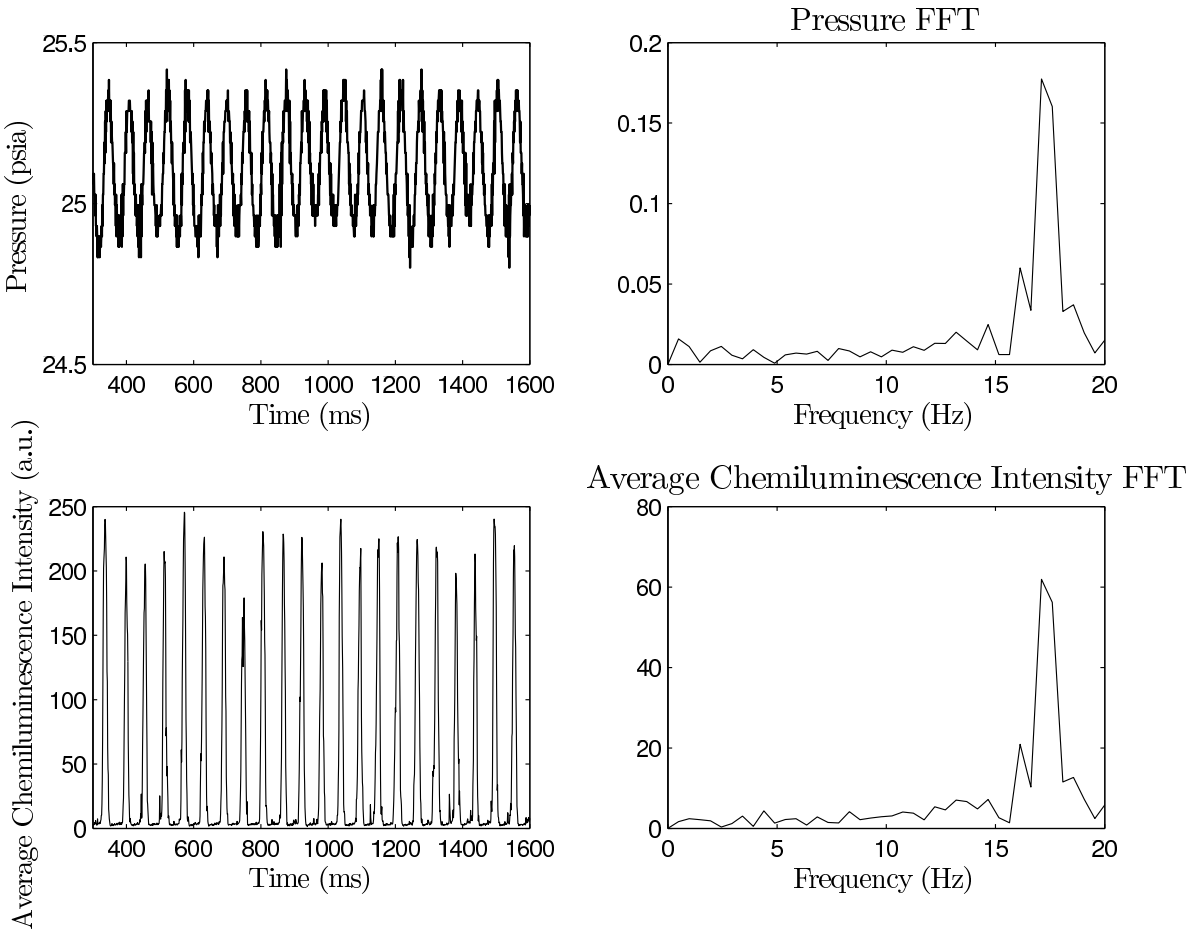

Figure 5.12: The absolute pressure and overall chemiluminescence intensity for $U/d = 4900$ s^{-1}. Also plotted are the power spectra. The spectra for both signals show a dominant peak at 17.11 Hz.

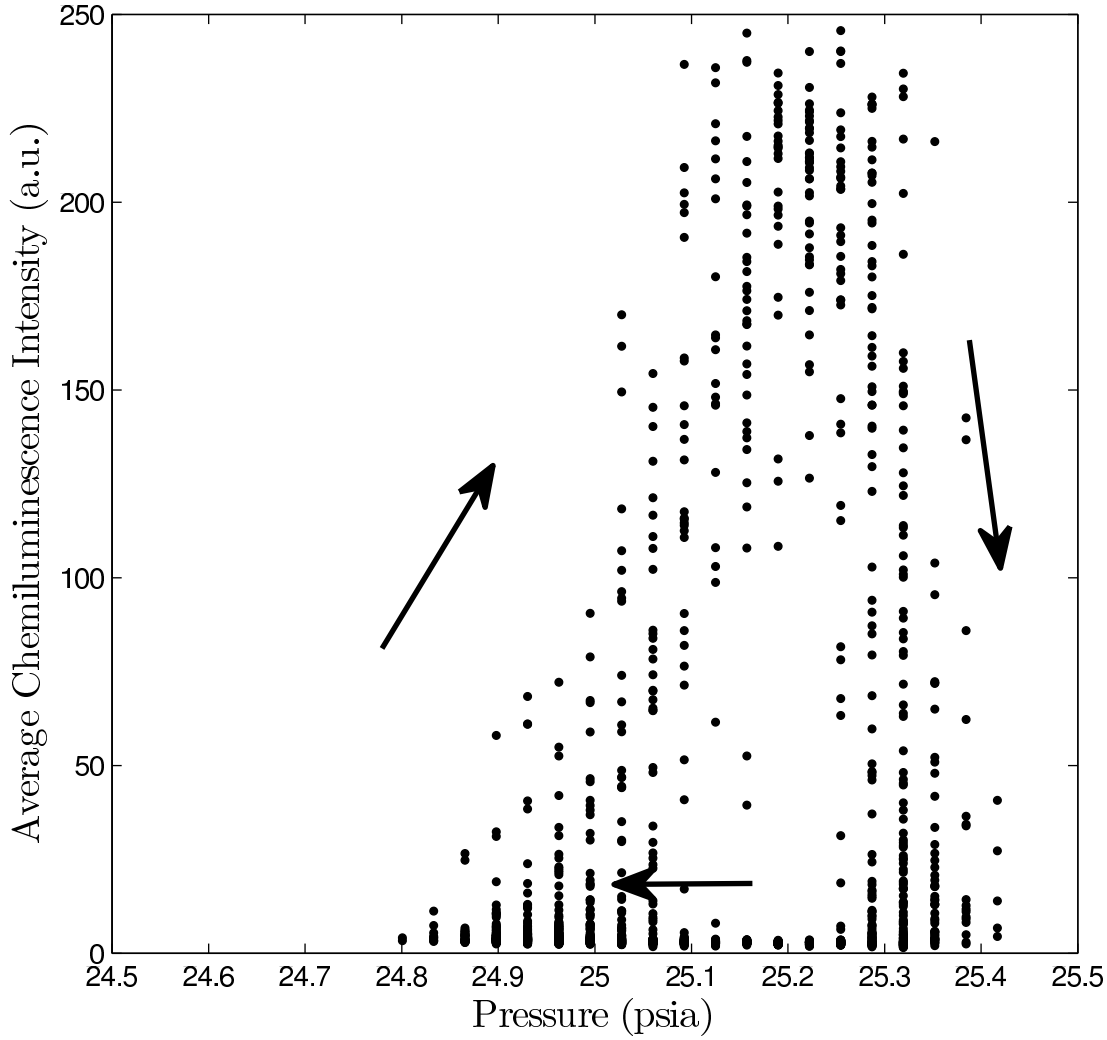

Figure 5.13: Scatter plot of the instantaneous pressure and overall luminescence intensity for $U/d = 4900$ s^{-1}. Each marker marks one instantaneous measurement and the arrows mark the direction of time. The three main phases of the instability are clearly visible.

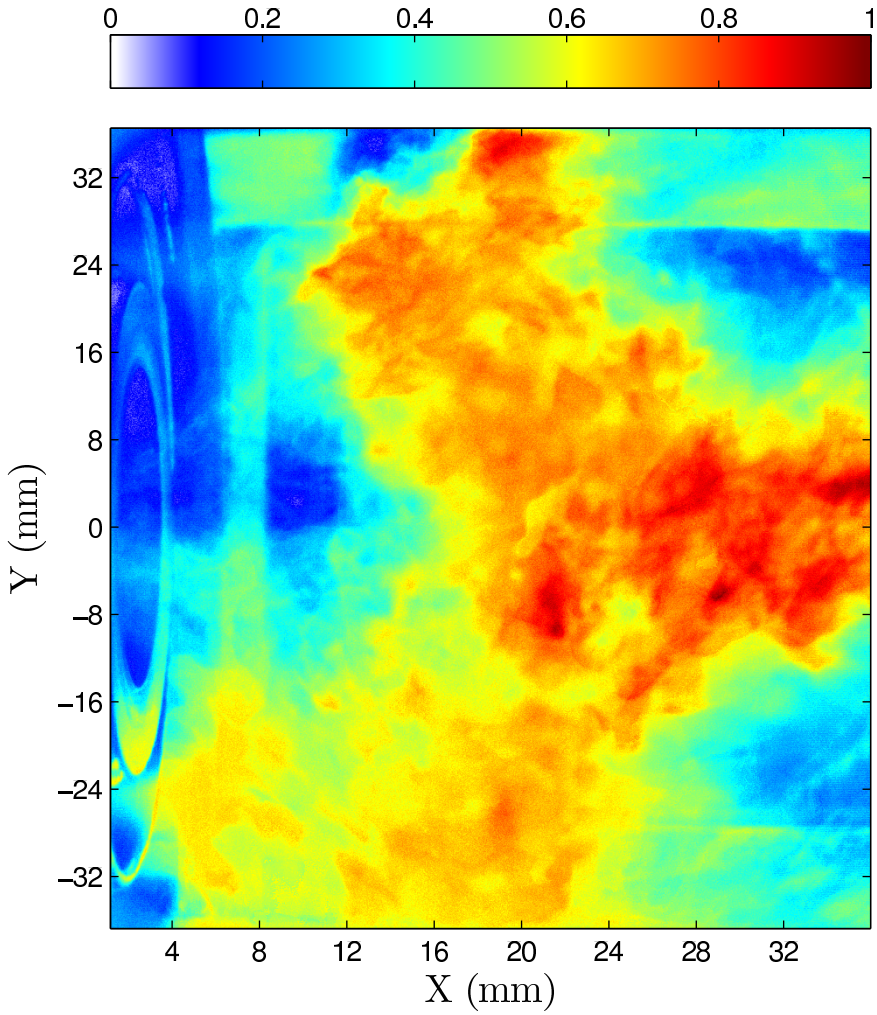

Figure 5.14: Rayleigh index distribution of $U/d = 4900\ \mathrm{s}^{-1}$.

relaxation of the heat release are not entirely independent of each other.

The Rayleigh index distribution shown in Fig. 5.19 provides a very clear picture of the regions of the combustor that amplify and dampen the oscillations. The pilot cone for this condition has negative values of the Rayleigh index which confirms that the pilot is stable as expected. The highest indices are in the corners since the heat release fluctuations that drive the pressure fluctuations are in the corners. The presence of a high index in the corners lends credence to the suggestion by Huang and Yang (2004) that the addition of cold flow into the corners should lead to a more stable system.

5.4 The Flashback Mechanism

The results shown in the previous section allow us to formulate a mechanism for gas turbine combustion instability that explains not only the results from the GE TAPS combustor but the results of other researchers as well. As explained in §1.2.3, there are two mechanisms that are widely regarded as being the most important: flame-vortex interaction and equivalence ratio oscillations. Both of these mechanisms however fail in explaining the trends described earlier. The chemiluminescence images clearly show a much larger variation in the flame surface area and subsequent heat release than can be accredited to flame-vortex interaction. While pressure fluctuations in the combustor do cause fluctuations in the fuel flowrates (but not in the air mass flowrate), the percentage variation in the combustor pressure are too low to effect an appreciable oscillation in the equivalence ratio. Furthermore, the high speeed chemiluminescence images and simultaneous pressure measurements suggest that the dominant mechanism driving the instability is a flashback mechanism caused by a premixed flame front propagating into a premixed reactant pool in

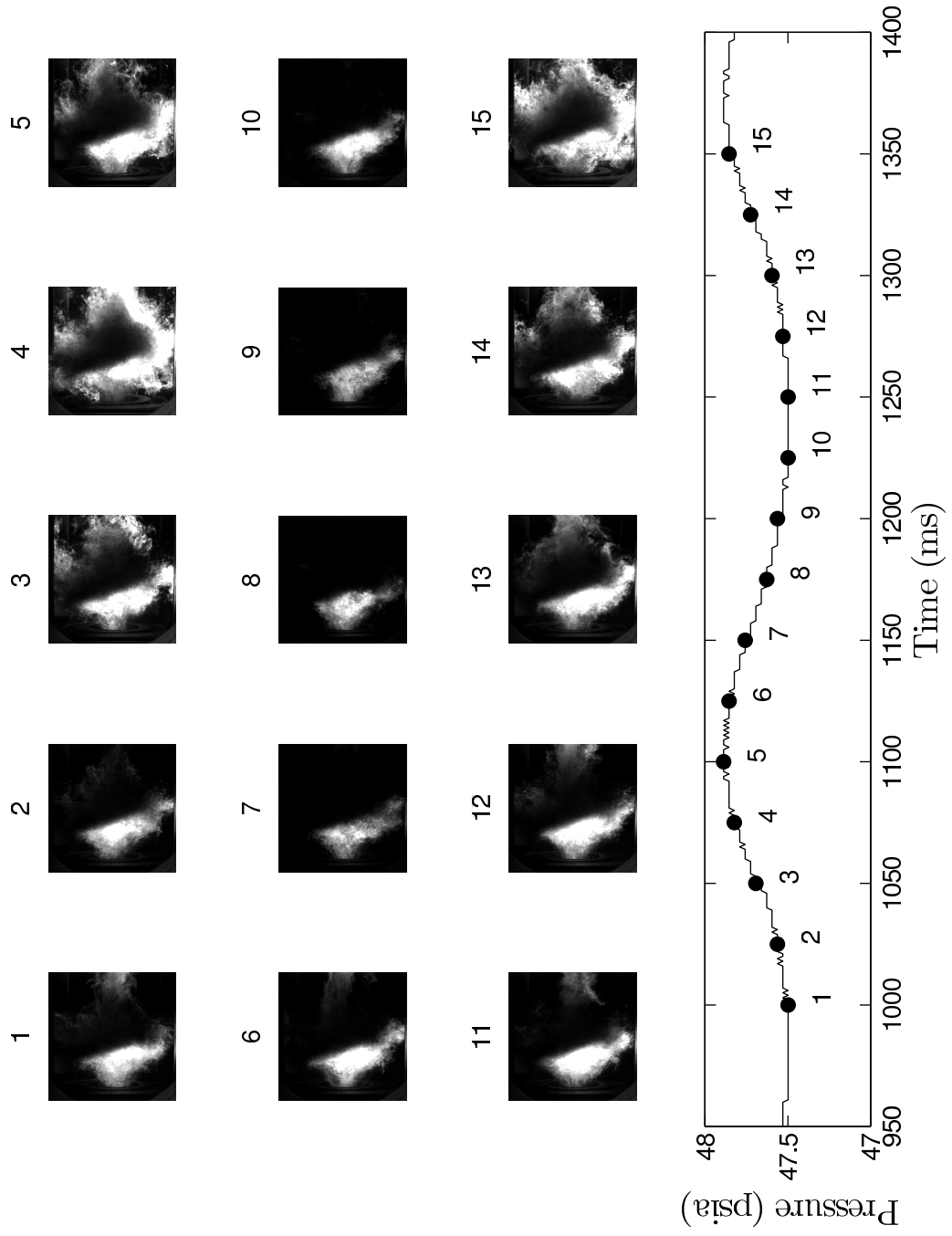

Figure 5.15: Simultaneously acquired chemiluminescence images and pressure measurements for $U/d = 2100$ s^{-1}. The images are shown for two periods of the combustion instability.

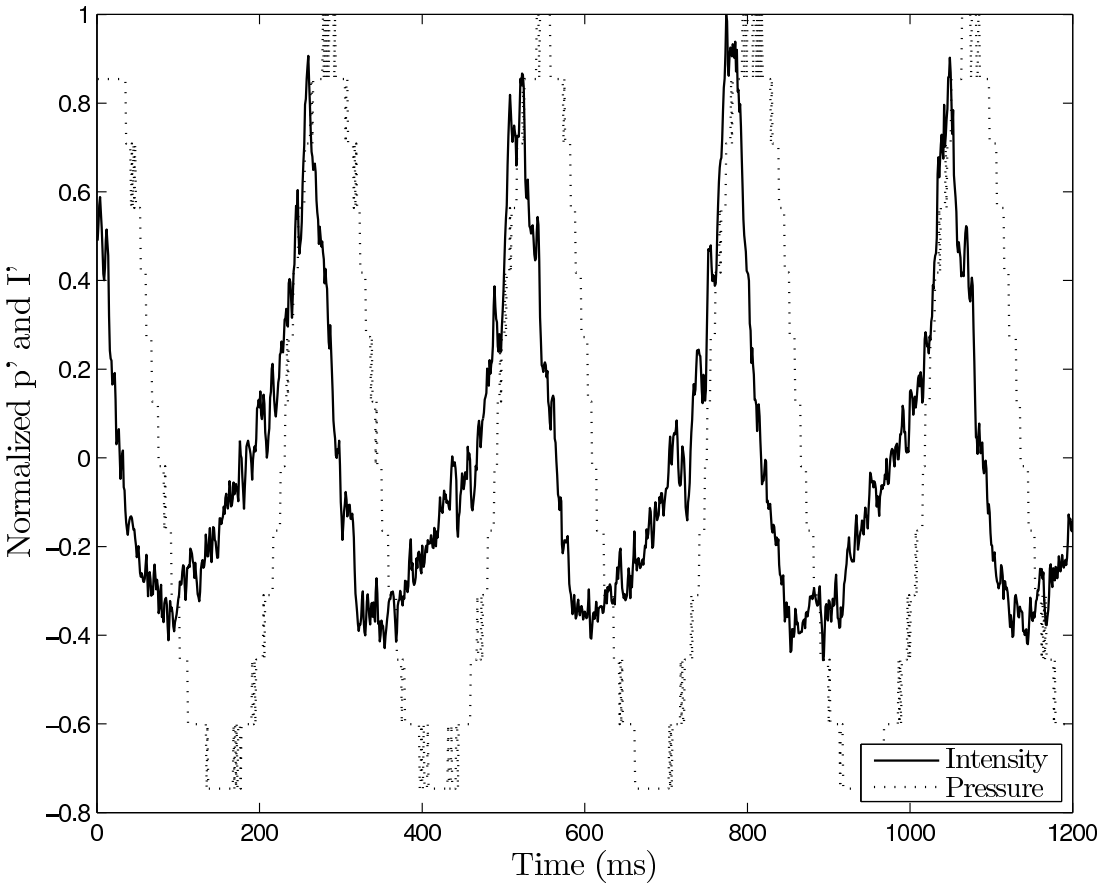

Figure 5.16: The fluctuating pressure and overall chemiluminescence intensity plotted over multiple periods for $U/d = 2100$ s^{-1}. It is clear that the combustor pressure lags the heat release in the combustor.

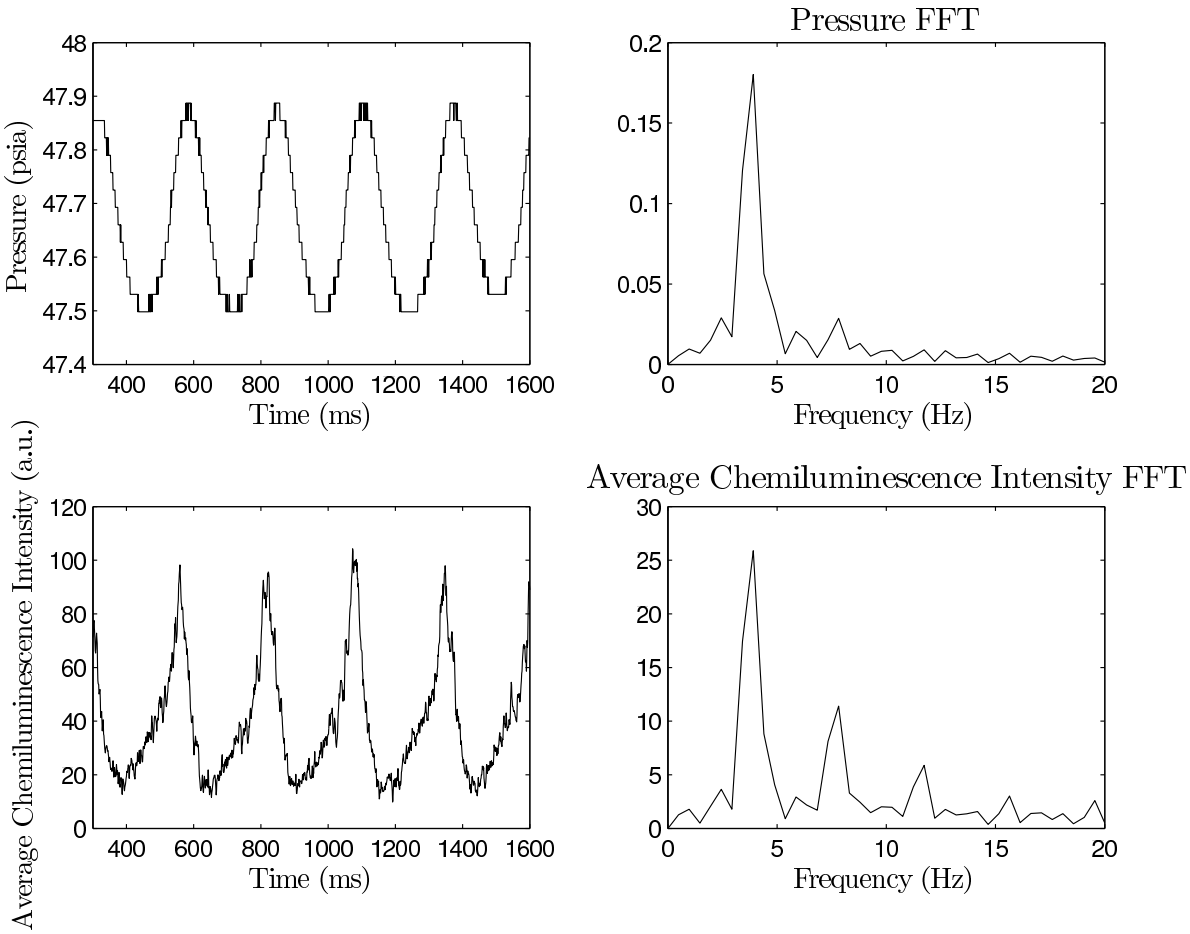

Figure 5.17: The absolute pressure and overall chemiluminescence intensity for $U/d = 2100$ s^{-1}. Also plotted are the power spectra. The spectra for both signals show a dominant peak at 3.91 Hz.

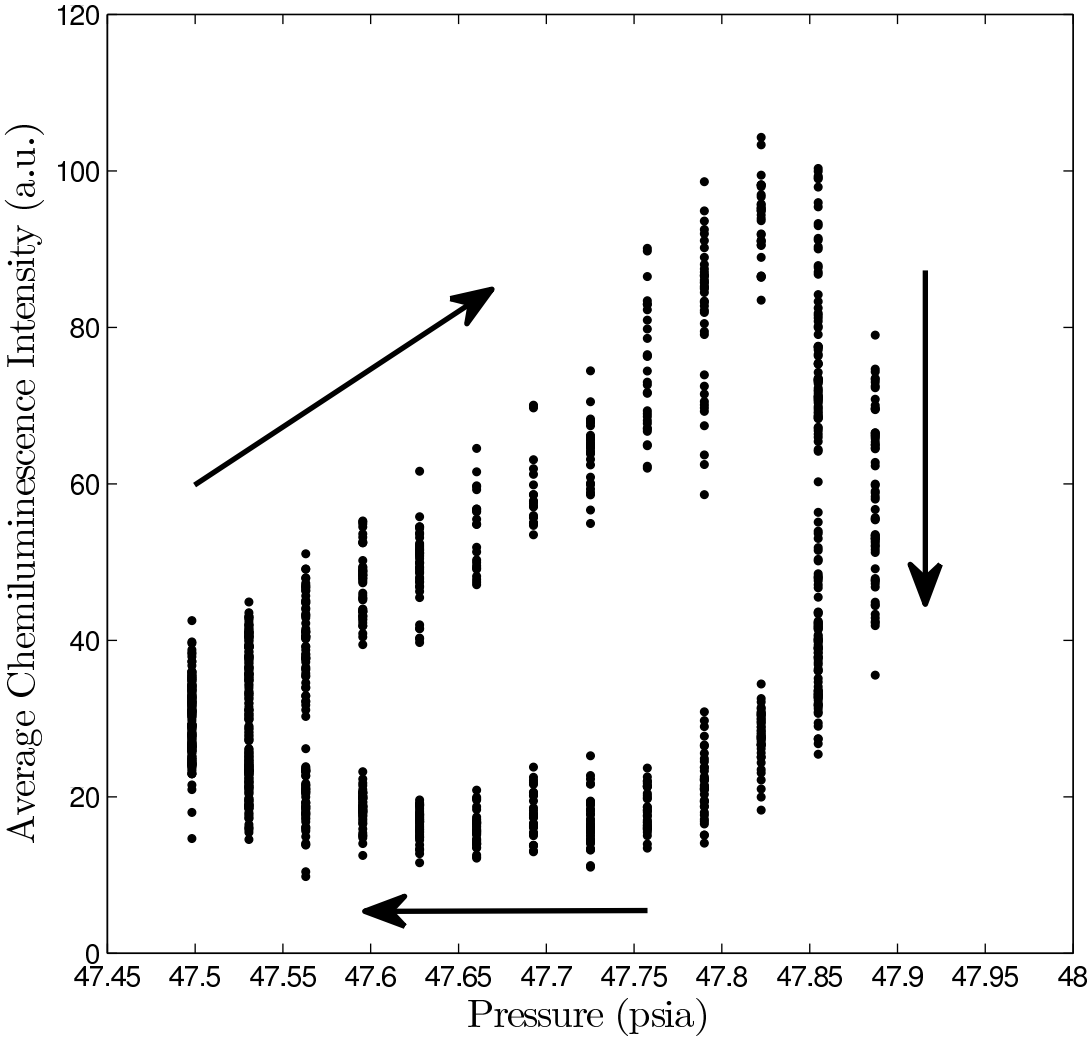

Figure 5.18: Scatter plot of the instantaneous pressure and overall luminescence intensity for $U/d = 2100$ s^{-1}. Each marker marks one instantaneous measurement and the arrows mark the direction of time. The three main phases of the instability are clearly visible.

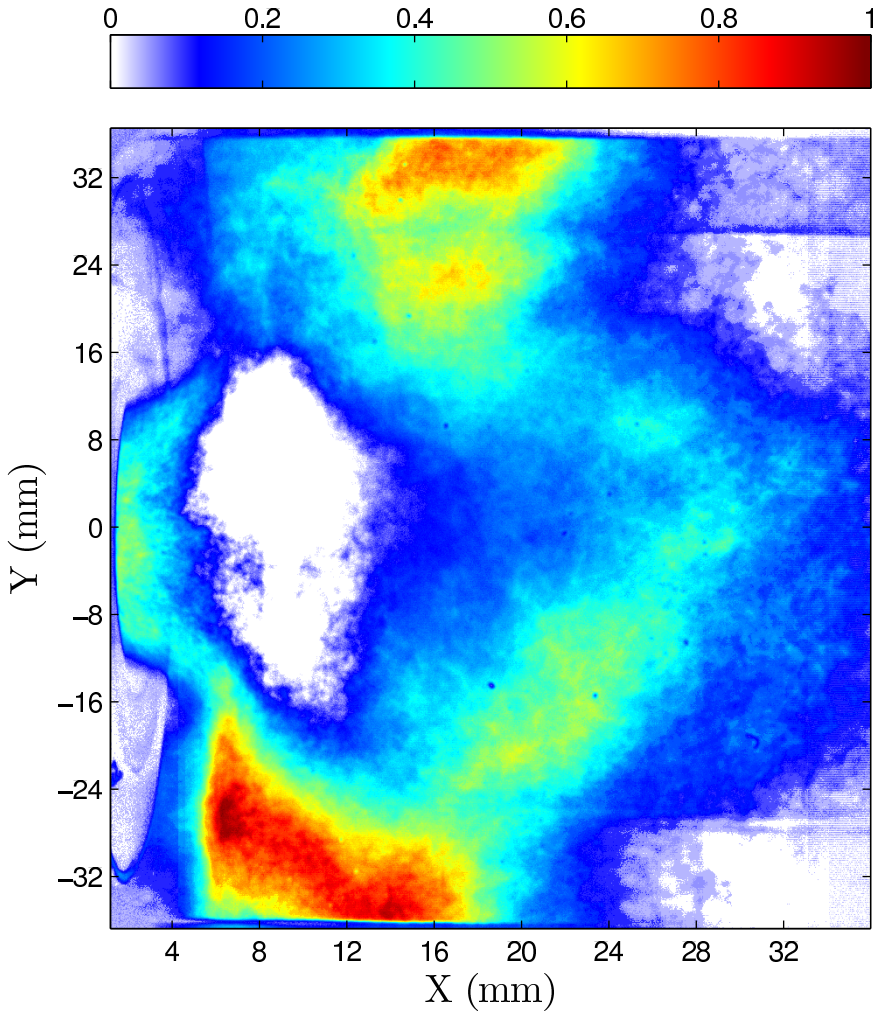

Figure 5.19: Rayleigh index distribution of $U/d = 2100\ \mathrm{s}^{-1}$.

the corner recirculation zone.

A schematic of the mechanism is shown in Fig. 5.20 where the instability process has been broken into two primary steps. In the first, reactants from the main flame collect in the Corner Recirculation Zone (CRZ) instead of burning stably in the mixing layer near the main annulus. This happens because of a weak velocity gradient in the mixing layer. As shown in Fig. 5.21, the local velocity gradient in the mixing layer is directly proportional to the global velocity gradient defined earlier and used to characterize the conditions. Therefore, as the main fuelling rate is increased, the effective equivalence ratio of the main increases, which correspondingly increases the flame speed of the main reactants. The increased flame speed means that an insufficiently high velocity gradient would be unable to sustain a stable flame. This explains why at lower values of U/d, the instability starts at lower values of the equivalence ratio. Along with velocity issuing from the main, the Lip RZ (LRZ) plays an important role in determining the velocity gradient in the mixing layer. The LRZ not only provides hot products from the pilot flame but slows down the flow from the pilot annulus, which further increases the velocity ratio across the mixing layer. Typically the flame needs to be perturbed to be pushed from its normally stable position in the mixing layer. As was seen from the velocity results, these perturbations come about through the vortices that are shed from the lip of the TAPS. The magnitude of these perturbations means that a velocity gradient that might otherwise be sufficient may be unable to sustain a stable main flame. In the absence of a stable flame in the mixing layer, the fresh incoming reactants collect in the CRZ. Some of the reactants also reach the pilot flame cone and burn as part of the pilot flame, causing the gradual increase in heat release from the pilot seen in the high speed images (cf. Fig. 5.5). At a certain point, the temperature and equivalence ratio

of the reactants rises (through heating by the pilot flame) to a sufficient level and a premixed flame propagates through the reactants in the CRZ. The flame front flashes back until it reaches the aft wall of the combustor, at which time it is extinguished due to the lack of any further reactants. This causes a rapid decline in the overall heat release before the combustor pressure has a chance to similarly relax, leading to an almost iso-baric decrease in the chemiluminescence intensity (cf. Fig. 5.8). A rapid decline in the combustor pressure follows with no change in the heat release. This process continues to drive the instability with striking repeatability as was seen for all three conditions.

The flashback mechanism as described above is shown in detail in Fig.'s 5.22 and 5.23. In Fig. 5.22 a sequence of images from the top half of the combustor shows a premixed flame front propagating towards the main annulus and into the CRZ. Another randomly selected sequence from the bottom half of the combustor is shown in Fig. 5.23 where the premixed flame front develops into a nearly vertical front (from 4 ms to 8 ms) and flashes back into the CRZ. Similar results were obtained by Huang and Yang (2004) in their computational study of instabilities in a dump combustor. Their result is shown in Fig. 5.24 where a flame front is clearly seen propagating into the CRZ towards the dump plane.

5.4.1 Proposed Model of the Flashback Oscillation Frequency

The flashback mechanism proposed here can be used to develop a model of the instability that predicts the frequency of the oscillations. As described earlier, the instability starts with the fact that a main flame does not sit in its stable location and therefore does not provide a fixed location for the incoming reactants to combust. Thus, the cycle begins with a given volume being filled with premixed reactants. The

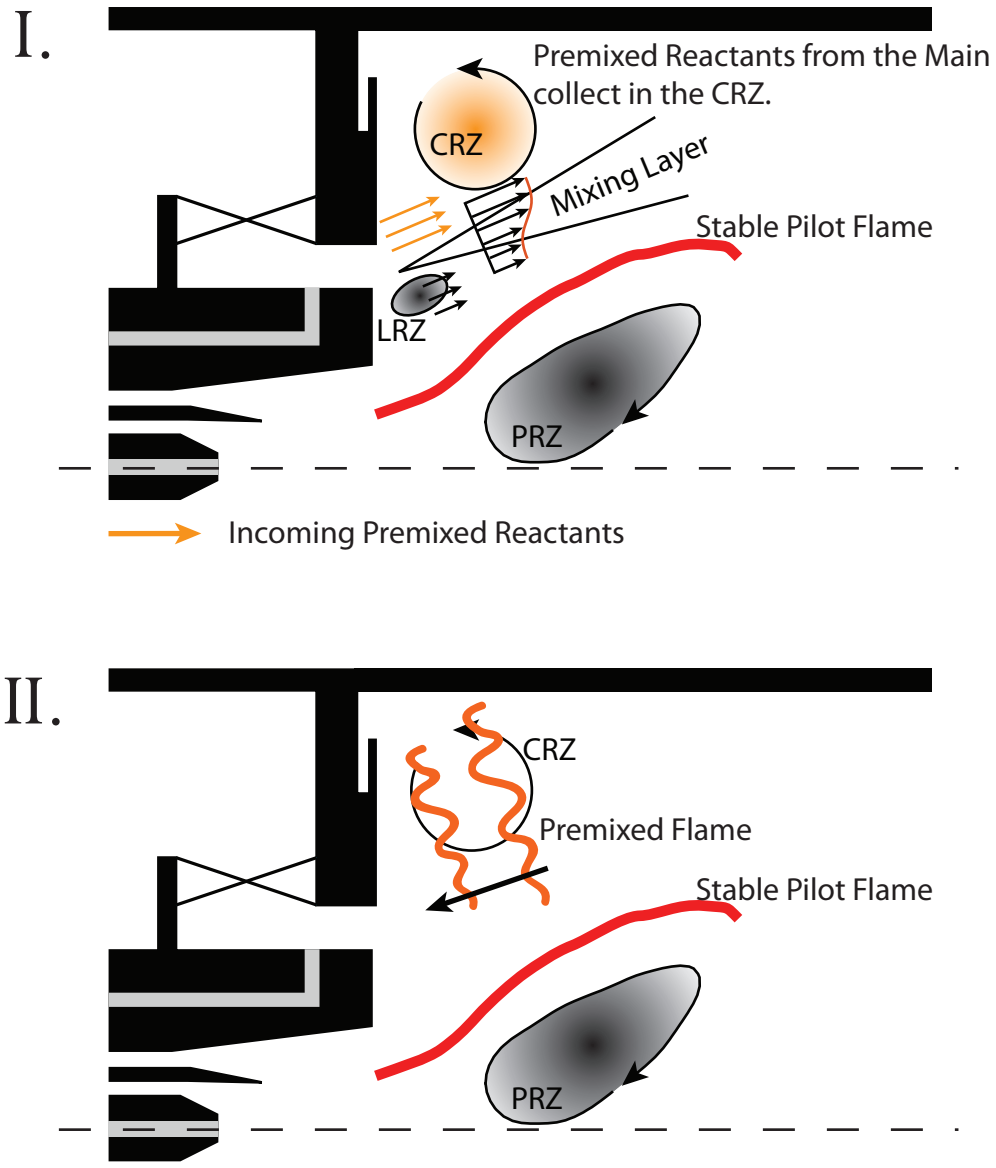

Figure 5.20: A schematic illustrating the flashback phenomena driving the instability in the GE TAPS combustor. In the first phase, large perturbations combined with a weak velocity gradient prevent the existence of a stable main flame in the mixing layer. In the absence of a flame, reactants from the main annulus collect in the CRZ. After a gradual process wherein the heat release in the pilot increases, a premixed flame propagates through the reactants in the CRZ as shown in II. CRZ: Corner RZ, PRZ: Primary RZ, LRZ: Lip RZ.

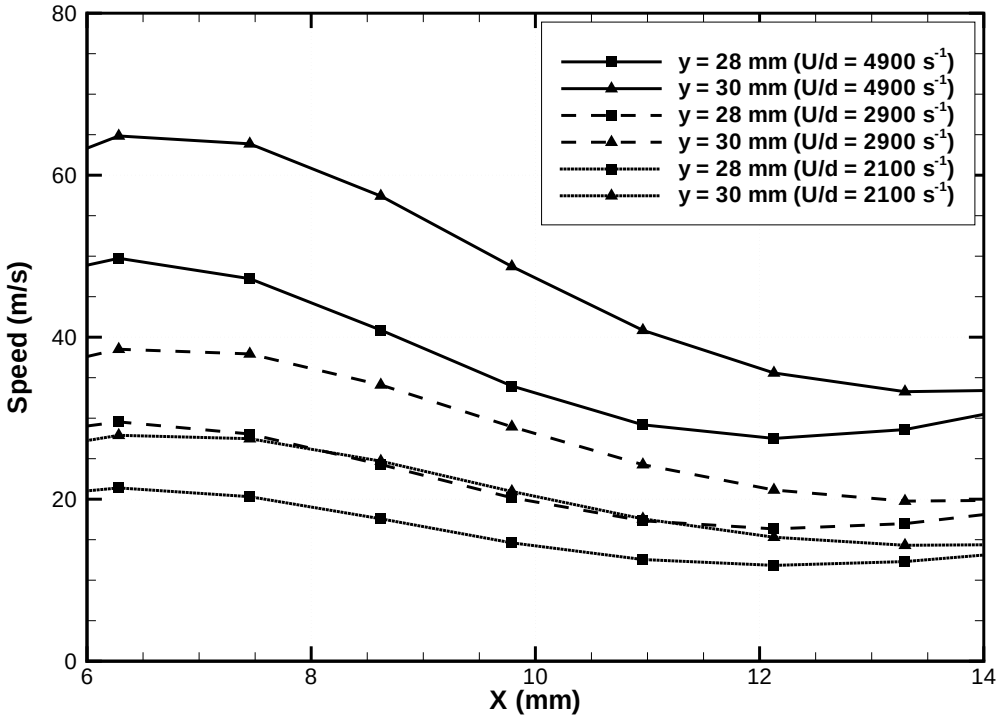

Figure 5.21: The speed of the flow exiting the main annulus at two different radial locations and at the three U/d tested. The negative slope of the curves quantifies the local velocity gradient ($\mathrm{d}U/\mathrm{d}x$), which is directly proportional to the global velocity gradient (U/d).

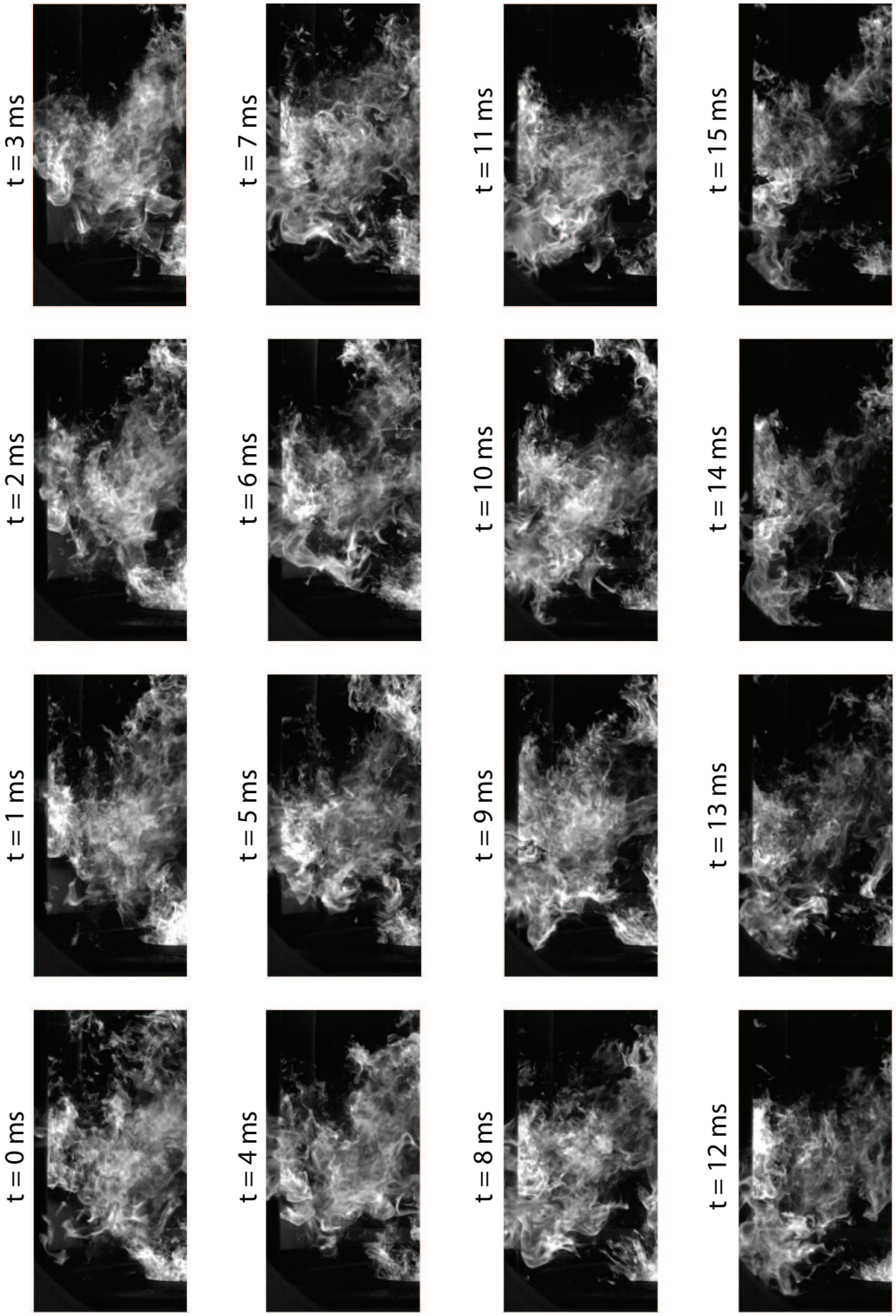

Figure 5.22: A sample sequence of chemiluminescence images showing the flashback process. Only the top half of the combustor is shown. A flame front can be seen propagating upstream of the pilot flame cone near the top of the images.

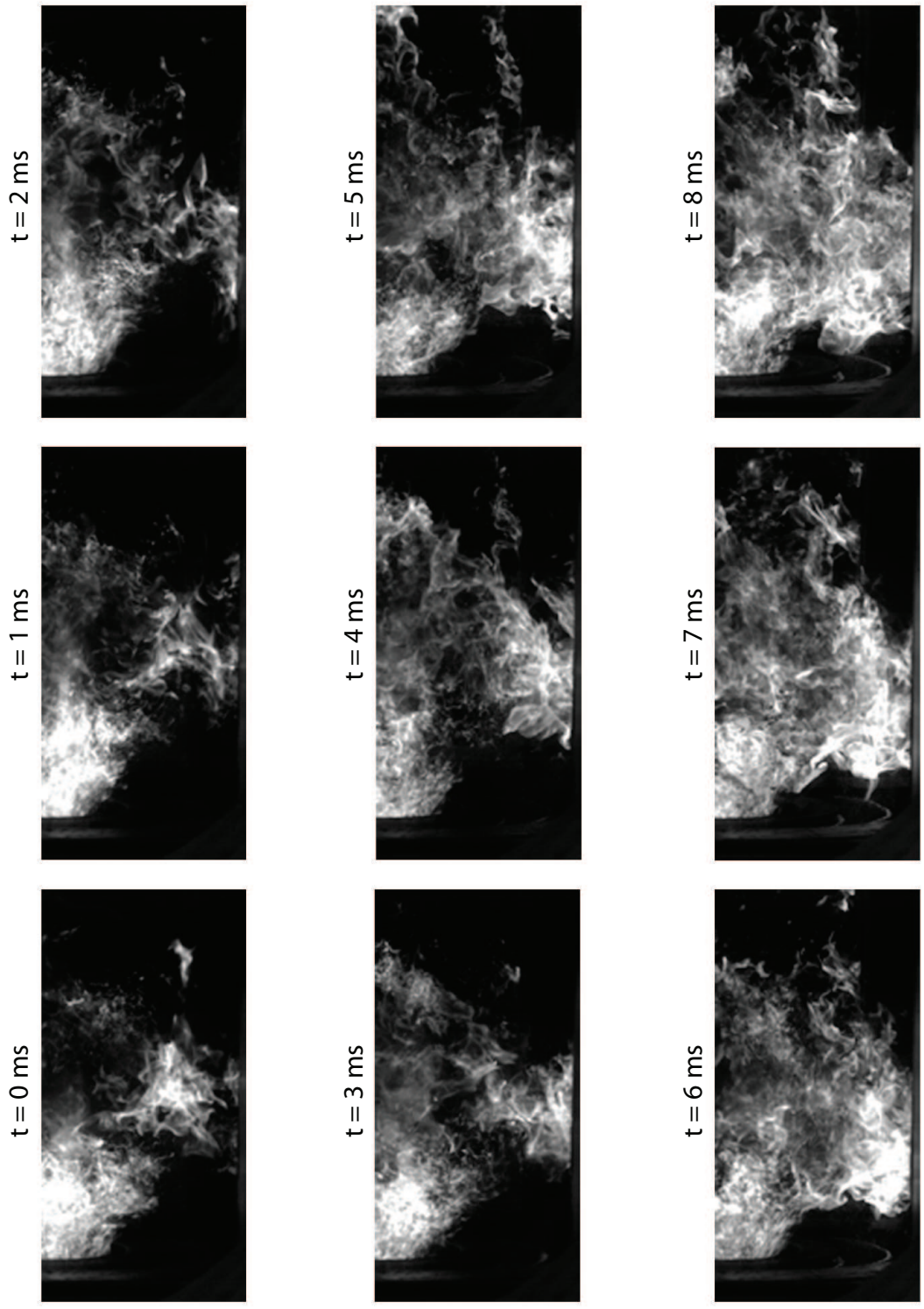

Figure 5.23: A sample sequence of chemiluminescence images showing the flashback process. Only the bottom half of the combustor is shown. A nearly vertical flame front flashes back towards the main annulus in the CRZ.

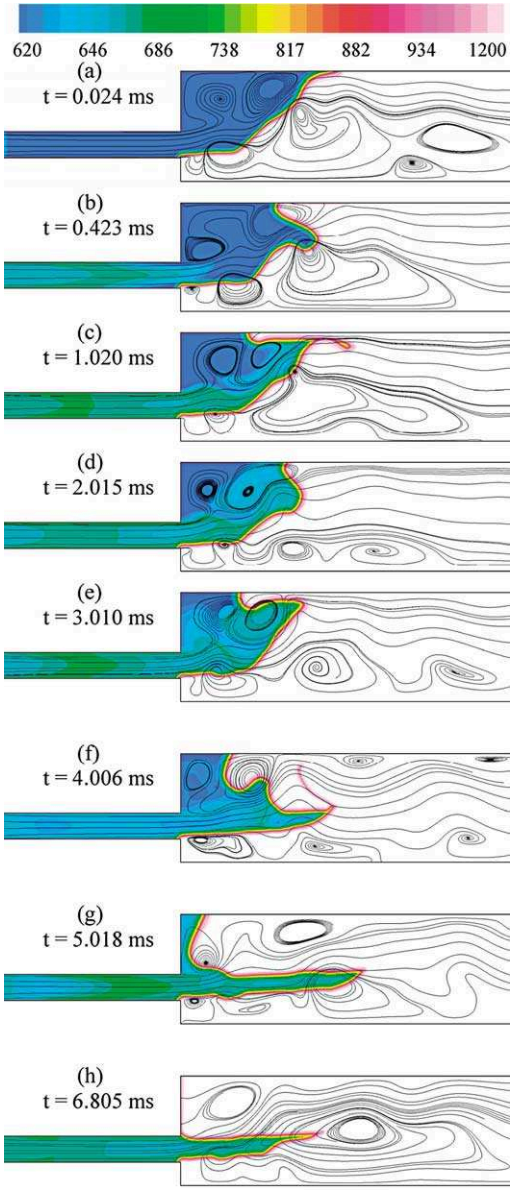

Figure 5.24: LES simulation of the flashback phenomena in a dump combustor by Huang and Yang (2004).

associated timescale of this process is then

$$\tau_{fill} = \frac{V}{\dot{Q}}, \tag{5.3}$$

where V is the volume being filled and $\dot{Q}$ is the volume flowrate of the reactants out of the main annulus. Upon being filled, a flame propagates into the length of this volume with a characteristic timescale,

$$\tau_{burn} = \frac{L}{S_b}, \tag{5.4}$$

where L is the length of the premixed region (the CRZ) and S_b is the laminar burning velocity of premixed Jet-A and air. The total period of the process will therefore be $T = \tau_{fill} + \tau_{burn}$. The geometry used to define the timescales is shown schematically in Fig. 5.25. The volume (V) being filled with premixed reactants is assumed to be a torus with an inner radius (r_{inner}), an outer radius (r_{outer}), and length (L). The volume used in the model therefore is $V = \pi \left(r_{outer}^2 - r_{inner}^2\right) L$. Based on the chemiluminescence images, the dimensions of the torus were set to a constant with $r_{outer} = 60$ mm and $r_{inner} = 40$ mm. Since the flame is idealized as propagating through the length of the CRZ, the length (L) should be equal to the size of the recirculation zone. Although the CRZ could not be resolved with PIV, its size is expected to be on the order of the step height creating the recirculation zone. Therefore L was set equal to the dimensions of one step height, or $L = 30$ mm, making $V = 1.88 \times 10^{-4}$ m^3.

The volumetric flowrate ($\dot{Q}$) of the reactants was measured from the PIV results. The laminar burning velocity was obtained from the empirical relationship given for JP-10-Air mixtures by Parsinejad et al. (2006) as

$$S_b = 62 \left(1 - 1.51 \left(1 - \phi\right) - 0.89 \left(1 - \phi\right)^2\right) \left[\frac{T_u}{450}\right]^{2.02} [p]^{-0.16}, \tag{5.5}$$

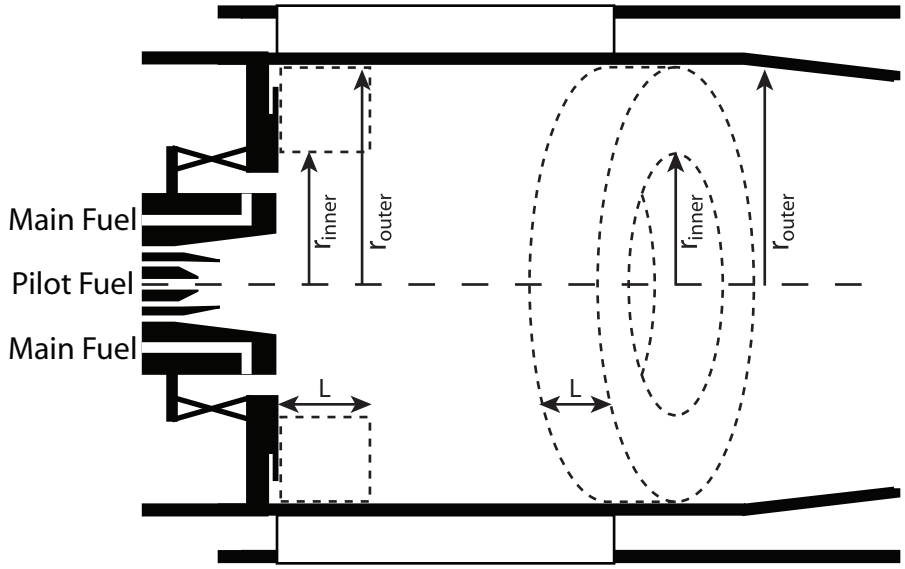

Figure 5.25: Schematic of the combustor defining the relevant geometry for the frequency model. The "boxes" indicated by the dashed lines are a cross-sectional cut of the volume (V). Shown in the right (inset within the combustor) is a three-dimensional view of the volume.

where S_b is the laminar burning velocity (in cm/s), ϕ is the equivalence ratio of the reactants, T_u is the incoming reactant temperature (in K), and p is the combustor pressure (in atm). As can be seen, the burning velocity is only weekly dependent on pressure and is predominantly affected by the incoming reactant temperature and equivalence ratio. For all the cases tested, the temperature was kept constant at 505 K. The equivalence ratio of the reactants was computed in the same manner as was done for Fig. 5.2 and shown in Fig. 5.4. However, since the main fuel was not fully vaporized (Fig. 2.12) and due to incomplete mixing, the equivalence ratio of the reactants in the CRZ is less than that if complete mixing is assumed. To account for this, the equivalence ratio used in Eqn. 5.5 was $\phi = \eta_{mixing}\phi_{main}$ with the mixing efficiency set to $\eta_{mixing} = 0.9$. With this definition, it was assumed that the during the instability, the flame flashes back through a leaner mixture than that issuing from the main annulus.

With these two timescales, the frequency of the oscillations becomes

$$f = \frac{1}{\tau_{fill} + \tau_{burn}}. \tag{5.6}$$

Due to the high velocities issuing from the main annulus, it was found that $\tau_{fill} \ll \tau_{burn}$. The frequency of the oscillations therefore is effectively $f = 1/\tau_{burn} = S_b/L$. From this model, it emerges that the frequencies of the instabilities are directly proportional to the burning velocity of the reactants issuing from the main annulus. The results of this model, along with the measured frequencies are shown in Fig. 5.26. The conditions for the experimental results shown in Fig. 5.26 are given in Table 5.2 and include the three cases described in detail in §5.3.1 and §5.3.2. The measured frequencies are seen to be linearly proportional to the laminar burning velocity and the model does a good job at predicting the frequency of the combustor instability. This result further bolsters the instability mechanism described in §5.4 as being the dominant mechanism driving the instabilities. The negative slope observed in Fig. 5.2 can also be explained through the dependence of the frequency on S_b. As noted, there is a short duration between the flashback events during which time the CRZ is filled with reactants and heated by the pilot flame. With higher pilot fuel flowrate, and corresponding increase in pilot flame length (Fig. 3.7), there is more heat release from the pilot flame. This increases the heat transfer into the CRZ and the higher temperature of the reactants in the CRZ allows for a reaction to occur at a lower equivalence ratio.

The frequency model as described could be further enhanced primarily through a better model for the laminar burning velocity and the properties of the unburnt reactants in the CRZ. Currently, Eqn. 5.5 is the best available fit for the laminar burning velocity of Jet-A and is reported as being valid only for $0.7 < \phi < 1$. The

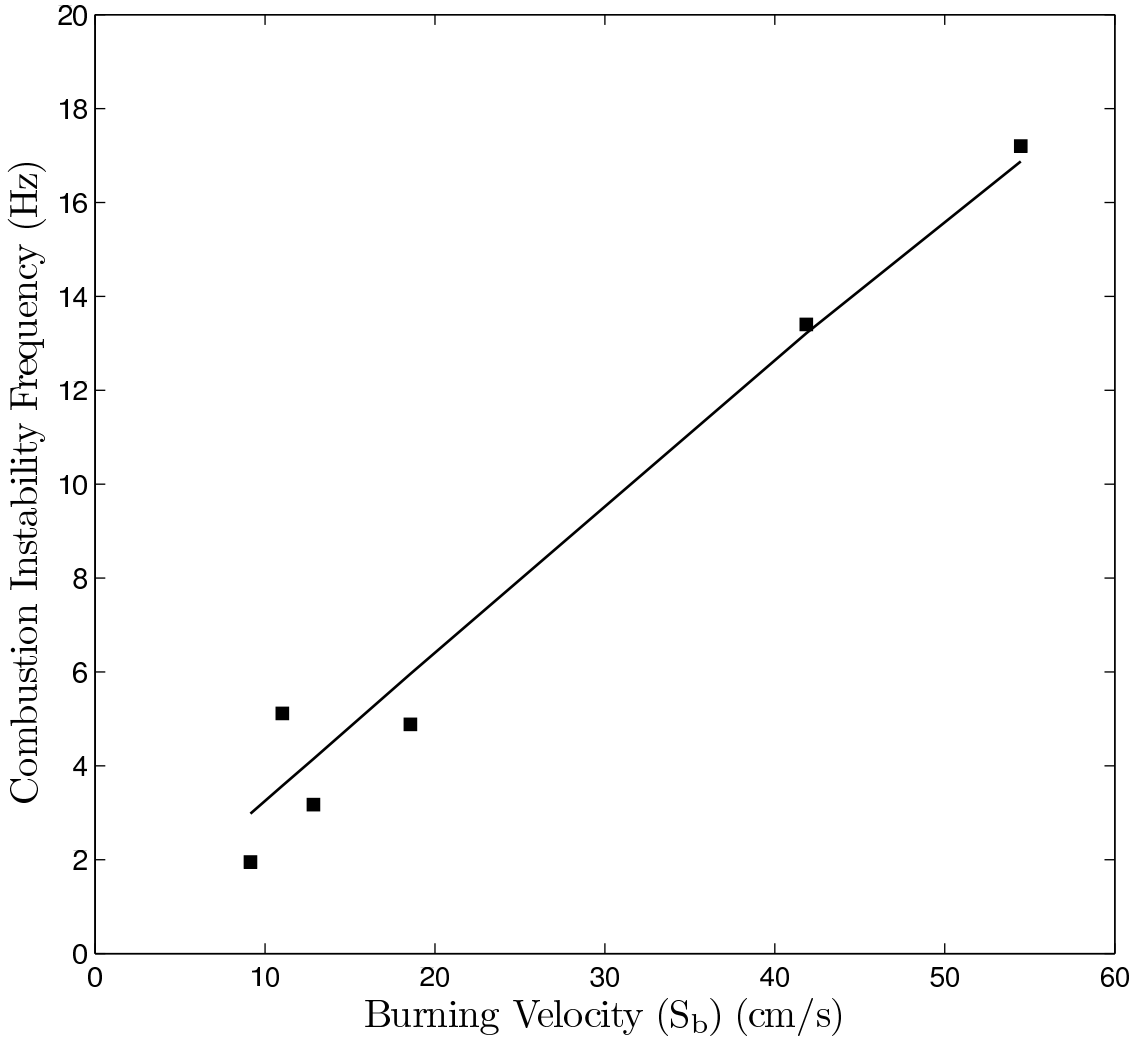

Figure 5.26: The model used to predict the frequencies of the combustor instabilities. The square markers are experimentally measured frequencies and the straight line is the model given by Eqn. 5.6.

lack of other results in the published literature therefore necessitated extending this burning velocity correlation to the leaner mixtures encountered in the TAPS combustor. Since the burning velocity is strongly dependent on the equivalence ratio, this undoubtedly affects the accuracy of the model's predictions. Also, a better understanding of the mixing efficiency and temperature of the unburnt reactants will help to enhance the model. It is clear through the chemiluminescence images that there is a finite residence time of the reactants in the CRZ during which time they are presumably pre-heated by the pilot flame. As it was not possible to accurately ascertain the temperature of the reactants immediately prior to the flashback phenomena, they were assumed to be equal to the temperature of the fresh incoming reactants issuing from the main annulus. Even with these simplistic assumptions however, Fig. 5.26 shows good agreement between the measured and predicted frequencies and confirms that the instabilities in the combustor are caused by a periodic flashback of the flame through the premixed reactants in the CRZ.

Global Velocity Gradient (U/d) s^{-1}	Main Fuel Flowrate ($\dot{m}_{f,m}$) g/s	Pilot Fuel Flowrate ($\dot{m}_{f,p}$) g/s	Total Volumetric Flowrate ($\dot{Q}$) $\times 10^{-2}$ m^3/s	ϕ'	S_b cm/s	τ_{fill} $\times 10^{-3}$ s	τ_{burn} $\times 10^{-2}$ s	Predicted Instability Frequency (f) Hz
4900	1.41	3.47	4.50	0.85	54.5	4.2	5.5	16.9
4900	1.41	3.08	4.71	0.75	41.8	4.0	7.2	13.2
2900	1.41	2.49	3.04	0.61	18.6	6.2	16.2	5.96
2100	1.10	2.35	2.41	0.57	12.8	7.8	23.3	4.14
2100	1.10	2.30	2.43	0.56	11.0	7.8	27.2	3.57
2100	1.41	2.25	2.38	0.55	9.15	7.9	32.8	2.98

Table 5.2: The five experimental conditions for the data plotted in Fig. 5.26. The global velocity gradient is computed based on the incoming flow velocity that was altered by altering the combustor pressure. ϕ' is the equivalence ratio of the reactants in the CRZ. S_b is the laminar burning velocity computed from Eqn. 5.5. The predicted instability frequency is the frequency computed based on the two relevant timescales (τ_{fill} and τ_{burn}) and the model (Eqn. 5.6). $T_3 = 505$ K and $\dot{m}_{air,total} = 0.228$ kg/s for all cases.

CHAPTER VI

Conclusions

This study has produced data for and insight into the stable and unstable modes of operation in an LPP gas turbine combustor. A GE TAPS injector was mounted in a new high pressure gas turbine combustor facility at the University of Michigan. The facility was designed and built during the course of this study. This unique facility allowed for the operation of the combustor with high flowrates of preheated air at elevated pressures. The use of liquid Jet-A fuel also ensured that the spray dynamics, vaporization characteristics, and heat release from the actual fuel used in gas turbine combustors was captured. High optical access through fused silica windows allowed the use of advanced laser diagnostics including in the ultra-violet range to probe both the flow field and flame properties.

Particle Imaging Velocimetry was used to obtain quantitative data on the flow field. Two components of velocity on a plane intersecting the centerline of the combustor provided insight into the location, shape, and strength of key flow features such as shear layers and recirculation zones. Derived turbulence and gradient quantities shed further light on the flow field. PIV was especially used to understand the instantaneous flow field and unsteady nature of the combustor.

Planar Laser Induced Fluorescence of the formaldehyde molecule was used to

study the flame location and structure. In order to further the understanding of the PLIF signal, calibration experiments were conducted with the simultaneous use of CH PLIF in an unconfined calibration burner. The average flame location data was used to assess instantaneous flow structures in the vicinity of the flame.

High speed chemiluminescence images along with simultaneous measurements of the combustor pressure were used to formulate a mechanism describing the unstable mode of operation of the combustor. A simple model based on the stable results and the proposed mechanism was developed to predict the frequencies of the instabilities. The major findings and conclusions from this work follow.

6.1 The Stable Operation

1. **Isothermal Flow Field**

    a. The non reacting flow showed the existence of a large recirculation zone (denoted the Primary Recirculation Zone - PRZ) encompassing almost the entire field of view with reverse axial flow (negative axial velocities). The PRZ was clearly the artefact of the combined effects of vortex breakdown and wake of the injector.

    b. A smaller recirculation denoted the Lip Recirculation Zone (LRZ) existed near the outer edge of the injector between the pilot and main flows. The LRZ was caused by the wake behind the lip of the injector.

    c. Two primary regions of positive axial flow representing the pilot flow and main flow were visible. Both flows issued at an angle from the injector as indicated by the positive radial velocities in those regions. These regions of flow issuing into the combustor also had markedly higher values of

turbulence intensity than the turbulence in the PRZ.

d. Strong shear layers were present at the edges of the recirculation zones. Instantaneous images highlighted discrete eddies at the edges of the recirculation zones with flow issuing from the pilot flow into the PRZ and vice versa. There was considerable spatial variation in the edge of the PRZ and the average flow field masked the instantaneous flow structures.

2. **Reacting Flow Field**

a. Significant differences in the mean flow field were observed between the non-reacting and reacting flows. The presence of a pilot flame caused a drastic reduction in the size and shape of the PRZ. Acceleration due to heat release caused the PRZ to appear as an oval shaped zone on either side of the centerline. Positive axial velocities along the centerline meant that the PRZ was now a toroidal recirculation zone.

b. The area of the PRZ computed from the mean flow field was considerably lower than the mean of the instantaneous areas. This discrepancy was found to be due to the positive skewness in the distribution of the axial velocities along the edge of the PRZ. It is suggested that accurately predicting the skewness is an important parameter for any model.

c. The size and location of the LRZ remained constant between the non-reacting and reacting flow fields confirming that the LRZ is the wake behind the lip of the TAPS injector. The LRZ was found to enhance the local velocity gradients in the mixing layer between the pilot flow and main flow.

d. The mean flame contour obtained from PLIF showed the PRZ to be completely inside the pilot flame cone.

e. The region between the pilot flow and PRZ can be approximated as a flow over a cavity. This suggested that a first order insight can be obtained by modelling the flow in this region as a mixing layer. It was shown that the growth rate of the mixing layer is not constant, consistent with an axially varying density through the mixing layer. The density ratio between the pilot flow and flow in the PRZ increased monotonically as the flame tip was approached.

f. Heat release from the pilot flame created significant turbulence intensities along the centerline. Strong shear layers existed in the region between the pilot flow and PRZ and between the pilot flow and main flow, as evidenced by regions of high vorticity and shear strain rate.

g. Instantaneous flow fields highlight significant detail in the flow that is masked in the mean. Vortical structures and stagnation points are observed in the vicinity of the flame in all instances.

h. The presence of the main flame does not drastically change the flow field in the available field of view. The single biggest difference is in the turbulence intensities in the main flow. These are considerably reduced by the presence of the flame.

i. The instantaneous images show a significant exchange of fluid between the pilot flow and main flow. Of special importance is the large volume of flow originating in the main annulus that was seen to turn towards the centerline and merge with the pilot flow. In the PLIF results, there was

an increase in the PLIF signal from the pilot flame with the existence of a main flame. Finally, the blowout results showed that blowout of the pilot flame occurred at a lower fuel flowrate when a non-trivial amount of main fuel was injected. The conclusion from all three of these separate results is that some percentage of fuel injected in the main annulus reacts in the pilot flame. Therefore, not all of the main fuel reacts as a lean premixed flame but rather as a diffusion flame, leading to important implications for the emissions of the combustor.

3. **Flame**

   a. The pilot existed as a hollow conical flame with reactions occurring on both the inner side and outer side of the fuel-rich spray region. Key parameters such as the flame length and cone angle were computed for a range of pilot fuel flowrates. These parameters serve as useful validation results for a model.

   b. The contours of flame surface density indicated higher densities along the outer edge of the flame than the inner edge. This difference is due to the presence of the LRZ near the outer edge which leads to increased wrinkling in that region. No analogous flow feature exists near the inner edge to cause the high degree of flame wrinkling.

   c. The main flame appeared as a separate flame issuing from the main annulus. No instantaneous images captured the base of the main flame so conclusions cannot be drawn on whether the flame is lifted or not. However, the main flame could not be stabilized without a pilot flame and it is unlikely that the main flame is attached to the main injectors, since then

it would not be dependent on the presence of the pilot flame considerably downstream.

d. A small region corresponding to the LRZ existed between the main flame and pilot flame where there was not measurable PLIF signal. This region is filled with hot products from the pilot flame which aids in the stability of the main flame. As noted earlier, this region also contains fresh reactants from the main annulus that react in the pilot flame. It is hypothesized that the region immediately downstream of the injector's lip is an important region for future studies. This region contains significant exchange of fluid between the pilot flow and main flow and it is likely that the base of the main flame is also anchored here.

6.2 The Unstable Operation

1. **Stability Limits**

   a. Low frequency (< 20 Hz) combustion dynamics were observed at different main fuel flowrates that were a function of the global velocity gradient issuing from the main. The global velocity gradient was defined as the average velocity issuing from the main annulus divided by the height of the main annulus. Based on the behavior of the dynamics, they have been termed flashback oscillations.

   b. At a given global velocity gradient, the flashback oscillations were observed when the main fuel flowrate (main equivalence ratio) was increased beyond a critical value. The critical main fuel flowrate was lower for lower global velocity gradients.

2. **Flashback Oscillations Mechanism**

   a. Simultaneous high speed chemiluminescence images and pressure measurements have allowed for the development of a mechanism that explains the instability. At a reduced global velocity gradient, the local velocity gradient in the mixing layer between the pilot flow and main flow is too weak to allow a stable main flame to exist. In the absence of the main flame, fresh reactants collect in the Corner Recirculation Zone (CRZ). A flame initiated by the pilot flame then propagates upstream through the reactants in the CRZ until it is extinguished at the upstream combustor wall. This process continues at a well defined frequency.

   b. The proposed mechanism also suggests that the frequency of the oscillations is inversely proportional to the time required to fill the CRZ and the time required to burn through the length of the CRZ. Since the time required to fill is negligible, it was found that the frequency scales linearly with the flame speed of the Jet-A/air mixture issuing from the main annulus. The measured frequencies agree well with the model.

BIBLIOGRAPHY

BIBLIOGRAPHY

Adrian, R., Christensen, K., Liu, Z., 2000. Analysis and interpretation of instantaneous turbulent velocity fields. Experiments in Fluids 29, 275–290.

Al-Abdeli, Y., Masri, A., 2003. Recirculation and flow field regimes of unconfined non-reacting swirling flows. Experimental Thermal and Fluid Science 27, 655–665.

Al-Abdeli, Y., Masri, A., 2004. Precession and recirculation in turbulent swirling isothermal jets. Combustion Science and Technology 176, 645–665.

Allen, M. G., Howe, R. D., Hanson, R. K., 1986. Digital imaging of reaction zones in hydrocarbon-air flames using planar laser-induced fluorescence of CH and C_2. Optics Letters 11 (3), 126–128.

Anderson, D., 1975. Effects of equivalence ratio and dwell time on exhaust emissions from an experimental premixing prevaporizing burner. In: ASME Paper 75-GT-69.

Ashcroft, G., Zhang, X., 2005. Vortical structures over rectangular cavities at low speed. Physics of Fluids 17, 015104.

Bäuerle, B., Hoffmann, F., Behrendt, F., Warnatz, J., 1994. Detection of hot spots in the end gas of an internal combustion engine using two-dimensional LIF of formaldehyde. Proceedings of the Combustion Institute 25, 135–141.

Beér, J., Chigier, N., 1983. Combustion Aerodynamics, 2nd Edition. Robert E. Krieger Publishing Company.

Bell, J., Day, M., Grcar, J., Lijewski, M., Driscoll, J. F., Filatyev, S. A., 2007. Numerical simulation of a laboratory scale turbulent slot flame. Proceedings of the Combustion Institute 31, 1299–1307.

Bento, D., Thomson, K., Gulder, O., 2006. Soot formation and temperature field structure in laminar propane-air diffusion flames at elevated pressures. Combustion and Flame 145, 765–778.

Bernier, D., Lacas, F., Candel, S., 2004. Instability mechanisms in a premixed prevaporized combustor. Journal of Propulsion and Power 20, 648–656.

Böckle, S., Kazenwadel, J., Kunzelmann, T., Shin, D.-I., Schulz, C., 2006. Single-shot laser-induced fluorescence imaging of formaldehyde with XeF excimer excitation. Applied Physics B - Lasers and Optics 70, 733–735.

Bombach, R., Käppeli, B., 1999. Simultaneous visualization of transient species in flames by planar-laser-induced fluorescence using a single laser system. Applied Physics B - Lasers and Optics 68, 251–255.

Brackmann, C., Nygren, J., Bai, X., Li, Z., Bladh, H., Axelsson, B., Denbratt, I., Koopmans, L., Bengtsson, P., Aldén, M., 2003. Laser-induced fluorescence of formaldehyde in combustion using third harmonic Nd:YAG laser excitation. Spectrochimica Acta, Part A: Molecular and Biomolecular Spectroscopy 59, 3347–3356.

Bray, K., 1990. Studies of the turbulent burning velocity. Proceedings: Mathematical and Physical Sciences 431, 315–335.

Brown, G., Roshko, A., 1974. On density effects and large structure in turbulent mixing layers. Journal of Fluid Mechanics 64, 775–816.

Bryant, A., 1998. Planar laser-induced fluorescence imaging of fuel mixing and the reacion zone in a supersonic combustor. Ph.D. thesis, University of Michigan.

Buckmaster, J., 2002. Edge-flames. Progress in Energy and Combustion Science 28, 435–475.

Bushe, W., Bilger, R., 1998. Direct numerical simulation of turbulent non-premixed combustion with realistic chemistry. Tech. rep., Center for Turbulent Research, Annual Research Briefs.

Candel, S., Poinsot, T., 1990. Flame stretch and the balance equation for the flame area. Combustion Science and Technology 70, 1–15.

Cantwell, B., 1981. Transition in the axisymmetric jet. Journal of Fluid Mechanics 104, 369–386.

Carter, C., Donbar, J., Driscoll, J., 1998. Simultaneous CH planar laser-induced fluorescence and particle image velocimetry in turbulent nonpremixed flames. Applied Physics B - Lasers and Optics 66 (1), 129–132.

Chao, Y., Leu, J., Hung, Y., Lin, C., 1991. Downstream boundary effects on the spectral characteristics of a swirling flowfield. Experiments in Fluids 10, 341–348.

Chong, M., Perry, A., Cantwell, B., 1990. A general classification of three-dimensional flow fields. Physics of Fluids 2, 765–777.

Clemens, N., 2002. Flow Imaging. John Wiley and Sons, pp. 390–419.

Clemens, N., Mungal, M., 1991. A planar Mie scattering technique for visualizing supersonic mixing flows. Experiments in Fluids 11, 175–185.

Clemens, N., Paul, P., 1995. Effects of heat release on the near field flow structure of hydrogen jet diffusion flames. Combustion and Flame 102, 271–284.

Coats, C., 1980. Comment on "Review of flashback reported in prevaporizing/premixing combustor". Combustion and Flame 37, 331–333.

Correa, S., 1992. A review of NO_x formation under gas-turbine combustion conditions. Combustion Science and Technology 87, 329–362.

Dallman, U., Hilgenstock, A., Riedelbauch, S., Schulte-Werning, B., Vollmers, H., 1991. On the footprints of three-dimensional separated vortex flows around blunt bodies. In: AGARD Conference Proceedings.

De Zilwa, S., Uhm, J., Whitelaw, J., 2000. Combustion oscillations close to the lean flammability limit. Combustion Science and Technology 160, 231–258.

Dimotakis, P., 1986. Two-dimensional shear layer entrainment. AIAA Journal 24, 1791–1796.

Donbar, J., Driscoll, J., Carter, C., 2000. Reaction zone structure in turbulent nonpremixed jet flames - from CH-OH PLIF images. Combustion and Flame 122, 1–19.

Donbar, J. M., 1998. Reaction zone structure and velocity measurements in permanently blue nonpremixed jet flames. Ph.D. thesis, University of Michigan.

Eckbreth, A., 1996. Laser Diagnostics for Combustion Temperature and Species. Vol. 3 of Combustion Science and Technology Book Series. Gordon and Breach Publishers.

Escudier, M., 1988. Vortex breakdown: Observations and explanations. Progress in Aerospace Sciences 25, 189–229.

Escudier, M., Keller, J., 1985. Recirculation in swirling flow: A manifestation of vortex breakdown. AIAA Journal 23, 111–116.

Fichot, F., Delhaye, B., Veynate, D., Candel, S., 1994. Strain rate modelling for a flame surface density equation with application to non-premixed turbulent combustion. Proceedings of the Combustion Institute 25, 1273.

Filatyev, S. A., Driscoll, J. F., Carter, C. D., Donbar, J. M., 2005. Measured properties of turbulent premixed flames for model assessment, including burning velocities, stretch rates, and surface densities. Combustion and Flame 141, 1–21.

Flower, W., Bowman, C., 1988. Soot production in axisymmetric laminar diffusion flames at pressures from one to ten atmospheres. Proceedings of the Combustion Institute 21, 1115–1124.

Fric, T., 1993. Effects of fuel-air unmixedness on nox emissions. Journal of Propulsion and Power 9, 708–713.

Fu, Y., Cai, J., Jeng, S., Mongia, H., 2005a. Confinement effects on the swirling flow of a counter-rotating swirl cup. In: ASME Paper GT2005-68622.

Fu, Y., Cai, J., Jeng, S., Mongia, H., 2005b. Reacting spray structure of a counter-rotating swirl cup. In: ASME Paper GT2005-68490.

Gaydon, A., Wolfhard, H., 1979. Flames, Their Structure, Radiation, and Temperature. Chapman and Hall.

Geers, L., Tummers, M., Hanjalic, K., 2005. Particle imaging velocimetry based identification of coherent structures in normally impinging multiple jets. Physics of Fluids 17, 1–13.

Ghosh, S., Hunt, J., 1998. Spray jets in a cross-flow. Journal of Fluid Mechanics 365, 109–136.

Glarborg, P., Alzueta, M., Kjærgaard, K., Dam-Johansen, K., 2003. Oxidation of formaldehyde and its interaction with nitric oxide in a flow reactor. Combustion and Flame 132, 629–638.

Gopala, Y., Lubarsky, E., Bibik, O., Zinn, B., 2007. Measurements of spray characteristics in preheated crossflowing air. 45th AIAA Aerospace Sciences Meeting and Exhibit 2007-1179, 1–13.

Gouldin, F., Depsky, J., Lee, S., 1985. Velocity field characteristics of a swirling flow combustor. AIAA Journal 23, 95–102.

Grumer, J., Harris, M., 1952. Flame-stability limits of methane, hydrogen, and carbon monoxide mixtures. Industrial and Engineering Chemistry 44, 1547–1553.

Grumer, J., Harris, M., Schultz, H., 1955. Flame-stability limits of ethylene, propane, methane, hydrogen, and nitrogen mixtures. Industrial and Engineering Chemistry 47, 1760–1767.

Hall, M., 1972. Vortex breakdown. Annual Review of Fluid Mechanics 4, 195–218.

Hanson, R. K., Seitzman, J. M., Paul, P. H., 1990. Planar laser-induced fluorescence imaging of combustion gases. Applied Physics B - Lasers and Optics 50, 441–454.

Harrington, J., Smyth, K., 1993. Laser-induced fluorescence measurements of formaldehyde in a methane/air diffusion flame. Chemical Physics Letters 202, 196–202.

Heitor, M., Moreira, A., 1992. Velocity characteristics of a swirling recirculating flow. Experimental Thermal and Fluid Science 5, 369–380.

Hochgreb, S., Dryer, F., 1992. A comprehensive study on CH_2O oxidation kinetics. Combustion and Flame 91, 257–284.

Howe, M., 1997. Edge, cavity, and aperture tones at very low mach numbers. Journal of Fluid Mechanics 33, 61–84.

Hsieh, A., Dahm, W., Driscoll, J., 1998. Scaling laws for NO_x emission performance of burners and furnaces from 30 kW to 12 MW. Combustion and Flame 114, 54–80.

Huang, Y., Yang, V., 2004. Bifurcation of flame structure in a lean-premixed swirl-stabilized combustor: transition from stable to unstable flame. Combustion and Flame 136, 383–389.

Huang, Y., Yang, V., 2005. Effect of swirl on combustion dynamics in a lean premixed swirl stabilized combustor. Proceedings of the Combustion Institute 30, 1775–1782.

Ikeda, Y., Kojima, J., Hashimoto, H., 2002. Local chemiluminescence spectra measurements in a high-pressure laminar methane/air premixed flame. Proceedings of the Combustion Institute 29, 1495–1501.

Ji, J., Gore, J., 2002. Flow structure in lean premixed swirling combustion. Proceedings of the Combustion Institute 29, 861–867.

Joedicke, A., Peters, N., Mansour, M., 2005. The stabilization mechanism and structure of turbulent hydrocarbon lifted flames. Proceedings of the Combustion Institute 30, 901–909.

Kalghatgi, G., 1984. Lift-off heights and visible lengths of vertical turbulent jet diffusion flames in still air. Combustion Science and Technology 41, 17–29.

Keller, J., Vaneveld, L., Korschelt, D., Hubbard, G., Ghoniem, A., Daily, J., Oppenheim, A., 1982. Mechanism of instabilities in turbulent combustion leading to flashback. AIAA Journal 20, 254–262.

Kortschik, C., Plessing, T., Peters, N., 2004. Laser optical investigation of turbulent transport of temperature ahead of the preheat zone in a premixed flame. Combustion and Flame 136, 43–50.

Law, C. K., 2006. Combustion Physics. Cambridge University Press.

Lee, J., Kim, K., Santavicca, D., 2000. Measurement of equivalence ratio fluctuation and its effect in heat release during unstable combustion. Proceedings of the Combustion Institute 28, 415–421.

Lee, J., Santavicca, D., 2003. Experimental diagnostics for the study of combustion intabilities in lean premixed combustors. Journal of Propulsion and Power 19, 735–750.

Lefebvre, A., 1999. Gas Turbine Combustion. Taylor and Francis.

Leibovich, S., 1978. The structure of vortex breakdown. Annual Review of Fluid Mechanics 10, 221–246.

Leong, M., McDonell, V., Samuelsen, G., 2001. Effect of ambient pressure on an airblast spray injected into a crossflow. Journal of Propulsion and Power 17, 1076–1084.

Less, D., Schetz, J., 1986. Transient behavior of liquid jets injected normal to a high-velocity gas stream. AIAA Journal 24, 1979–1986.

Li, G., Gutmark, E., 2004. Experimental study of large coherent structure in a swirl dump combustor. In: AIAA Paper 2004-133.

Li, G., Gutmark, E., 2005. Effect of exhaust nozzle geometry on combustor flow field and combustion characteristics. Proceedings of the Combustion Institute 30, 2893–2901.

Lieuwen, T., McManus, K., 2003. Combustion dynamics in lean-premixed prevaporized (LPP) gas turbines. Journal of Propulsion and Power 19, 721–721.

Lieuwen, T., Torres, H., Johnson, C., Zinn, B., 2001. A mechanism of combustion instability in lean premixed gas turbine combustors. ASME Transactions 123, 182–189.

Lieuwen, T., Zinn, B., 1998. The role of equivalence ratio oscillations in driving combustion instabilities in low NO_x gas turbines. Proceedings of the Combustion Institute 27, 1809–1816.

Lin, J., Rockwell, D., 2001. Organized oscillations of initially turbulent flow past a cavity. AIAA Journal 39, 1139–1150.

Lucca-Negro, O., O'Doherty, T., 2001. Vortex breakdown: a review. Progress in Energy and Combustion Science 27, 431–481.

Lyons, V., 1981. Fuel/air nonuniformity: Effect on nitric oxide emissions. AIAA Journal 20, 660–665.

Marble, F., Broadwell, J., 1977. Tech. rep., Project Squid Report TRW-9-PU.

Mazallon, J., Dai, Z., Faeth, G., 1999. Primary breakup of nonturbulent round liquid jets in gas crossflows. Atomization and Sprays 9, 291–311.

McCrain, L., Roberts, W., 2005. Measurements of the soot volume field in laminar diffusion flames at elevated pressures. Combustion and Flame 140, 60–69.

Meier, W., Duan, X. R., Weigand, P., 2006. Investigations of swirl flames in a gas turbine model combustor II: Turbulence-chemistry interactions. Combustion and Flame 144, 225–236.

Melling, A., 1997. Tracer particles and seeding for particle image velocimetry. Measurement Science and Technology 8, 1406–1416.

Menon, S., Patel, N., 2006. Subgrid Modeling for Simulation of Spray Combustion in Large-Scale Combustors. AIAA Journal 44, 709–723.

Midgley, K., Spencer, A., McGuirk, J., 2005. Unsteady flow structure in radial swirler fed fuel injectors. Journal of Engineering for Gas Turbine and Power 127, 755–764.

Mongia, H. C., 2003. TAPS - A 4^{th} generation propulsion combustor technology for low emissions. AIAA Paper, 2003–2657.

Najm, H., Knio, O., Paul, P., Wyckoff, P., 1998a. A study of flame observables in premixed methane-air flames. Combustion Science and Technology 140, 369–403.

Najm, H., Paul, P., Mueller, C., Wyckoff, P., 1998b. On the adequacy of certain experimental observables as measurements of flame burning rate. Combustion and Flame 113, 312–332.

Najm, H. N., Ghoniem, A., 1994. Coupling between vorticity and pressure oscillations in combustion instability. Journal of Propulsion and Power 10, 769–776.

Nakagawa, M., 2001. Experimental study of compressibility effects on entrainment and mixing in supersonic planar turbulent bluff-body wakes. Ph.D. thesis, University of Michigan.

Olofsson, J., Richter, M., Alden, M., Auge, M., 2006. Development of high temporally and spatially (three-dimensional) resolved formaldehyde measurements in combustion environments. Review of Scientific Instruments 77 (013104).

Panduranga Reddy, A., Sujith, R., Chakravarthy, S., 2006. Swirler flow field characteristics in a sudden expansion combustor geometry. Journal of Propulsion and Power 22, 800–808.

Parsinejad, F., Arcari, C., Metghalchi, H., 2006. Flame structure and burning speed of JP-10 air mixtures. Combustion Science and Technology 178, 975–1000.

Paul, P. H., Najm, H. N., 1998. Planar laser-induced fluorescence imaging of flame heat release rate. Proceedings of the Combustion Institute 27, 43–50.

Peeters, J., Mahnen, G., 1973. Reaction mechanisms and rate-constants of elementary steps in methane-oxygen flames. Proceedings of the Combustion Institute 14, 133–146.

Phillips, H., 1965. Flame in a buoyant methane layer. Proceedings of the Combustion Institute 10, 1277–1283.

Plee, S., Mellor, A., 1978. Review of flashback reported in prevaporizing/premixing combustors. Combustion and Flame 32, 193–203.

Poinsot, T., Trouve, A., Veynante, D., Candel, S., Esposito, E., 1987. Vortex driven acoustically coupled combustion instabilities. Journal of Fluid Mechanics 177, 265–292.

Porter, R. P., Clark, A. H., Kaskan, W. E., Browne, W. E., 1966. A study of hydrocarbon flames. Proceedings of the Combustion Institute 11, 907–917.

Rachner, M., Becker, J., Hassa, C., Doerr, T., 2002. Modelling of the atomization of plain liquid fuel jet in crossflow at gas turbine conditions. Aerospace Science and Technology 6, 495–506.

Raffel, M., Willert, C., Kompenhans, J., 2002. Particle Image Velocimetry: A Practical Guide (Experimental Fluid Mechanics). Springer.

Rasmussen, C., 2006. An experimental study of flame stability in a directly-fueled wall cavity with a supersonic free stream. Ph.D. thesis, University of Michigan.

Rasmussen, C., Dhanuka, S., Driscoll, J., 2007. Visualization of flameholding mechanisms in a supersonic combustor using PLIF. Proceedings of the Combustion Institute 31, 2505–2512.

Ratner, A., Driscoll, J. F., Donbar, J. M., Carter, C. D., Mullin, J. A., 2000. Reaction zone structure of non-premixed turbulent flames in the "intensely wrinkled" regime. Proceedings of the Combustion Institute 28, 245–252.

Rayleigh, J., 1994. The Theory of Sound. Macmillan.

Richter, M., Collin, R., Nygren, J., Alden, M., Hildingsson, L., Johansson, B., 2005. Studies of the combustion process with simultaneous formaldehyde and OH PLIF in a direct-injected HCCI engine. JSME International Journal Series B - Fluids and Thermal Engineering 48 (4), 701–707.

Robinson, S., Kline, S., Spalart, P., 1989. Quasi-coherent structures in the turbulent boundary layer. Part II: Verification and new information from numerically simulated flat-plate boundary layer. In: Kline, S., Afgan, N. (Eds.), Proceedings of Zaric Memorial Conference. Hemisphere, pp. 218–247.

Rockwell, D., Naudascher, E., 1978. Review - self sustaining oscillations of flow past cavities. Journal of Fluids Engineering 100, 152–165.

Sadanandan, R., Stohr, M., Meier, W., 2008. Simultaneous OH-PLIF and PIV measurements in a gas turbine model combustor. Applied Physics B - Lasers and Optics 90, 609–618.

Samaniego, J., Egolfopoulos, F., Bowman, C., 1995. CO_2^* chemiluminescence in premixed flames. Combustion Science and Technology 109, 183–203.

Samimy, M., Lele, S., 1991. Motion of particles with inertia in a compressible free shear layer. Physics of Fluids A 3, 1915–1923.

Schadow, K., Gutmark, E., Parr, T., Parr, D., Wilson, K., Crump, J., 1989. Large scale coherent structures as drivers of combustion instability. Combustion Science and Technology 64, 167–186.

Schetz, J., Padhye, A., 1977. Penetration and breakup of liquids in subsonic airstreams. AIAA Journal 15, 1385–1390.

Seyfried, H., Brackmann, C., Lindholm, A., Linne, M., Barreras, F., Bank, R., 2007. Optical diagnostics applied to a gas turbine pilot burner. AIAA Journal 45, 2702–2709.

Slessor, M., Zhuang, M., Dimotakis, P., 2000. Turbulent shear layer mixing: growth-rate compressibility scaling. Journal of Fluid Mechanics 414, 35–45.

Smith, W., 1990. Modern Optical Engineering: The Design of Optical Systems, 2nd Ed. McGraw Hill, NY.

Smooke, M., Mitchell, R., Keyes, D., 1989. Numerical solution of two-dimensional axisymmetric laminar diffusion flames. Combustion Science and Technology 67, 85–122.

Squire, H., 1960. Analysis of the vortex breakdown phenomenon. Tech. rep., Imperial College of Science and Technology Aeronautics.

Stouffer, S., Ballal, D., Zelina, J., Shouse, D., Hancock, R., Mongia, H., 2005. Development and combustion performance of a high pressure WSR and TAPS combustor. AIAA Paper, 2005–1416.

Sutton, J., 2005. Mixture fraction and scalar dissipation rate imaging in turbulent nonpremixed flames near exctinction. Ph.D. thesis, University of Michigan.

Syred, N., Beér, J., 1974. Combustion in swirling flows - a review. Combustion and Flame 23, 143–201.

Tambe, S., Jeng, S., Mongia, H., Hsiao, G., 2005. Liquid jets in subsonic crossflow. In: 43^{rd} AIAA Aerospace Sciences Meeting and Exhibit.

Taylor, E., Martin, M., Smits, A., 2005. Preliminary study of the turbulence structure in supersonic boundary layers using DNS data. In: 35th AIAA Fluid Dynamics Conference and Exhibit.

Thomson, K., Gulder, O., Weckman, E., Fraser, R., Smallwood, G., Snelling, D., 2005. Soot concentration and temperature measurements in co-annular, non-premixed CH_4/air laminar flames at pressures up to 4 MPa. Combustion and Flame 140, 222–232.

Ukeiley, L., Murray, N., 2005. Velocity and surface pressure measurements in an open cavity. Experiments in Fluids 38, 656–671.

Vandooren, J., deGuertechin, L., van Tiggelen, P., 1986. Kinetics in a lean formaldehyde flame. Combustion and Flame 64, 127–139.

Vaneveld, L., Hom, K., Oppenheim, A., 1982. Secondary effects in instabilities leading to flashback. AIAA Journal 22, 81–82.

Vanquickenborne, L., van Tiggelen, A., March 1966. The stabilization mechanism of lifted diffusion flames. Combustion and Flame 10, 59–72.

Venkataraman, K., Preston, L., Simons, D., Lee, B., Santavicca, D., 1999. Mechanism of combustion instability in a lean premixed dump combustor. Journal of Propulsion and Power 15, 909–918.

Watson, K., Lyons, K., Donbar, J., Carter, C., 1999a. Observations on the leading edge in lifted flame stabilization. Combustion and Flame 119, 199–202.

Watson, K., Lyons, K., Donbar, J., Carter, C., 1999b. Scalar and velocity field measurements in a lifted CH_4-air diffusion flame. Combustion and Flame 117, 257–271.

Watson, K., Lyons, K., Donbar, J., Carter, C., 2000. Simultaneous Rayleigh imaging and CH PLIF measurements in a lifted jet diffusion flame. Combustion and Flame 123, 252–265.

Weber, R., Dugue, J., 1992. Combustion accelerated swirling flows in high confinements. Progress in Energy and Combustion Science 18, 349–367.

Weigand, P., Meier, W., Duan, X. R., Stricker, W., Aigner, M., 2006. Investigations of swirl flames in a gas turbine model combustor I. Flow field, structures, temperature, and species distributions. Combustion and Flame 144 (1-2), 205–224.

Westerweel, J., 1997. Fundamentals of digital particle image velocimetry. Measurement Science and Technology 8, 1379–1392.

Westerweel, J., Dabiri, D., Gharib, M., 1997. The effect of a discrete window offset on the accuracy of cross-correlation analysis of digital PIV recordings. Experiments in Fluids 23, 20–28.

Wu, P., Kirkendall, K., Fuller, R., Nejad, A., 1997. Breakup process of liquid jets in subsonic crossflows. Journal of Propulsion and Power 13, 64–73.

Yoon, Y., 1994. An experimental study of a generic supersonic combustor. Ph.D. thesis, University of Michigan.

Yule, A., Chigier, N., Ralph, S., Boulderstone, R., Ventura, J., 1981. Combustion-transition interaction in a jet flame. AIAA Journal 19, 752–760.

Zhou, J., Adrian, R., Balachandar, S., Kendall, T., 1999. Mechanisms for generating coherent packets of hairpin vortices in channel flow. Journal of Fluid Mechanics 387, 353–396.